Air foil thrust bearings:

A thermo-elasto-hydrodynamic analysis

Vom Fachbereich Maschinenbau

an der Technischen Universität Darmstadt

zur

Erlangung des Grades eines Doktor-Ingenieurs (Dr.-Ing.)

genehmigte

DISSERTATION

vorgelegt von

Dipl.-Ing. Andreas Lehn

aus Karaganda

Berichterstatter:	Prof. Dr.-Ing. Bernhard Schweizer
Mitberichterstatter:	Prof. Dr.-Ing. Olaf Wünsch
Tag der Einreichung:	18.10.2016
Tag der mündlichen Prüfung:	01.02.2017

Darmstadt 2017

D17

Erklärung

Hiermit erkläre ich, dass ich die vorliegende Arbeit, abgesehen von den in ihr ausdrücklich genannten Hilfen, selbständig verfasst habe.

Baunatal, den 11.10.2016

Acknowledgements

First and foremost, I would like to express my gratitude to my academic advisor Professor Bernhard Schweizer for the possibility to write this work. Thank you for the intensive support, the freedom of research, and the encouragement throughout the whole time.

I am grateful to Professor Olaf Wünsch for reviewing this work and accommodating me for one year at the mechanical department of the university of Kassel.

Special thanks go to Dietmar Metz and his team from BorgWarner Turbosystems for the financial support, the constructive cooperation and the optical temperature measurements that are presented in this work.

Between all of my friendly colleagues I would like to express particular gratitude to Robert Schmoll and Marcel Mahner.

Robert, thank you for the countless discussions at lunch where you taught me about the difference between parsnip and parsley root, the architecture of micro-computers, and timbered houses. Your unlimited general knowledge and stringent way of thinking enriched my mind.

Marcel, it was a real pleasure for me to observe your exceptional mathematical talent every day in our shared office. Your kind of working served as an example for me and I account myself lucky for having such a valuable discussion partner on foil bearings and friend.

Abstract

A computational model for bump type air foil thrust bearings, which belong to the class of compliant hydrodynamic bearings, is developed. The computational model is able to calculate the pressure and temperature distribution in the bearing as well as the structural deformations of the bearing parts. Hydrodynamic, elastic, and thermal aspects of air foil thrust bearings are analysed in detail and design guidelines are derived. Systematic optimisation studies are performed for the shape of the lubricating gap with respect to a maximal load capacity. A Reissner-Mindlin type shell theory is applied for the top and the bump foil and different mechanisms that influence the stiffness of the compliant structure are discussed. The performance of air foil thrust bearings is compared to rigid thrust bearings for aligned, distorted and misaligned operating conditions. Based on a comprehensive thermal model, the main heat fluxes in the bearing are identified. Load capacity limiting effects as the compressibility of air, the compliance of the bearing surface, and thermally induced deformations of the rotor disk are analysed separately. Measurements of the temperature distribution in an air foil thrust bearing, based on an infrared radiation technique, are presented and compared to the predictions of the computational model.

Zusammenfassung

Es wird ein Berechnungsprogramm für axiale Folienlager, welche zur Klasse der hydrodynamischen Gleitlager mit elastischer Lagerfläche gehören, entwickelt. Das Programm ist in der Lage, die Druck- und Temperaturverteilung im Lager sowie die Deformationen der Lagerbauteile zu berechnen. Hydrodynamische, elastische und thermale Aspekte von axialen Folienlagern werden im Detail analysiert und auf dieser Grundlage Gestaltungsempfehlungen abgeleitet. Es werden systematische Optimierungsstudien für die Form der hydrodynamischen Schmierfilmfunktion mit Hinblick auf eine maximale Tragfähigkeit durchgeführt. Die elastischen Elemente des Lagers, das sogenannte Top- und Bumpfoil, werden über eine Schalentheorie vom Reissner-Mindlin Typ abgebildet. Verschiedene Mechanismen, welche die Steifigkeit der elastischen Lagerfläche beeinflussen, werden vorgestellt und diskutiert. Zentrale Lagerkenngrößen von axialen Folienlagern werden für die drei Fälle einer ideal parallelen Lagergeometrie, einer verformten Rotorscheibe und eines verkippten Lagers im Vergleich zu denjenigen von starren Axiallagern untersucht. Die Identifizierung der wesentlichen Wärmeströme in axialen Folienlagern erfolgt auf Grundlage eines umfangreichen thermischen Modells. Die Tragfähigkeit begrenzende Faktoren wie die Kompressibilität von Luft, die Nachgiebigkeit der Lagerfläche und thermisch induzierte Deformationen der Rotorscheibe werden getrennt analysiert. Messungen der Temperaturverteilung auf Grundlage eines optischen Verfahrens werden präsentiert und mit den Vorhersagen des Berechnungsprogramms verglichen.

Contents

1 Introduction

1.1 Motivation

The first application of air foil bearings (AFBs) on an industrial scale was in air cycle machines for aircrafts in the early 1970s. The high reliability of AFBs led to a systematic replacement of rolling ball bearings by AFBs in the following 20 years in civil and military aviation [Agr97]. But a further spreading of AFBs began only in the early 1990s. To that time, several start-ups were founded by leading experts for AFBs. The particular aim of some of those like R&D Dynamics Coorporation and Mohawk Innovative Technology has been the transfer of AFB technology to different types of high speed turbomachinery. As well in the 1990s, NASA intensified its oil-free turbomachinery program pursuing the same goal. Since then, AFBs have been continuously improved and successfully applied in various high speed rotating machines like cryogenic turboexpanders [XWH$^+$97], gas turbines [KLC14, VWP$^+$06], turbochargers [LKCS11, LKKS13, SLKL12, SLK14] and turbojet engines [HWT05].

To understand the persistent expansion of AFBs, it is necessary to study their structure and functional principle. Figure 1 shows a typical turbomachine (here a turbocharger) consisting of a rotor, a turbine wheel and a compressor wheel. Two journal bearings are used to support gravitational and unbalance excited forces whereas axial forces, originating from the turbine wheel and the compressor wheel, are supported by a thrust bearing in each direction. For both, journal and thrust bearings, principally different types as rolling-element bearings, magnetic bearings or fluid film bearings can be used. Within the class of fluid film type bearings a further distinction is made between hydrostatic and hydrodynamic bearings depending on the principle of function. Finally, hydrodynamic bearings are mainly categorised, with respect to the used fluid, in hydrodynamic oil and hydrodynamic air bearings.

Air foil bearings represent a special type of hydrodynamic air bearings. Figure 1 shows a cross-sectional view of an air foil journal bearing (AFJB) and an isometric view of an air foil thrust bearing (AFTB). For the journal case, the rotating rotor is separated from the bearing sleeve by a thin air film, the top foil and the bump foil. Top and bump foil are thin metal sheets with a thickness that is of the order of $100\mu m$. They give the bearing a well defined compliance and are the key feature of AFBs in comparison to rigid hydrodynamic air bearings which only consist of a rotor and a bearing sleeve. The structure of air foil thrust bearings is analogous to that of air foil journal bearings. The bump foil is fixed on the base plate and represents the elastic foundation for the top foil which is separated from the rotating rotor disk by a thin air film.

Whereas the top foil is present in all types of AFBs, its elastic foundation can be realised in different ways. Among others, compression spring [SK07], metal mesh [LKKK12] or multiwound [Fen09] constructions have been presented in the literature. Nevertheless, the bump type version shown in figure 1.1 is the most widespread variant and therefore subject to the analysis in this thesis.

Figure 1.2 illustrates the functional principle of a bump type AFB. Due to the boundary layer that sticks to

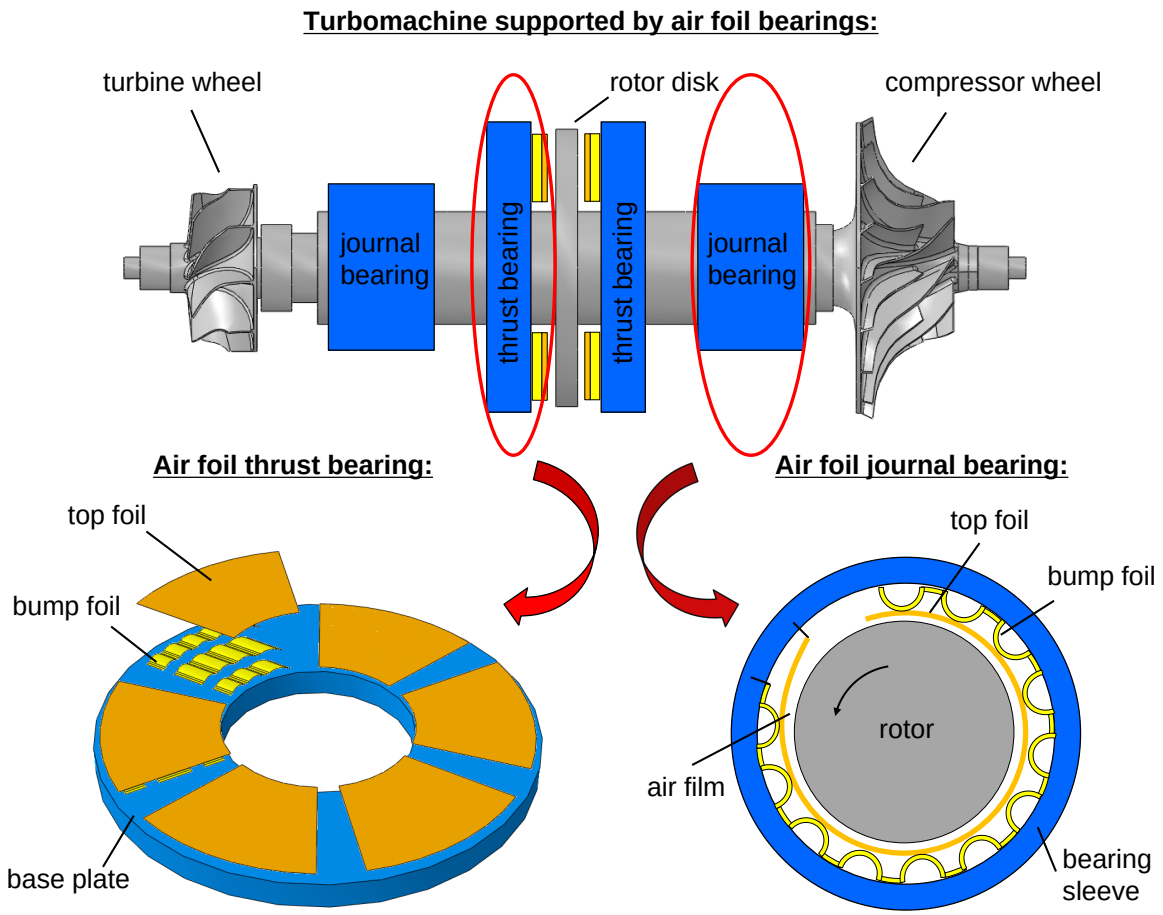

Figure 1.1: Air foil bearing system in a turbomachine.

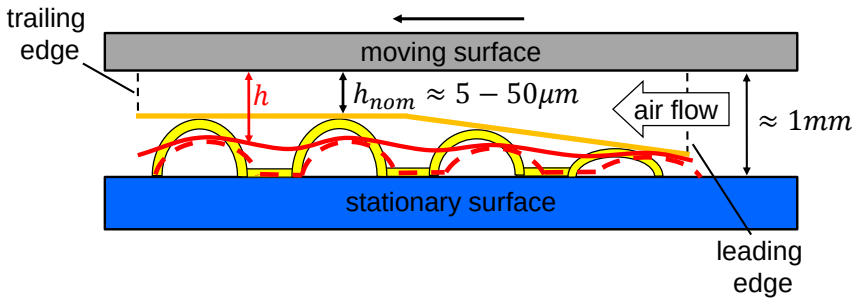

Figure 1.2: Function principle of AFBs.

the moving surface, air is dragged into the gap between the moving surface and the top foil. The nominal height distribution h_{nom} of the gap is designed to converge from the leading edge to the trailing edge. This is often realised by an increasing height of the bumps. The convergent gap leads to a hydrodynamic pressure build-up within the air flow that separates the top foil from the moving surface. Hence, loads that are acting on the moving surface can be balanced by the bearing in a contactless way resulting in low friction. In contrast to rigid hydrodynamic air bearings, the real gap height h during operation is not equal to the nominal gap height h_{nom} for AFBs. Top and bump foil deflect under the impact of the hydrodynamic pressure (shown in red in figure 1.2) which significantly changes the gap height. This, in turn, has an effect on the pressure build-up in the gap.

1.2 Advantages and disadvantages of AFBs

Depending on the application, AFBs can have different advantages in comparison to other bearing types. First of all, their compliant structure enables operation in conditions where rigid hydrodynamic bearings (air and oil) might fail. This is because AFBs can be expected to be more tolerant towards centrifugal and thermal growth of the rotor (journal bearing) and towards misalignment (journal and thrust bearing). Especially, since rotational speeds of turbomachines have been continuously increasing in the last decades, these advantages have become more pronounced. Another beneficial effect of the compliant structure is the additional amount of damping it produces. In rigid air or oil bearings, damping is only generated by squeeze film effects within the fluid. For AFBs, additional damping is generated by dry friction that occurs between the bump foil and the stationary part and between the bump foil and the top foil. The additional damping is beneficial for rotordynamic stability and enables higher rotational speeds.

Compared to hydrodynamic oil bearings, which base on the same physical principle for pressure generation, the main advantages of AFBs originate from the properties of the operating fluid. Air can be directly taken from the environment. Thus, no supply system is needed as in the case of oil bearings which simplifies system complexity and reduces the weight of the whole system. Furthermore, air is a clean lubricant. This was one of the reasons for the successful application of AFBs in air cycle machines where a contamination of the passenger cabine with oil is forbidden. Another upcoming application with high standards concerning oil contamination are fuel cell blowers for hydrogen driven cars [LKA+05]. In contrast to oil,

air is much more appropriate for the operation under extreme temperatures. As an example, AFBs have been successfully applied for cryogenic turboexpanders [XWH+97] where the dynamic viscosity of oil can be too high due to the very low temperatures. On the other hand, AFBs have proven to work under high temperatures [DLV+00] where many oil lubricants break down. One example is the successful application in the very hot environment (up to 650°C) behind the turbine of a turbojet [HWT05].

Compared to rolling-element bearings, the main advantages of AFBs are a lower noise emission, no need for a scheduled maintenance [Agr97] and an increasing load capacity with speed. Finally, with respect to their simple structure (compare figure 1.1), it is obvious that the manufacturing costs of AFBs are very low, especially in comparison to magnetic bearings.

This long list of advantages is faced by only a few, but severe disadvantages.

Low load capacity: The dynamic viscosity of air is two to three orders of magnitude smaller than the dynamic viscosity of typical oils. Since load capacity is roughly proportional to the dynamic viscosity (neglecting compressibility effects), the load capacity of AFBs is as well two to three orders of magnitude smaller compared to equal-sized oil bearings. Thus, replacing oil bearings by AFBs in a turbomachine leads to considerably higher diameters of the rotor (journal bearing) and the rotor disk (thrust bearing). If inertia of the rotor is a crucial point, as it is for example the case with automotive turbochargers, AFBs are possibly not the appropriate bearing technology.

Start-stop friction: Since the load capacity of AFBs decreases with decreasing rotor speed, the separating air film between the rotor and the top foil breaks down below a critical minimal speed. A continuous operation below the critical speed is therefore not recommended for AFBs. But even for an operation at sufficiently high speeds, solid lubrication occurs during start-stop conditions. Therefore, the top foil or/and the rotor are coated with low friction solid lubricants as Teflon in order to enhance the possible number of start-stop cycles and to reduce the friction during overload conditions [Bru04, DLV+00, DZR04]. By this approach, more than 100,000 start-stop cycles could be demonstrated [DLV+00]. For even higher requirements, hybrid air foil bearings are developed which significantly reduce wear during start-stop operation due to a hydrostatic load carrying component [KL10, KZ12].

Thermal management: Because of its low density, air has a very low heat capacity compared to oil or other liquid lubricants. The generated heat due to viscous dissipation can not be effectively removed by the lubricating air film. It is because of this, that AFBs are often provided with an extra cooling flow [SKK13, Ryu11], which enhances system complexity.

1.3 Challenges in the analysis of AFBs

The performance of AFBs is completely determined by two factors: The concrete shape of the gap height and the properties of the operating fluid. But, as shown in figure 1.2, the real gap height is not identical to the nominal gap height in case of AFBs. The deformation of top and bump foil as well as thermal distortions of the rotor (journal bearing) or the rotor disk (thrust bearing) have a direct impact on the gap height. In

addition, the operating fluid properties such as the dynamic viscosity and the density are a function of the pressure and the temperature of the fluid. The temperature distribution, in turn, depends on the dissipated energy in the air flow and the heat transfer between the bearing parts. It becomes evident from this, that the analysis of AFBs includes several physical disciplines, namely

- fluid dynamics (hydrodynamics of the air film),
- solid mechanics (deformation of the foils),
- thermodynamics (heat transfer between air film and bearing parts),

and their interaction. This represents a considerable challenge for both, modeling and measuring approaches.

The main problem for the analysis of AFBs by measurements originates from the thin air film height of approximately $5 - 50\mu m$. In addition, the air film is purely accessible since it is surrounded by the top foil on the one side and the rotor or the rotor disk on the other side. In general, only integral values (load capacity and power loss) or discrete values (temperature at discrete points behind the top foil) are measured. On the one hand, these values are the most interesting for the overall characterisation of bearing performance. On the other hand, the performed measurements are not able to explain certain phenomena. The question why a bearing failed at a certain operational point can not be answered by the established measurements. It can be deduced from a sudden increase in power loss that solid lubrication must have occured and therefore that the maximum load capacity has been exceeded. Eventually, some information about the position of solid lubrication is given by the wear scars after testing. But this does not explain the reason for the bearing failure. Instead, measurements of

- the deformation of the foils and the thermal distortion of the rotor/the rotor disk,
- the field information about the real height function $h(x, y)$,
- and the temperature field of the foils and the rotor/the rotor disk

would be necessary for a clear identification of the reasons for the bearing failure. Unfortunately, these measurements are very difficult to perform and therefore have not been done in the literature to the knowledge of the author.

1.4 Goals and structure of this thesis

In this thesis, a detailed multiphysical model of an air foil thrust bearing is developed. Certainly, the prediction of bearing performance is the main goal of a modeling approach as it is presented herein. But besides, this work is additionally intended to focus on the following aspects:

- Identification of the dominating physical effects in AFTBs.

- Comparison of modeling approaches of different complexity.
- Recommendations for designers of AFTBs.
- Where possible, comparisons are drawn to the widely used hydrodynamic oil bearings.

For this purpose, this work is divided into several constitutive parts.

Chapter 2 starts with an analysis of the lubricating gap function for the basic case of a rigid air thrust bearing operating under isothermal conditions. Certain phenomena, as compressibility and side leakage effects, are studied neglecting the superimposing effects of foil deformations at this point. Optimisations for several classic gap functions are performed and compared to more refined designs.

Chapter 3 includes foil deformations and their influence on the pressure distribution in AFTBs. A detailed shell model is presented for the modeling of arbitrary bump and top foil geometries and a comparison is drawn to reduced modeling approaches from the literature. The influence of the bump and the top foil stiffness on the performance of AFTBs is studied for aligned, distorted and misaligned conditions.

Chapter 4 presents a thermal model for AFTBs. The energy equation is solved for the air film and relevant reduction approaches are discussed to enhance computational efficiency. Detailed models for the heat flow through the foils and the backside of the rotor disk are developed and the main heat flow paths are identified. Thermal deformations of the rotor disk are shown to be a load capacity limiting factor.

Chapter 5 contains a comparison between predicted temperatures of the developed model and measured temperatures for a tested AFTB. Due to the use of an infrared camera, a more detailed information of top foil temperatures is achieved than has been presented in the literature up to date.

It should be mentioned that in spite of the similar structure of air foil journal and air foil thrust bearings, compare figure 1.1, different aspects have different weights for each bearing type. For example, rotordynamic stability is a very important issue in turbomachinery, but it is mostly determined by AFJBs and less by AFTBs. Another aspect is the preload of AFJBs which requires a nonlinear description of the foil structure. By contrast, a preload does not exist for AFTBs resulting in small foil deformations which can be accurately described by a linear deformation model. Considering that AFTBs operate at higher surface velocities than AFJBs due to the bigger diameter of the rotor disk compared to the diameter of the rotor, thermal management is more difficult for AFTBs than for AFJBs. Because of these and other differences, this thesis focuses only on AFTBs.

1.5 Fundamental equations of fluid film lubrication

As has been mentioned, the modeling of AFTBs requires a multiphysical approach. Therefore, the equations, which describe the different physical aspects, will be introduced in the chapters where they are used. As an exception, the fundamental equations of classical lubrication theory are discussed at this stage as they are needed in all chapters.

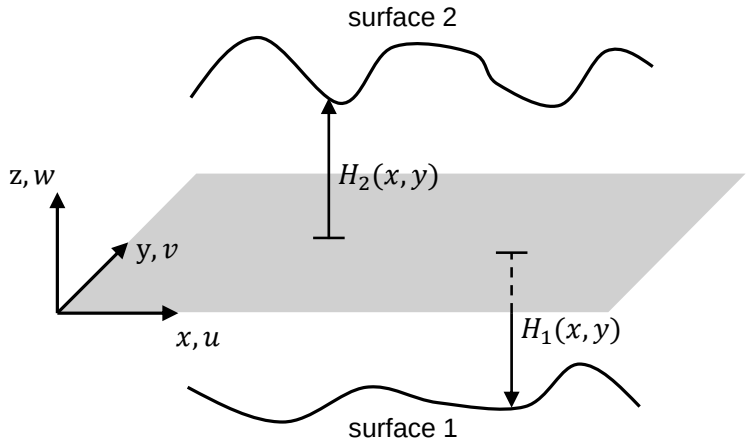

Figure 1.3: Lubricating gap between two surfaces.

1.5.1 The generalized Reynolds equation

Figure 1.3 illustrates the general situation in a lubrication problem. A fluid with density ρ, dynamic viscosity η and velocity $\mathbf{u} = (u, v, w)$ is confined by two surfaces. The motion of the fluid is governed by the general laws for conservation of mass

$$\frac{\partial \rho}{\partial t} + \frac{\partial(\rho u)}{\partial x} + \frac{\partial(\rho v)}{\partial y} + \frac{\partial(\rho w)}{\partial z} = 0 \tag{1.1}$$

and conservation of momentum. Inserting the stress tensor for a Newtonian fluid, which applies for all gases and most lubricating oils, in the momentum equations results in the Navier-Stokes equations

$$\rho\frac{Du}{Dt} = f_x - \frac{\partial p}{\partial x} + \frac{\partial}{\partial x}\left[\eta\left(2\frac{\partial u}{\partial x} - \frac{2}{3}\operatorname{div}\mathbf{u}\right)\right] + \frac{\partial}{\partial y}\left[\eta\left(\frac{\partial u}{\partial y} + \frac{\partial v}{\partial x}\right)\right] + \frac{\partial}{\partial z}\left[\eta\left(\frac{\partial w}{\partial x} + \frac{\partial u}{\partial z}\right)\right], \tag{1.2}$$

$$\rho\frac{Dv}{Dt} = f_y - \frac{\partial p}{\partial y} + \frac{\partial}{\partial y}\left[\eta\left(2\frac{\partial v}{\partial y} - \frac{2}{3}\operatorname{div}\mathbf{u}\right)\right] + \frac{\partial}{\partial z}\left[\eta\left(\frac{\partial v}{\partial z} + \frac{\partial w}{\partial y}\right)\right] + \frac{\partial}{\partial x}\left[\eta\left(\frac{\partial u}{\partial y} + \frac{\partial v}{\partial x}\right)\right], \tag{1.3}$$

$$\rho\frac{Dw}{Dt} = f_z - \frac{\partial p}{\partial z} + \frac{\partial}{\partial z}\left[\eta\left(2\frac{\partial w}{\partial z} - \frac{2}{3}\operatorname{div}\mathbf{u}\right)\right] + \frac{\partial}{\partial x}\left[\eta\left(\frac{\partial w}{\partial x} + \frac{\partial u}{\partial z}\right)\right] + \frac{\partial}{\partial y}\left[\eta\left(\frac{\partial v}{\partial z} + \frac{\partial w}{\partial y}\right)\right]. \tag{1.4}$$

These equations represent a balance of (from left to right) inertial forces, body forces, pressure forces and viscous forces. In lubrication problems, the ratio between the gap height (z-direction) and a characteristic bearing length in the x, y-plane is typically of the order of 10^{-3}. Under these circumstances an order of magnitude analysis in classical lubrication theory [HSJ04, Dow62] reduces the equations (1.2)-(1.3) to

$$\frac{\partial p}{\partial x} = \frac{\partial}{\partial z}\left(\eta\frac{\partial u}{\partial z}\right), \tag{1.5}$$

$$\frac{\partial p}{\partial y} = \frac{\partial}{\partial z}\left(\eta \frac{\partial v}{\partial z}\right), \tag{1.6}$$

whereas the reduced version of equation (1.4) simply states that the pressure is nearly constant along the gap height, hence $p = p(x, y)$. The reduced equations (1.5)-(1.6) represent a balance between the pressure forces on the left and the dominating viscous forces on the right. In particular, inertia forces have been completely neglected. As speeds are continuously increasing in AFB applications, the influence of inertia forces can become relevant under certain circumstances. Nevertheless, in this thesis, classical lubrication theory without inertia forces is applied. A justification for this assumption and a discussion of different inertia effects is postponed to section 1.5.4.

Basically, the continuity equation (1.1) and the reduced Navier-Stokes equations (1.5) and (1.6) can be used to calculate the pressure distribution in the lubricating film. Besides, further manipulations can be applied in order to get a generalized Reynolds equation for fluid film lubrication [Dow62]. Assuming no slip conditions at the surfaces 1 and 2 (slip flow on the boundaries can be accounted for as well, see [Bru04]), the general boundary conditions for the fluid are

$$\begin{aligned} u(z = H_1) &= U_1\,, & u(z = H_2) &= U_2\,, \\ v(z = H_1) &= V_1\,, & v(z = H_2) &= V_2\,, \\ w(z = H_1) &= W_1\,, & w(z = H_2) &= W_2\,, \end{aligned} \tag{1.7}$$

where U_1, V_1, and W_1 are the velocities of surface 1 and U_2, V_2, and W_2 are the velocities of surface 2, respectively. Integrating the reduced momentum equations (1.5) and (1.6) twice with respect to z, the expressions

$$u(z) = \frac{\partial p}{\partial x}\int_{H_1}^{z} \frac{z}{\eta} dz + \left(\frac{U_2 - U_1}{F_0} - \frac{\partial p}{\partial x}\frac{F_1}{F_0}\right)\int_{H_1}^{z} \frac{1}{\eta} dz + U_1\,, \tag{1.8}$$

$$v(z) = \frac{\partial p}{\partial y}\int_{H_1}^{z} \frac{z}{\eta} dz + \left(\frac{V_2 - V_1}{F_0} - \frac{\partial p}{\partial y}\frac{F_1}{F_0}\right)\int_{H_1}^{z} \frac{1}{\eta} dz + V_1 \tag{1.9}$$

are obtained for the fluid velocities with F_0, F_1 being defined in equations (1.12). Inserting these velocities in the integrated form of the continuity equation

$$\int_{H_1}^{H_2} \frac{\partial \rho}{\partial t} dz + \int_{H_1}^{H_2} \frac{\partial (\rho u)}{\partial x} dz + \int_{H_1}^{H_2} \frac{\partial (\rho v)}{\partial y} dz + \int_{H_1}^{H_2} \frac{\partial (\rho w)}{\partial z} dz = 0 \tag{1.10}$$

results after some lengthy manipulations [Dow62, LS15] in the generalized Reynolds equation

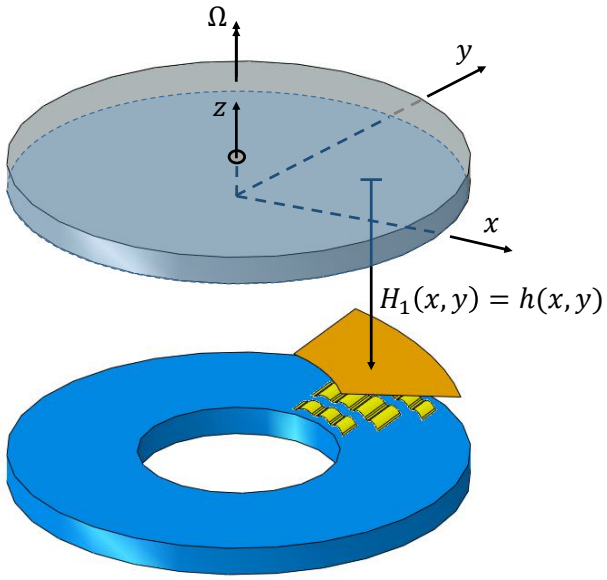

Figure 1.4: Gap function definition for AFTBs.

$$\begin{aligned}\frac{\partial}{\partial x}\left[(F_2+G_1)\frac{\partial p}{\partial x}\right]+\frac{\partial}{\partial y}\left[(F_2+G_1)\frac{\partial p}{\partial y}\right] =& H_2\left[\frac{\partial}{\partial x}(\rho u)_2+\frac{\partial}{\partial y}(\rho v)_2\right]-H_1\left[\frac{\partial}{\partial x}(\rho u)_1+\frac{\partial}{\partial y}(\rho v)_1\right]\\ &-\frac{\partial}{\partial x}\left[\frac{U_2-U_1}{F_0}(F_3+G_2)+G_3U_1\right]\\ &-\frac{\partial}{\partial y}\left[\frac{V_2-V_1}{F_0}(F_3+G_2)+G_3V_1\right]\\ &+\int_{H_1}^{H_2}\frac{\partial\rho}{\partial t}dz+(\rho w)_2-(\rho w)_1\,.\end{aligned} \tag{1.11}$$

Herein, the brackets $(\cdot)_1$ and $(\cdot)_2$ indicate function evaluation at surface 1 and surface 2 and the expressions F_i, G_i are defined by

$$\begin{aligned}&F_0=\int_{H_1}^{H_2}\frac{1}{\eta}dz\,,\quad F_1=\int_{H_1}^{H_2}\frac{z}{\eta}dz\,,\quad F_2=\int_{H_1}^{H_2}\frac{\rho z}{\eta}\left(z-\frac{F_1}{F_0}\right)dz\,,\quad F_3=\int_{H_1}^{H_2}\frac{\rho z}{\eta}dz\,,\\ &G_1=\int_{H_1}^{H_2}z\frac{\partial\rho}{\partial z}\left[\int_{H_1}^{z}\frac{z}{\eta}dz-\frac{F_1}{F_0}\int_{H_1}^{z}\frac{1}{\eta}dz\right]dz\,,\quad G_2=\int_{H_1}^{H_2}z\frac{\partial\rho}{\partial z}\left[\int_{H_1}^{z}\frac{1}{\eta}dz\right]dz\,,\quad G_3=\int_{H_1}^{H_2}z\frac{\partial\rho}{\partial z}dz\,.\end{aligned} \tag{1.12}$$

Equations (1.11) and (1.12) enable the calculation of the pressure distribution in the generalized lubrication problem of figure 1.3 with a spatially varying density and dynamic viscosity.

1.5.2 Generalized Reynolds equation for AFTBs

The specific lubrication problem in an AFTB is illustrated in figure 1.4 (the space between top and bump foil is only for illustration purpose). Identifying the rotor disk as surface 2 and the top foil as surface 1, three specifications are made compared to the generalized lubrication problem of figure 1.3:

- The global coordinate system is placed in the middle of the rotor disk surface that faces the top foil. It follows from this that $H_2(x,y) = 0$ and therefore the gap height is described by $h(x,y) = H_1(x,y)$, which is always negative according to this definition.
- Since the top foil is at rest, $U_1 = V_1 = W_1 = 0$ holds. The rotor disk is assumed to rotate with the angular velocity Ω and to perform no squeezing motion in the z-direction. Therefore, the boundary conditions for the fluid close to the rotor disk are $U = U_2 = -\Omega y$, $V = V_2 = \Omega x$ and $W_2 = 0$.
- Only stationary flow is considered.

For these conditions the generalized Reynolds equation reduces to

$$\frac{\partial}{\partial x}\left[(F_2+G_1)\frac{\partial p}{\partial x}\right] + \frac{\partial}{\partial y}\left[(F_2+G_1)\frac{\partial p}{\partial y}\right] = -\frac{\partial}{\partial x}\left[\frac{U}{F_0}(F_3+G_2)\right] - \frac{\partial}{\partial y}\left[\frac{V}{F_0}(F_3+G_2)\right] \tag{1.13}$$

with F_i, G_i being

$$\begin{aligned} F_0 &= \int_h^0 \frac{1}{\eta}dz\,, \quad F_1 = \int_h^0 \frac{z}{\eta}dz\,, \quad F_2 = \int_h^0 \frac{\rho z}{\eta}\left(z - \frac{F_1}{F_0}\right)dz\,, \quad F_3 = \int_h^0 \frac{\rho z}{\eta}dz\,, \\ G_1 &= \int_h^0 z\frac{\partial \rho}{\partial z}\left[\int_h^z \frac{z}{\eta}dz - \frac{F_1}{F_0}\int_h^z \frac{1}{\eta}dz\right]dz\,, \quad G_2 = \int_h^0 z\frac{\partial \rho}{\partial z}\left[\int_h^z \frac{1}{\eta}dz\right]dz\,. \end{aligned} \tag{1.14}$$

The fluid velocities in the lubricating gap between the rotor disk and the top foil are given by

$$u(z) = \frac{\partial p}{\partial x}\int_h^z \frac{z}{\eta}dz + \left(\frac{U}{F_0} - \frac{\partial p}{\partial x}\frac{F_1}{F_0}\right)\int_h^z \frac{1}{\eta}dz\,, \tag{1.15}$$

$$v(z) = \frac{\partial p}{\partial y}\int_h^z \frac{z}{\eta}dz + \left(\frac{V}{F_0} - \frac{\partial p}{\partial y}\frac{F_1}{F_0}\right)\int_h^z \frac{1}{\eta}dz\,. \tag{1.16}$$

The equations (1.13) to (1.16) in combination with the energy equation (4.13) form the basis for the calculation of the pressure and temperature distribution in an AFTB. Finally, with the reference pressure p_0 (e.g. ambient pressure) the load capacity for one pad of the thrust bearing can be calculated by

$$W = \iint_{A_{pad}} (p - p_0)dxdy \tag{1.17}$$

and the torque (evaluated at the rotor disk surface) is given by

$$M = \iint_{A_{pad}} \left[\eta\left(x\frac{\partial v}{\partial z} - y\frac{\partial u}{\partial z}\right)\right]\Big|_{z=0} dxdy\,. \tag{1.18}$$

1.5.3 Reynolds equation for isothermal conditions

In general, density and dynamic viscosity are a function of the pressure and the temperature. The magnitude of order analysis of the Navier-Stokes equations showed the pressure distribution to be nearly constant in the z-direction, $p = p(x, y)$. If it is assumed that the temperature field $T = T(x, y, z)$ can be approximated by a two-dimensional temperature field $T \approx T_m(x, y)$, the density and the dynamic viscosity become as well only a function of the x-, and the y-coordinate

$$\eta = \eta\big(p(x,y), T_m(x,y)\big) = \eta(x,y), \quad \rho = \rho\big(p(x,y), T_m(x,y)\big) = \rho(x,y)\,. \tag{1.19}$$

Since for this case the integral expressions (1.14) can be solved analytically, the generalized Reynolds equation (1.13) considerably simplifies to the reduced form

$$\frac{\partial}{\partial x}\left[\frac{\rho(p,T_m)h^3}{12\eta(T_m)}\frac{\partial p}{\partial x}\right] + \frac{\partial}{\partial y}\left[\frac{\rho(p,T_m)h^3}{12\eta(T_m)}\frac{\partial p}{\partial y}\right] = \frac{\partial}{\partial x}\left[\frac{\rho(p,T_m)Uh}{2}\right] + \frac{\partial}{\partial y}\left[\frac{\rho(p,T_m)Vh}{2}\right]. \tag{1.20}$$

Herein, the pressure dependence of the dynamic viscosity has been already neglected which is valid for air pressures below 10 bar without loss of accuracy. For this pressure range and temperatures above room temperature, which is the case in most applications of AFBs, the ideal gas law

$$p = \rho R_{spec} T \tag{1.21}$$

is sufficiently precise as an equation of state for air ($R_{spec} = 287\frac{J}{kgK}$ is the specific gas constant of air). In case of isothermal conditions, the dynamic viscosity and density of air are therefore given by

$$\eta = const., \quad \rho = \frac{\rho_0}{p_0} p\,, \tag{1.22}$$

where ρ_0 is the reference density at the reference pressure p_0. Inserting these expressions in equation (1.20) results in the compressible isothermal Reynolds equation

$$\frac{\partial}{\partial x}\left[\frac{ph^3}{12\eta}\frac{\partial p}{\partial x}\right] + \frac{\partial}{\partial y}\left[\frac{ph^3}{12\eta}\frac{\partial p}{\partial y}\right] = \frac{\partial}{\partial x}\left[\frac{pUh}{2}\right] + \frac{\partial}{\partial y}\left[\frac{pVh}{2}\right]. \tag{1.23}$$

In essence, the three presented versions of the Reynolds equation (1.13)-(1.14), (1.20) and (1.23) only differ in the spatial dependence of the density and the dynamic viscosity on temperature. Equation (1.23) is isothermal, whereas the version (1.20) accounts for temperature variations in the x, y-plane and the generalized Reynolds equation (1.13)-(1.14) considers the temperature dependence of the density and the dynamic viscosity in all three coordinate directions x, y, z. For a clear analysis of hydrodynamic and structural effects, the isothermal Reynolds equation is very helpful since it eliminates superimposed thermal effects and is therefore used in chapters 2 and 3 of this thesis. The generalized Reynolds equation is the

most accurate formulation but computationally very expensive. It serves in chapter 4 as a reference for the reduced Reynolds equation (1.20) which will be shown to be sufficiently accurate for AFBs.

1.5.4 Influence of inertia forces

As has been discussed, AFBs are predestinated to be used in rotordynamic applications with very high speeds. Since inertia forces scale with the square of speed, it is evident that they can significantly affect the performance of AFBs. Applying a magnitude of order analysis to the Navier-Stokes equations [HSJ04] in cylindrical coordinates leads to the modified Reynolds number

$$Re^* = \frac{\rho\Omega}{\eta} h_{ref}^2 \,. \tag{1.24}$$

It describes the approximate ratio between the magnitude of inertia forces and the magnitude of the dominating viscous forces in hydrodynamic thrust bearings. Hence, for flow conditions for which the modified Reynolds number Re^* approaches unity, inertial forces can not be neglected and predictions of the classical lubrication theory will not be accurate. In this thesis, AFTBs with angular speeds of up to $\Omega = 15,000 \frac{rad}{s}$ and typical minimum film thicknesses of $h_{min} = 2 - 35 \mu m$ are analysed. Taking h_{min} as reference gap height, as it is done in [Buc87, MTM85, ALA87], the modified Reynolds number becomes

$$\begin{aligned} Re^*(\Omega = 15,000 \frac{rad}{s}, h_{min} = 10\mu m) &= 0.06 \qquad \text{(moderate loads)}\,, \\ Re^*(\Omega = 15,000 \frac{rad}{s}, h_{min} = 35\mu m) &= 0.8 \qquad\quad \text{(light loads)}\,. \end{aligned} \tag{1.25}$$

It can be concluded from this estimation that classical lubrication theory is accurate and can be applied for moderate to high load conditions. Especially, since it is only for these conditions where structural and thermal effects become prevalent. Nonetheless, it is of interest how inertia forces can influence the bearing performance. Several effects have been identified in the literature.

Inertia effects in the lubricating gap (except for centrifugal forces): For one-dimensional plane sliders, Snyder [Sny63] investigated the influence of inertia terms in the Navier-Stokes equations by an analytical series solution. He showed inertia terms to generally increase load capacity.

Centrifugal forces: In case of thrust bearings, centrifugal forces are always apparent. Mori et al. [MTM85] performed a detailed analysis for isothermal conditions taking into account all inertia forces. According to this work centrifugal forces always diminish load capacity. But this effect is partly or fully canceled out by other inertia forces depending on the exact geometry of the thrust bearing.

Ram-pressure effect: Figure 1.5 illustrates the flow situation at the leading edge of a hydrodynamic bearing. The fluid mass, that is dragged by the moving bearing part within its boundary layer, can be considerably higher than the fluid mass that actually enters the bearing gap at the leading edge. Because of this, a ram pressure develops, which levitates the pressure boundary condition at the leading edge, resulting in a higher pressure level within the whole bearing [Buc87, HE88].

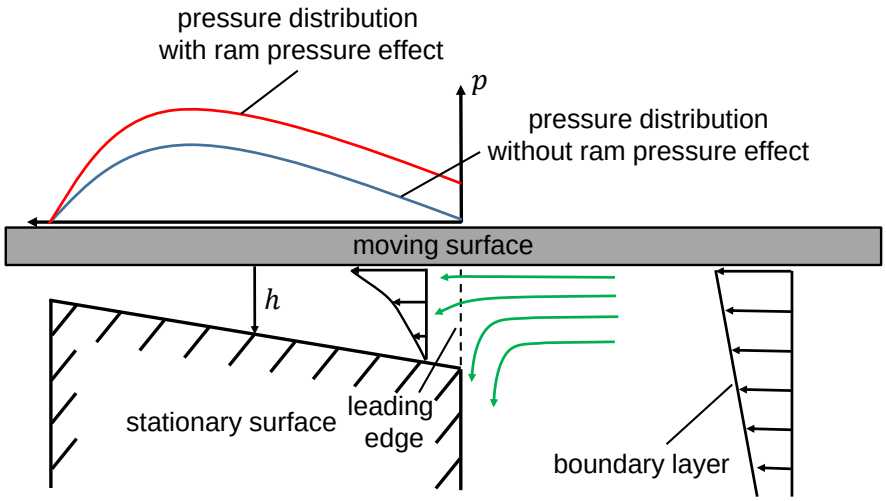

Figure 1.5: Ram pressure effect in hydrodynamic bearings.

Turbulent conditions: For modified Reynolds numbers above unity the flow in the bearing can become turbulent [ALA87]. Constantinescu [Con64] comes to the result that turbulence does not alter the pressure distribution qualitatively and generally leads to higher pressures. Furthermore, he points out that turbulence effects are smaller in gas bearings than in oil bearings, especially for higher compressibility numbers (see equation (2.12) for the definition of the compressibility number).

Summarizing, the neglect of inertia forces leads in most cases to conservative predictions. It is only because of centrifugal effects that the real load capacity may be lower than predicted by classical lubrication theory. For the AFTBs analysed in this thesis, the influence of centrifugal forces was checked by a modified Reynolds equation according to Hori [Hor06]. For moderate to high bearing loads, the reduction of load capacity due to centrifugal effects was found to be always below 5%.

2 Hydrodynamics of AFTBs

The physical principle for the pressure generation in self-acting AFTBs is the same as for rigid hydrodynamic oil or air bearings. It follows from classical lubrication theory [HSJ04] that hydrodynamic bearing types need a physical wedge, that is a convergent gap profile from the leading edge to the trailing edge, in order to create significant pressures for the separation of bearing components. Besides fluid properties, it is mainly the concrete shape of the gap profile that influences the bearing performance. Compared to rigid bearings, the design of the gap profile in case of AFTBs is more complicated because of two factors. First of all, the real gap function $h(x, y)$ is different from the nominal gap function $h_{nom}(x, y)$ due to the deformation of both, top foil and bump foil. A well designed nominal gap function may convert to a disadvantageous real gap function under the influence of the hydrodynamic pressure resulting in a bad bearing performance. Secondly, the realisation of the convergent gap profile is completely different for AFTBs. In case of rigid bearings, the gap profile can be milled in the base plate of the bearing. By contrast, for AFTBs the gap profile has to be incorporated in the design of top and bump foil. Hereby, manufacturing accuracy for these flexible elements needs to be high since the thickness of the air film is only of the order of $10\mu m$.

It is because of these complicating aspects that up to day no special design has been established as a standard for AFTBs. Between others, the following designs have been proposed in the literature:

- Dykas [DBD$^+$08] used a bump foil with all bumps having the same height. The top foil is placed on the bump foil which results in a constant nominal air film height in the so-called land region of the gap. Close to the leading edge the top foil is bended and fixed to the base plate. By this approach, a taper is created with a maximal air film thickness at the top foil fixing and a minimal film thickness at the first bump of the bump foil.

- Taper and taper land geometries can be realised as well by bumps with increasing heights from the leading to the trailing edge. In this case, the convergent geometry is completely incorporated in the bump foil design and the top foil is simply placed on the bump foil [LKKK11].

- Lee and Kim [LK11] presented a step design where the step is embossed in the top foil and the bumps are radially arranged.

A closer examination of each of these designs reveals that they lead to different gap functions. Therefore, in order to evaluate the possible performance of different designs, it is an absolute necessity to understand how the gap function influences the performance of hydrodynamic thrust bearings. In this thesis, the analysis of this issue is divided into two parts. In chapter 3, effects of bump and top foil deformation on the performance of AFTBs will be considered. But before, optimal gap functions of a rigid thrust bearing are analysed in this chapter. The rigid design is of special interest in case of thrust bearings, since it leads to the optimal bearing performance for an aligned configuration of the rotor disk and the stationary bearing surface. This is because if an elasto-hydrodynamic set up resulted in a more favorable gap function, this

concrete gap function could be as well milled in the rigid base plate leading to the same bearing performance for the rigid case. It is pointed out that this is not the case for air foil journal bearings. Here, Peng [PK04] demonstrated that at least theoretically air foil journal bearings can achieve higher load capacities than rigid air journal bearings.

The following aspects of rigid thrust bearing behaviour are investigated in this chapter:

Section 2.1 analyses the performance of low-parameter gap functions - as for example taper or taper land geometries - with respect to the pressure distribution, the load capacity and the friction coefficient. Optimal design values are tabulated for different operational conditions.

Section 2.2 presents an optimisation of high-parameter geometries. Optimal performance of cylindrically sector-shaped pad type thrust bearings is explored and compared to low-parameter geometries.

Section 2.3 performs a topological optimisation of a thrust pad with respect to a minimal friction coefficient.

Section 2.4 compares optimal sector-shaped geometries to grooved geometries as the spiral groove bearing.

All calculations in this chapter base on the assumption of isothermal fluid behaviour. It will be shown in chapter 4, that this assumption leads to satisfying results for air bearings as long as thermally induced deformations of the rotor disk can be neglected. This is mainly because of the relatively weak nonlinear viscosity-temperature relation of air compared to the highly nonlinear viscosity-temperature relation of oils. An averaged approach for the dynamic viscosity leads therefore to more accurate results for air bearings in comparison to oil bearings.

2.1 Optimisation of low-parameter gap functions for cylindrically sector-shaped pads

Besides groove type thrust bearings, which are discussed in section 2.4, sector-shaped pad type geometries are mostly used for thrust bearings. In this design, the complete bearing surface is divided into a number of subareas, the so-called pads. Assuming all pads having identical designs, the pressure distribution in the whole thrust bearing (for aligned conditions) constitutes of the identical pressure distribution in each of the pads. Thus, except for misaligned conditions, which are analysed in chapter 3, the calculation can be reduced to one pad.

Concerning the design of the pad, a further distinction can be drawn between the *topology* on the one side and the *gap function* on the other side. The topology describes the shape of the pad in x-, and y-direction. By contrast, the gap function represents the height of the lubricating air film in z-direction. Both, topology and gap function, influence the bearing performance. Since in the vast majority of thrust bearing designs cylindrically sector-shaped topologies are used, compare figures 1.1 and 1.4, this analysis mainly focuses on the optimisation of the gap function for cylindrically sector-shaped pads. More complex topologies are considered in section 2.3.

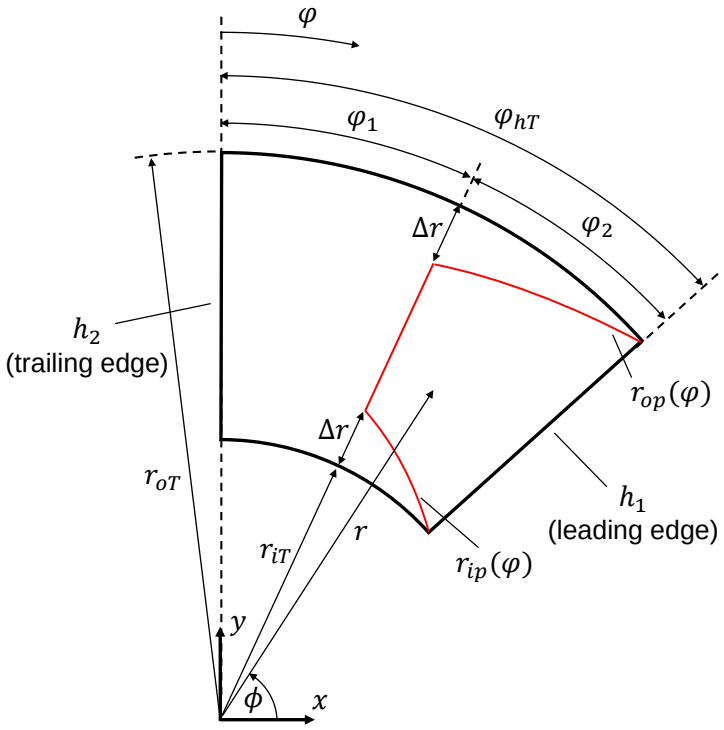

Figure 2.1: Geometry of a pad with a low-parameter gap function.

2.1.1 Geometry, Reynolds equation and optimisation problem for LPGFs

Geometry of LPGFs

Figure 2.1 shows the general geometry of a class of low-parameter gap functions (LPGF) including a taper, taper land, step and pocket shaped gap function. The inner and outer radii r_{iT} and r_{oT} as well as the angular extent φ_{hT} determine the pad topology. h_1 and h_2 are the gap heights at the leading and the trailing edge. φ_1 denotes the angular extent of the land region that is characterised by a constant gap height of h_2. The part of the pad that is marked by the angle φ_2 can have different gap height distributions depending on the concrete LPGF. For instance, in case of a pocket geometry the whole pad has the constant gap height h_2 except for the region surrounded by the leading edge and the red lines which is characterised by the constant gap height h_1. Defining the real gap height (no thermal and structural deformations) to be identical to the nominal gap height

$$h(x, y) = -h_{nom}(x, y)\,, \tag{2.1}$$

the considered LPGFs of this section are

$$h_{nom,t} = h_2 + \frac{h_1 - h_2}{\varphi_{hT}}\varphi, \quad \text{(taper)} \tag{2.2}$$

$$h_{nom,tl} = h_2 + \frac{h_1 - h_2}{\varphi_2}(\varphi - \varphi_1)(\varphi > \varphi_1), \quad \text{(taper land)} \tag{2.3}$$

$$h_{nom,s} = h_2 + (h_1 - h_2)(\varphi > \varphi_1), \quad \text{(step)} \tag{2.4}$$

$$h_{nom,p} = h_2 + (h_1 - h_2)(\varphi > \varphi_1)(r > r_{ip})(r < r_{op}), \quad \text{(pocket)} \tag{2.5}$$

where the linear functions $r_{ip}(\varphi)$, $r_{op}(\varphi)$ for the pocket geometry are given by

$$\begin{aligned} r_{ip}(\varphi) &= (r_{iT} + \Delta r) - \frac{\Delta r}{\varphi_2}(\varphi - \varphi_1), \\ r_{op}(\varphi) &= (r_{oT} - \Delta r) + \frac{\Delta r}{\varphi_2}(\varphi - \varphi_1) \end{aligned} \tag{2.6}$$

and for example $(\varphi > \varphi_1)$ is an abbreviated notation for

$$(\varphi > \varphi_1) = \begin{cases} 1, & \varphi > \varphi_1, \\ 0, & \varphi \leq \varphi_1. \end{cases} \tag{2.7}$$

Introducing the dimensionless geometric parameters

$$\lambda_\varphi = \frac{\varphi_1}{\varphi_{hT}}, \quad \lambda_r = \frac{r_{iT}}{r_{oT}}, \quad \lambda_{\Delta r} = \frac{\Delta r}{r_{oT}}, \quad \lambda_h = \frac{h_1}{h_2}, \tag{2.8}$$

it can be shown that the dimensionless nominal LPGF $\overline{h}_{nom} = \frac{h_{nom}}{h_2}$ of a cylindrically sector-shaped pad is only a function of the six parameters r_{oT}, φ_{hT}, λ_r, λ_φ, $\lambda_{\Delta r}$, and λ_h. The first three define the topology of the pad, the latter three determine the concrete low-parameter gap function.

Dimensionless Reynolds equation in cylindrical coordinates

The isothermal Reynolds equation (1.23) has been derived in Cartesian coordinates since this formulation will be applied for the elasto-hydrodynamic modelling of AFTBs. For the purely hydrodynamic analysis of rigid thrust bearings, the isothermal Reynolds equation in cylindrical coordinates

$$\frac{\partial}{\partial \phi}\left[\frac{1}{r}\frac{ph^3}{12\eta}\frac{\partial p}{\partial \phi}\right] + \frac{\partial}{\partial r}\left[r\frac{ph^3}{12\eta}\frac{\partial p}{\partial r}\right] = \frac{\Omega}{2}\frac{\partial}{\partial \phi}\left[rph\right] \tag{2.9}$$

is more convenient. Defining the dimensionless variables

$$\overline{r} = \frac{r}{r_{oT}}, \quad \overline{p} = \frac{p}{p_0}, \quad \overline{h} = \frac{h}{h_2}, \tag{2.10}$$

where p_0 is the reference pressure at the boundaries of the pad, yields the nondimensional form of the Reynolds equation

$$\frac{\partial}{\partial\phi}\left[\frac{1}{\overline{r}}\overline{p}\overline{h}^3\frac{\partial\overline{p}}{\partial\phi}\right]+\frac{\partial}{\partial\overline{r}}\left[\overline{r}\overline{p}\overline{h}^3\frac{\partial\overline{p}}{\partial\overline{r}}\right]=\Lambda\frac{\partial}{\partial\phi}\left[\overline{r}\overline{p}\overline{h}\right] \tag{2.11}$$

with the compressibility number Λ being defined as

$$\Lambda=\frac{6\eta\Omega}{p_0}\frac{r_{oT}^2}{h_2^2}\,. \tag{2.12}$$

Equation (2.11) is a nonlinear differential equation in the nondimensional pressure field $\overline{p}(\overline{r},\phi)$. The character of the solution is highly influenced by the compressibility number. For the limit case of $\Lambda\to 0$ the fluid behaves incompressible, in particular the pressure rise $\frac{p-p_0}{p_0}=\overline{p}-1$ in the pad is directly proportional to the compressibility number. For $\Lambda\to\infty$ the pressure rise reaches an asymptote and becomes independent of the compressibility number [HSJ04]. In general, it follows from equation (2.11) that the dimensionless pressure field is only a function of

$$\overline{p}=\overline{p}(\varphi_{hT},\lambda_r,\Lambda,\overline{h}) \tag{2.13}$$

for cylindrically sector-shaped pads. The dimensionless load capacity

$$\overline{W}=\frac{W}{p_0A_{pad}} \tag{2.14}$$

(A_{pad} is the surface area of the pad) and the friction coefficient

$$f=\frac{M}{h_2W} \tag{2.15}$$

can be shown to be as well of the form

$$\overline{W}=\overline{W}(\varphi_{hT},\lambda_r,\Lambda,\overline{h})=\frac{2}{\varphi_{hT}(1-\lambda_r^2)}\iint\limits_{\overline{A}_{pad}}(\overline{p}-1)\overline{r}d\phi d\overline{r}\,, \tag{2.16}$$

$$f=f(\varphi_{hT},\lambda_r,\Lambda,\overline{h})=\frac{1}{\varphi_{hT}(1-\lambda_r^2)\overline{W}}\iint\limits_{\overline{A}_{pad}}\left(-\overline{r}\overline{h}\frac{\partial\overline{p}}{\partial\phi}-\frac{\Lambda}{3}\frac{\overline{r}^3}{\overline{h}}\right)d\phi d\overline{r}\,. \tag{2.17}$$

Finally, it is concluded that the pressure distribution, load capacity and friction coefficient of cylindrically pad type rigid thrust bearings with LPGFs only depend on the six parameters φ_{hT}, λ_r , Λ (topology and operational conditions) and λ_φ, $\lambda_{\Delta r}$, λ_h (gap function parameters).

Formulation of the optimisation problem

Instead of analysing thrust bearing performance on the basis of several examples, we look directly at optimised configurations. The optimisation problem is formulated as follows: For given topological and

operational parameters φ_{hT}, λ_r and Λ, find

$$\min_{\lambda_h,\lambda_\varphi,\lambda_{\Delta r}} Q(\lambda_h,\lambda_\varphi,\lambda_{\Delta r}) \tag{2.18}$$

with the explicit constraints

$$1 \leq \lambda_h \leq 10\,, \tag{2.19}$$

$$0 \leq \lambda_\varphi \leq 1\,, \tag{2.20}$$

$$0 \leq \lambda_{\Delta r} \leq \frac{1}{2}(1-\lambda_r) \tag{2.21}$$

for the control variables. Objective functions of interest are either the dimensionless load capacity $Q = -\overline{W}$ or the friction coefficient $Q = f$. Depending on the concrete LPGF the number of control variables varies from 1 (taper geometry) to 3 (pocket geometry).

Solution procedure

A finite element method is used in order to solve the nondimensional Reynolds equation (2.11) for the nondimensional pressure distribution in one pad of the rigid thrust bearing. For the reference topology, defined by the parameters $\varphi_{hT} = 40°$ and $\lambda_r = 0.5$, a mesh consisting of 150x150 quadrileteral Lagrange elements of quadratic order is applied. This rather fine discretisation is necessary since for high compressibility numbers steep gradients are apparent in the pressure distribution. For other values of φ_{hT} and λ_r the number of elements is adjusted appropriately. On all four boundaries of the pad a Dirichlet boundary condition $\overline{p} = 1$ is applied. A damped Newton-Raphson method with the initial value $\overline{p}(\overline{r},\phi) = 1$ is used to solve the nonlinear system of equations. Once the pressure distribution is obtained, the friction coefficient and the dimensionless load capacity are calculated. A commercial gradient-based optimisation solver is used to find the sets of gap function parameters λ_h, λ_φ and $\lambda_{\Delta r}$ that maximize the load capacity or minimize the friction coefficient as a function of the compressibility number Λ and the topological parameters φ_{hT} and λ_r.

2.1.2 Optimisation results for LPGFs

Pressure distributions and gap functions

Figure 2.2 shows with respect to load capacity optimised gap functions and the corresponding pressure distributions for the four considered LPGFs. The left column illustrates the results for a small compressibility number of $\Lambda = 1$. This case represents the limit case $\Lambda \to 0$ where air behaves incompressible. Therefore, these results are valid as well for hydrodynamic oil bearings where the lubricating fluid is incompressible. The right column depicts results for a large compressibility number of $\Lambda = 500$ which arises in practical applications with high rotor speeds and narrow lubricating gaps (high loads).

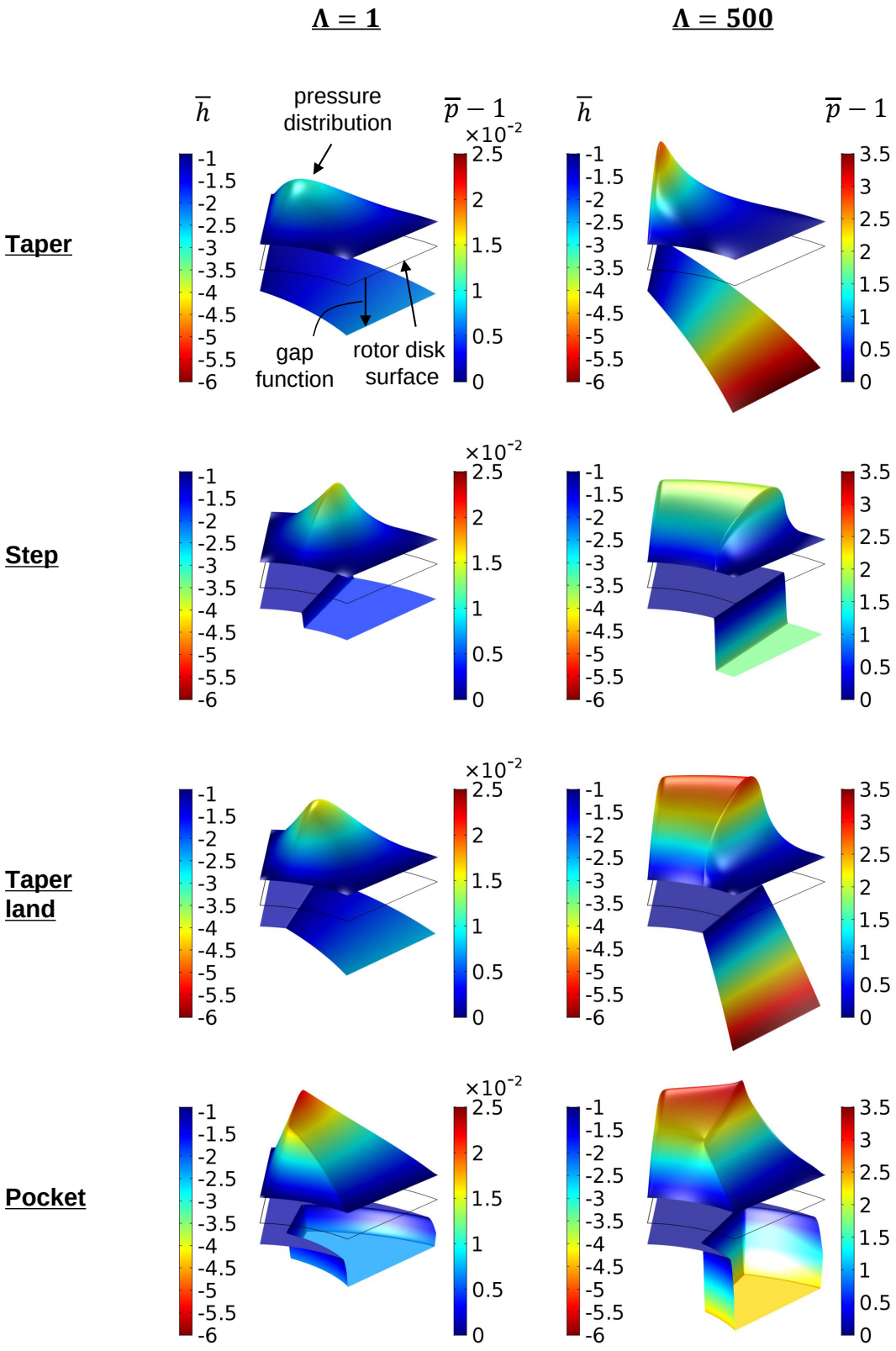

Figure 2.2: Gap function and pressure distribution for optimised LPGFs (with respect to load capacity).

Starting with the results for the nearly incompressible case ($\Lambda = 1$), two factors can be identified that improve the pressure development in the pad:

- Sealing in circumferential direction: The pressure level for the taper geometry is significantly lower than for the step, taper land and pocket geometry. The reason for this is that the taper gap function is the only one that has no land region at the trailing edge. The land region is the part of the pad with a constant minimal film distribution $\overline{h} = -1$. It represents an effective flow resistance in circumferential direction resulting in a higher pressure level.
- Sealing in radial direction: It can be observed that the pocket geometry shows a considerably higher pressure level than the step and the taper land geometry. The only extension of the pocket gap function compared to the step gap function are the regions of constant minimal fluid film height $\overline{h} = -1$ near to the inner and outer radius of the pad. These small areas represent a flow resistance in radial direction, effectively reduce side leakage of the fluid and thus lead to a higher pressure level in the whole pad.

The influence of compressibility can be directly studied by comparing the results of the right column ($\Lambda = 500$) to the results of the left column ($\Lambda = 1$) of figure 2.2. Concerning the pressure distribution, it is striking that there is no pronounced pressure peak for high compressibility numbers (except for the taper geometry). Instead, a broad pressure plateau extends over the land region in circumferential direction. Furthermore, compared to the optimal parameters for the incompressible case, optimal values for the control variables have significantly changed. The ratio λ_h between inlet and outlet film thicknesses rises for all four LPGFs and the extension of the land region nearly doubles for the step, taper land and pocket geometry.

For the herein considered rigid case of a hydrodynamic thrust bearing, the most important findings are that the pressure level and the optimal values for the control variables of the gap function change with the compressibility number. In case of AFTBs the qualitative change in the pressure distribution is of additional importance since the design of the elastic structure (bump and top foil) should be adapted to the concrete pressure distribution.

Load capacity and friction coefficient

Figure 2.3 shows the dimensionless load capacity $\overline{W}$ and the friction coefficient f as a function of the compressibility number for all four LPGFs. The left column of figure 2.3 illustrates the results for an optimisation with respect to a maximal load capacity whereas in the right column results for an optimisation with respect to a minimal friction coefficient are presented. Focusing first on the load optimised case, it can be clearly stated that the dimensionless load capacity rises degressively with the compressibility number for air bearings. This effect can be clearly ascribed to the compressibility of air since incompressible fluids show a linear relationship between the dimensionless load capacity and the compressibility number (note, that the load capacity does not depend on the reference pressure p_0 for incompressible fluids). Comparing

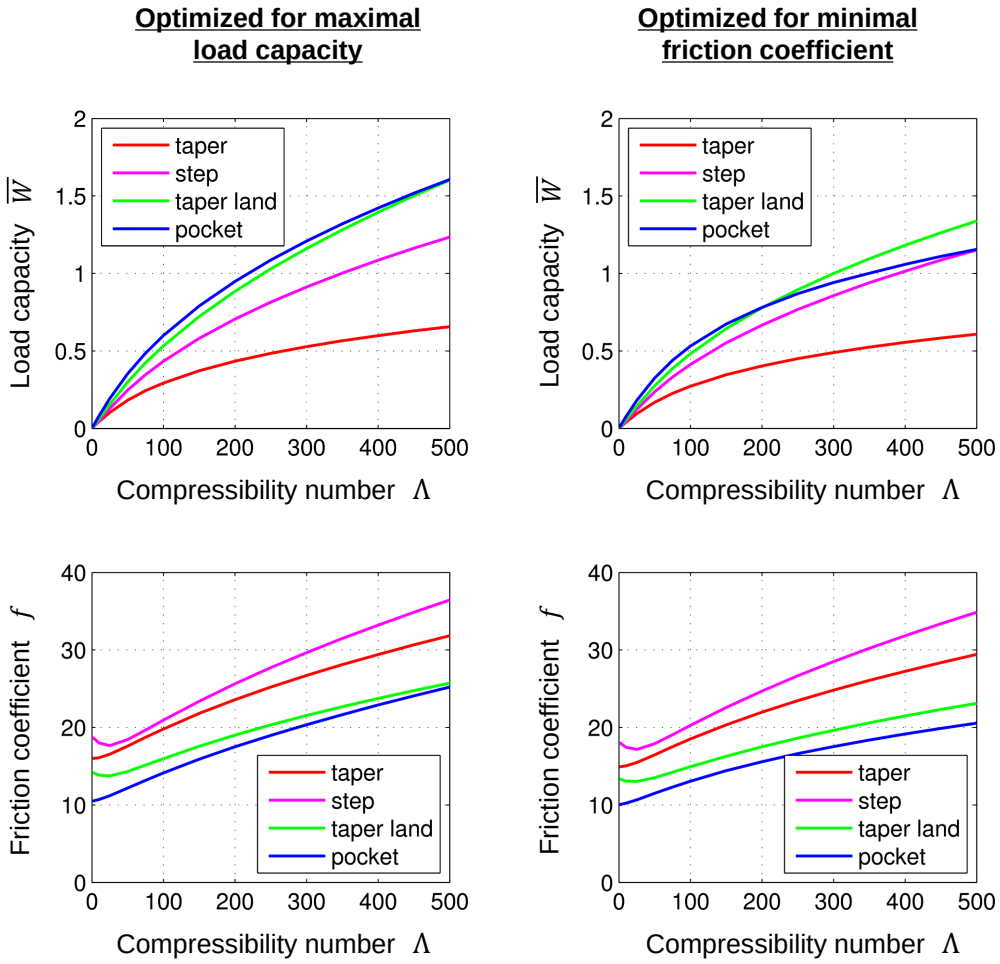

Figure 2.3: Dimensionless load capacity $\overline{W}$ and friction coefficient f for optimised LPGFs. Left column: Optimisation with respect to a maximal load capacity. Right column: Optimisation with respect to a minimal friction coefficient.

the low-parameter gap functions (LPGFs), a clear order can be identified for the load optimised case over the whole range of compressibility numbers: Pocket and taper land gap functions bear the highest load and have as well the lowest friction coefficient. The taper geometry shows the lowest load capacity whereas the step geometry has the highest friction coefficient. These relations are found analogously for the optimisation with respect to a minimal friction coefficient (right column of figure 2.3). Here, e.g. for $\Lambda = 500$ pocket and step geometry have nearly the same dimensionless load capacity of $\overline{W} = 1.15$. But the friction coefficient of the step geometry is 75% (!) higher. This example and the other plots of figure 2.3 make clear that taper and step geometries perform significantly worse than pocket and taper land gap functions with respect to both, load capacity and friction coefficient. Therefore, they should be avoided in designs of air foil thrust bearings. Of course, this statement bases to that time only on the analysis of the reference topology ($\varphi_{hT} = 40°$ and $\lambda_r = 0.5$). It will be shown in section 2.2 that it is valid for a wide range of cylindrically sector-shaped topologies.

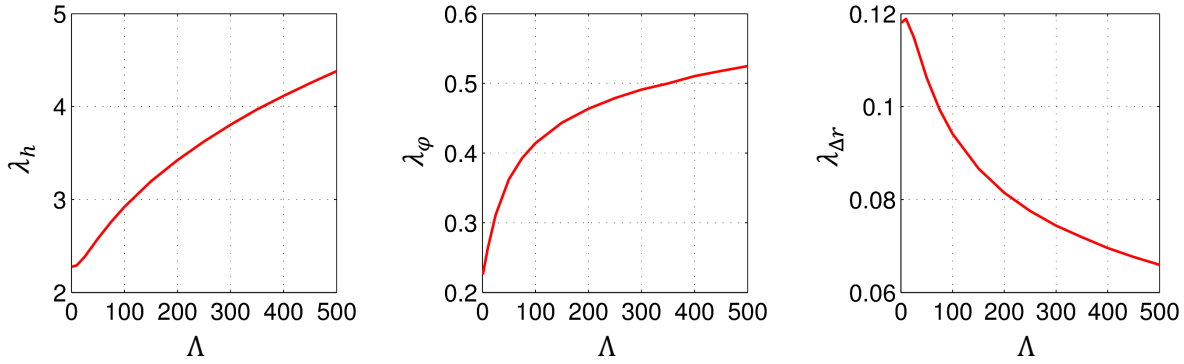

Figure 2.4: Optimal gap parameters for the pocket geometry as a function of the compressibility number Λ for the load optimised case.

Non-optimal configurations

It should be reminded that the results of figure 2.3 show the dimensionless load capacity and friction coefficient for optimised configurations. Given a certain type of LPGF as for example the pocket geometry, the gap parameters $\lambda_h, \lambda_\varphi$ and $\lambda_{\Delta r}$ of this geometry have been optimised for each compressibility number. Figure 2.4 shows the development of each gap parameter as a function of the compressibility number for the pocket geometry (load optimised case). It is evident that all three optimised parameters strongly depend in a nonlinear way on the compressibility number.

To illustrate the performance of non-optimal gap functions, the dimensionless load capacity is plotted as a function of the compressibility number for the three configurations indicated by Opt_1, Opt_{100} and Opt_{500} in figure 2.5. Herein, Opt_i represents a fixed pocket type gap function with gap parameters optimised for the compressibility number i, e.g. $\mathrm{Opt}_{100} = \{\lambda_h = 2.92, \lambda_\varphi = 0.41, \lambda_{\Delta r} = 0.094\}$. As to be expected, each configuration is superior to the others for a range of compressibility numbers close to the compressibility number it has been optimised for. As well interesting to note is that Opt_1 and Opt_{100} converge against an asymptote for high compressibility numbers. The great differences in dimensionless load capacity between the three configurations lead to two conclusions for air thrust bearings:

- It is essential for the bearing designer to know the operational conditions (e.g. speed, thrust load, temperature) of the rotating system as precisely as possible. Knowing these conditions, the compressibility number Λ can be calculated for the operational point of interest according to equation (2.12). Based on this estimation, appropriate optimal gap parameters can be chosen which are tabulated in the appendix for the taper land and the pocket geometry.

- If an air thrust bearing is to be designed not only for one operational point but for a whole range of compressibility numbers, the gap function parameters should be optimised for higher compressibility numbers of the range in order to avoid the danger of running into the load capacity asymptote.

Finally, it should be stressed that these findings are valid as well for air foil thrust bearings without loss of

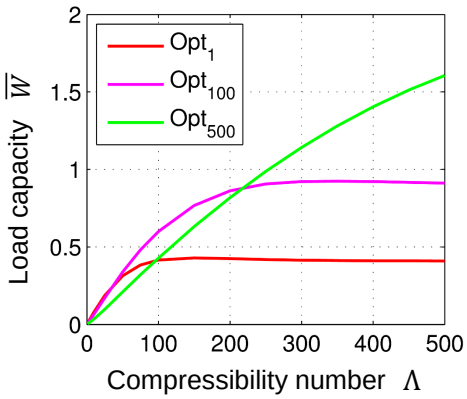

Figure 2.5: Dimensionless load capacity as a function of the compressibility number for three different gap functions. Opt_i represents a fixed pocket type gap function with gap parameters optimised for the compressibility number i (with respect to a maximal load capacity).

generality. Especially, the tabulated data for optimal gap parameters, shown in the appendix of this work, represents an orientation for the design of AFTBs. The particular choice of bump and top foil thickness as well as the design of the foils determine the elastic properties of AFTBs, which influence the real gap function and therefore superimpose to the already presented effects of rigid thrust bearings.

2.2 Optimisation of high-parameter gap functions for cylindrically sector-shaped pads

The presented results of section 2.1 base on relatively simple low-parameter gap functions (LPGFs) that are defined by at most three geometrical parameters. The comparison of different LPGFs already revealed basic design elements - e.g. the sealing in radial and circumferential direction - as key features for a good bearing design. Nevertheless, it is obvious that a further refinement of the gap function will improve the bearing performance. The main questions of interest in this section are therefore:

- Assuming to have no manufacturing limitations, what is the optimal gap function for cylindrically sector-shaped pads?
- How big is the difference in load capacity and friction coefficient between the optimal gap function and the already analysed LPGFs?

In order to investigate these two questions, the optimal gap function $h_{opt}(\overline{r},\phi)$ is approximated by a high-parameter gap function (HPGF) $h_{HPGF}(\overline{r},\phi)$ that consists of piecewise constant functions $h^*_{ij}(\overline{r},\phi)$. In dimensionless form (division by h_2) this yields

$$\overline{h}_{opt}(\overline{r},\phi) \approx \overline{h}_{HPGF}(\overline{r},\phi) = \sum_{i,j} \overline{h}^*_{ij}(\overline{r},\phi)\,, \tag{2.22}$$

where the dimensionless piecewise constant functions are defined by

$$\overline{h}_{ij}^{*}(\overline{r},\phi)=\begin{cases}\overline{h}_{ij}, & \overline{r}_i\le\overline{r}<\overline{r}_{i+1},\ \phi_j\le\phi<\phi_{j+1}\,,\\ 0, & \text{elsewhere}\,.\end{cases} \tag{2.23}$$

The optimisation problem is formulated analogously to section 2.1.1: For given topological and operational parameters φ_{hT}, λ_r and Λ, find

$$\underset{\overline{h}_{ij}}{min}\ Q(\overline{h}_{ij}) \tag{2.24}$$

with the explicit constraints

$$-10\le\overline{h}_{ij}\le-1 \tag{2.25}$$

for the control variables. Objective functions of interest are either the dimensionless load capacity $Q=-\overline{W}$ or the friction coefficient $Q=f$. The concrete number of control variables depends on the applied grid. For the reference topology, defined by the parameters $\varphi_{hT}=40^\circ$ and $\lambda_r=0.5$, a 40x40-grid is used resulting in 1600 control variables $\overline{h}_{ij}$. For other values of φ_{hT} and λ_r the grid is adjusted appropriately. The nondimensional Reynolds equation (2.11) is discretised on the same grid by quadriletaral Lagrange elements of quartic order. A commercial gradient based optimisation solver is used to optimise the control variables with respect to a maximal load capacity or a minimal friction coefficient. Similar optimisations have been performed by Rohde et al. [RM76] for slider bearings and Jai et. al. [JBI04] for journal bearings.

2.2.1 Optimisation results for HPGFs

Figure 2.6 illustrates the results for the optimisation of HPGFs with respect to a maximal load capacity. The shape of the optimised gap function and the corresponding pressure distribution are shown for the compressibility numbers of $\Lambda=1$ (left) and $\Lambda=500$ (right). At first glance, the optimal HPGF is of similar shape for the two cases. Close to the trailing edge and the inner and outer radius of the pad, the dimensionless piecewise constant elements of the gap function take the maximal value of $\overline{h}_{ij}=-1$ which results in a pocket type geometry. A further common feature of both HPGFs is the radially directed taper that has not been accounted for by any of the LPGFs. On the other hand, some differences that have already been observed for LPGFs are found as well for the HPGFs. For example, the land region close to the trailing edge extends and the inlet film height rises with increasing compressibility number.

The most interesting point of the HPGF analysis can be found in the pocket shaped subarea of the pad. For the low compressibility number of $\Lambda=1$, the optimal HPGF shows only a very slight taper in circumferential direction. Therefore, in absence of the radially directed taper, the film height in the pocket shaped subarea would be of nearly constant height $\overline{h}\approx-2.5$ what equals the corresponding value for the LPGF of pocket type (compare figure 2.2). By contrast, for the high compressibility number of $\Lambda=500$ the optimised HPGF shows a steep circumferentially directed taper within the pocket shaped subarea of the

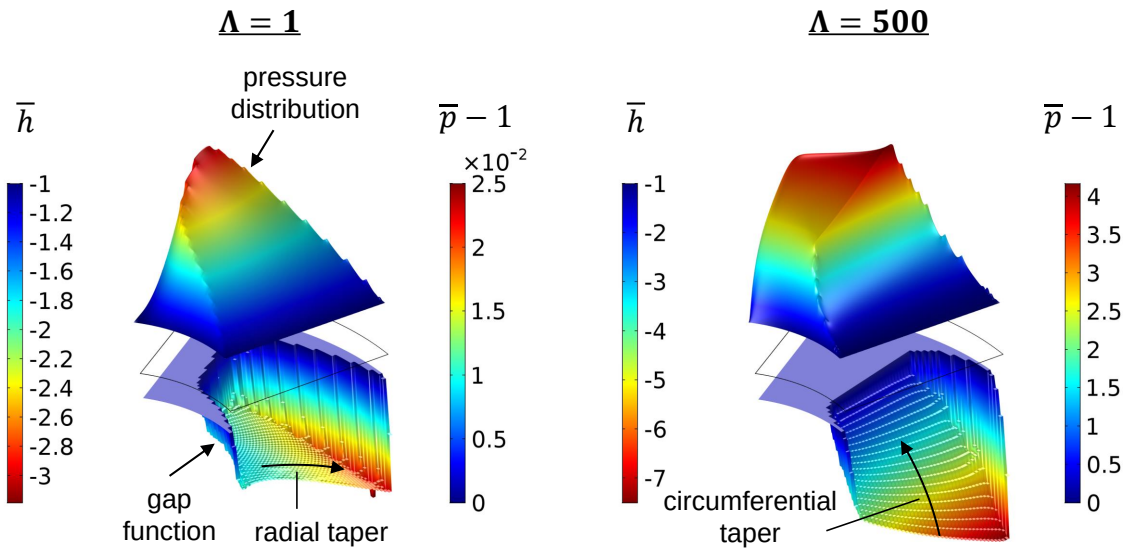

Figure 2.6: Gap function and pressure distribution of optimised HPGFs (with respect to load capacity) for two different compressibility numbers Λ.

pad. In addition, the land region next to the inner and outer radius of the pad is considerably smaller than for the low compressibility number of $\Lambda = 1$. These two tendencies result in a gap shape that is very close to the LPGF of taper land type.

It can be therefore concluded that the optimal gap function of a circumferentially sector-shaped pad is well approximated by a combination of the LPGFs of taper land and pocket type. In general, the geometry of the pocket LPGF is predominant for the incompressible limit of $\Lambda \to 0$ whereas the taper land part becomes more dominant for increasing compressibility numbers.

This conclusion is supported by the results of figure 2.7. It shows the dimensionless load capacity $\overline{W}$ and the friction coefficient f as a function of the compressibility number Λ for the load optimised case. The plot for the friction coefficient clearly illustrates that the pocket type LPGF has nearly the same friction coefficient as the optimised HPGF for the limit case of $\Lambda \to 0$. This supports the thesis that the optimal gap function is close to the pocket type LPGF for incompressible fluids. With increasing compressibility number, the blue line of the pocket type LPGF diverges from the dashed black line of the HPGF for both, load capacity and friction coefficient. This tendency can be traced back to the fact that the pocket type LPGF has no taper in the pocket shaped subarea of the pad in contrast to the HPGF.

Nevertheless, for the high compressibility number of $\Lambda = 500$ the difference in load capacity and friction coefficient between the optimised HPGF and the pocket type LPGF is only about 15%. This proves that relatively simple LPGFs can perform close to the optimum that can be achieved with cylindrically sector-shaped pads.

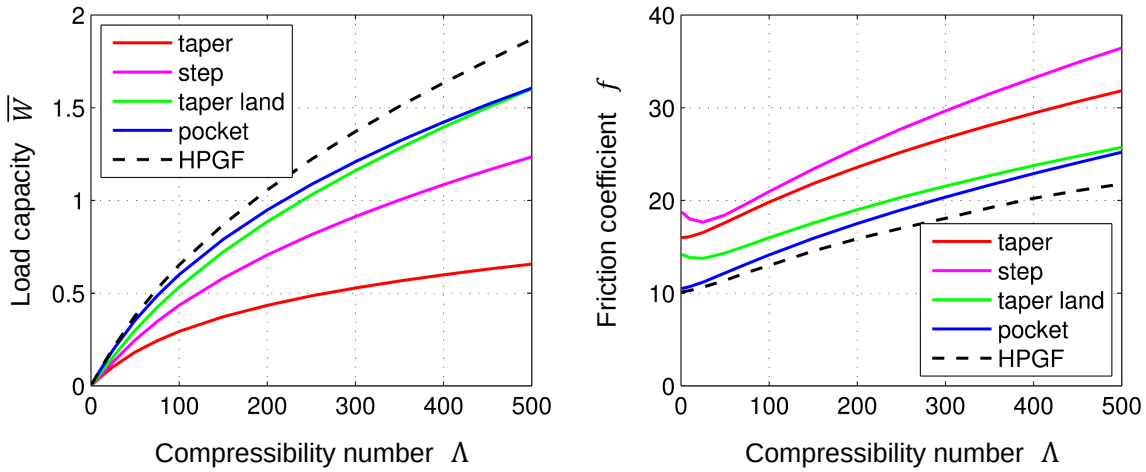

Figure 2.7: Dimensionless load capacity $\overline{W}$ and friction coefficient f for the optimised (with respect to load capacity) HPGF in comparison to the optimised LPGFs.

2.2.2 Optimisation results for different cylindrically sector-shaped topologies

It has been shown in section 2.1.1 that the dimensionless pressure $\overline{p}$ and load capacity $\overline{W}$ as well as the friction coefficient f are only functions of the three topological and operational parameters φ_{hT}, λ_r, Λ and the dimensionless gap height $\overline{h}$ (for a cylindrically sector-shaped pad). In the already presented optimisations of sections 2.1.2 and 2.2.1, the topological parameters were fixed to $\lambda_r = 0.5$, $\varphi_{hT} = 40°$ and the LPGFs and the HPGF were optimised as a function of the compressibility number. In order to study the influence of the pad topology, the above described optimisations are repeated for the ranges of topological parameters $\lambda_r = 0.3..0.7$ and $\varphi_{hT} = 30°..60°$, which cover the vast majority of thrust bearing applications. The results are illustrated in figure 2.8 for the load optimised case. In contrast to previous representations, the normalised dimensionless load capacity $\overline{W}/(\Lambda \cdot \overline{W}_{tl,\Lambda=1})$ is plotted versus the compressibility number. Here, $\overline{W}_{tl,\Lambda=1}$ is the dimensionless load capacity of the taper land LPGF for a compressibility number of $\Lambda = 1$.

The chosen representation has two advantages. Firstly, for an incompressible fluid the normalised dimensionless load capacity of a taper land LPGF is independent of the compressibility number $\overline{W}_{tl,incompr}/(\Lambda \cdot \overline{W}_{tl,\Lambda=1}) = 1$. Thus, a direct comparison between the performance of air bearings and oil bearings can be drawn for taper land LPGFs that are the most widespread LPGFs in thrust bearing applications. Secondly, the chosen representation enables a comparison of the different types of gap functions over the whole range of compressibility numbers. In particular, the incompressible limit case $\Lambda \to 0$ becomes more clear than in the former used presentation of the form $\overline{W}(\Lambda)$. Finally, it should be mentioned that $\overline{W}_{HPGF,\,\Lambda=1}$ and $\overline{W}_{HPGF,\,\Lambda=500}$ give the maximal dimensionsless load capacities of the different topologies for the nearly incompressible ($\Lambda = 1$) and highly compressible ($\Lambda = 500$) case.

The main results of figure 2.8 are:

- Taper and step configurations are inferior to taper land and pocket type LPGFs and should be avoided

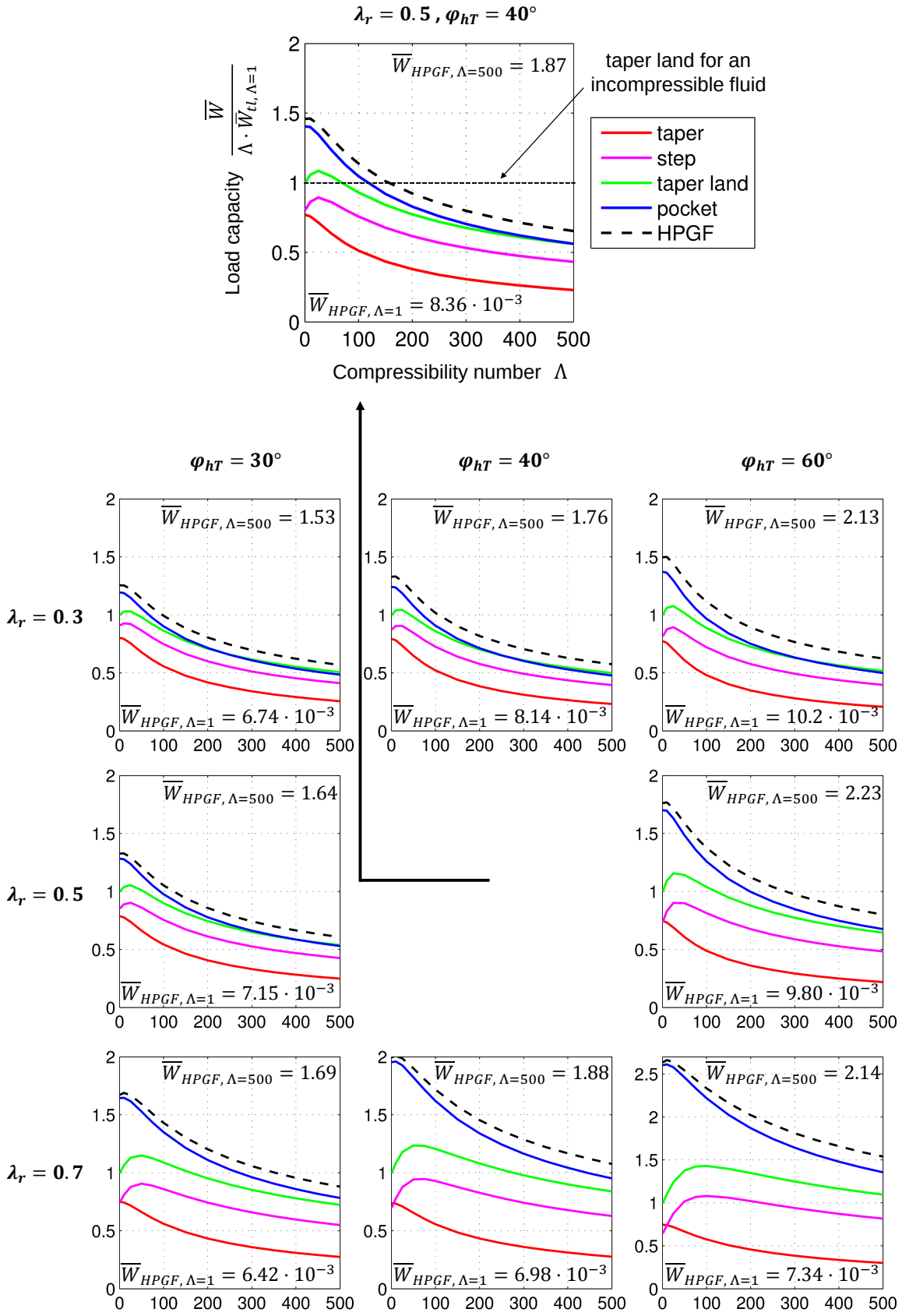

Figure 2.8: Normalised dimensionless load capacity $\overline{W}/(\Lambda \cdot \overline{W}_{tl,\Lambda=1})$ as a function of the compressibility number Λ for the load optimised case. $\overline{W}_{tl,\Lambda=1}$ is the dimensionless load capacity of the taper land LPGF for the compressibility number of $\Lambda = 1$.

therefore.

- The pocket LPGF is always superior to the taper land LPGF for small compressibility numbers. For incompressible fluids the difference ranges from 20% ($\varphi_{hT} = 30°$, $\lambda_r = 0.3$) up to 160% ($\varphi_{hT} = 60°$, $\lambda_r = 0.7$). But with increasing compressibility number the advantages of the pocket LPGF reduce rapidly. The lower the ratio λ_r between the outer and inner radius of the pad and the smaller the angular extent φ_{hT} of the pad, the smaller is the value of the critical compressibility number for which the taper land LPGF starts showing a higher dimensionless load capacity than the pocket LPGF. This behaviour can be refered to the fact that the taper land LPGF has no radial sealing element and thus suffers from side leakage for radially tight (large λ_r) and circumferentially long (large φ_{hT}) pad shapes.

- For all topologies, a range of compressibility numbers exists for which a taper land LPGF reaches higher dimensionless load capacities with compressible fluids than with incompressible fluids. The extent of the range rises with increasing φ_{hT} and λ_r.

- The pocket type LPGF is close to the HPGF for all topologies. In case of incompressible fluids, the deviation in dimensionless load capacity is at most 10% whereas for the highly compressible case of $\Lambda = 500$ the maximal deviation is 25%.

- The optimal dimensionless load capacities of cylindrically sector-shaped pads rise with increasing angular extent φ_{hT}.

Finally, it is remarked that the results of figure 2.8 can be directly used for the design of both, oil and air bearings. The optimal set of gap parameters for the pocket and taper land LPGFs are tabulated as a function of the different topologies and compressibility numbers in the appendix.

2.2.3 Limits of air thrust bearings

In general, the choice of a suitable bearing technology for a certain rotordynamic application is a difficult task. The reason for this lies in the fact that not only the properties of the turbomachine define the requirements on the bearing technology, but the bearings frequently have a fundamental influence on the machine design in turn. Therefore, knowledge about the limits of a bearing technology are of high value for the designer of a turbomachine. In case of AFTBs, the limiting factor for a possible application is mostly the poor load capacity which has its origin in the very low dynamic viscosity of air.

A criterion for a possible application of an AFTB can be estimated from figure 2.9. It shows the dimensionless load capacity $\overline{W}$ (left) and the friction coefficient f (right) for a cylindrically sector-shaped pad of taper land and pocket type. Based on the findings of the previous section, the topology of the pad is chosen to be $\varphi_{hT} = 90°$ and $\lambda_r = 0.5$ since higher pad angles have been identified to be beneficial for the load capacity. Additionally, the range of compressibility numbers has been extended up to the very high value of $\Lambda = 2500$.

It can be seen from figure 2.9 that even for very high compressibility numbers the gap parameters of the two LPGFs can be optimised in order to avoid the load capacity limit that has been encountered for non-optimised pad geometries. Thus, at least theoretically, arbitrary load capacities can be achieved by an increase of the compressibility number (e.g. bigger diameter, higher speeds, etc., see definition (2.12)).

But a closer examination of the corresponding friction coefficient reveals that the operation of air bearings for very high compressibility numbers is not reasonable. Compared to an oil bearing (incompressible fluid, dashed lines), the friction coefficient of an air bearing is 3-5 times higher for $\Lambda = 2500$.

Assuming the same minimal film height h_2 for both bearing technologies, this fact has two consequences:

- In general, air bearings are frequently said to be more efficient than oil bearings because they do not have losses due to sealing rings and oil supply systems. But with increasing compressibility number this advantage is cancelled out. For $\Lambda = 2500$ the purely hydrodynamic power loss of the air bearing is 3-5 times higher than for a comparable oil bearing. It is doubtful whether this is acceptable since efficiency requirements are increasing in modern turbomachinery.

- Air bearings are prone to thermal distortions of the rotor disk that limit the load capacity as will be shown in chapter 4. The increase of the friction coefficient with the compressibility number is therefore extremely unfavourable and effectively leads to a friction induced load capacity limit.

Remembering its definition $\overline{W} = \frac{W}{p_0 A_{pad}}$, the dimensionless load capacity gives the specific load in bar for atmospheric conditions ($p_0 = 1\,bar$). Therefore, it can be directly concluded from figure 2.9 that $5\,bar$ is probably an upper limit and $1 - 2\,bar$ a realistic value for most applications of AFTBs. Especially, since foil deformations and misalignment (see chapter 3) are further factors that can reduce the load capacity.

The presented estimation is confirmed by published experimental results. Iordanoff [Ior99] described a method for a rapid design of AFTBs and achieved a specific load capacity of $3\,bar$. Heshmat [Hes05] even reported $5.5\,bar$ for a high temperature application ($815°C$).

2.3 Topological optimisation

So far, the analysis has been restricted to cylindrically sector-shaped pads. This topology is widely used since it effectively exploits the bearing surface. For small compressibility numbers, thermal deformations of the rotor disk are negligible and the highest possible load capacity is achieved if the pressure generating pads cover nearly 100% of the bearing surface. But for high compressibility numbers, a load capacity limit due to thermal deformations of the rotor disk will be revealed in chapter 4. Furthermore, Bruckner [Bru13] identified the fluid mixing in the bearing cavity between two pads as an effective method to cool the thrust bearing. In his experiments, an AFTB with pads covering only a part of the bearing surface achieved higher load capacities (for high rotor speeds) than a fully covered thrust bearing. Two conclusions may be drawn from these findings:

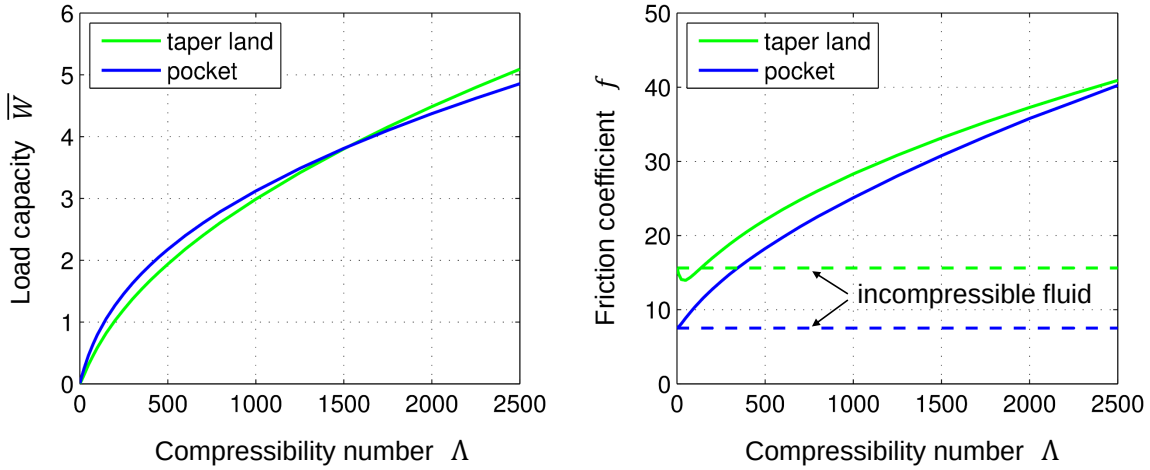

Figure 2.9: Dimensionless load capacity $\overline{W}$ (left) and friction coefficient f (right) as a function of the compressibility number Λ for a cylindrically sector-shaped pad with topological parameters $\varphi_{hT} = 90°$ and $\lambda_r = 0.5$ (load optimised case).

- For high compressibility numbers, friction optimised bearings can lead to higher load capacities than load optimised bearings because of reduced thermal deformations.
- If the cavity between two pads can be essential for an effective cooling of the bearing, there is no need to use cylindrically sector-shaped pads in order to fully exploit the bearing surface.

Therefore, in this section a topological optimisation with respect to a minimal friction coefficient is performed. After that, the power loss of a load optimised cylindrically sector-shaped taper land pad is compared to the power loss of a friction optimised pad with a more complex topology.

2.3.1 Topological optimisation with respect to a minimal friction coefficient

The approach in this section is not a general topology optimisation comparable to the use of HPGFs in section 2.2 for the identification of an optimal gap function for cylindrically sector-shaped pads. Instead, an attempt is made to identify at least some features of a friction optimised topology.

For this purpose the optimised HPGF, with respect to a minimal friction coefficient, is depicted in figure 2.10 (left). Without any claim to completeness, three features are noteworthy in the optimised HPGF.

1. The isolines of constant gap height are of spiral shape in the pocket area.
2. Close to the trailing edge at the outer radius, the height function suddenly takes the minimal allowed value of $\overline{h} = -10$ (compare the explicit constraint (2.25)). Apparently, the reduction of the torque by the big gap size in this region is higher than the loss of load capacity resulting in a smaller friction coefficient.
3. A deep chamber exists at the intersection line of the pocket region and the land region of the pad. The chamber reduces the torque without significantly diminishing the pressure in this region.

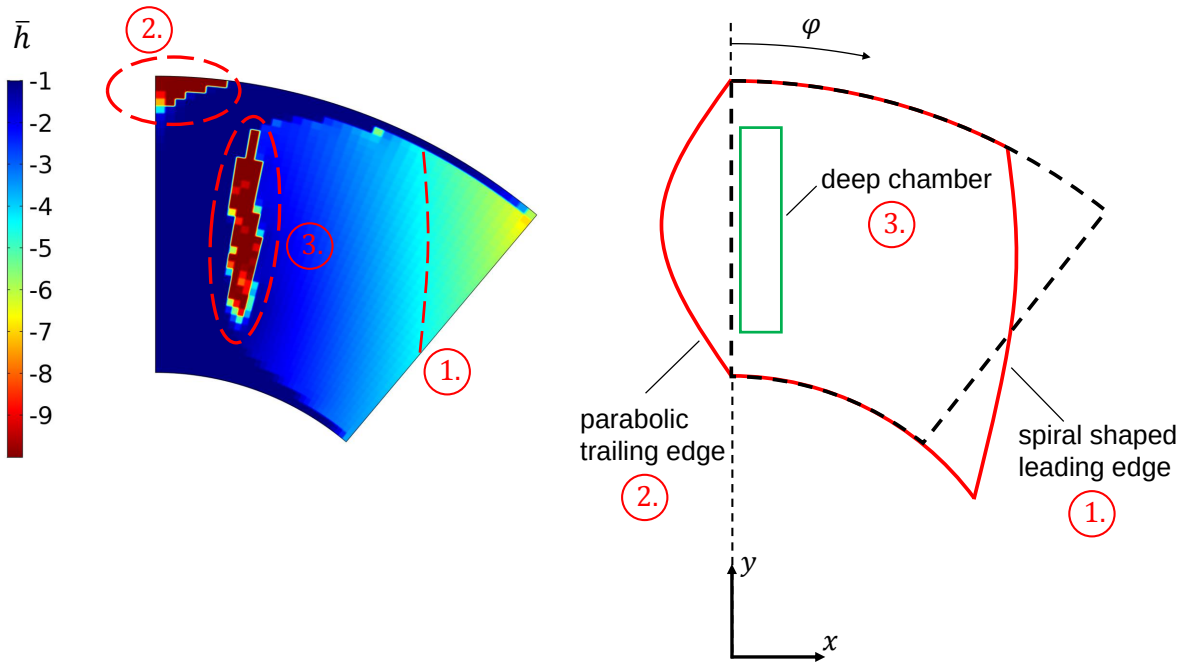

Figure 2.10: Optimised HPGF with respect to a minimal friction coefficient (left). Features of the topologically optimised pad (right).

The first two observed effects are used in order to design a new pad topology that is illustrated in figure 2.10 (right) by the red lines. The leading edge is now of spiral and the trailing edge of parabolic shape. This results in two additional design parameters in comparison to the cylindrically sector-shaped pad. In order to compare the new design to the reference pad of cylindrical shape ($\varphi_{hT} = 40°$, $\lambda_r = 0.5$), it is demanded that the surface area of the new topology is equal to the surface area of the reference pad.

As in case of the cylindrically sector-shaped pad, different gap functions are possible for the new topology. For this comparison a taper land gap function is applied since it is widely used in AFTB applications. Because of manufacturing reasons, in most thrust bearing designs the slope of the taper is not a function of the pad angle φ (compare equation (2.3)) but of the cartesian coordinate x. The nominal height function of this cartesian taper land type is

$$h_{nom,tl,cart} = h_2 + m(x - x_{land})(x > x_{land}) \,, \tag{2.26}$$

where m represents the slope of the taper and x_{land} is the x-coordinate at which the land region ends and the taper starts.

This cartesian taper land gap function is applied in the following to the cylindrically sector-shaped topology and the new topological design. Both pad designs are optimised with respect to a minimal friction coefficient for different compressibility numbers. In case of the cylindrically sector-shaped pad, only the gap parameters m and x_{land} are used as control variables. For the new design, the spiral angle at the leading edge and a parameter describing the shape of the parabolic trailing edge are additional control variables.

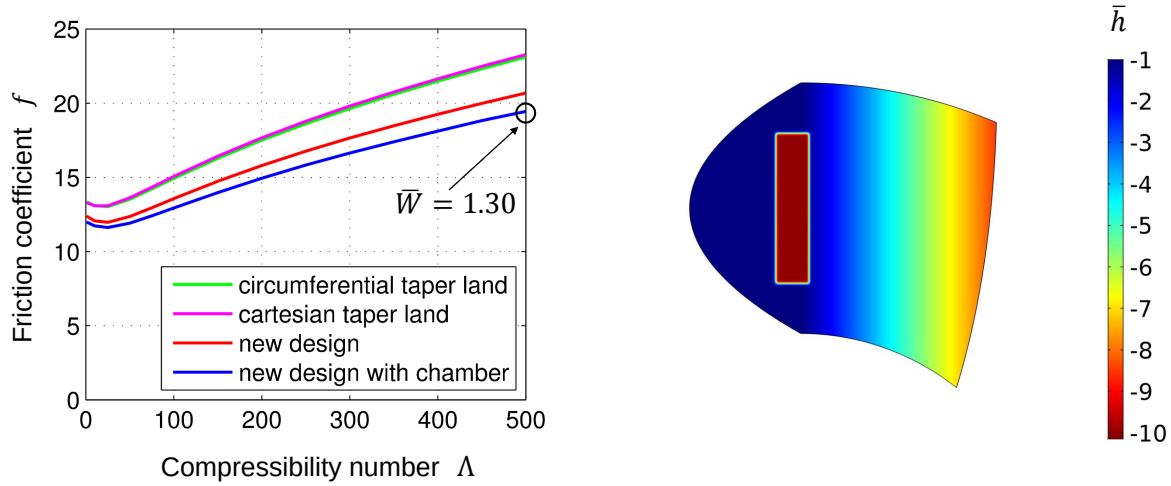

Figure 2.11: Left: Friction coefficient f for the cylindrically sector-shaped pad (with a circumferential and a cartesian taper) and the topologically optimised new design of figure 2.10. Right: Topology and gap function of the optimised new design with a deep chamber for a compressibility number of $\Lambda = 500$.

Figure 2.11 shows the optimisation results for the analysed topologies. It can be clearly seen, that for all compressibility numbers the new design has a lower friction coefficient than the cylindrical pad design with the cartesian taper land. Furthermore, it is evident that for the considered small pad angle of $\varphi_{hT} = 40°$, the cartesian taper land gap function has the same friction coefficient as the in section 2.1 analysed circumferential taper land gap function (compare, green line in the right column of figure 2.3).

The third friction reducing feature that has been identified in the optimised HPGF of figure 2.10 (left) is the deep chamber next to the trailing edge. Incorporating such a chamber in the gap function of the new topological design results in a further reduction of the friction coefficient over the whole range of compressibility numbers. For $\Lambda = 500$ the difference between the cylindrically sector-shaped pads and the new design with a chamber is nearly 20%!

To sum up, it has been shown that an optimisation of the pad topology can lead to a significant reduction in the friction coefficient. From a manufacturing point of view, complex pad designs are no problem in case of AFTBs since the top foil can be lasered.

2.3.2 Comparison of load optimised and friction optimised thrust bearings with respect to power loss

Two questions may arise after the analysis of topologically optimised pads of the previous section.

1. What is the ratio in power loss between a load optimised thrust bearing and a friction optimised thrust bearing?

2. Is it possible that friction optimised thrust bearings can have a higher load capacity than load optimised thrust bearings if thermal distortions are taken into account?

To clarify these points, two pad configurations are chosen for a comparison: The first pad is of cylindrical sector shape with a circumferential taper land gap function that is optimised with respect to a maximal load capacity. The friction coefficient f_{cyl} and the dimensionless load capacity $\overline{W}_{cyl}$ of this pad type can be taken from figure 2.7 (green lines). The second pad in the comparison is the new design with a deep chamber that has been optimised for a minimal friction coefficient in the last section. All variables referring to this design are indexed in the following by 'nC'.

The requirements on both pad types are the same: A thrust load W is to be balanced in a turbomachine for a fixed angular velocity Ω. Both pads have identical outer radii r_{oT} and surface areas $A_{cyl} = A_{nC}$. The dynamic viscosity η of the lubricating fluid and the reference pressure p_0 are as well the same for both configurations.

The thrust load W is assumed to be

$$W = \overline{W}_{nC}(\Lambda_{nC} = 500) p_0 A_{nC}\,, \tag{2.27}$$

that is the new design with the deep chamber operates for the given thrust load at a compressibility number of $\Lambda_{nC} = 500$ resulting in a dimensionless load capacity of $\overline{W}_{nC}(\Lambda_{nC} = 500) = 1.30$. Since the reference pressure p_0 and the pad area are identical for both pad configurations, it follows

$$\overline{W}_{cyl}(\Lambda_{cyl}) = \overline{W}_{nC}(\Lambda_{nC} = 500) = 1.30 \tag{2.28}$$

from the definition of the dimensionless load capacity. As the cylindrical pad has a higher load capacity than the pad of the new design with the deep chamber, it will operate at a lower compressibility number which can be found to be $\Lambda_{cyl} = 360$ from figure 2.7 (left). The corresponding friction coefficient of the cylindrical pad is (see, figure 2.7 (right))

$$\overline{f}_{cyl}(\Lambda_{cyl} = 360) = 22.90\,. \tag{2.29}$$

From the definition of the friction coefficient $f = \frac{M}{h_2 W}$ it follows for the ratio of power losses for the two pad configurations

$$\frac{P_{cyl}}{P_{nC}} = \frac{M_{cyl}}{M_{nC}} = \frac{f_{cyl}}{f_{nC}} \cdot \frac{h_{2,cyl}}{h_{2,nC}}\,. \tag{2.30}$$

Using the definition of the compressibility number $\Lambda = \frac{6\eta\Omega}{p_0}\frac{r_{oT}^2}{h_2^2}$, the ratio of power losses is found to be

$$\frac{P_{cyl}}{P_{nC}} = \frac{f_{cyl}}{f_{nC}} \cdot \sqrt{\frac{\Lambda_{nC}}{\Lambda_{cyl}}} = \frac{22.90}{19.44} \cdot \sqrt{\frac{500}{360}} = 1.178 \cdot 1.179 = 1.39\,. \tag{2.31}$$

The calculation clearly shows that the load optimised cylindrically sector-shaped pad has a nearly 40% higher power loss than the friction optimised new design for identical conditions of load and bearing size. This difference diminishes for smaller compressibility numbers, e.g. it is 29% for $\Lambda_{nC} = 100$. It can be

concluded that for low to moderate loads W, both pad types will carry the thrust load, but the new design will have a considerably lower power loss. The interesting condition is that of a very high load that approaches the load capacity limit of the new designed pad. Assuming $h_{2,cyl} = 5\mu m$ as the critical minimal film height for full hydrodynamic lubrication, it can be directly followed from equations (2.30) and (2.31) that the same load will lead to a minimal film height of $h_{2,cyl} = 5\mu m \cdot 1.179 = 5.90\mu m$ for the load optimised cylindrical pad. Thus, the cylindrical pad operates at a $0.9\mu m$ higher minimal gap height but has a 40% larger power loss. Under these circumstances it is likely that the thermal distortions due to the additional power loss outweigh the $0.9\mu m$ higher minimal gap height. As a consequence, the friction optimised bearing could carry a higher thrust load than the load optimised bearing if thermal distortions are taken into account.

2.4 Optimisation of the spiral groove bearing

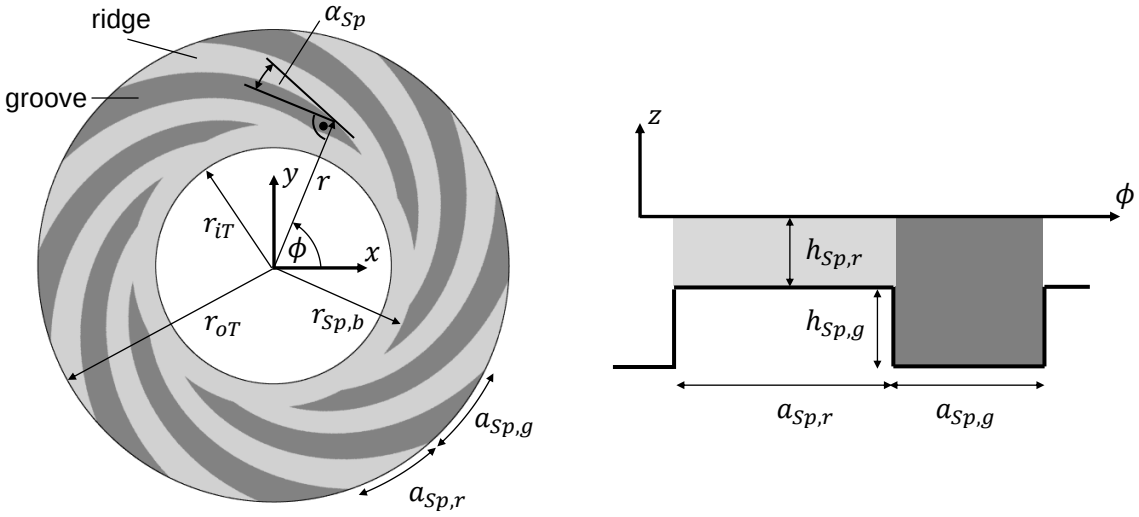

Figure 2.12: Geometrical parameters of a spiral groove thrust bearing.

Almost all applications of AFTBs base on a pad type topology. An alternative are groove type thrust bearings. Muijderman [Mui64] analysed different types of spiral groove bearings (SGB) for incompressible fluids and found the partially grooved SGB with a resistance at the inner radius to have the highest load capacity. Figure 2.12 illustrates the geometry of this SGB. Basically, it consists of a flat bearing surface with spiral shaped grooves of the depth $h_{Sp,g}$. For an aligned configuration, the minimal gap height in the lubricating gap is $h_{Sp,r}$. The widths of a groove and a ridge are given by $a_{Sp,g}$ and $a_{Sp,r}$ at the outer radius r_{oT} of the bearing. The spiral shaped grooves do not start at the inner radius r_{iT}, but at the radius $r_{Sp,b}$ and have the spiral angle α_{Sp}. Table 2.1 summarizes the geometrical parameters that fully describe the geometry of the partially grooved SGB. The pressure distribution in a SGB can be found analogously to the case of pad type bearings by solving the Reynolds equation (2.11). The compressibility number is then defined as $\Lambda = \frac{6\eta\Omega}{p_0}\frac{r_{oT}^2}{h_{Sp,r}^2}$. Details to the numerical solution are not presented here, but have been published in [LS15].

The main aim of this analysis is a comparison of optimised SGBs to the previously analysed pad type

		Optimal values ($\Lambda = 1$)	Optimal values ($\Lambda = 500$)
Number of grooves	$E_{Sp} = 15$		
Ratio of radii	$\lambda_r = \frac{r_{iT}}{r_{oT}} = 0.5$		
Ratio of radii (resistance)	$\lambda_{Sp,b} = \frac{r_{Sp,b}}{r_{oT}}$	0.640	0.697
Spiral angle	α_{Sp}	$13.3°$	$9.01°$
Relative groove width	$\kappa_{Sp} = \frac{a_{Sp,g}}{a_{Sp,g}+a_{Sp,r}}$	0.572	0.608
Relative groove height	$\gamma_{Sp} = \frac{h_{Sp,g}}{h_{Sp,g}+h_{Sp,r}}$	0.776	0.839
Dimensionless load capacity	$\overline{W}$	$9.17 \cdot 10^{-3}$	3.94
Friction coefficient	f	7.78	8.64

Table 2.1: Geometrical parameters of the partially grooved SGB. Optimal parameters for an optimisation with respect to a maximal load capacity for two different compressibility numbers of $\Lambda = 1$ and $\Lambda = 500$.

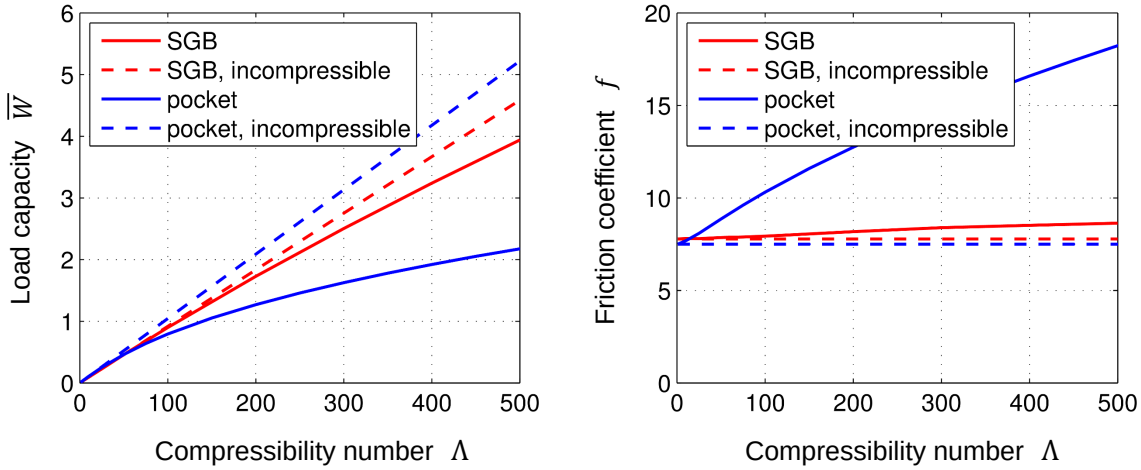

Figure 2.13: Dimensionless load capacity $\overline{W}$ (left) and friction coefficient f (right) for the optimised (with respect to load capacity) SGB and pocket type LPGF ($\varphi_{hT} = 90°$, $\lambda_r = 0.5$).

thrust bearings. For this purpose, a SGB with $E_{Sp} = 15$ grooves and $\lambda_r = 0.5$ is considered (see [LS15, GS13, Mui64] for the influence of the number of grooves E_{Sp} on the bearing performance). Applying an optimisation with respect to a maximal load capacity for the four control variables $\lambda_{Sp,b}$, α_{Sp}, κ_{Sp} and γ_{Sp}, results in the optimal geometrical parameters given in table 2.1. Note, that the optimisation is performed as a function of the compressibility number analogously to section 2.1.1.

Figure 2.13 illustrates the dimensionless load capacity $\overline{W}$ (left) and the friction coefficient f (right) for a load optimised SGB in comparison to a load optimised pad type thrust bearing with a pocket LPGF ($\varphi_{hT} = 90°$, $\lambda_r = 0.5$). It is interesting to note that for an incompressible fluid, the pocket LPGF achieves a 13% higher load capacity and a slightly lower friction coefficient than the SGB. Therefore, optimised pad type thrust bearings definitely can compete to SGBs for incomressible conditions. But if air is used as lubricating fluid, the situation is completely different. Whereas for $\Lambda = 500$ the load capacity of the pocket LPGF diminishes to only 42% of the corresponding incompressible pocket LPGF, the difference between the compressible and the incompressible SGB is only 15%.

As a consequence, for $\Lambda = 500$ the SGB has a nearly two times higher dimensionless load capacity than the pocket LPGF. It is only for a nearly three times higher compressibility number of $\Lambda = 1600$ where the

pocket LPGF achieves a comparable dimensionless load capacity of $\overline{W} \approx 4$ (compare figure 2.9).

The same discrepancy is found with regard to the friction coefficient. Whereas the pocket LPGF shows a significant increase of the friction coefficient up to a value of $f(\Lambda = 500) = 18.2$, the increase is only about 10% in case of the SGB for the same range of compressibility numbers.

In summary, it can be stated that the compressibility effect is far less pronounced for SGBs than for pad type thrust bearings. Therefore, at least theoretically SGBs can achieve considerably higher load capacities and significantly lower power losses. Unfortunately, SGBs are reported to suffer from instability phenomena that can limit the operation at high compressibility numbers [MP65, HSJ04].

3 Elasto-hydrodynamics of AFTBs

The previous analysis of AFTBs in chapter 2 based on the assumption of rigid bearing components. This assumption enabled a clear identification of fundamental hydrodynamic effects without superimposing effects of the foil structure. Furthermore, the presented purely hydrodynamic model can be regarded as the simplest possible model for AFTBs. It is accurate for small loads - what equals small compressibility numbers - or thick and therefore stiff foils. In both cases, the deformations of the foils due to the hydrodynamic pressure are small compared to the minimal film thickness in the AFTB. Thus, the real gap height in the Reynolds equation is well approximated by the nominal gap height of the undeformed bearing configuration.

Historically, foil bearings have been developed as a supplement to rigid bearings. The main idea of using foils was to give the bearing a significant compliance in order to improve its performance. Therefore, in most AFTB applications the foils are intended to deform in a magnitude of order that is of the same order as the gap size. Obviously, for these conditions the purely hydrodynamic model of chapter 2 is no longer accurate. Instead, a model for the deformation of the foils is needed.

It is therefore the aim of section 3.1 to develop a coupled elasto-hydrodynamic model for an AFTB. The foil deformations are described by a shell model that is coupled to the isothermal Reynolds equation. Particular attention is placed on several structural effects of the foils that are often not accounted for by reduced models published in the literature.

In section 3.2, the detailed elasto-hydrodynamic model is used in order to determine advantages and disadvantages of the installed compliance in AFTBs. For this purpose, AFTBs are compared to rigid thrust bearings for aligned, distorted and misaligned conditions.

Note that throughout chapter 3, thermal aspects are again neglected in order to clearly identify effects resulting from the elastic properties of the bearing.

3.1 Structural model for top and bump foil

3.1.1 Introduction

Figure 3.1a illustrates the structure of a bump type AFTB. Several corrugated foils (bump strips) are placed on a rigid base plate and act as an elastic foundation for the top foil. Every bump strip consists of an alternating series of arc-shaped bumps and straight bridges. The top lines of the bumps are in contact with the top foil and balance the hydrodynamic pressure forces that act on the top foil (in figure 3.1a only a part of the top foil is shown in order to illustrate the bump strips).

The stiffness of the bearing depends on the geometrical parameters of the bump strips and can be controlled by well-documented manufacturing techniques [DRBH08, DBD$^+$08]. Using several bump strips and a different spacing between the bumps, enables varying stiffness distributions in radial and circumferential directions. Thus, the stiffness distribution can be adjusted to tilting motions of the runner or specific hydro-

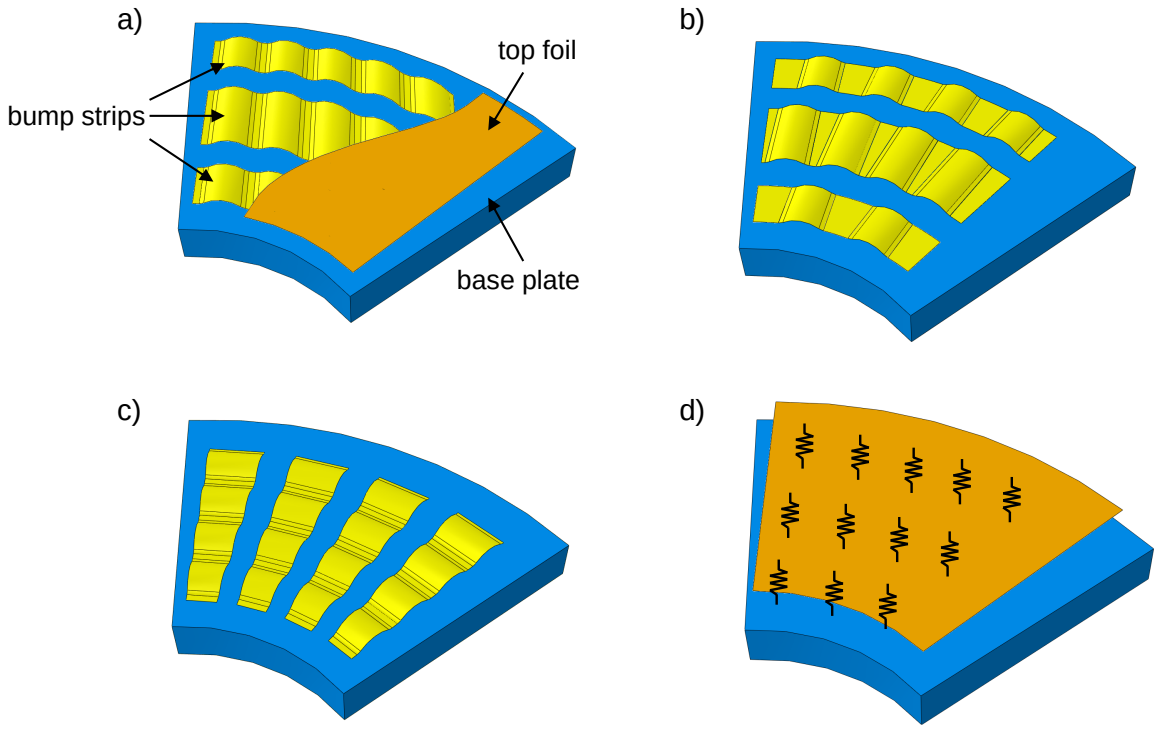

Figure 3.1: Various types of AFTB pads. a) Cartesian pattern of bumps as presented in [Ior99]. b) Circumferential pattern of bumps [Bru12]. c) Radial arrangement of bump strips [LK11]. d) Reduced elastic foundation type model of an AFTB.

dynamic pressure profiles. A further advantage of bump type air foil bearings is the high amount of damping that they can produce [LLAF07b, IBSMB08, KH94, SHW03]. When the bearing is loaded, dry friction occurs due to the motion of the bump strips on the base plate and the relative motion between the bump strips and the top foil, leading to energy dissipation. Friction does not only affect rotordynamic stability, but has a great impact on the stiffness distribution of an air foil bearing [KH92].

As already mentioned, the deflections of the foils due to the applied load have a considerable influence on the generated pressure in an air foil bearing, since they directly affect the real gap size between the top foil and the rotor disk. For this reason, detailed structural models of the foil sandwich are essential in order to calculate the performance characteristics of bump type air foil bearings.

An early structural model of a single bump including friction has been provided by Walowit and Anno [WA75]. Heshmat et al. used their formula for the case without friction in order to calculate the pressure distribution in compliant thrust [HWP83a] and journal bearings [HWP83b]. They assumed the stiffness of the bump foils to be uniformly distributed over the top foil. Thus, the deflection of the top foil was directly proportional to the pressure at every point of the top foil. Later, Ku and Heshmat [KH92] developed an analytical model for an one-dimensional bump strip including friction effects. Iordanoff [Ior99] calculated the compliance of a single welded bump (fixed at one end and simply touching at the other end) and a single free bump, and assumed the stiffness distribution of a bump strip to be a linear function of these two stiffness values. Carpino [CMP94] studied the effects of membrane stresses in the top foil on the performance of a

journal bearing. Le Lez et al. [LLAF07b] performed a comprehensive static and dynamic characterisation of a linear bump strip with the help of a commercial finite element software and used their results in order to develop an analytical model of an one-dimensional bump strip [LLAF07a]. Lee et al. [LKK08] studied the static performance of foil journal bearings, considering two-dimensional shape of the foil structure but neglecting friction.

In summary, a number of models have been presented for the characterisation of one-dimensional bump strips. Since the bump strips in journal bearings have always a linear straight shape, the one-dimensional model can be regarded as a good approach for journal bearings. In case of thrust bearings, the situation is different. Firstly, it can be seen from figure 3.1 that the bump strips are not straight but curved. Obviously, it is not straightforward - or simply impossible - to approximate a curved bump strip by an one-dimensional model. Secondly, in contrast to journal bearings a lot of different bump strip geometries have been presented for thrust bearings [Ior99, Bru12, LK11] (compare figure 3.1a-c). They differ mainly in the relative position of the distinct bumps of a bump strip which is realised by different shapes of the bridges. In some cases, the arrangement of bump strips is radially [LK11], resulting in a non-constant width of the bump strip.

For these reasons, the structural behaviour of AFTBs is often modeled as a plate (top foil) with a distributed independent elastic foundation [LK11, Bru04] (compare figure 3.1d). The main uncertainty in this simplified model stems from the estimation of the spring constant for the elastic foundation. Mostly, the spring constant is chosen either on the basis of single bump calculations [Ior99] or by measurements of the overall stiffness of the whole air foil thrust bearing [Bru04, LKKK11].

In this thesis, a fully coupled model for top and bump foil in combination with the compressible Reynolds equation is presented for an accurate description of air foil thrust bearings. The novelty of the presented approach is:

- There is no need for an estimation of the spring constant as the exact geometry of bump and top foil is described by a shell model. This is a major advantage in comparison to elastic foundation type models that are frequently used in the literature.
- The current approach can handle different bump foil geometries due to the chosen flexible shell formulation for the foils. This is an important feature of the presented model due to the variety of thrust bearing designs that have been presented in foil bearing applications.
- The curvature of the bump foil of thrust bearings can not be accounted for by one-dimensional models from the literature. By contrast, a two-dimensional bump foil description is chosen in this work. The influence of two-dimensional effects, namely the bump foil curvature and two-dimensional friction, is studied in detail and shown to be important.
- Due to the chosen special formulation of the shell equations, it is possible to study the effect of different interaction mechanisms between bumps separately (accumulated friction stiffening, interactive bending moments).

The chosen shell theory for top and bump foil is of Reissner-Mindlin type. Thus, membrane, bending, and shear effects are accounted for. A penalty contact including Coulomb friction is formulated between the base plate and the bump foil as well as between the bump foil and the top foil. The structural model is coupled with the compressible Reynolds equation and a finite element method is used in order to solve the nonlinear fully coupled system of equations.

The next sections are organised as follows: Firstly, the fundamentals of thick shell theory, which is applicable to arbitrary AFB geometries, are briefly recapitulated. In section 3.1.3, the general thick shell equations are specified for the AFTB geometry considered in this work. Section 3.1.4 contains a comparison between the presented approach and well established models from the literature for the one-dimensional bump strip. Herein, the influence of different bump interaction mechanisms, friction, and contact models is discussed. In section 3.1.5, differences in the structural behaviour of curved and straight bump strips are shown and results for a fully coupled AFTB are presented.

3.1.2 Theory for thick shells

As structural model for the top foil as well as for the bump foil, a thick shell model of Reissner-Mindlin type is chosen. The general tensor formulation of this theory according to [BK00, BK85, ES93] enables the analysis of arbitrarily shaped smooth shells. The main assumptions for the linear elastic theory are:

- The shell thickness is small in comparison to the minimal curvature and a characteristic length of the middle surface of the shell.
- Transversal shear is assumed to be constant across the thickness of the shell.
- Elongations of the shell thickness are neglected.

In this section, the main equations of the theory are presented for general shell structures. In the next section, the governing shell equations are specified for the air foil thrust bearing geometry considered in this work. The well-established convention in shell theory that greek indices range from 1 to 2 and latin indices from 1 to 3 is used in addition to Einsteins summation convention.

Metrical and curvature properties of a surface

Figure 3.2a shows a representative section of an arbitrary shell middle surface F which is described by a set of convective (curvilinear) coordinates Θ^α. Based on differential geometry, in every point of the shell middle surface a local covariant basis $\mathbf{a}_i$ is defined by

$$\mathbf{a}_\alpha = \frac{\partial \mathbf{r}}{\partial \Theta^\alpha} = \mathbf{r}_{,\alpha} \ , \qquad \mathbf{a}_3 = \frac{\mathbf{a}_1 \times \mathbf{a}_2}{|\mathbf{a}_1 \times \mathbf{a}_2|} \, . \tag{3.1}$$

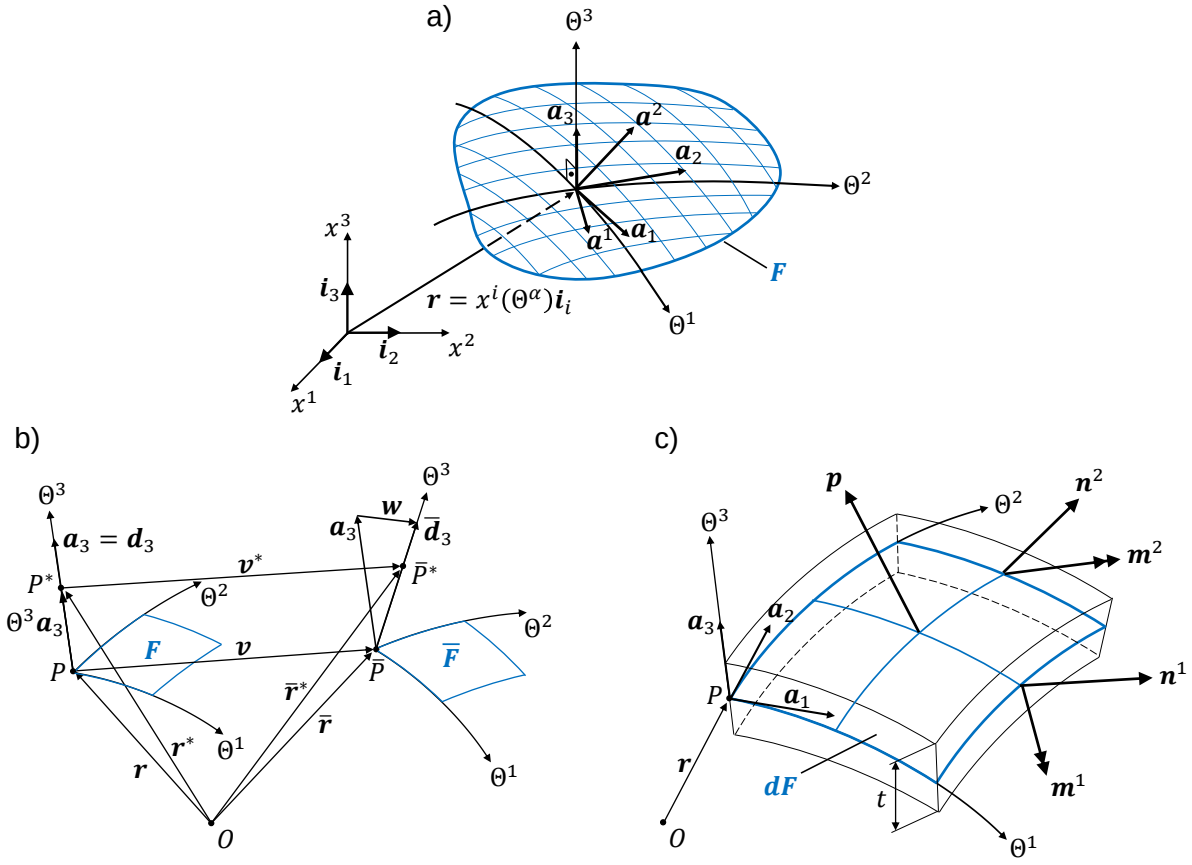

Figure 3.2: Metrical properties (a), kinematic relations (b), and force variables (c) of an arbitrary shell.

The covariant metric tensor that describes the metric properties of the shell middle surface is given by

$$a_{\alpha\beta} = \mathbf{a}_\alpha \cdot \mathbf{a}_\beta \,. \tag{3.2}$$

For the contravariant metric tensor and the contravariant base vectors we have

$$a_{\alpha\rho}a^{\rho\beta} = \delta^\beta_\alpha \,, \qquad \mathbf{a}^\alpha = a^{\alpha\beta}\mathbf{a}_\beta \,, \qquad \mathbf{a}^3 = \mathbf{a}_3 \,, \tag{3.3}$$

where δ^β_α denotes the Kronecker delta. The curvature of the shell middle surface is described by the curvature tensor which is given in the covariant and mixed form by

$$b_{\alpha\beta} = \mathbf{a}_3 \cdot \mathbf{a}_{\alpha,\beta} \,, \qquad b^\alpha_\beta = a^{\alpha\rho}b_{\rho\beta} \,. \tag{3.4}$$

Kinematic relations

Figure 3.2b illustrates a point P of the shell middle surface F and an arbitrary point P^* of the shell continuum that lies on a line normal to F in the initial configuration (i.e., in direction of $\mathbf{d}_3$). In the deformed state, it

is assumed that all points of the originally normal line to F are still located on a line, but with the direction $\overline{\mathbf{d}}_3$ (assumption of plane cross sections). Thus, the displacement $\mathbf{v}^*$ of point P^* is given according to figure 3.2b by

$$\mathbf{v}^* = \overline{\mathbf{r}}^* - \mathbf{r}^* = \overline{\mathbf{r}} - \mathbf{r} + \Theta^3(\overline{\mathbf{d}}_3 - \mathbf{a}_3) = \mathbf{v} + \Theta^3\mathbf{w}\,. \tag{3.5}$$

Consequently, the displacement field of the shell continuum is described by five variables v_i, w_α and can be divided in two parts: The displacement vector $\mathbf{v} = v_\alpha\mathbf{a}^\alpha + v_3\mathbf{a}^3$ describes the deformation of the shell middle surface and the components w_α of the difference vector $\mathbf{w} = w_\alpha\mathbf{a}^\alpha$ account for rotations and shear deformation of cross sections.

Finally, the kinematic relations referring the displacement variables v_i, w_α to the strain variables $\varphi_{\alpha\beta}$, $\kappa_{\alpha\beta}$ and γ_α are given by

$$\begin{aligned} \varphi_{\alpha\beta} &= v_{\beta|\alpha} - v_3 b_{\alpha\beta}\,, \\ \kappa_{\alpha\beta} &= \frac{1}{2}(w_{\alpha|\beta} + w_{\beta|\alpha})\,, \\ \gamma_\alpha &= w_\alpha + v_{3,\alpha} + v_\lambda b^\lambda_\alpha\,, \end{aligned} \tag{3.6}$$

where the vertical line in the index (for example $v_{\beta|\alpha}$) denotes a covariant differentiation.

Equilibrium equations

In Figure 3.2c the forces and moments acting on a middle surface element dF of the shell can be seen. Herein,

$$\mathbf{p} = p^\alpha\mathbf{a}_\alpha + p^3\mathbf{a}_3 \tag{3.7}$$

represents the vector of external forces and

$$\begin{aligned} \mathbf{n}^\alpha &= n^{\alpha\beta}\mathbf{a}_\beta + q^\alpha\mathbf{a}_3\,, \\ \mathbf{m}^\alpha &= m^{\alpha\beta}\mathbf{a}_3 \times \mathbf{a}_\beta \end{aligned} \tag{3.8}$$

are the internal force variables. In detail, $n^{\alpha\beta}$ is the stress resultant tensor, q^α the transverse shear stress vector, and $m^{\alpha\beta}$ the moment tensor. The connection between the external and internal force variables is given by the five equilibrium equations

$$\begin{aligned} -p^\beta &= n^{\alpha\beta}|_\alpha - q^\alpha b^\beta_\alpha\,, \\ -p^3 &= n^{\alpha\beta}b_{\alpha\beta} + q^\alpha|_\alpha\,, \\ 0 &= m^{\alpha\beta}|_\alpha - q^\beta\,. \end{aligned} \tag{3.9}$$

Constitutive equations

Using the elasticity tensor for a linear elastic, homogenous, and isotropic material, namely

$$H^{\alpha\beta\lambda\mu} = \frac{1-\nu}{2}(a^{\alpha\lambda}a^{\beta\mu} + a^{\alpha\mu}a^{\beta\lambda} + \frac{2\nu}{1-\nu}a^{\alpha\beta}a^{\lambda\mu})\,, \tag{3.10}$$

the constitutive equations that refer the strain variables (3.6) to the internal force variables (3.8) are

$$\begin{aligned} q^{\alpha} &= Gt \cdot a^{\alpha\lambda}\gamma_{\lambda} \cdot k_S\,, \\ m^{\alpha\beta} &= BH^{\alpha\beta\lambda\mu}(\kappa_{\lambda\mu} - b^{\sigma}_{\lambda}\varphi_{\mu\sigma})\,, \\ n^{\alpha\beta} &= DH^{\alpha\beta\lambda\mu}\varphi_{\lambda\mu} - b^{\beta}_{\rho}m^{\alpha\rho}\,, \end{aligned} \tag{3.11}$$

where D is the stretching stiffness, B the bending stiffness and Gt the shear stiffness defined by

$$D = \frac{Et}{1-\nu^2}\,, \qquad B = \frac{Et^3}{12(1-\nu^2)}\,, \qquad Gt = \frac{Et}{2(1+\nu)} \tag{3.12}$$

with the shear correction factor k_S, the elastic modulus E, Poisson's ratio ν and the shell thickness t as constants.

To sum up, the kinematic relations (3.6), the equilibrium equations (3.9), and the constitutive equations (3.11) form together with appropriate boundary conditions a boundary value problem in the unknowns v_i, w_{α}, $\varphi_{\alpha\beta}$, $\kappa_{\alpha\beta}$, γ_{α}, $n^{\alpha\beta}$, q^{α} and $m^{\alpha\beta}$. The equations (3.6), (3.9) and (3.11) are functions of the metric and curvature tensors of the shell middle surface.

Thus, in order to obtain a structural model for a specific AFB geometry, only a representation $\mathbf{r} = \mathbf{r}(\Theta^{\alpha}) = x^i(\Theta^{\alpha})\mathbf{i}_i$ with respect to a global reference system x^i has to be found for the middle surfaces of the bump and top foil. Based on this representation, the metric and curvature tensors can directly be computed from equations (3.1 - 3.4) and can be used for the governing equations of the boundary value problem.

3.1.3 Geometry and governing shell equations for the considered AFTB

Geometry of the air foil thrust bearing

As already mentioned, different geometries for air foil thrust bearings have been presented in the literature [Ior99, Bru12, LK11]. In this analysis, focus is placed on a well-established bump strip configuration that is, for instance, also used in [Ior99, LKKK11, PKJL08]. Figure 3.3a illustrates the main characteristics of the considered bump strips which are fixed at $x^1 = 0$. The distinct bumps are patterned along the x^1-direction in contrast to other configurations (e.g., [Bru12]), where the bumps are patterned in circumferential direction. Each bump strip is cut to a cylindrical shape with the inner radius r_{iB} and the outer radius r_{oB} in order to obtain a good fitting to the cylindrically sector-shaped top foil, see figure 3.1. Due to the manufacturing process, there is always a rounding between a bump and a bridge, which is mostly neglected in bump foil

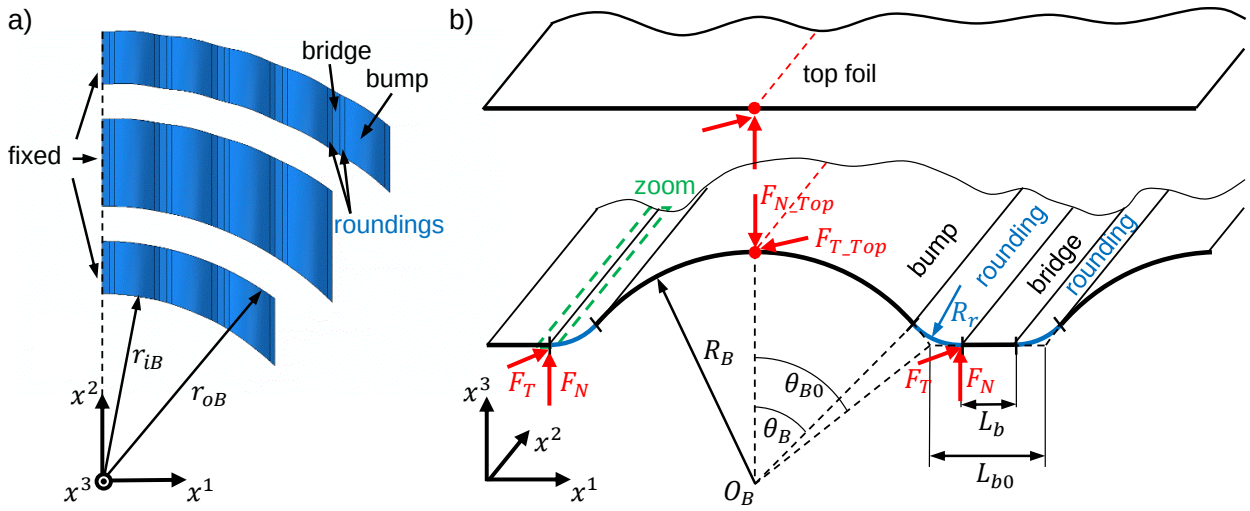

Figure 3.3: a) Two-dimensional bump strip geometry. b) Cut view through a bump strip parallel to the x^1,x^3-plane.

models but incorporated in the current analysis. Figure 3.3b shows a cut view through a bump strip parallel to the x^1, x^3-plane. For the case without roundings, the bump radius R_B, the nominal bump angle θ_{B0}, and the nominal length of the bridge L_{b0} define the geometry of an one-dimensional bump strip. If roundings (radius of curvature R_r) are included in the analysis, the effective bump angle can be calculated by

$$\theta_B = arccos\left(\frac{R_B cos(\theta_{B0}) + R_r}{R_B + R_r}\right) \tag{3.13}$$

and the effective length of the bridges is given by

$$L_b = L_{b0} - 2 \cdot \left[(R_B + R_r)sin(\theta_B) - R_B sin(\theta_{B0})\right]. \tag{3.14}$$

Therefore, the geometry of a bump strip with roundings is completely determined by the four parameters R_B, θ_{B0}, L_{b0}, and R_r in combination with the bump foil thickness t_B and the inner and outer radii r_{iB} and r_{oB}. It can be seen from equations (3.13) and (3.14) that for $R_r \to 0$, the bump strip without roundings is obtained as a special case.

Shell equations for the considered AFB geometry

In this paragraph, the general shell equations (see, section 3.1.2) are specified to the geometry of the bump and top foil of the considered AFTB (figure 3.1a). It can be seen from figure 3.3b (top and bump foil are shown in a non-contact condition only for illustration purpose) that the structural elements of top and bump foil can be divided into two groups: The elements of the first group, consisting of the top foil and the bridges of the bump strips, have a flat geometry without a curvature. The elements of the second group, consisting of the bumps and the roundings, have a curvature in the x^1, x^3-plane, but no curvature in the x^2-direction.

For the derivation of the shell equations for both groups, the shell middle surface of figure 3.3a is consid-

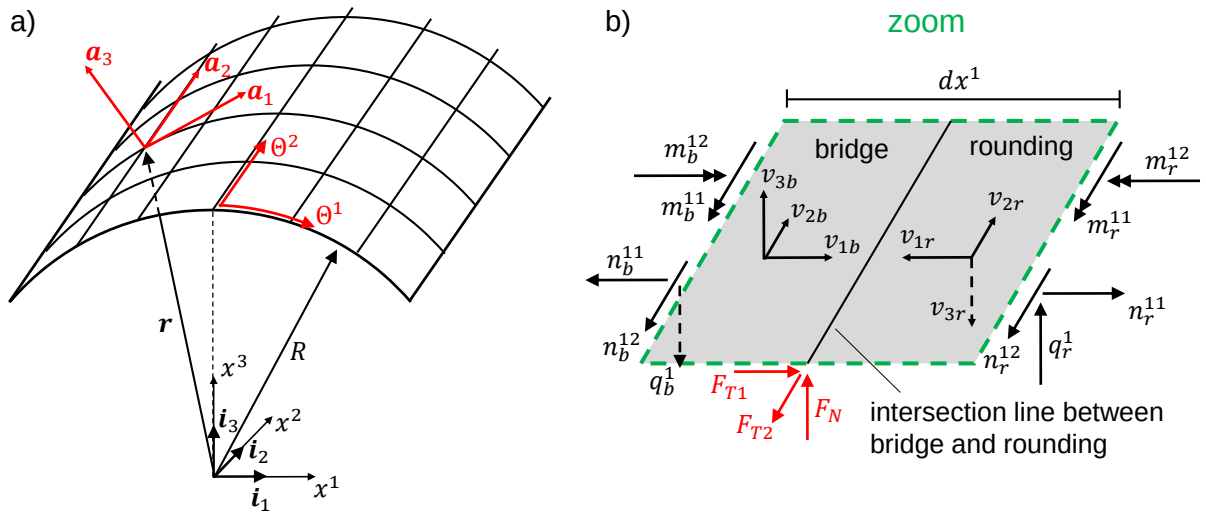

Figure 3.4: a) General, representative shell middle surface. b) Contact forces and inner force variables for an infinitesimal shell segment at the intersection between bridge and rounding, zoom of figure 3.3b.

ered as a general, representative shell geometry. It has a constant radius of curvature R and is described by two convective coordinates Θ^α.

With respect to the global reference system x^i, the middle surface is represented by

$$\mathbf{r} = Rsin\left(\frac{\Theta^1}{R}\right)\mathbf{i}_1 + \Theta^2\mathbf{i}_2 + Rcos\left(\frac{\Theta^1}{R}\right)\mathbf{i}_3\,. \tag{3.15}$$

Due to the definitions (3.1), the local basis vectors are

$$\begin{bmatrix}\mathbf{a}_1\\ \mathbf{a}_2\end{bmatrix} = \begin{bmatrix} cos\left(\frac{\Theta^1}{R}\right)\mathbf{i}_1 - sin\left(\frac{\Theta^1}{R}\right)\mathbf{i}_3 \\ \mathbf{i}_2\end{bmatrix}, \qquad \mathbf{a}_3 = cos\left(\frac{\Theta^1}{R}\right)\mathbf{i}_3 + sin\left(\frac{\Theta^1}{R}\right)\mathbf{i}_1\,. \tag{3.16}$$

Since the basis $\mathbf{a}_i$ is orthonormal, covariant and contravariant variables are identical. Therefore, $\mathbf{a}_i = \mathbf{a}^i$ holds and the metric and curvature tensors

$$a_{\alpha\beta} = a^{\alpha\beta} = \begin{bmatrix}1 & 0\\ 0 & 1\end{bmatrix}, \qquad b_{\alpha\beta} = b^\alpha_\beta = \begin{bmatrix}-\frac{1}{R} & 0\\ 0 & 0\end{bmatrix} \tag{3.17}$$

fully describe the geometrical properties of the considered middle surface of a shell.

Inserting the special geometry (3.17) in the general equilibrium equations (3.9), leads to the equilibrium equations

$$\begin{aligned} -p^1 &= n^{11},_1 + n^{21},_2 + \underline{\frac{1}{R}q^1}\,, & 0 &= m^{11},_1 + m^{21},_2 - q^1\,,\\ -p^2 &= n^{12},_1 + n^{22},_2\,, & 0 &= m^{12},_1 + m^{22},_2 - q^2\,,\\ -p^3 &= \underline{-\frac{1}{R}n^{11}} + q^1,_1 + q^2,_2 \end{aligned} \tag{3.18}$$

for the considered shell. Introducing the kinematic relations (3.6) into the constitutive equations (3.11) and

considering the metric and curvature tensors from (3.17) yields

$$
\begin{aligned}
n^{11} &= D(v_{1,1} + \nu v_{2,2} + \underline{\frac{1}{R} v_3}) + \underline{\frac{1}{R} m^{11}}\,, \\
n^{12} &= D\frac{1-\nu}{2}(v_{2,1} + v_{1,2}\,)\,, \\
n^{21} &= n^{12} + \underline{\frac{1}{R} m^{21}}\,, \\
n^{22} &= D(v_{2,2} + \nu v_{1,1} + \underline{\frac{\nu}{R} v_3})\,,
\end{aligned}
$$

$$
\begin{aligned}
q^1 &= Gt(w_1 + v_{3,1} - \underline{\frac{1}{R} v_1}) \cdot k_S\,, \\
q^2 &= Gt(w_2 + v_{3,2}\,) \cdot k_S\,,
\end{aligned}
\tag{3.19}
$$

$$
\begin{aligned}
m^{11} &= B(w_{1,1} + \nu w_{2,2} + \underline{\frac{1}{R} v_{1,1}} + \underline{\frac{1}{R^2} v_3})\,, \\
m^{12} &= B\frac{1-\nu}{2}(w_{1,2} + w_{2,1} + \underline{\frac{1}{R} v_{1,2}})\,, \\
m^{21} &= m^{12}\,, \\
m^{22} &= B(w_{2,2} + \nu w_{1,1} + \underline{\frac{\nu}{R} v_{1,1}} + \underline{\frac{\nu}{R^2} v_3})\,,
\end{aligned}
$$

which is a representation of the inner force variables as a function of the kinematic variables. Finally, inserting (3.19) into the equilibrium equations (3.18) results in a system of five partial differential equations in the five kinematic variables v_i, w_α. In combination with appropriate boundary conditions, these partial differential equations fully describe the structural behaviour of the considered shell.

The specification of these shell equations to the top and bump foil of the air foil thrust bearing is now straightforward. For the bumps and the roundings, the radius R has to be replaced by the bump radius R_B and the radius of the rounding R_r, respectively. The equations for the top foil and the bridges are obtained for the condition $R \to \infty$. In this case, the underlined expressions in (3.18) and (3.19) vanish. In the following, variables associated with the top foil are denoted by the index ”T” (”b” for the bridge, ”B” for the bump and ”r” for the rounding).

So far, the shell equations for the four structural elements bump, rounding, bridge, and top foil have been derived. In order to describe the behaviour of a whole bump strip, the shell equations are applied to all segments of a bump strip separately. Regarding, for instance, the inner bump strip shown in figure 3.3a, 12 shell segments have to be coupled and solved simultaneously, resulting in a system of 60 partial differential equations. The interaction between a bump strip and the base plate is modeled by normal and frictional forces F_N and F_T, acting on the intersection lines of the roundings and the bridges, see figure 3.3b. Analogously, top foil and bump strips are connected on the top line of the bumps by an appropriate contact model.

Coupling equations and contact forces

In this paragraph, the coupling of two shell segments is described in detail. Therefore, we consider - as a representative example - the coupling equations for the interaction between a bridge and a rounding, compare the green dashed region in figure 3.3b. Figure 3.4b shows an infinitesimal element of the intersection region. The internal force variables of the bridge act on the left side of the element, the corresponding internal force variables of the rounding on the right side. Along the intersection line, the element is exposed to normal and friction forces from the base plate. Because of equilibrium, we get the five coupling equations

$$\begin{aligned} n_r^{11} &= n_b^{11} - F_{T1}\,, \\ q_r^{1} &= q_b^{1} - F_N\,, \\ m_r^{11} &= -m_b^{11}\,, \\ n_r^{12} &= -n_b^{12} - F_{T2}\,, \\ m_r^{12} &= m_b^{12} \end{aligned} \tag{3.20}$$

for the internal force variables. Additionally, on a kinematic level bridge and rounding are coupled by

$$\begin{aligned} v_{1b} &= -v_{1r}\,, \\ v_{3b} &= -v_{3r}\,, \\ w_{1b} &= w_{1r}\,, \\ v_{2b} &= v_{2r}\,, \\ w_{2b} &= -w_{2r}\,. \end{aligned} \tag{3.21}$$

Please note the different orientations of the local basis vectors of bridge and rounding, see figure 3.4b. Equations (3.20) are implemented as Neumann boundary conditions for the rounding, whereas equations (3.21) are used as Dirichlet boundary conditions for the bridge. In a similar manner, the coupling between bump and rounding is formulated.

For the normal contact force, that acts on the intersection line, a penalty approach (penalty stiffness c) according to

$$F_N = \begin{cases} c \cdot v_{3r}\,, & v_{3r} \geq 0\,, \\ 0\,, & v_{3r} < 0 \end{cases} \tag{3.22}$$

is used. The dry friction between the base plate and the intersection line is modeled as Coulomb friction. Since only the loading condition of the air foil thrust bearing is considered, it is assumed that the velocity of an arbitrary point has the same direction as the displacement of this point. Therefore, the friction forces

F_{T1} and F_{T2} in x^1- and x^2-direction are formulated as a function of the two displacements $v_{\alpha r}$

$$F_{T\alpha} = \mu_u \cdot step(v_{\alpha r}) F_N \frac{|v_{\alpha r}|}{\sqrt{v_{1r}^2 + v_{2r}^2}}\,, \tag{3.23}$$

where μ_u is the friction coefficient between the base plate and the bump strip (please note that the summation convention is not applied in equation (3.23)). $step(\cdot)$ is a smoothed step function, being -1 for negative and $+1$ for positive values of $v_{\alpha r}$. The smoothing parameter in the step function is chosen small enough in order to have a negligible influence on the solution in case that stick conditions occur. The normal and friction forces between the top foil and the bumps are modeled analogously. Instead of v_{ir} the relative displacements between the top foil and the top line of the bumps are used and the friction coefficient μ_u is replaced by μ_o.

The discretisation approach and the solution procedure for the fully coupled elasto-hydrodynamic case are as follows: The Reynolds equation as well as the shell equations for top and bump foil are discretised by finite elements (second order for the pressure and fifth order for the displacements of the shells). Due to the nonlinearity of the Reynolds equation and the contact model a damped Newton-Raphson method is used in order to solve the fully coupled nonlinear system of equations. For improving convergence, a continuation method with respect to the angular velocity is applied. In the first step a very low angular velocity is used since for this case the pressure and therefore the contact forces are small resulting in a good convergence behaviour. This first solution is used as initial solution for the Newton-Raphson method of the next step where the angular velocity is increased. This procedure is repeated until the final angular velocity is achieved. Within one step the Newton-Raphson iterations are terminated if the relative error is smaller than 1e-6.

3.1.4 Results for the 1D analysis

The presented shell model is used in order to analyse the structural behaviour of an one-dimensional bump strip and its influence on the hydrodynamic pressure in a taper land foil slider. In the one-dimensional case, the equilibrium equations (3.18) reduce to

$$-p^1 = n^{11},_1 + \underline{\frac{1}{R} q^1}\,, \qquad -p^3 = -\underline{\frac{1}{R} n^{11}} + q^1,_1\,, \qquad 0 = m^{11},_1 - q^1 \tag{3.24}$$

and the inner force variables (plane stress assumption) are given by

$$\begin{aligned} n^{11} &= D(1-\nu^2)(v_1,_1 + \underline{\frac{1}{R} v_3}) + \underline{\frac{1}{R} m^{11}}\,, \\ q^1 &= Gt(w_1 + v_3,_1 - \underline{\frac{1}{R} v_1}) \cdot k_S\,, \\ m^{11} &= B(1-\nu^2)(w_1,_1 + \underline{\frac{1}{R} v_1,_1} + \underline{\frac{1}{R^2} v_3})\,. \end{aligned} \tag{3.25}$$

The considered bump foil starts with a fixed bridge at the left end of the strip, consists of 6 bumps and ends with a rounding that simply touches the base plate at the right end of the strip. Table 3.1 summarizes the chosen parameters of the bump foil strip.

Young's modulus	E	$210GPa$
Poisson's ratio	ν	0.3
Radius of bump	R_B	$2mm$
Nominal bump angle	θ_{B0}	$41.41deg$
Radius of rounding	R_r	$0.5mm$
Nominal bridge length	L_{b0}	$0.8mm$
Bump foil thickness	t_B	$75\mu m$

Table 3.1: Geometrical parameters of the 1D bump foil strip and material parameters for bump and top foil.

For a comparison of the presented shell model to models from the literature, the coupling equations (3.20) and (3.21) are rewritten for the one-dimensional case

$$\begin{aligned} n_r^{11} &= n_b^{11} - F_{T1}\,, & v_{1b} &= -v_{1r}\,, \\ q_r^1 &= q_b^1 - F_N\,, & v_{3b} &= -v_{3r}\,, \\ m_r^{11} &= -m_b^{11}\,, & w_{1b} &= w_{1r}\,. \end{aligned} \tag{3.26}$$

Two bump foil models that are very similar to those by Heshmat et al. [HWP83a] and Ku et al. [KH92] are chosen for the comparison.

Heshmat model: Heshmat et al. assume the bumps to deform independently from each other. Friction as well as the connection between bumps due to the bridges are neglected. The stiffness coefficient for all bumps is the same and is calculated by a formula that is valid for a centrally loaded bump with free-free boundary conditions. This kind of bump foil model can be realised within the framework of the presented shell model if the coupling conditions (3.26) between the bridges and the roundings are modified as follows

$$\begin{aligned} n_r^{11} &= 0\,, & v_{1b} &= 0\,, \\ q_r^1 &= -F_N\,, & v_{3b} &= 0\,, \\ m_r^{11} &= 0\,, & w_{1b} &= 0\,. \end{aligned} \tag{3.27}$$

It can be seen from the left formulae that - except for the normal force F_N - no other forces or moments act on the rounding at its boundary. Especially, there are no forces from the bridge transmitted to the rounding, resulting in a decoupling of the bridge and the rounding. It should be stressed that the other end of the rounding stays fully coupled to the bump.

Ku model: Ku et al. introduced horizontally directed interaction forces between the bumps and considered friction between the bump foil and the base plate and the bump foil and the top foil. In their model, no outer bending moments act on the end of a bump. Effectively, this equals the bridge to be modeled as a rod. Within the framework of the presented shell model, this situation can be realised by the modified coupling

equations

$$\begin{aligned} n_r^{11} &= n_b^{11} - F_{T1}\,, & v_{1b} &= -v_{1r}\,, \\ q_r^1 &= -F_N\,, & v_{3b} &= 0\,, \\ m_r^{11} &= 0\,, & w_{1b} &= 0\,. \end{aligned} \tag{3.28}$$

By means of the above equations, the normal forces between the rounding and the bridge as well as the horizontal displacements are coupled, but there is no transmission of bending moments. The Heshmat and the Ku model are chosen for comparison in this work because of two reasons. Firstly, they are very popular and widely used in the air foil bearing literature. Secondly, in comparison to the fully coupled shell model, they allow a systematic analysis of the influence of different interaction mechanisms.

Bump strip without top foil

In order to characterise the structural behaviour of a bump strip, the top foil is neglected in a first step. Instead, each of the 6 bumps is loaded at its top point by a force of $400\frac{N}{m}$.

Figure 3.5 shows the vertical displacement v_{3B} of the bumps for the friction coefficients $\mu_u = 0$ (left) and $\mu_u = 0.2$ (right). For the case without friction, the Heshmat and Ku models lead to identical results. It can be clearly seen that both predict a far too high compliance of the bump strip. This stems from the fact that both models do not account for a transmission of bending moments between the bumps, and therefore the ends of the bumps can freely rotate. By contrast, in the shell model a bump has to bend the neighbouring bridges if its ends try to rotate, resulting in a stiffer behaviour of the bump. Figure 3.5 shows the vertical displacements of the bumps for nominal bridge lengths of $L_{b0} = 1.6mm$ and $L_{b0} = 3.2mm$ in addition. It is evident, that the bridge length - neglected in most studies in the literature - has a considerable effect on the stiffness of the bump strip.

In the right plot of figure 3.5, the influence of friction on the bump foil stiffness can be seen. The general trend of increasing stiffness towards lower bump numbers is correctly predicted by the Ku model. This indicates that the coupling of bumps by horizontal interaction forces is useful to capture friction induced stiffness variations within the bump strip. Nevertheless, the displacements of the bumps in the Ku model are approximately three times higher than the values predicted by the shell model. This factor is nearly the same as in the case without friction showing that the neglecting of bending moment effects leads for all friction conditions to considerable deviations. In the analysed configuration with six bumps, it would be even a better approximation to neglect friction effects (shell model with $\mu_u = 0$) than to neglect the bending moments (Ku model) in order to calculate the stiffness of the bump strip for $\mu_u = 0.2$. Finally, it should be mentioned that the results of the shell model have been compared successfully to a commercial finite element software in order to validate the shell model.

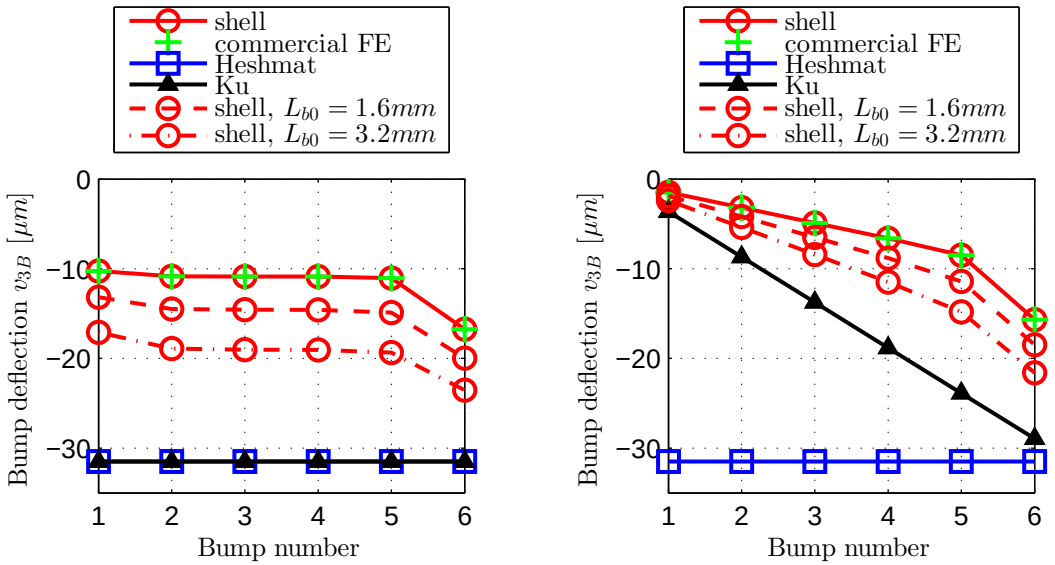

Figure 3.5: Vertical deflection v_{3B} of the bump top points for friction coefficients $\mu_u = 0$ (left) and $\mu_u = 0.2$ (right). Each of the six bumps is loaded at its top point by a force of $400\frac{N}{m}$.

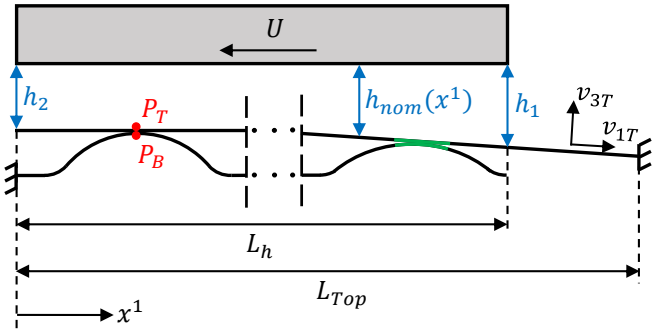

Figure 3.6: Geometry of an one-dimensional taper land foil slider.

Bump strip with top foil

Figure 3.6 illustrates an one-dimensional taper land foil slider. The nominal gap function $h_{nom}(x^1)$ between the top foil and the slider is defined along the hydrodynamically active length L_h by

$$h_{nom}(x^1) = \begin{cases} h_2\,, & 0 \le x^1 \le \frac{1}{2}L_h\,, \\ h_2 + \frac{2(h_1-h_2)}{L_h}(x^1 - \frac{1}{2}L_h)\,, & \frac{1}{2}L_h < x^1 \le L_h\,, \end{cases} \tag{3.29}$$

where $h_1 = 30\mu m$ is the gap height at the leading edge and $h_2 = 10\mu m$ the gap height at the trailing edge. L_h is chosen to be exactly the length of the bump strip (6 bumps) that was introduced in the previous paragraph. The top foil has a thickness of $t_T = 100\mu m$, consists of the same material as the bump foil, and is fixed at the right end far enough away ($L_{Top} - L_h = 6mm$) from the leading edge. This is done in order to minimize the influence of the top foil fixing on the compliance of the foil sandwich within the hydrodynamically active region. The inclination of the top foil in the tapered region is enforced by decreasing

bump heights towards the leading edge, see figure 3.6. Since the difference in the bump heights is at most $30\mu m$, which is small against the total bump height of $500\mu m$, variations in the bump height are neglected in the structural model of the bump strip. However, in general, different bump geometries within a bump strip can be easily accounted for in the presented shell model.

Before top and bump foil are coupled to the fluid film in the next section, attention is drawn to the contact situation between the bump foil and the top foil. Due to the curved geometry of the bumps, the contact region between the top foil and each bump of the bump strip is limited to the region close to the top of each bump. In general, a line-to-line contact occurs at this location which is illustrated by the green sections in figure 3.6. Appropriate contact formulations for general line-to-line contact types are available in the literature [Wri06] and can be found in commercial finite element software. Nevertheless, in this work a point-to-point contact between the top point of the bump P_B and the point P_T of the top foil is assumed, see figure 3.6. Compared to a full line-to-line contact formulation, the point-to-point contact approach has mainly two advantages. Firstly, the mesh does not have to be refined in the contact region. Secondly, a faster convergence behaviour is observed for the point-to-point contact approach.

In order to obtain the accuracy of the simplified point-to-point contact approach, the top foil is loaded by a constant pressure $p = 10^5 Pa$ acting along the hydrodynamically active region L_h. The vertical displacement v_{3B} of the top point P_B of each bump is calculated with a full line-to-line contact approach (commercial FE) and the simplified point-to-point contact approach (shell model). Figure 3.7 shows the relative error between both models. It can be stated that the relative error is below 1% for all bumps yielding results with sufficient accuracy. Furthermore, the highest relative error can be observed at the first and second bump. This is due to the free end condition of the top foil at its left end. Because of this, the top foil deflection at the left end is considerably higher than for the rest of the top foil resulting in a stronger violation of the point-to-point contact assumption between the first two bumps and the top foil. Finally, it should be mentioned that for the shell model a rather coarse mesh is applied. Finite elements of order five are used in order to prevent shear locking effects. A bump arc is meshed by two elements, the roundings and bridges by only one element. For each top foil section between two contact points two elements are used. Hence, although a rather course discretisation and a simplified contact formulation are used, accurate results are obtained with this very efficient modeling approach.

For the two-dimensional case, a simplified line-to-line contact approach is used between the top line of the bump foil and an appropriate line along the top foil (see, red dashed lines in figure 3.3) instead of a full surface-to-surface contact formulation.

Coupling to 1D-Reynolds equation

Finally, the influence of the foil models on the pressure distribution in a taper land foil slider (see figure 3.6) is studied. The pressure p within the slider is calculated by the one-dimensional form of the isothermal

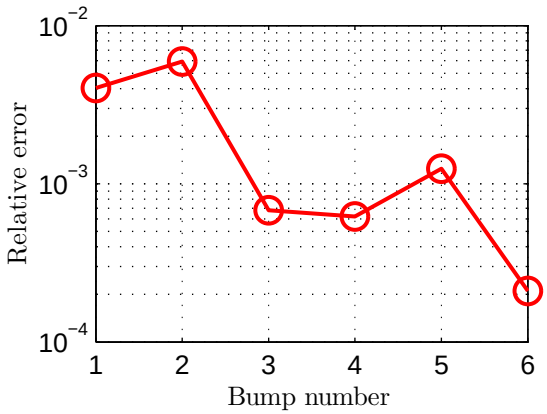

Figure 3.7: Relative error of the point-to-point contact approach applied in the 1D shell model.

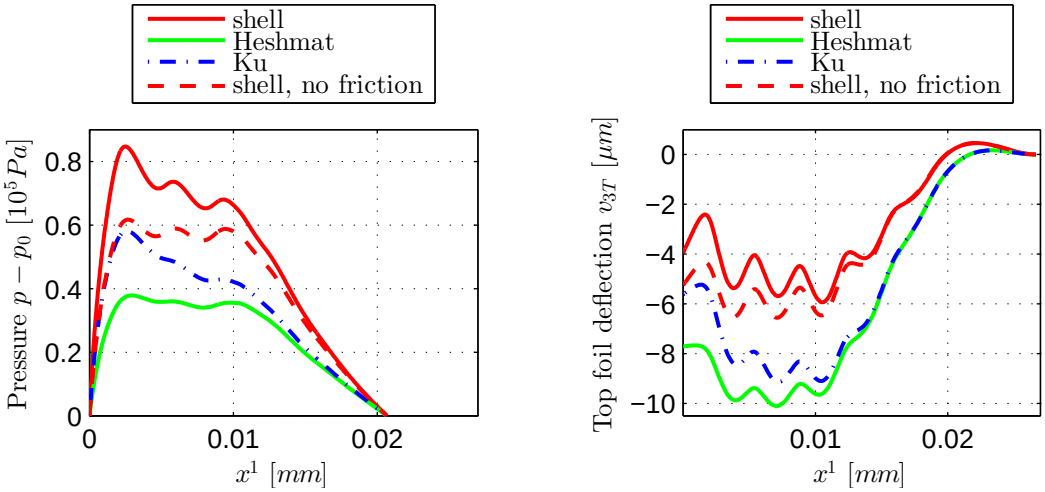

Figure 3.8: Pressure distribution (left) and top foil deflection (right) for the taper land foil slider.

Reynolds equation (1.23)

$$\frac{d}{dx^1}\left(\frac{ph^3}{12\eta}\frac{dp}{dx^1} - \frac{pUh}{2}\right) = 0 \tag{3.30}$$

with the dynamic viscosity $\eta = 20 \cdot 10^{-6} Pas$ and the velocity $U = 200m/s$ of the slider. As boundary conditions $p(x^1 = 0) = p(x^1 = L_h) = p_0$ are used with $p_0 = 10^5 Pa$ being the ambient pressure. The real fluid film height

$$h(x^1) = -\left(h_{nom}(x^1) - v_{3T}(x^1)\right) \tag{3.31}$$

is the negative difference between the nominal fluid film height and the vertical displacement v_{3T} of the top foil. The pressure distribution of the air film is used as external load variable

$$p_T^3 = -(p - p_0) \tag{3.32}$$

in the equilibrium equations (3.24) of the top foil. Equations (3.31) and (3.32) represent the coupling between the foil sandwich and the air film.

Figure 3.8 shows the pressure distribution (left) and the vertical top foil displacement (right) for the taper

land foil slider. The friction coefficients are chosen to be $\mu_u = \mu_o = 0.1$. Additionally, the results for the shell model without friction are shown. The Heshmat model predicts the lowest pressure level and the highest top foil deformation. The real fluid film height in the land region is nearly twice as high as the nominal fluid film height. As the Ku model accounts for friction forces, the bumps become stiffer towards the trailing edge, see also figure 3.5. The consequence of this is a gradually increasing pressure in the land region towards the trailing edge compared to the Heshmat model. The same effect can be observed for the shell model without friction in comparison to the shell model with friction.

Furthermore, a significant difference in the overall pressure level between the models with interacting bending moments (both shell models) and the models which do not account for interacting bending moments (Heshmat and Ku model) can be stated. For this configuration the shell model without friction is a better approximation than the Ku model, indicating that interactive bending moments are more important than friction effects.

3.1.5 Results for the 2D analysis

After the one-dimensional bump strip has been studied extensively in section 3.1.4, effects of two-dimensional bump strips are considered in this section. Specifically, focus is put on the curvature of the bump strip and two-dimensional friction. Both are not accounted for in one-dimensional bump strip models for air foil thrust bearings.

Curvature effects

Figure 3.9 (left) illustrates a straight two-dimensional bump strip as it is used in journal bearings and a curved bump strip taken from the bump foil of a thrust bearing (see, figure 3.3a). Both consist of a linear bump pattern of four bumps with the same one-dimensional parameters as presented in section 3.1.4, see table 3.1. The width of the straight bump strip is $3mm$ and the radii of the curved bump strip are $r_{iB} = 21mm$ and $r_{oB} = 24mm$, resulting in comparable bump strip widths for both configurations. As in the one-dimensional case, a load of $400\frac{N}{m}$ is applied along the top line of the bumps and the bump strips are fixed at the left end. The friction coefficient μ_u between the bump strip and the base plate is set to zero. In figure 3.9 (right), the vertical displacement v_{3B} is plotted for the top lines of bumps 3 and 4 of each bump strip. In the straight case, the deflection is very homogeneous along the width of the bumps. Furthermore, the deflections are very similar to the deflections of bumps 5 and 6 of the one-dimensional bump strip analysed in section 3.1.4, see figure 3.5 (left). For the curved bump strip, a completely different behaviour is observed. In spite of the homogeneous loading, the deflection of bump 4 decreases along the normalised bump width s. For bump 3 of the curved bump strip, an opposite behaviour is observed. This inhomogeneous deformation is due to the curvature of the bump strip. It is obvious that this behaviour cannot be captured by one-dimensional bump strip approximations for the curved bump foil structure of thrust bearings.

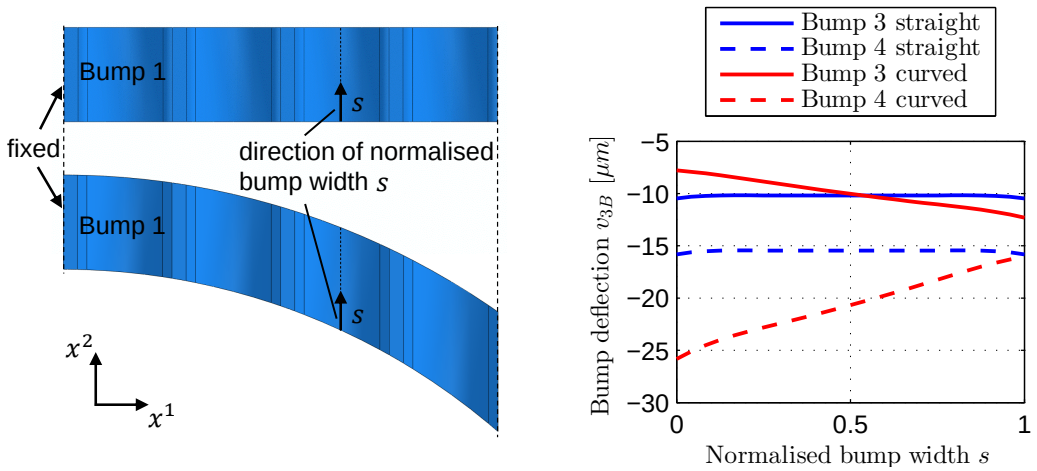

Figure 3.9: Geometry (left) and vertical bump deflections (right) for straight and curved bump foil strips.

Friction effects

As bump strip models from the literature are mostly one-dimensional, they expect the bumps to slide only in the x^1-direction. For a homogeneously loaded straight bump strip, this assumption is certainly valid even in the two-dimensional case. If this assumption is applied to the curved bump strip as well, the friction law

$$F_T^{1D} = F_{T1}^{1D} = \mu_u step(v_{1r}) F_N \tag{3.33}$$

has to be used instead of the full two-dimensional friction law

$$F_T = \sqrt{F_{T1}^2 + F_{T2}^2}\,, \tag{3.34}$$

where F_{T1} and F_{T2} are defined by equation (3.23). Figure 3.10 shows the deflections of bumps 1 and 2 along the normalised bump width s for the curved bump strip from figure 3.9. For both friction models F_T and F_T^{1D}, the friction coefficient $\mu_u = 0.2$ is used and all bumps of the strip are homogeneously loaded at their top line as in section 3.1.5.

It can be clearly seen that - compared to the full two-dimensional friction model - the one-dimensional friction model F_T^{1D} leads to considerable deviations. This is due to the fact that in contrast to the straight bump strip, non-negligible sliding in the x^2-direction occurs in case of the curved bump strip. If the bumps can freely move in the x^2-direction but are hindered in the x^1-direction by friction forces, the whole bump strip will be stretched along its outer radius in the circumferential direction. This results in higher deformations at high values of the normalised bump width s which are observed in figure 3.10.

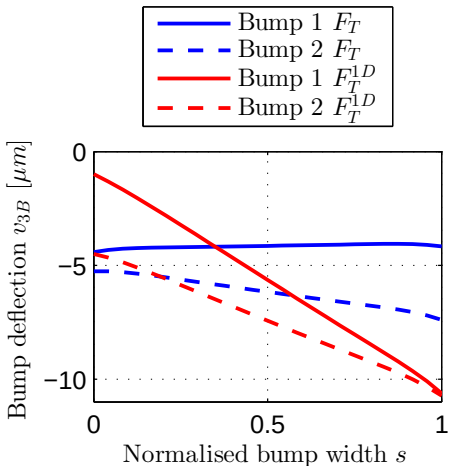

Figure 3.10: Comparison of bump deflections for one-dimensional (F_T^{1D}) and two-dimensional (F_T) friction forces.

Calculation results for the fully coupled model

Finally, calculation results for an air foil thrust bearing are presented. Two-dimensional shell models for the foils including a two-dimensional friction law are fully coupled to the compressible Reynolds equation for the air film.

Figure 3.11 (left) shows the cylindrically sector-shaped top foil of an AFTB that is referred to as reference AFTB in the following. The short lines indicate the contact lines to the underlying bump foil. The top foil has a thickness of $t_T = 100\mu m$ and its inner and outer radii are $r_{iT} = 15mm$, $r_{oT} = 30mm$. Its total circumferential width is defined by the angle $\varphi_{Top} = 48°$, but the hydrodynamically active region is restricted to $\varphi_{hT} = 40°$ because of the fixing on the base plate at the right end of the top foil. The bump foil consists of three strips (see also, 3.3a) with 3, 4 and 5 bumps. The inner radii of the strips are $16mm$, $20mm$ and $26mm$, the outer radii are $19mm$, $25mm$ and $29mm$, respectively. As in the one-dimensional case, the bump strips are fixed at their left end. Top and bump foil consist of the same material which is typically a nickel-based superalloy such as Inconel X-750, compare [Dyk06]. All material, geometrical and operational parameters for the herein considered reference AFTB are summarized in table 3.2.

The nominal fluid film height is defined by

$$h_{nom}(x,y) = \begin{cases} h_2, & x \leq x_{land}\,, \\ h_2 + m(x - x_{land}), & x > x_{land} \end{cases} \tag{3.35}$$

for the reference AFTB and the isothermal Reynolds equation (1.23) is used

$$\frac{\partial}{\partial x}\left[\frac{ph^3}{12\eta}\frac{\partial p}{\partial x}\right] + \frac{\partial}{\partial y}\left[\frac{ph^3}{12\eta}\frac{\partial p}{\partial y}\right] = \frac{\partial}{\partial x}\left[\frac{pUh}{2}\right] + \frac{\partial}{\partial y}\left[\frac{pVh}{2}\right], \tag{3.36}$$

where $U = -\Omega y$ and $V = \Omega x$ are the velocities of the runner in the x- and y-direction induced by the angular

Material parameters	Young's modulus	E	$210GPa$
	Poisson's ratio	ν	0.3
	Friction coeff. bump/top	μ_o	0.1
	Friction coeff. bump/base	μ_u	0.1
Geometry bump foil	Inner bump strip radii	r_{iB}	$16mm, 20mm, 26mm$
	Outer bump strip radii	r_{oB}	$19mm, 25mm, 29mm$
	Radius of bump	R_B	$2mm$
	Nominal bump angle	θ_{B0}	$41.41deg$
	Radius of rounding	R_r	$0.5mm$
	Nominal bridge length	L_{b0}	$0.8mm$
	Bump foil thickness	t_B	$75\mu m$
Geometry top foil	Inner top foil radius	r_{iT}	$15mm$
	Outer top foil radius	r_{oT}	$30mm$
	Top foil angle	φ_{Top}	$48°$
	Hydrodyn. active pad angle	φ_{hT}	$40°$
	Top foil thickness	t_T	$100\mu m$
Nominal gap size	Width of land region	x_{land}	$6mm$
	Inclination of taper region	m	$2.90\mu m/mm$
	Gap size in land region	h_2	$10\mu m$
	Number of pads	E_{pad}	6
Operational parameters	Viscosity of air	η	$20 \cdot 10^{-6} Pas$
	Ref. pressure at boundaries	p_0	$10^5 Pa$

Table 3.2: Parameters of the reference AFTB.

velocity Ω.

Top foil and fluid film are coupled analogously to the one-dimensional case, see equations (3.31) and (3.32).

Figure 3.12 shows the pressure distribution $p - p_0$ in the hydrodynamically active region of the air film (left) and the vertical deformation v_{3T} of the top foil (right) for an angular velocity of $\Omega = 10^4 \frac{rad}{s}$. The highest deflection of the top foil can be observed in the space between the vertical bump lines. This effect is known as top foil sagging. Its influence on the load capacity will be discussed in detail in section 3.2. The maximum pressure occurs near to the first bumps of the middle and the outer strip. Nevertheless, the deformation of these bumps is not higher than the deformation of the third bumps of these strips where the pressure has a considerably lower level. Here, the effect of the friction forces can be clearly observed which are the reason for a stiffening of bumps from the leading edge to the trailing edge.

Figure 3.11 illustrates the predicted load capacity due to equation (1.17) for one pad of the reference AFTB as a function of the angular velocity. Results are shown for a rigid bearing, the shell model with and without friction, and the Heshmat model.

For $\Omega \to 0$, the load capacity of all models has the same slope, representing the limit case of an incompressible rigid solution, where compressibility effects and foil deflections are negligible. For the maximal angular velocity $\Omega = 10^4 \frac{rad}{s}$ the predicted load capacity of the shell model is nearly half of that of the rigid model and 75% higher than the predictions of the Heshmat model. It can be stated that among all the possible bump foil models, the Heshmat model represents the softest one, because it bases on the assumption of a single unconnected bump with a free-free boundary situation. Therefore, the results of the Heshmat model and the rigid model can be regarded as limiting cases. Within these limits, no general tendency can

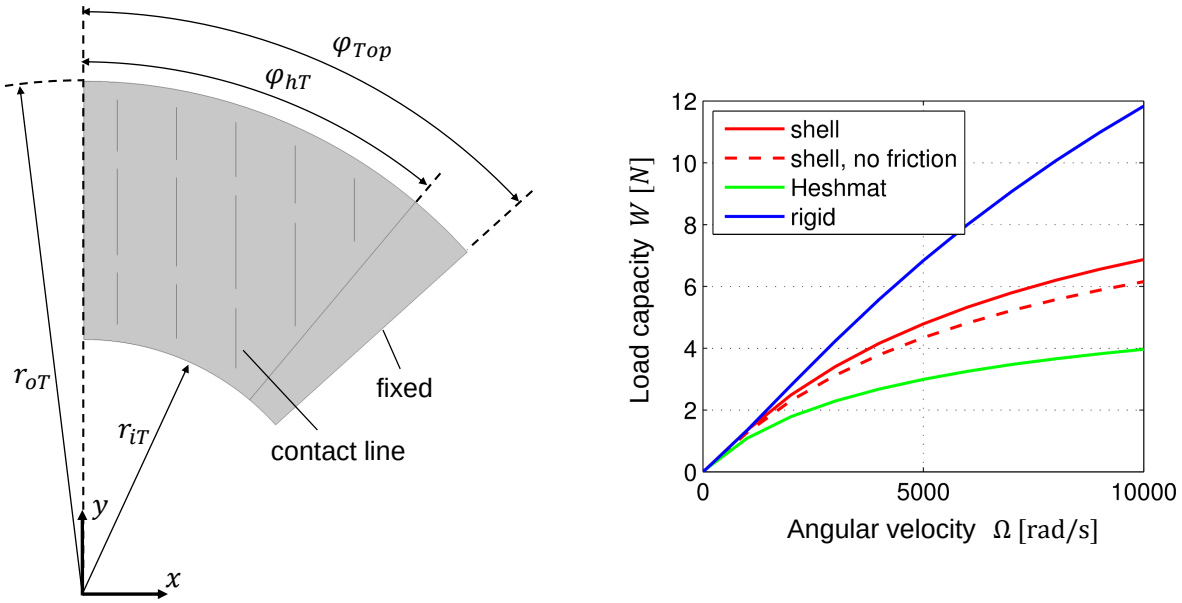

Figure 3.11: Geometry of top foil and contact lines between top and bump foil for one pad of the reference AFTB (left). Predictions of different foil models for the load capacity of one pad of the reference AFTB.

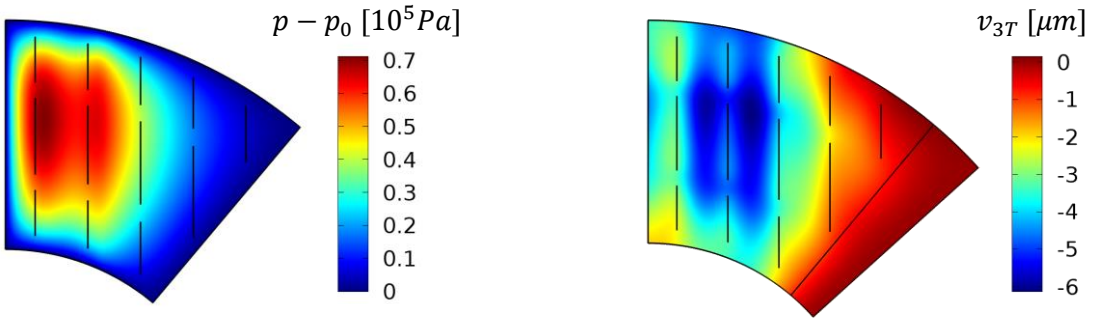

Figure 3.12: Pressure distribution (left) and top foil deflection (right) for one pad of the AFTB.

be seen. Up to $\Omega = 4000\frac{rad}{s}$, the shell model is nearer to the rigid limit, whereas for higher angular velocities the Heshmat model represents a better approximation for the shell model. In general, however, the difference between the shell model and the limiting cases is too high in order to use the limiting cases for reliable predictions. Even the shell model without friction shows a nearly 12% lower load capacity indicating that two-dimensional friction forces cannot be disregarded. This difference can be considerably higher if the bump strips consist of more bumps.

3.1.6 Summary and conclusions

The structural properties of foil sandwiches and their influence on the load capacity of air foil thrust bearings have been analysed in detail. A general shell formulation has been specified to a frequently used bump and top foil geometry from the literature. The chosen thick shell theory can be adjusted to different foil geometries and accounts for shear, membrane, and bending effects. A penalty approach has been used for the contact between top and bump foil including Coulomb friction. For the one-dimensional case, the

influence of different bump interaction mechanisms on the stiffness of a bump strip has been discussed. It could be shown that the interaction between bumps by bending moments can have a more significant effect than the interaction by horizontal forces. Furthermore, in comparison to the results of a commercial FE software, the accuracy of the presented foil model and the assumption of a point contact between top and bump foil have been verified successfully. Coupling the shell equations to the compressible Reynolds equation, the influence of different foil models on the pressure distribution in an one-dimensional taper land foil slider was shown. Especially, it was demonstrated that former models from the literature underestimate the pressure distribution and that interacting bending moments between bumps are essential for predicting the foil bearing performance.

For the two-dimensional case, the structural properties of a curved bump strip, as it is frequently used in air foil thrust bearings, were studied. Fundamental differences in comparison to straight bump strips could be shown, having their origin in the curvature of the strip and the two-dimensional friction forces. Therefore, one-dimensional bump strip models can be used for straight bump strips in air foil journal bearings, but are rather inappropriate for the modeling of curved bump strips as they occur in air foil thrust bearings.

Finally, the two-dimensional shell model for the foils, including two-dimensional friction forces, was coupled to the compressible Reynolds equation in order to calculate the pressure distribution, top foil deflection, and load capacity of an air foil thrust bearing. Compared to results from the literature (Heshmat model), significant differences in the load capacity were found for a wide range of operating conditions.

All the mentioned findings indicate, that reduced elastic foundation type models - frequently used in the literature - cannot describe the performance of air foil thrust bearings with a high degree of accuracy. In the opinion of the author, it is nearly impossible to find an appropriate effective stiffness for the elastic foundation of the top foil. The effects, that govern the stiffness behaviour of bump strips, namely

- interacting horizontal forces between the bumps,
- interacting bending moments that strongly depend on the length of the bridges,
- two-dimensional curvature effects and
- two-dimensional friction forces,

can only be accounted for by a detailed structural model and not by simplified single bump calculations.

3.2 Comparison of rigid and foil thrust bearings

The aim of the previous section 3.1 was to develop an accurate structural model for the foils of an AFTB. Focus was put on the identification of different mechanisms that influence the stiffness of the foil sandwich. Finally, a detailed fully coupled elasto-hydrodynamic model for AFTBs has been presented.

In this section, the question of interest is how the compliance of AFTBs influences their performance. For this purpose, the reference pad of table 3.2 with an angular velocity of $\Omega = 10^4 \frac{rad}{s}$ is chosen as a basis configuration. The bearing load can be controlled by different minimal gap heights in the bearing pad. The compliance of top and bump foil is changed through a variation of the foil thicknesses t_T and t_B. All calculations are performed with the fully coupled elasto-hydrodynamic model of the previous section that has been shown to account for the relevant stiffness effects in AFTBs.

Especially, advantages and disadvantages of foil bearings for different operational conditions are of particular interest. Therefore, the analysis starts in section 3.2.1 for aligned bearing configurations where the rotor disk is absolutely flat and parallel to the base plate of the bearing (this condition was assumed in all previous calculations of chapter 2 and section 3.1).

Section 3.2.2 is concerned with distorted conditions which may be a consequence of thermally induced deformations of the rotor disk.

Finally, in section 3.2.3 the ability of foil bearings to compensate for misaligned conditions is investigated.

3.2.1 Aligned conditions

Factors limiting the load capacity of rigid thrust bearings have been analysed thoroughly in chapter 2. The concrete nominal gap function and the compressibility number were shown to have controlling influence on the performance. In case of AFTBs, the compliance of the foils can be a further limiting factor.

To investigate its influence, a criterion for the comparison of different AFTBs among each other or to rigid thrust bearings has to be defined. The main problem herein is that for AFTBs the real gap function and the nominal gap function are different due to the deformation of the foils. As a consequence, two AFTBs with identical nominal gap functions but for example different foil thicknesses will have different real gap functions for all operating conditions.

The criterion proposed in this work is based on the minimal gap height h_{min} in the bearing, which is the shortest distance between the (deformed) rotor disk and the deformed top foil. Defining the compressibility number in a more general sense on the basis of the minimal gap height

$$\Lambda = \frac{6\eta\Omega}{p_0} \frac{r_{oT}^2}{h_{min}^2} , \tag{3.37}$$

two AFTBs are said to operate under comparable conditions if they have the same compressibility number (note that the former definitions of the compressibility number for the rigid sector-shaped pad (section 2.1) and the spiral groove bearing (section 2.4) are in agreement with equation (3.37)). More precisely, for

the calculations of this section, two AFTBs are said to operate under comparable conditions if they have the same minimal gap height h_{min}. This is because all other parameters are constant for the considered reference pad of table 3.2 with an angular velocity of $\Omega = 10^4 \frac{rad}{s}$.

The minimal gap height appears to be a sensible criterion for an additional reason. In practice, a thrust bearing can only operate in the full hydrodynamic regime above a certain critical gap height. Below this critical value, which is estimated to be $2-5\mu m$ in [Ior99, Day76, Kim07] for AFTBs, mixed lubrication occurs and the bearing fails. Therefore, the limiting performance characteristics (load capacity, power loss, etc.) under the condition of a minimal possible film thickness are of special interest for the bearing designer.

Computationally, the minimal film thickness h_{min} is realised by an extended definition of the real gap height

$$\begin{aligned} h(x,y) &= -(h_{nom} - v_{3T}) + h_{shift}\,, \\ h_{shift} &= min(h_{nom} - v_{3T}) - h_{min}\,, \end{aligned} \tag{3.38}$$

which mimics the evolution of the real gap size in an AFTB application: In the initial configuration, the real gap height $h(x,y)$ is given by the negative nominal gap height h_{nom}. Due to the influence of the hydrodynamic pressure, the foils deflect and the real gap height becomes a sum of the nominal gap height and the top foil deformation v_{3T} (note, that v_{3T} is directed towards the rotor disk, compare figure 3.6). If the thrust load can not be balanced by this configuration, the rotor disk moves in axial direction towards the top foil what is accounted for by h_{shift}. The resulting smaller gap size leads to a higher hydrodynamic pressure and to higher top foil deformations. In practice, the procedure is finished when the applied thrust load on the rotor is balanced by the AFTB. In the herein applied computational model for the comparison of different AFTBs, according to equation (3.38) the iterations are repeated until the predefined minimal gap height h_{min} is reached in at least one point of the lubricating gap.

Comparison to rigid thrust bearings

Figure 3.13 illustrates the influence of the foil stiffness on the load capacity of an AFTB for aligned conditions. High, moderate and low load conditions are realised by the three minimal gap heights of $4\mu m$, $10\mu m$ and $16\mu m$. For each minimal gap height four configurations are considered within this comparison.

The blue lines depict the load capacity for the reference pad with a rigid bump and top foil. It represents the limiting solution of an infinitely stiff foil sandwich. Obviously, the rigid pad achieves the highest load capacity for all considered minimal film thicknesses h_{min}.

The influence of the top foil stiffness can be studied on the basis of the green lines in figure 3.13. They represent a configuration where the bump foil is assumed to be rigid and the top foil thickness is varied between $75\mu m$ and $150\mu m$. It can be clearly seen that stiffer top foils lead to higher load capacities and that even for a very thick top foil of $t_T = 150\mu m$ the difference to the rigid solution is still about 25% for the highly loaded case of $h_{min} = 4\mu m$. Note in this context that a doubling of the top foil thickness results in an eight

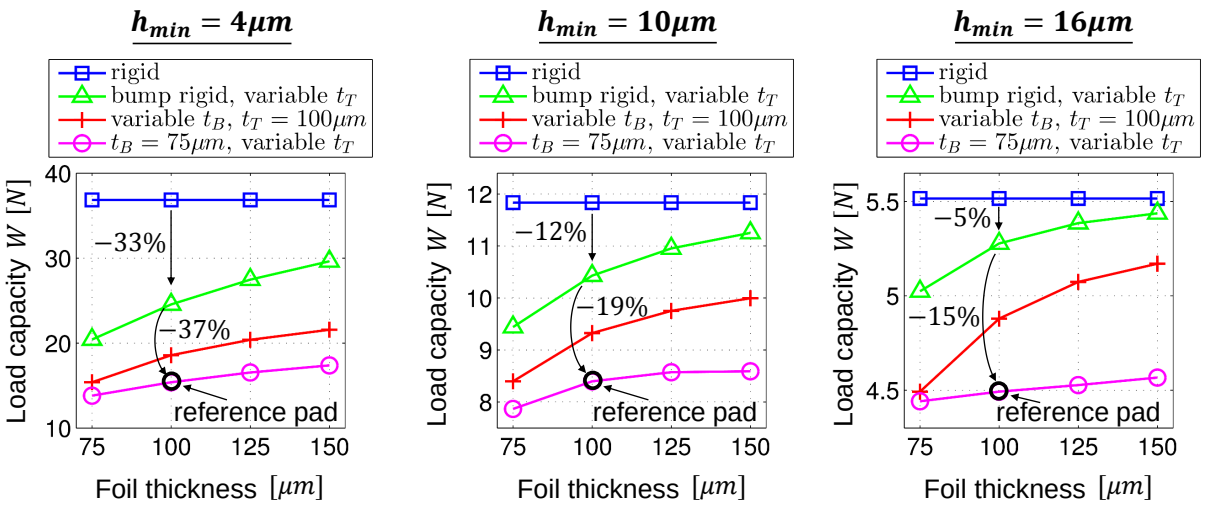

Figure 3.13: Load capacity as a function of the foil thickness for different compliant pad configurations.

times higher bending stiffness, compare equation (3.12).

The red and the magenta lines in figure 3.13 illustrate foil thickness variations on the basis of the reference pad, which has a $t_B = 75\mu m$ thick bump foil and a $t_T = 100\mu m$ thick top foil (see table 3.2). It can be observed that an increase of the bump foil stiffness (red line) has a greater effect on load capacity than an increase of the top foil stiffness (magenta line). In general, this tendency is not strictly valid but highly dependent on the concrete foil thicknesses of the reference pad that are used as a baseline.

To sum up, it is evident that softer foils lead to lower load capacities for all three considered compliant configurations. Comparing the rigid pad with the compliant reference pad (black circle) for the highly loaded case, a decrease of 33% in load capacity can be clearly referred to the compliance of the top foil. A further reduction of 37% can be traced back to the compliance of the bump foil. In total, the reference pad has a load capacity of $W = 15.8N$ which is only 42% of the value for the corresponding rigid pad ($W = 36.8N$). As to be expected, this difference is smaller for the moderately and lightly loaded cases.

Top foil sagging

In the previous paragraph a sensitive relation between load capacity and foil compliance has been found for AFTBs. This paragraph is intended to investigate the origin of the observed phenomenon and focuses on the top foil deformation. For this purpose, foil sandwich configurations with a rigid bump foil are considered, and the influence of the top foil stiffness is analysed (compare green lines in figure 3.13).

The left column of figure 3.14 shows the height function and the corresponding pressure distribution for a moderate load condition ($h_{min} = 10\mu m$) and a very thick top foil of $t_T = 150\mu m$. Small waves can be observed in the nominally flat land region of the taper land height function indicating the small deformations of the top foil due to the hydrodynamic pressure in the pad. In particular, the existence of a broad high pressure plateau near to the trailing edge is found as it has been already seen for the optimised rigid pad

configurations in combination with a high compressibility number (see figure 2.2). As a consequence, the difference in load capacity between the rigid and the foil pad is only about 5%, compare figure 3.13.

If the top foil thickness is considerably reduced to $t_T = 75\mu m$ (middle column of figure 3.14), significant deformations of the top foil in the region between two bump lines are observed. The corresponding pressure field does no longer show a broad pressure plateau but two distinct pressure peaks close to the bump lines. The origin of that can be found in the fact that the top foil deformations are already of the order of the minimal gap height. Because of this, the global taper land height function is superimposed by a local elastically induced taper between the first and the second bump line leading to two distinct pressure peaks. Since the deformed height function has a considerably lower flow resistance in the land region of the pad, the loss in load capacity is already 25% compared to the rigid pad with the nominal taper land height function.

The right column of figure 3.14 illustrates that the described effects are more pronounced for smaller minimal film heights. Firstly, the pressure level rises with decreasing minimal film height resulting in higher top foil deformations. Secondly, even small top foil deformations are of the order of the small minimal film height and therefore already significantly disturb the global taper land gap function. This explains why for the highly loaded case of $h_{min} = 4\mu m$ considerable losses in load capacity are observed even for rather thick top foils, compare figure 3.13.

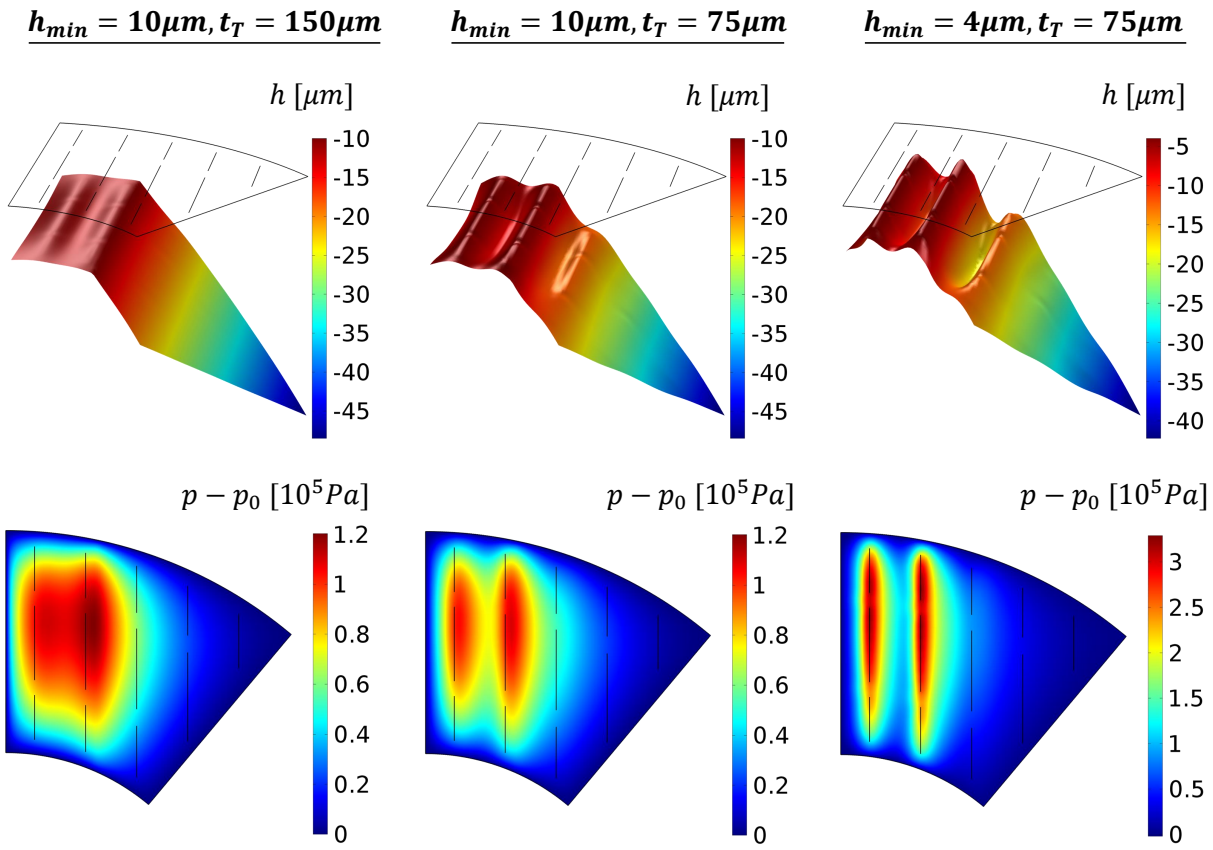

Figure 3.14: Real gap function $h(x, y)$ and corresponding pressure distribution $p(x, y)$ for different minimal film thickness conditions h_{min} and top foil thicknesses t_T. Illustration of the top foil sagging effect.

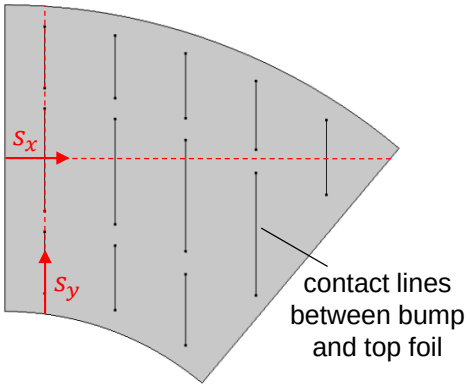

Figure 3.15: Definition of coordinate directions s_x and s_y used to illustrate bump foil deformations in figure 3.16.

Details of bump foil deformation

Besides the top foil sagging between the contact lines of the bump foil, the deformation of the bump foil itself has been shown to be a limiting factor for the load capacity. To find an explanation for that, the reference pad with a thick top foil of $t_T = 150\mu m$ is analysed for a highly loaded condition of $h_{min} = 4\mu m$. In particular, the height function is studied along the directions s_x and s_y (see figure 3.15) for a thin bump foil of $t_B = 75\mu m$ and a thick bump foil of $t_B = 150\mu m$ thickness.

The left plot in figure 3.16 shows that the real gap function h of the thick bump foil configuration keeps close to the nominal gap function of the rigid pad. In contrast, considerable deviations can be stated for the thin bump foil configuration. Whereas the top foil sagging disturbed the nominal gap function mainly locally, the deformations of the bump foil are of global character. Firstly, the inclination of the taper is considerably lower for the thin bump foil than for the thick bump foil configuration. Secondly, the observed minimal film height along the s_x-direction is about $6\mu m$ and thus considerably higher than the $h_{min} = 4\mu m$ of the rigid pad.

The reason for the latter aspect can be found more clearly in the right plot of figure 3.16. It illustrates that the minimal film height of $h_{min} = 4\mu m$ occurs for the compliant configurations only at the inner bump close to the inner radius of the pad. Especially for the thin bump foil, the height function shows a significant deviation in direction of larger radii (high values of s_y). This effect can be explained by the higher pressure level that occurs for larger radii due to the higher circumferential velocity of the rotor disk. It is obvious, that the observed increase of the height function in radial direction leads to a land region with a significantly lower flow resistance. As a consequence, the real gap function of the bearing is less efficient leading to considerably lower load capacities.

In summary, the reasons for the worse load capacity of foil bearings can be clearly referred to the top foil sagging and the unequal bump foil deformations. It can be therefore concluded that for aligned conditions of the rotor disk and the thrust bearing, AFTBs will always have a lower load capacity and a higher power loss compared to optimised rigid thrust bearings. This statement is of special importance, since it is in

contradiction to early studies of AFTBs that are frequently cited in the literature. Heshmat [HWP83a], for example, reported an increasing load capacity for a rising bearing compliance. Without a detailed discussion, it should be pointed out that Heshmat's calculations based on a very simplified foil model that can not account for top foil sagging or identify the region in the pad where the minimal film thickness occurs.

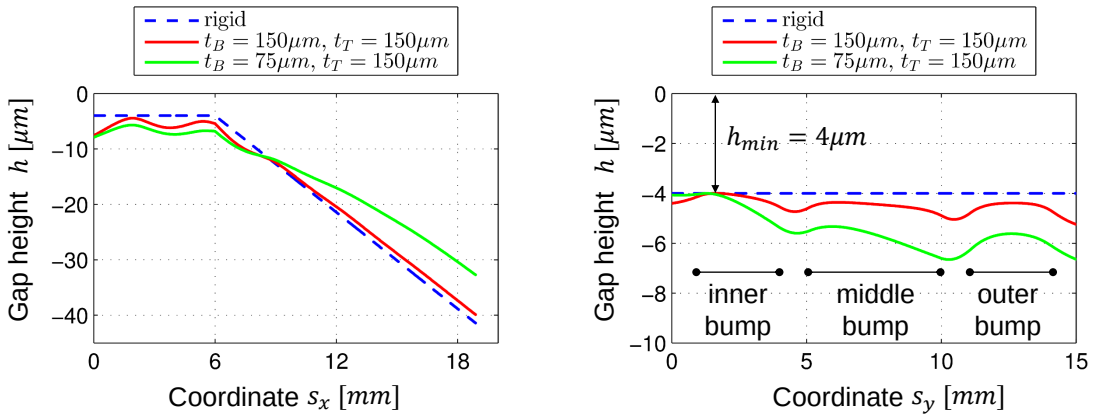

Figure 3.16: Real gap function along the coordinates s_x (left) and s_y (right) of the reference pad, compare also figure 3.15.

Comparison to measurements

Another example for the importance of a detailed elasto-hydrodynamic model as it is presented in this work is depicted in figure 3.17.

Iordanoff [Ior99] measured the power loss as a function of the load capacity for a complete AFTB and compared the experimental results to the theoretical predictions of his reduced foil model (figure 3.17b). It is striking that the predicted power loss is a linear function of the load capacity whereas the measured power loss shows a nonlinear behaviour. For comparison, figure 3.17a shows the power loss as a function of the load capacity for the analysed reference pad of this work (green line). Four distinct regions can be identified in the plot.

For very low loads with a minimal film height larger than $35\mu m$, the modified Reynolds number defined in equation (1.24) is close to one indicating that the Reynolds equation is not valid for this region. The power loss on the rotor disk surface can only be calculated by the Navier-Stokes equations (1.2)-(1.4). The dashed blue line shows the trend for this case.

The second region ranges from $h_{min} = 35\mu m$ to approximately $h_{min} = 10\mu m$ and represents low to moderate load conditions. This region is characterised by two properties. Firstly, the power loss has a slightly decreasing slope. This behaviour is well known from rigid thrust bearings and can be as well found in Iordanoff's measurements. Secondly, a comparison to the power loss of the reference configuration with a very thick bump foil (red line) shows practically no difference. This indicates that foil deformations are of subordinate importance for the power loss in region 2.

In the third region, a significant rise in power loss can be observed for the reference pad (green line).

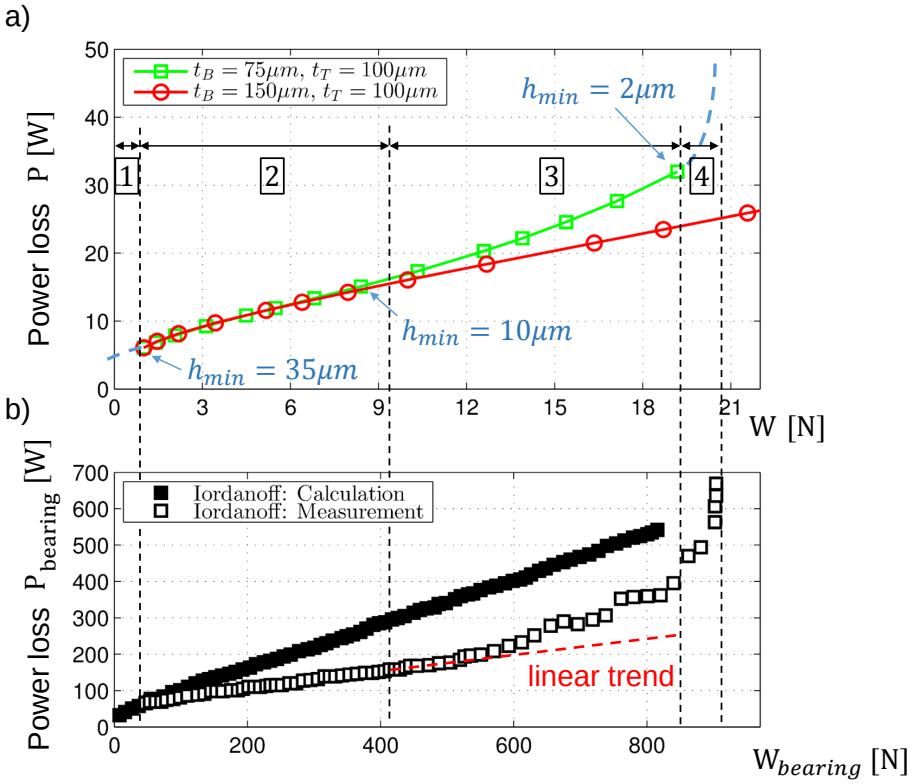

Figure 3.17: a) Calculated power loss (in Watts) as a function of the load capacity for the reference pad and a pad with a very thick bump foil ($t_B = 150\mu m$). b) Calculation and measurement by Iordanoff [Ior99] for the power loss of a complete eight pad AFTB as a function of the load capacity.

In particular, the slope of the power loss shows the same increasing behaviour as has been measured by Iordanoff. This nonlinear behaviour can be explicitly referred to the unequal deformations of the bump foil that have been discussed in the last section. This is because the reference pad with the thick bump foil still shows a nearly linear relationship even for high loads. Furthermore, it can be clearly stated that the measured nonlinear behaviour in region 3 is not a top foil sagging effect since both reference pad configurations have the same top foil thickness of $t_T = 100\mu m$ (as has the top foil of Iordanoff's bearing).

Finally, the fourth region is characterised by a sudden increase in power loss. This again can not be predicted by a Reynolds equation based model since the origin of the sudden increase is a mixed lubrication condition where dry friction occurs between the top foil and the rotating disk. The sudden increase in power loss is often used as a criterion for the definition of the load capacity limit of AFTBs.

The main conclusion from this paragraph is that a detailed model for AFTBs can predict nonlinear phenomena that are not captured by reduced models as presented in [Ior99]. Furthermore, thicker bump foils are found to be favorable not only in terms of higher load capacities but as well for a lower power loss (aligned conditions). Note, that the measurements by Dykas et al. [DBD+08] confirm the characteristic behaviour of the power loss as a function of the load capacity that has been discussed in this paragraph for AFTBs.

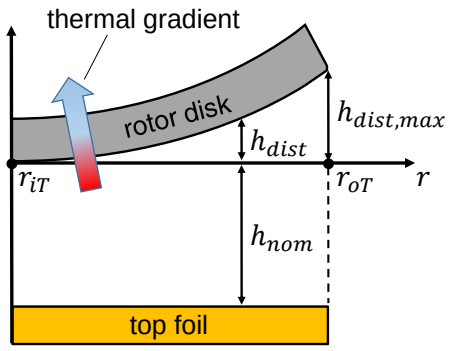

Figure 3.18: Schematic illustration of the rotor disk bending due to a thermal gradient in axial direction.

3.2.2 Distorted conditions

A frequently claimed advantage of AFBs is that they are expected to show beneficial characteristics for disturbed conditions of the nominal gap function. It is assumed that the compliance of AFBs is able to compensate for the disturbed condition resulting in a more favorable real gap height. Possible perturbations of the nominal gap function are caused by manufacturing inaccuracies, thermal distortions of the bearing parts or misaligned conditions. The latter are analysed in section 3.2.3.

In this section, disturbances as they are frequently induced by a thermal bending of the rotor disk due to temperature gradients are investigated. For this purpose, the nominal gap function is assumed to be superimposed by a parabolic function h_{dist} that accounts for the distortion of the rotor disk, see figure 3.18. The real gap function (3.38) is extended in this case to

$$\begin{aligned} h(x,y) &= -(h_{nom} + h_{dist} - v_{3T}) + h_{shift}\,, \\ h_{shift} &= min(h_{nom} + h_{dist} - v_{3T}) - h_{min}\,, \\ h_{dist} &= h_{dist,max}\frac{(r - r_{iT})^2}{(r_{oT} - r_{iT})^2}\,. \end{aligned} \tag{3.39}$$

Figure 3.19a shows the load capacity of one reference pad for a moderately distorted rotor disk ($h_{dist,max} = 5\mu m$). Although a thick top foil of $t_T = 150\mu m$ has been chosen for the comparison in order to minimize top foil sagging effects, the foil pads show a lower load capacity than the rigid thrust pad. Especially, it is astonishing that even for distorted configurations higher load capacities are achieved with thicker bump foils. The same result is found in figure 3.19b that depicts the load capacity as a function of the distortion parameter $h_{dist,max}$. It can be clearly seen that the foil pads are inferior to the rigid pad over the whole range of distortion parameters. At least, it can be stated that the difference diminishes with increasing $h_{dist,max}$.

The reason for the poor ability of the foil bearings to compensate for the distortion is depicted in figure 3.20. The left plot shows the pressure distribution for a foil pad ($t_B = 75\mu m$, $t_T = 150\mu m$) and the right plot for a rigid pad. The distortion parameter $h_{dist,max} = 5\mu m$ and the minimal film thickness of $h_{min} = 4\mu m$ are

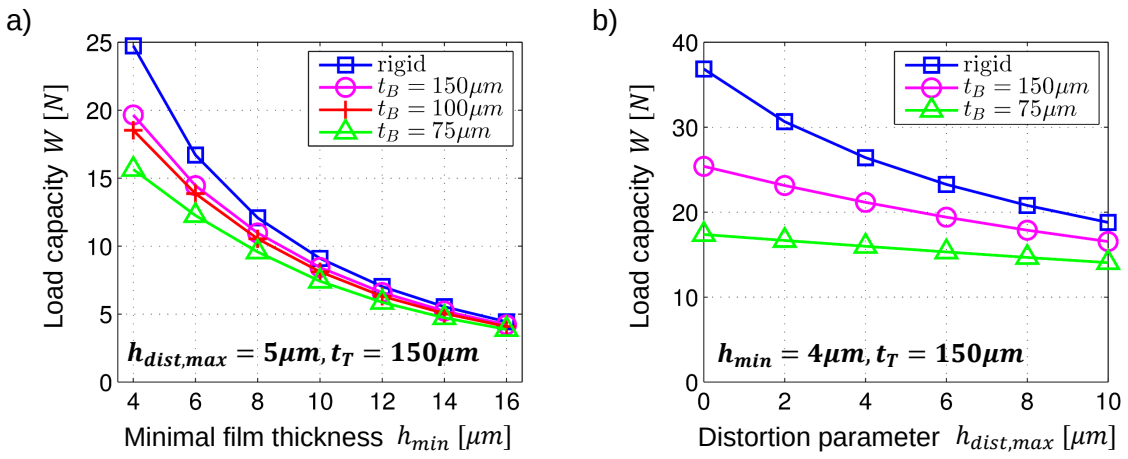

Figure 3.19: Load capacity of the distorted pad configuration for a) the distortion parameter $h_{dist,max} = 5\mu m$ and b) the minimal film thickness $h_{min} = 4\mu m$. In both cases a thick top foil of $t_T = 150\mu m$ is chosen in order to minimize top foil sagging effects.

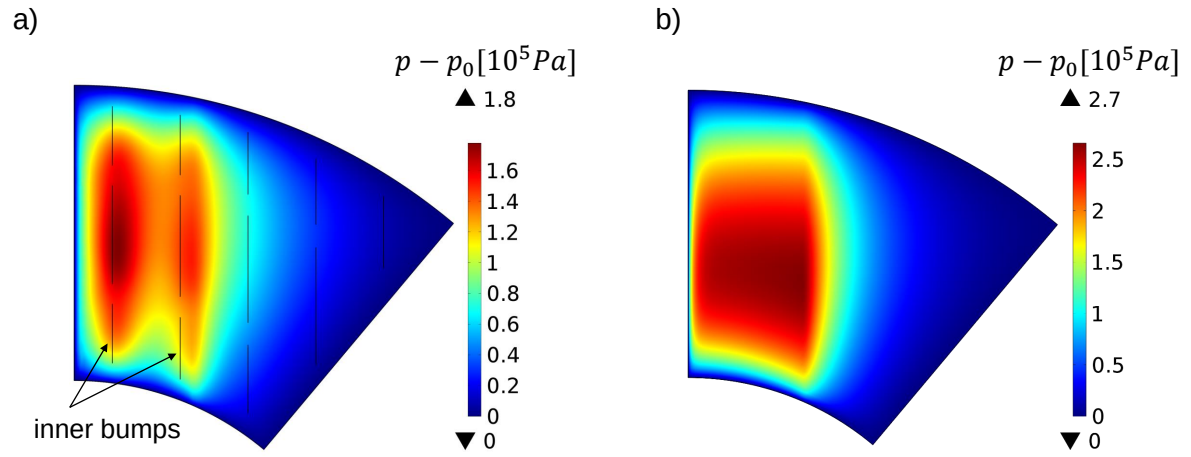

Figure 3.20: Pressure distribution for a) the foil pad ($t_B = 75\mu m$, $t_T = 150\mu m$) and b) the rigid pad for a minimal film thickness condition of $h_{min} = 4\mu m$ and a distortion parameter of $h_{dist,max} = 5\mu m$.

the same for both plots. In order to effectively compensate for the distorted height function, the maximum pressure should be near to the inner radius where the minimal film thickness occurs. But, it can be clearly seen that the maximum pressure is only slightly shifted towards the inner radius for the rigid pad. In case of the foil pad this tendency is even smaller. As a consequence, the inner bumps of the foil pad do not show a significantly higher deformation than the middle and outer bumps. Thus, it is not possible for the foil pad to effectively compensate for the thermally induced distortions of the rotor disk. As for the aligned case of the previous section 3.2.1, load capacity reducing factors like an unequal bump foil deformation and top foil sagging are also apparent for the distorted case and lead to lower load capacities in comparison to the rigid pad.

3.2.3 Misaligned conditions

Misalignment between the base plate and the rotor disk is frequently caused by manufacturing or assembly inaccuracies and can not be avoided completely. Figure 3.21 illustrates the 6 pad reference AFTB of table

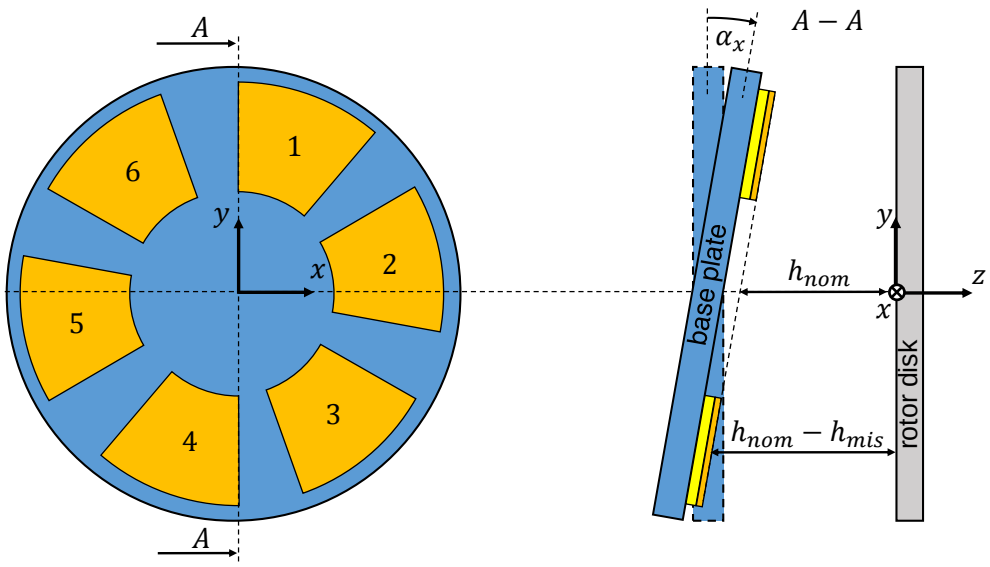

Figure 3.21: Misaligned reference AFTB.

3.2 in a misaligned condition. The orientation of the base plate relative to the rotor disk is described by the misalignment angles α_x and α_y, which are zero for the special case of aligned conditions. The real gap function is given by

$$\begin{aligned} h(x,y) &= -(h_{nom} - h_{mis} - v_{3T}) + h_{shift}\,, \\ h_{shift} &= min(h_{nom} - h_{mis} - v_{3T}) - h_{min}\,, \\ h_{mis} &= \alpha_x y - \alpha_y x\,, \end{aligned} \tag{3.40}$$

where h_{mis} accounts for the influence of the base plate orientation on the real gap function. Note that the misalignment angles are assumed to be small. Only because of this, the orientation of the base plate can be regarded as a superposition of rotations about the x-axis (α_x) and the y-axis (α_y).

A comparison of an AFTB to a rigid thrust bearing for misaligned conditions is shown in figure 3.22. The load capacity of the whole bearing is plotted against the minimal film thickness in the bearing for $\alpha_y = 0$ and different values of α_x. It is clearly to see that the AFTB outperforms the rigid bearing for higher misalignment parameters. Already for a small misalignment of $\alpha_x = 5\mu m/r_{oT}$, the AFTB is competitive to the rigid bearing for a wide range of minimal film thicknesses h_{min} and is only inferior for high load conditions. With rising misalignment parameter the difference between the AFTB and the rigid bearing increases, resulting in a 20% higher load capacity of the AFTB ($\alpha_x = 15\mu m/r_{oT}$) even for moderate load conditions of $h_{min} = 10\mu m$. This difference is noteworthy since for aligned conditions the load capacity of the AFTB has been shown to be only 70% of the value for the corresponding rigid bearing, compare figure 3.13.

Figure 3.23 shows the influence of the bump foil thickness (left) and the top foil thickness (right) for a misalignment parameter of $\alpha_x = 15\mu m/r_{oT}$. Whereas the load capacity of an AFTB with a thick bump foil of $t_B = 150\mu m$ (not shown in the plot) is comparable to the rigid bearing, a significant improving can be observed for thinner bump foils. For low to moderate loads a clear trend can be identified: The load

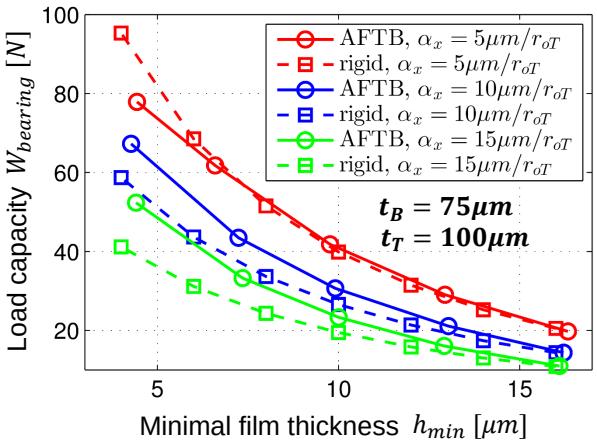

Figure 3.22: Load capacity $W_{bearing}$ for a whole thrust bearing as a function of the minimal film thickness in the bearing. Comparison between a rigid and foil configuration for different misalignment parameters α_x.

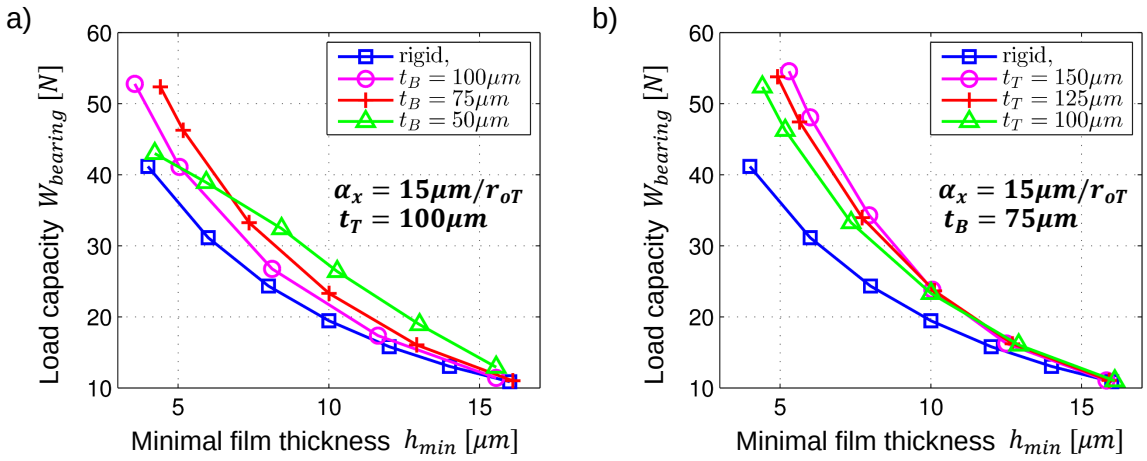

Figure 3.23: Variation of bump foil thickness (left) and top foil thickness (right) for the misalignment parameters $\alpha_x = 15\mu m/r_{oT}$, $\alpha_y = 0$.

capacity of the misaligned AFTB increases with decreasing bump foil thickness what is in contrast to the observed behaviour for aligned configurations, see figure 3.13. But in case of high load conditions (low minimal film thicknesses) a very thin bump foil of $t_B = 50\mu m$ shows a reduced load capacity indicating that an optimal value for the bump foil thickness exists for misaligned conditions. Regarding the top foil thickness, the situation is analogous to the aligned case. Thicker top foils lead to higher load capacities for the whole range of minimal film thicknesses.

To understand the reason for the improved behaviour of AFTBs under misaligned conditions, a closer investigation of the individual pads is helpful. For this purpose, the load capacity and minimal film thickness of each pad of the reference AFTB ($t_B = 75\mu m$, $t_T = 100\mu m$) is plotted in figure 3.24 for the misalignment parameters $\alpha_y = 0$, $\alpha_x = 15\mu m/r_{oT}$. A comparison to the rigid pads reveals an interesting behaviour: The globally minimal film thickness h_{min} occurs within the first pad for both bearings. Consequently, this pad shows the highest load capacity of all pads for both bearing configurations. Since the foil bearing has the higher bearing load capacity $W_{bearing}$ (sum of all pads), the individual pad with the highest load capacity

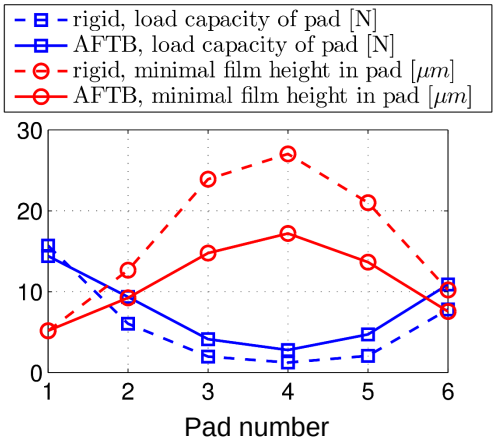

Figure 3.24: Minimal film height and load capacity of the individual pads within the foil and the rigid thrust bearing.

might be expected to occur as well in the foil bearing. But this is not the case. The highest load capacity for an individual pad is found for the first pad of the rigid bearing. This, once again, underlines the poor ability of foil pads to compensate for disturbed nominal gap functions as has been already stated in section 3.2.2. The reason for the superior behaviour of the AFTB with regard to the global load capacity lies in the fact that all other foil pads (numbers 2 to 6) perform better than the corresponding rigid pads. This is not astonishing since the minimal film height of these pads is considerably smaller for the AFTB.

The mechanism that is responsible for the smaller individual film heights is illustrated in figure 3.25. The special formulation of the height function (3.39) ensures that the globally minimal gap function h_{min} is the same for the AFTB and the rigid thrust bearing. Due to the considered choice of misalignment parameters α_y and α_x, h_{min} occurs within pad 1 for both bearings. But the crucial effect is that the bump foil (yellow) of the foil pad deflects under the hydrodynamic pressure. Because of this, the position of the rotor disk is closer to the base plate and thus the minimal film height $h_{min,4}$ of pad 4 and all other pads (except pad 1) is considerably smaller in the AFTB than in the rigid thrust bearing. As a result, the AFTB shows a higher load capacity $W_{bearing}$.

3.2.4 Summary and conclusions

The load capacity of AFTBs has been compared to rigid bearings for aligned, distorted and misaligned conditions. Unequal bump foil deformations and top foil sagging have been identified to be the main load capacity reducing factors for AFTBs. They can be clearly studied for aligned conditions but occur as well for distorted and misaligned conditions and were shown to be the origin of measured nonlinear effects reported in the literature [Ior99].

For the analysed reference configuration of an AFTB, bump and top foil are not able to effectively compensate for disturbed nominal gap functions within one pad. This is mainly because the balance of the disturbed gap function by an appropriate deformation of the foils is only possible if the foils have a con-

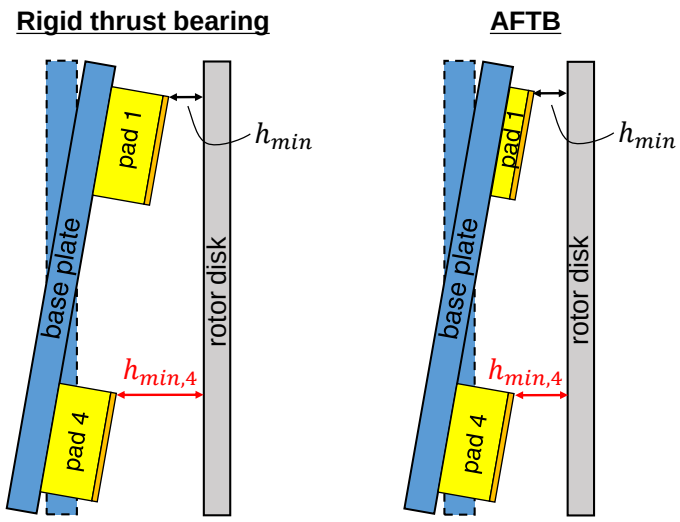

Figure 3.25: Illustration of minimal film height in the highest loaded pad (pad 1) and the lowest loaded pad (pad 4). Comparison between a rigid thrust bearing and an AFTB.

siderable compliance. But for this case, the negative effects of unequal bump foil deformation and top foil sagging are highly pronounced and predominate.

Of course, the frequently used, equal-spaced cartesian bump pattern of the analysed reference configuration could be modified in direction to more sophisticated designs as presented in [DBD+08]. Without claim of completeness, it is only mentioned that modified bump pattern geometries have been tested within the frame of this work, but no systematic advantage could be found for aligned and distorted conditions.

For misaligned conditions, AFTBs could be shown to have higher load capacities in comparison to rigid thrust bearings. But the superior behaviour is not due to stiffness variations within one pad as they are proposed for sophisticated bump foil designs. Instead, it could be clearly stated that the overall compliance of the highest loaded pad enables smaller film thicknesses in the remaining pads and thus higher load capacities. Again, this positive effect is only valid up to a critical minimal compliance of the bump foil. Below this minimal value, negative effects already identified for aligned conditions predominate and can lead to lower load capacities. Hereby, the critical compliance of the bump foil is a function of the expected amount of misalignment.

In summary, it can be said that the compliance of AFTBs helps to compensate for different gap functions between the distinct pads and not for disturbances of the nominal gap function within one individual pad. One possible situation, for which the individual pads of a bearing have different gap functions, is for misaligned conditions. But even for aligned conditions, different gap functions can be apparent in the distinct pads of a thrust bearing due to manufacturing inaccuracies. For instance, if the minimal gap function of one special pad is only $10\mu m$ lower than in the other pads, it follows clearly from the presented calculations (figure 3.13) that the load capacity of a rigid thrust bearing will be very poor. By contrast, for the AFTB the highly loaded pad will deform and enable the other pads to significantly contribute to the load capacity of the AFTB.

Besides favorable damping effects, it is this mechanism that can be regarded as the main advantage of AFTBs.

4 Thermo-elasto-hydrodynamics of AFTBs

In chapters 2 and 3, AFTBs have been studied under the assumption of isothermal conditions. Thermal aspects have been neglected in favour of a clear presentation of hydrodynamic and structural effects. Nevertheless, the vast amount of literature on thermal aspects of fluid film lubrication indicates the extraordinary importance of this issue. A historically prominent example is the experimentally observed load capacity of parallel surface thrust bearings. This effect could not be explained by isothermal lubrication theory since the isothermal Reynolds equation (1.23) predicts a zero load capacity for a lubricating gap of constant height. The search for an explanation of this phenomenon motivated researchers to include thermal considerations in their analysis. In general, the performance of fluid film bearings was found to be influenced by two different types of thermal effects. The first is due to the temperature dependence of the fluid properties [Zie57, Dow62, Pin90, Sny65, ER73, Hue74, Kho87], which led to the development of the generalized Reynolds equation (1.13)-(1.14) accounting for three dimensional variations of the dynamic viscosity and the density. As a second effect, the thermal distortion of bearing components was identified to may have a considerable influence on the gap function and therefore as well on the pressure development in a fluid film bearing [BBA96, PS65, PS67, RC75]. Indeed, in case of the parallel surface bearing, the thermal distortions were found to be responsible for the observed load capacity [EC65, EB86].

The main aim of this chapter is the development of a thermo-elasto-hydrodynamic model for an AFTB. Section 4.1 focuses on the thermal modeling of the air film without considering the heat transfer from the air film to the bearing parts (top foil, rotor disk, etc.). Fundamental differences between oil and air bearings are found and appropriate reductions of the generalized Reynolds equation and the energy equation are presented. In section 4.2, the heat transfer in the different bearing parts is modeled in detail and coupled to the air film. Finally, simulation results for the thermo-elasto-hydrodynamic (TEHD) model are presented in section 4.3.

4.1 Thermal modeling of the air film

This section focuses on thermal effects in fluid film bearings that are caused by the properties of the concrete lubricating fluid. For the isothermal case considered in chapter 2, the compressibility of air has been already found to be a distinguishing property of air bearings in comparison to oil bearings. Namely, the Reynolds equation becomes nonlinear and the compressibility number appears as an additional governing parameter next to the shape of the gap function.

Effects of similar magnitude can be observed if thermal properties of the fluid are included in the analysis. Therefore, in this section a rigid oil thrust bearing is compared to a rigid air thrust bearing for the case of adiabatic boundary conditions. The comparison of oil and air bearings is interesting because of two reasons. Firstly, both bearing types are well suited for high speed turbomachinery. Since an increasing demand on oil-free systems can be observed (e.g. fuel cell blowers), it is of significant interest if at all or under which

circumstances oil bearings can be substituted by air bearings. The second reason for the comparison is that thermal aspects of oil bearings have been investigated in the literature to a far deeper extend than those of air bearings. A consequence of this is that modeling approaches for oil bearings are frequently found in the literature to be as well mistakenly applied to air bearings. It is therefore the aim of this section to clearly identify the thermal characteristics of air bearings. Based on these results, appropriate reductions of the governing equations, namely the Reynolds equation and the energy equation, are suggested for an efficient simulation of AFTBs.

4.1.1 Generalized Reynolds equation and energy equation

The governing equations describing the fluid flow in a lubricating gap have been derived in section 1.5. The generalized Reynolds equation (1.13)-(1.14) has been shown to account for three-dimensional variations of the fluid's dynamic viscosity and density. As both properties are a function of the fluid temperature, a three-dimensional energy equation has to be solved in addition to the generalized Reynolds equation.

Energy equation

A starting point for the derivation of an appropriate energy equation for AFTBs is the general balance of energy for a fluid element of arbitrary material

$$\rho \frac{D\epsilon}{Dt} = -\operatorname{div} \mathbf{q} + \mathbf{S} \cdot \nabla \mathbf{u} \,. \tag{4.1}$$

Hierin, ϵ is the specific internal energy of the fluid, $\mathbf{q}$ is the heat flux over the boundary and $\mathbf{S} = -p\mathbf{I} + \mathbf{T}$ is the Cauchy stress tensor for a viscous fluid. The lubricant is assumed to be free of internal heat sources (e.g. from chemical reactions). Further specifications are made by:

1. The caloric equation of state for liquids and ideal gases

$$D\epsilon = c_V DT \,, \tag{4.2}$$

   where c_V is the isochoric specific heat capacity and T is the temperature of the fluid.

2. Fourier's law of heat conduction

$$\mathbf{q} = -k \nabla T \tag{4.3}$$

   with k being the thermal conductivity of the fluid.

3. The use of a Newtonian material law for the viscous stress tensor

$$\mathbf{T} = 2\eta \mathbf{D} - \frac{2}{3}\eta \operatorname{tr}(\mathbf{D})\mathbf{I} \,, \tag{4.4}$$

where $\mathbf{D} = \frac{1}{2}\big(\nabla\mathbf{u} + (\nabla\mathbf{u})^T\big)$ is the rate of strain tensor, $\mathbf{I}$ the identity tensor and $\mathrm{tr}(\cdot)$ the trace of a tensor.

Inserting equations (4.2)-(4.3) in the equation for the balance of energy (4.1) leads to

$$\rho c_V \frac{DT}{Dt} = \nabla(k\nabla T) - p\,\mathrm{div}\,\mathbf{u} + \Phi\,. \tag{4.5}$$

Hierin, the dissipation function reads in cartesian coordinates

$$\Phi = \mathbf{T}\cdot\nabla\mathbf{u} = 2\eta\left[\Big(\frac{\partial u}{\partial x}\Big)^2 + \Big(\frac{\partial v}{\partial y}\Big)^2 + \Big(\frac{\partial w}{\partial z}\Big)^2\right] + \eta\left[\Big(\frac{\partial v}{\partial x} + \frac{\partial u}{\partial y}\Big)^2 + \Big(\frac{\partial w}{\partial y} + \frac{\partial v}{\partial z}\Big)^2 + \Big(\frac{\partial u}{\partial z} + \frac{\partial w}{\partial x}\Big)^2 - \frac{2}{3}\Big(\frac{\partial u}{\partial x} + \frac{\partial v}{\partial y} + \frac{\partial w}{\partial z}\Big)^2\right]. \tag{4.6}$$

The energy equation (4.5) is valid for both, oil and air bearings. Since oil behaves nearly incompressible (only if the temperature dependence of the density is neglected), $\mathrm{div}\,\mathbf{u} = 0$ holds and the second term of the right hand sight vanishes. In case of air, further manipulations can be applied. Firstly, the continuity equation $\frac{D\rho}{Dt} + \rho\,\mathrm{div}\,\mathbf{u} = 0$ is used to rewrite the energy equation (4.5) to the form

$$\rho c_V \frac{DT}{Dt} = \nabla(k\nabla T) + \frac{p}{\rho}\frac{D\rho}{Dt} + \Phi\,. \tag{4.7}$$

Secondly, two properties of an ideal gas, namely

4. the thermal equation of state

$$p = \rho R_{spec} T\,, \tag{4.8}$$

5. and the relation between the isochoric and isobaric specific heat capacity

$$c_V = c_P - R_{spec} \tag{4.9}$$

are explored in order to get

$$\rho c_P \frac{DT}{Dt} = \nabla(k\nabla T) + \frac{Dp}{Dt} + \Phi\,. \tag{4.10}$$

Finally, specific assumptions of lubrication theory are applied to equation (4.10):

6. The pressure is nearly constant along the gap height

$$\frac{\partial p}{\partial z} = 0\,. \tag{4.11}$$

7. The velocity gradients $\frac{\partial u}{\partial z}$ and $\frac{\partial v}{\partial z}$ along the gap height are several magnitudes of order greater than all other velocity gradients. This results in the reduced dissipation function

$$\Phi = \eta\left[\Big(\frac{\partial u}{\partial z}\Big)^2 + \Big(\frac{\partial v}{\partial z}\Big)^2\right]. \tag{4.12}$$

Since only stationary flows are considered in this work, the resulting energy equation reads

$$\rho c_P \Big[\underbrace{u\frac{\partial T}{\partial x} + v\frac{\partial T}{\partial y}}_{\text{planar convection}} + \underbrace{w\frac{\partial T}{\partial z}}_{\text{vertical convection}} \Big] = \Big[\underbrace{\frac{\partial}{\partial x}\Big(k\frac{\partial T}{\partial x}\Big) + \frac{\partial}{\partial y}\Big(k\frac{\partial T}{\partial y}\Big)}_{\text{planar diffusion}} + \underbrace{\frac{\partial}{\partial z}\Big(k\frac{\partial T}{\partial z}\Big)}_{\text{vertical diffusion}} \Big] + \underbrace{\Big[u\frac{\partial p}{\partial x} + v\frac{\partial p}{\partial y}\Big]}_{\text{power of pressure forces}} + \underbrace{\eta\Big[\Big(\frac{\partial u}{\partial z}\Big)^2 + \Big(\frac{\partial v}{\partial z}\Big)^2\Big]}_{\text{dissipation}} . \tag{4.13}$$

In section 4.1.4, a magnitude of order analysis of the different terms in equation (4.13) will justify two further simplifications:

8. The planar diffusion can be neglected.

9. The vertical convection is of subordinate order for air bearings.

As a result, the energy equation used in this work for the calculation of the temperature distribution in an AFTB reads

$$\rho c_P \Big[\underbrace{u\frac{\partial T}{\partial x} + v\frac{\partial T}{\partial y}}_{\text{planar convection}} \Big] = \Big[\underbrace{\frac{\partial}{\partial z}\Big(k\frac{\partial T}{\partial z}\Big)}_{\text{vertical diffusion}} \Big] + \underbrace{\Big[u\frac{\partial p}{\partial x} + v\frac{\partial p}{\partial y}\Big]}_{\text{power of pressure forces}} + \underbrace{\eta\Big[\Big(\frac{\partial u}{\partial z}\Big)^2 + \Big(\frac{\partial v}{\partial z}\Big)^2\Big]}_{\text{dissipation}} . \tag{4.14}$$

As $c_V \approx c_P$ holds for liquids, oil bearings can be calculated as well by equation (4.14) if the term for the power of pressure forces is replaced by '$-p \operatorname{div} \mathbf{u}$', compare equation (4.5).

Coordinate transformation

Basically, the generalized Reynolds equation (1.13)-(1.14) and the energy equation (4.14) can be directly used in order to calculate the pressure and temperature fields in a rigid oil or air bearing. This approach turns out to be not very comfortable in practice. For the isothermal case, the concrete shape of the lubricating gap was accounted for by the gap function $h(x, y)$ which is only a factor in the (two-dimensional) isothermal Reynolds equation. For the thermal case, the presented energy equation (4.14) is of three-dimensional character and therefore the complete space of the lubricating gap has to be discretised. A consequence of this is that every time the gap function is changed, the domain on which the energy equation is solved has to be modified as well. Furthermore, for the full TEHD model of an AFTB, the real gap function is anyway not equal to the nominal gap function but influenced by the deformation of the foils and the rotor disk. Because of these reasons, a coordinate transformation is necessary for the governing equations in order to keep the discretisation domain constant.

In this work, the concrete coordinate transformation

$$z = \frac{1 - \overline{z}}{2} h(x, y) \tag{4.15}$$

is applied, where $\overline{z}$ is a nondimensional coordinate ranging from $\overline{z} = -1$ to $\overline{z} = 1$, compare also figure 4.1.

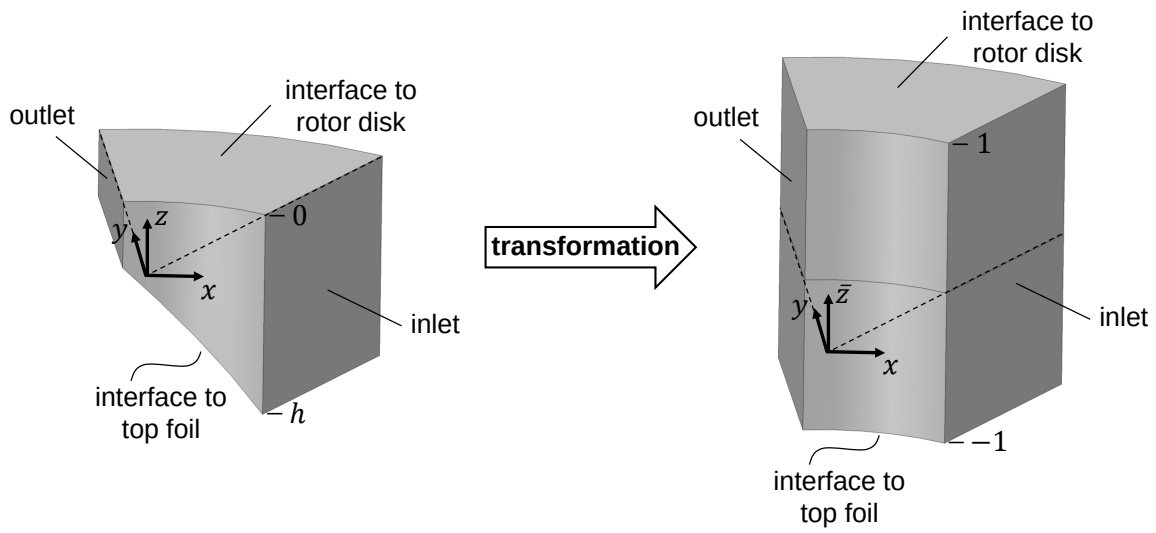

Figure 4.1: Illustration of the coordinate transformation for the lubricating gap.

The energy equation (4.14) transforms due to (4.15) to the nondimensional form

$$\rho c_P\left[u\Big(\frac{\partial T}{\partial x}+\frac{1-\overline{z}}{h}\frac{\partial h}{\partial x}\frac{\partial T}{\partial \overline{z}}\Big)+v\Big(\frac{\partial T}{\partial y}+\frac{1-\overline{z}}{h}\frac{\partial h}{\partial y}\frac{\partial T}{\partial \overline{z}}\Big)\right]=\left[\frac{\partial}{\partial \overline{z}}\Big(\frac{4k}{h^2}\frac{\partial T}{\partial \overline{z}}\Big)\right]+\left[u\frac{\partial p}{\partial x}+v\frac{\partial p}{\partial y}\right]+\frac{4\eta}{h^2}\left[\Big(\frac{\partial u}{\partial \overline{z}}\Big)^2+\Big(\frac{\partial v}{\partial \overline{z}}\Big)^2\right]. \tag{4.16}$$

Analogously, the nondimensional generalized Reynolds equation is given by (compare equations (1.13)-(1.14))

$$\frac{\partial}{\partial x}\left[\frac{h^3}{2}(\overline{F}_2+\overline{G}_1)\frac{\partial p}{\partial x}\right]+\frac{\partial}{\partial y}\left[\frac{h^3}{2}(\overline{F}_2+\overline{G}_1)\frac{\partial p}{\partial y}\right]=\frac{\partial}{\partial x}\left[\frac{U}{\overline{F}_0}h(\overline{F}_3+\overline{G}_2)\right]+\frac{\partial}{\partial y}\left[\frac{V}{\overline{F}_0}h(\overline{F}_3+\overline{G}_2)\right] \tag{4.17}$$

with $\overline{F}_i, \overline{G}_i$ being

$$\begin{aligned}
&\overline{F}_0=\int_{-1}^{1}\frac{1}{\eta}d\overline{z}\,,\quad \overline{F}_1=\int_{-1}^{1}\frac{1}{\eta}\frac{1-\overline{z}}{2}d\overline{z}\,,\quad \overline{F}_2=\int_{-1}^{1}\frac{\rho}{\eta}\frac{1-\overline{z}}{2}\left(\frac{1-\overline{z}}{2}-\frac{\overline{F}_1}{\overline{F}_0}\right)d\overline{z}\,,\quad \overline{F}_3=\int_{-1}^{1}\frac{\rho}{\eta}\frac{1-\overline{z}}{2}d\overline{z}\,,\\
&\overline{G}_1=\int_{-1}^{1}\frac{1-\overline{z}}{2}\frac{\partial\rho}{\partial\overline{z}}\left[\int_{-1}^{\overline{z}}\frac{1}{\eta}\frac{1-\overline{z}}{2}d\overline{z}-\frac{\overline{F}_1}{\overline{F}_0}\int_{-1}^{\overline{z}}\frac{1}{\eta}d\overline{z}\right]d\overline{z}\,,\quad \overline{G}_2=\int_{-1}^{1}\frac{1-\overline{z}}{2}\frac{\partial\rho}{\partial\overline{z}}\left[\int_{-1}^{\overline{z}}\frac{1}{\eta}d\overline{z}\right]d\overline{z}\,.
\end{aligned} \tag{4.18}$$

Finally, the fluid velocities in the lubricating gap (1.15)-(1.16) have to be expressed as a function of the nondimensional coordinate $\overline{z}$

$$u(\overline{z})=-\frac{h^2}{2}\frac{\partial p}{\partial x}\left[\int_{-1}^{\overline{z}}\frac{1}{\eta}\frac{1-\overline{z}}{2}d\overline{z}-\frac{\overline{F}_1}{\overline{F}_0}\int_{-1}^{\overline{z}}\frac{1}{\eta}d\overline{z}\right]+\frac{U}{\overline{F}_0}\int_{-1}^{\overline{z}}\frac{1}{\eta}d\overline{z}\,, \tag{4.19}$$

$$v(\overline{z})=-\frac{h^2}{2}\frac{\partial p}{\partial y}\left[\int_{-1}^{\overline{z}}\frac{1}{\eta}\frac{1-\overline{z}}{2}d\overline{z}-\frac{\overline{F}_1}{\overline{F}_0}\int_{-1}^{\overline{z}}\frac{1}{\eta}d\overline{z}\right]+\frac{V}{\overline{F}_0}\int_{-1}^{\overline{z}}\frac{1}{\eta}d\overline{z} \tag{4.20}$$

since they are needed in the nondimensional energy equation (4.16).

4.1.2 Properties of air

It has been shown in section 4.1.1 that the energy equation is of the same type for oil and air bearings except for the term in the power of the pressure forces. Similarly, it is for both fluids the generalized Reynolds equation that describes the pressure distribution in the lubricating gap. Therefore, the main differences in the performance of air and oil bearings stem from the material properties of the fluids, namely the dynamic viscosity η, the thermal conductivity k, the specific heat capacity c_P and the density ρ. For air, tabulated data can be found for example in [BS13]. In case of oil, a vast number of different types exists. In this work, a Castrol 5W-30 oil is chosen for the comparison between oil and air bearings. It is widely distributed in the automotive industry and can be therefore found to be used as a lubricant in the hydrodynamic oil bearings of turbochargers.

Equations (4.21)-(4.22) are the result of a regression analysis and show the temperature dependence of the fluid properties for a temperature range of $0-500°C$ in case of air and $50-200°C$ in case of the Castrol 5W-30 oil

$$\begin{aligned}
\eta_{air} &= \Big(-1.75\cdot 10^{-11}\Big(\frac{T}{[K]}\Big)^2 + 5.68\cdot 10^{-8}\Big(\frac{T}{[K]}\Big) + 3.06\cdot 10^{-6}\Big)\Big[\frac{kg}{m\cdot s}\Big]\,,\\
k_{air} &= \Big(-2.10\cdot 10^{-8}\Big(\frac{T}{[K]}\Big)^2 + 8.46\cdot 10^{-5}\Big(\frac{T}{[K]}\Big) + 2.89\cdot 10^{-3}\Big)\Big[\frac{W}{m\cdot K}\Big]\,,\\
c_{P,air} &= \Big(2.43\cdot 10^{-4}\Big(\frac{T}{[K]}\Big)^2 - 7.70\cdot 10^{-2}\Big(\frac{T}{[K]}\Big) + 1008\Big)\Big[\frac{J}{kg\cdot K}\Big]\,,\\
\rho_{air} &= \frac{p}{RT}\,,
\end{aligned} \tag{4.21}$$

$$\begin{aligned}
\eta_{oil} &= \Big(5.22\cdot 10^{4} e^{-0.0448\frac{T}{[K]}} + 0.721 e^{-0.0126\frac{T}{[K]}}\Big)\Big[\frac{kg}{m\cdot s}\Big]\,,\\
k_{oil} &= \Big(-7.60\cdot 10^{-5}\Big(\frac{T}{[K]}\Big) + 0.161\Big)\Big[\frac{W}{m\cdot K}\Big]\,,\\
c_{P,oil} &= \Big(3.70\Big(\frac{T}{[K]}\Big) + 811\Big)\Big[\frac{J}{kg\cdot K}\Big]\,,\\
\rho_{oil} &= \Big(-0.643\Big(\frac{T}{[K]}\Big) + 1037\Big)\Big[\frac{kg}{m^3}\Big]\,.
\end{aligned} \tag{4.22}$$

Note, that the density of air ρ_{air} is as well a function of the pressure and therefore modeled by the ideal gas law. An illustration of the tabulated fluid properties (circles) and the respective regression formulae (4.21)-(4.22) (solid lines) is shown in figure 4.2. It reveals fundamental differences in the properties of air (red) and oil (blue). For the most important property, the dynamic viscosity η, three aspects should be highlighted:

- The dynamic viscosity of oil is found to be about three orders of magnitude higher than the dynamic viscosity of air. This leads to considerably higher load capacities for oil bearings which will be discussed in detail in section 4.1.3.
- The temperature dependence shows an increasing behaviour for air but a decreasing behaviour for oil. This qualifies air bearings to be used in high temperature environments. Especially, since air is

not prone to thermal break down phenomena.

- The rate of change is considerably smaller for air than for the oil. For example, in the temperature range between $50 - 200°C$ an increase of only about 30% is observed for air. By contrast, the oil's dynamic viscosity at $200°C$ is only 5% of the corresponding dynamic viscosity at $50°C$. Because of this, the isothermal calculations of chapter 2 are more accurate for air bearings than for oil bearings.

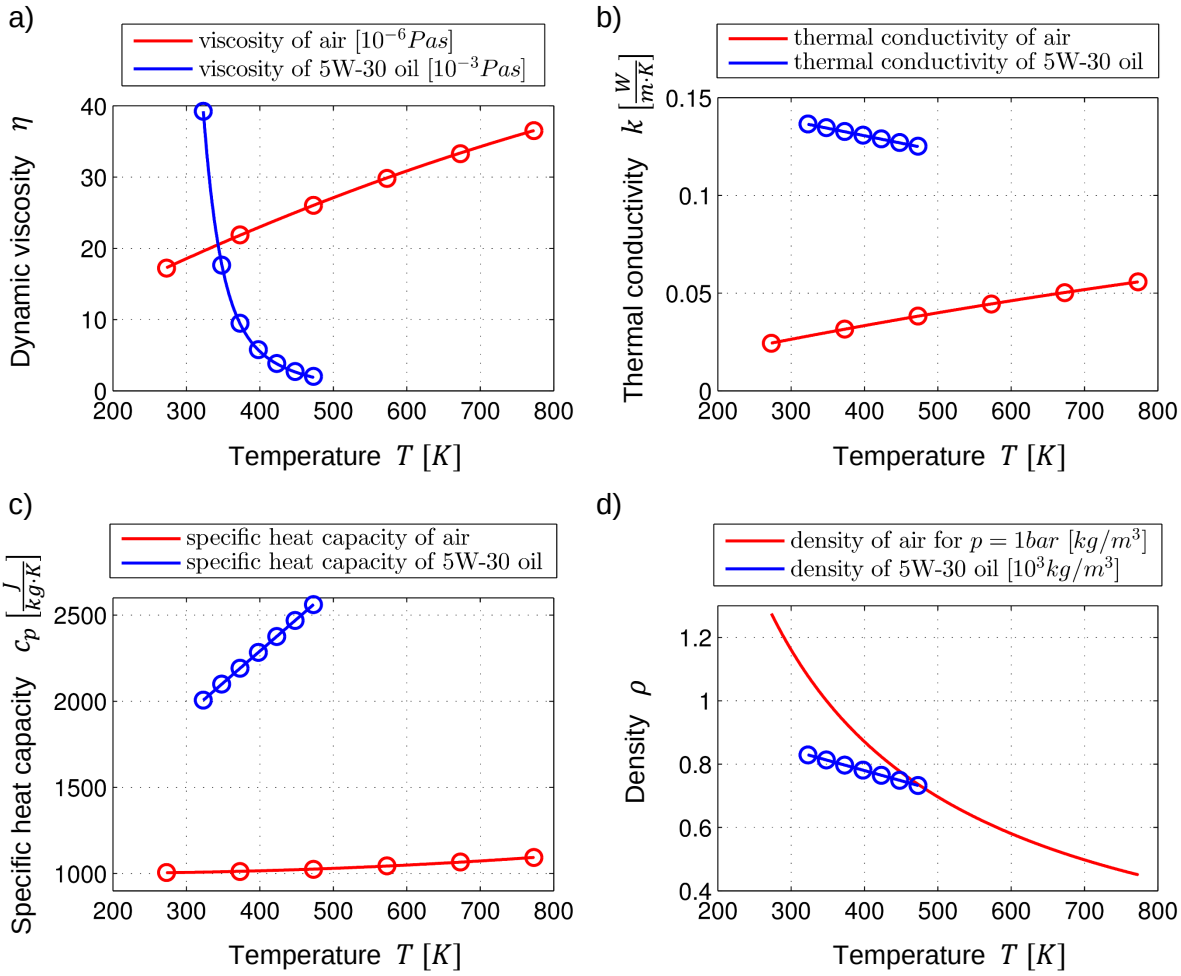

Figure 4.2: Comparison of fluid properties between air and a Castrol 5W-30 oil. a) Dynamic viscosity η. b) Thermal conductivity k. c) Specific heat capacity c_p. d) Density ρ.

4.1.3 Comparison of oil and air thrust bearings

In this section, the pressure and temperature distribution in the lubricating gap of a rigid oil thrust bearing and a rigid air thrust bearing is compared for adiabatic boundary conditions. The comparison is drawn in order to identify characteristic differences in the performance and in the thermal behaviour of oil and air bearings.

		air thrust pad	oil thrust pad
Inner top foil radius	r_{iT}	$15mm$	$3.5mm$
Outer top foil radius	r_{oT}	$30mm$	$7mm$
Hydrodyn. active pad angle	φ_{hT}	$40°$	$40°$
Width of land region	x_{land}	$6mm$	$1mm$
Inclination of taper region	m	$2.90\mu m/mm$	$6\mu m/mm$
Gap size in land region	h_2	$10\mu m$	$10\mu m$
Ref. pressure at boundaries	p_0	$10^5 Pa$	$10^5 Pa$

Table 4.1: Parameters for the rigid air and oil thrust pad.

Geometry

The principal requirement on a thrust bearing in a turbomachine is to carry a certain load for a given rotational speed of the rotor. Based on this criterion, the geometry of the two thrust bearings is chosen in order to produce nearly the same load capacity for an angular velocity of $\Omega = 10^3 \frac{rad}{s}$. For the rigid air thrust bearing, the geometrical parameters of the reference AFTB are taken, compare table 3.2. The oil thrust pad is chosen to be as well of cylindrical sector shape with a cartesian taper land gap function (see definition (3.35)). A comparison between the geometrical parameters of the rigid air and the rigid oil thrust pad is given in table 4.1.

Field equations

In order to obtain the temperature and pressure distribution for the air bearing, the nondimensional generalized Reynolds equation (4.17)-(4.18), the nondimensional energy equation (4.16), the equations for the velocities (4.19)-(4.20) and for the material properties (4.21) are to be solved simultaneously. These 14 equations represent a nonlinear equation system for the 14 unknown quantities p, $\overline{F}_0$-$\overline{F}_3$, $\overline{G}_1$-$\overline{G}_2$, T, u, v, η, k, c_P and ρ.

In principal, the calculation for the oil bearing is analogous except for the differences in the energy equation that have been pointed out in section 4.1.1. To simplify the calculation for the oil bearing, a constant oil density is assumed in this work. It can be seen from figure 4.2d that this assumption leads to accurate results if the temperature variations in the oil film are small (a variation of $10K$ means a 1% change in the density).

Boundary conditions

Figure 4.3 shows the calculation domains and the boundary conditions for the generalized Reynolds equation and the energy equation. Identical boundary conditions are applied to the air and the oil film. The fluid enters the pad with a temperature of $T = T_{in} = 100°C$. Due to the adiabatic boundary condition, the heat flux to the rotor disk and the top foil is zero. For the remaining three boundaries a free outlet condition is applied (the heat flux over the boundary is equal to the convective heat flux). The ambient pressure p_0 is used as boundary condition for the pressure. Note that in case of the oil bearing, the density is assumed to

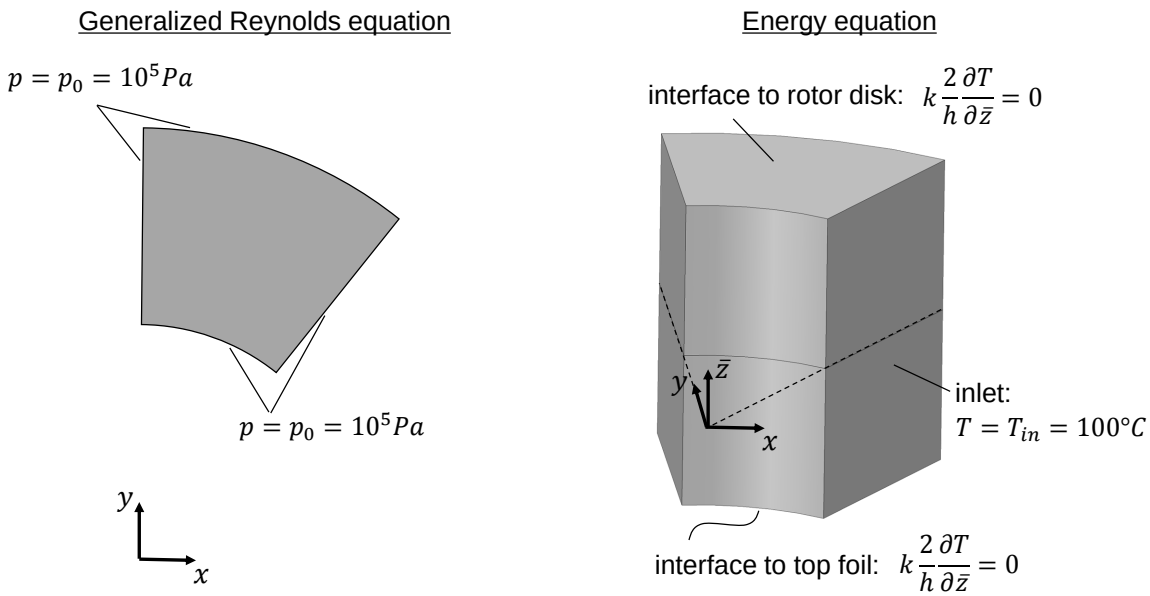

Figure 4.3: Boundary conditions for the oil and the air film.

be constant $\rho_{oil} = \rho_{oil}(T = 100°C)$.

Results

The calculation results for the oil thrust bearing and the air thrust bearing are discussed comparatively on the basis of figures 4.4 and 4.5. The first depicts the detailed temperature and pressure distribution in one pad of each thrust bearing for an angular velocity of $\Omega = 10^3 \frac{rad}{s}$. Figure 4.5 shows the load capacity (left) and the maximal temperature rise in the pad (right) as a function of the angular velocity. Several interesting conclusions can be drawn from these results.

Substitution of oil bearings by air bearings: It can be seen from figure 4.5a that for an angular velocity of $\Omega = 10^3 \frac{rad}{s}$ the load capacity of one pad is nearly $2N$ for both, the oil and the air thrust bearing. Thus, although the oil bearing is considerably smaller (outer radius $r_{oT,oil} = 7mm$) than the air bearing (outer radius $r_{oT,air} = 30mm$), both achieve a comparable load capacity. This is only possible, since the generated pressure level in the oil bearing is nearly 16 times higher than in the air bearing, see figure 4.4. This aspect of the comparison clearly reveals the extremely low load capacity to be a severe drawback of air bearings. A designer of a turbomachinery system who wants to replace oil bearings by air bearings in order to get the benefit of an oil-free system is therefore mainly concerned with a central question: What is the ratio of outer radii between the substituting air bearings and the currently used oil bearings? An answer of this question in terms of a rule of thumb can be given by the following calculation.

It has been seen in chapter 2 that the dimensionless load capacity $\overline{W} = \frac{W}{p_0 A_{pad}}$ of one pad of an oil thrust bearing is directly proportional to the compressibility number $\Lambda = \frac{6\eta\Omega}{p_0}\frac{r_{oT}^2}{h_2^2}$. Assuming this proportionality as well for an air thrust bearing, which holds approximately for low to moderate compressibility numbers (see for example figure 2.3), we get for a cylindrically sector-shaped pad with a taper land gap function

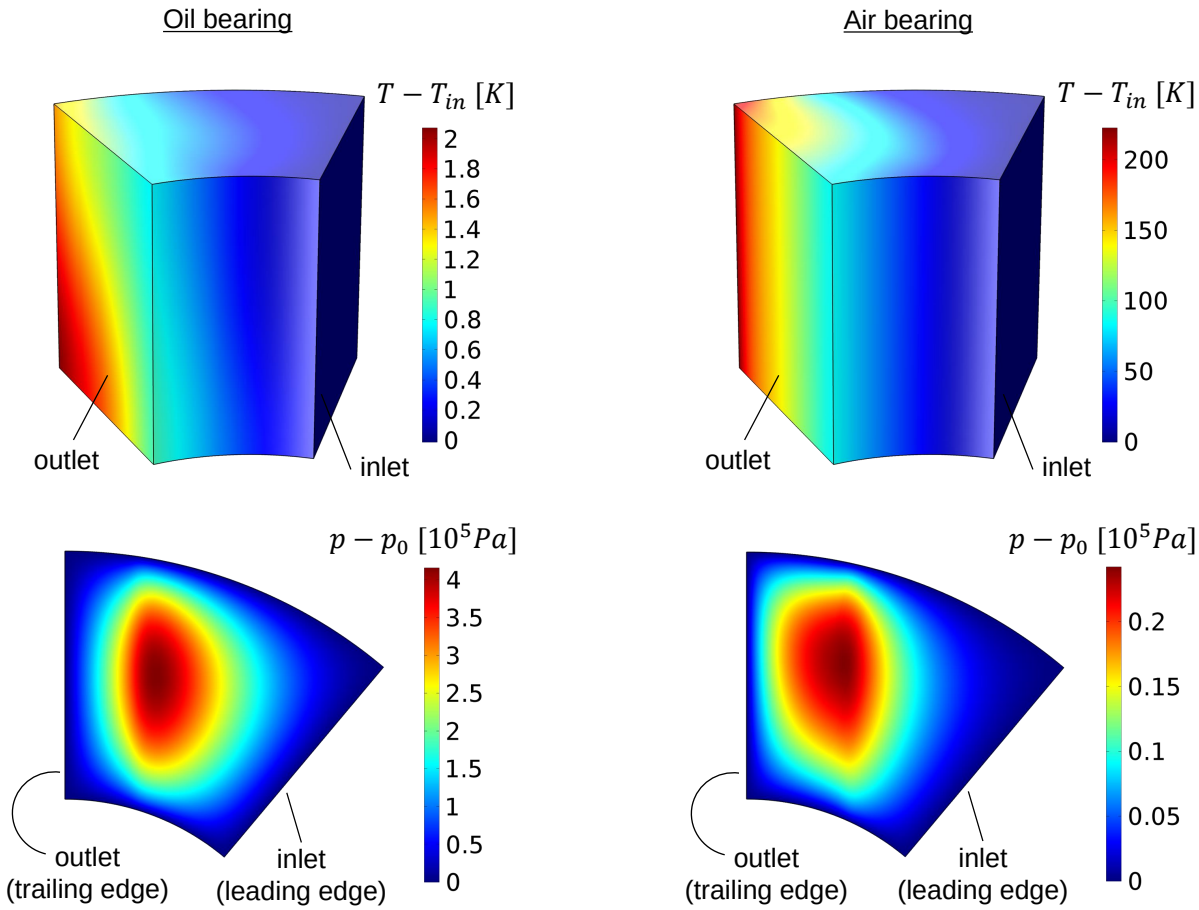

Figure 4.4: Temperature and pressure distribution in the adiabatic oil (left column) and air pad (right column) for an angular velocity of $\Omega = 10^3 \frac{rad}{s}$.

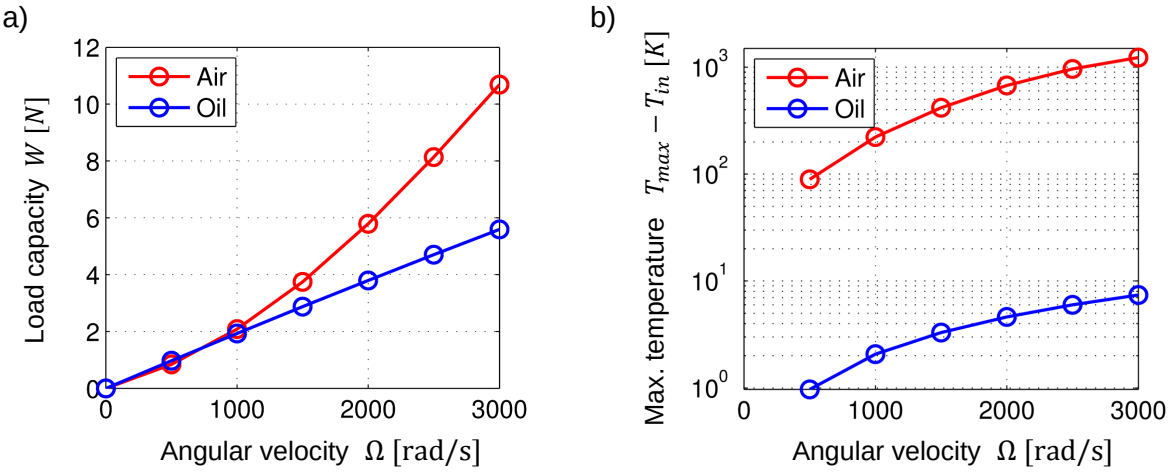

Figure 4.5: Comparison of load capacity (a) and maximal temperature rise (b) between the adiabatic oil and air pad.

$$W \propto p_0 r_{oT}^2 \overline{W} \propto p_0 r_{oT}^2 \Lambda \propto \eta \Omega \frac{r_{oT}^4}{h_2^2} \,. \tag{4.23}$$

Demanding an equal angular velocity Ω and minimal gap height h_2 for the air and the oil pad, the ratio of outer radii between the two pads is given by

$$\frac{r_{oT,air}}{r_{oT,oil}} = \left(\frac{\eta_{oil}}{\eta_{air}} \right)^{\frac{1}{4}} \,. \tag{4.24}$$

Since the dimensionless load capacity of air bearings shows a degressive behaviour for high compressibility numbers (compare figure 2.3), the derived ratio (4.24) should be regarded as a minimal value. Furthermore, due to the different viscosity levels of oils and their highly nonlinear viscosity-temperature dependence, see figure 4.2, it is not possible to give a general ratio for all applications.

In the specific case of turbochargers, which are frequently driven with the Castrol 5W-30 oil at temperatures around $100°C$, it can be concluded that the substitution of the oil thrust bearing by an air thrust bearing will lead to an approximately five times bigger rotor disk. Obviously, this ratio disqualifies air bearings as a possible bearing technology for automotive turbochargers since the corresponding inertia of the air bearing adapted turbocharger design would be too high for a good transient behaviour.

Load capacity as a function of the angular velocity: The dimensionless load capacity of thrust bearings has been shown in chapter 2 to be a degressive function of the compressibility number Λ. Since the compressibility number is proportional to the angular velocity Ω, isothermal lubrication theory predicts as well a degressive dependence of the load capacity on the angular velocity. In contrast to this, a progressive dependence of the load capacity on the angular velocity can be observed in figure 4.5a for the THD model of an air thrust bearing. The origin of this effect is to be found in the increasing viscosity-temperature relation of air, compare figure 4.2a. An increasing angular velocity enhances the dissipation in the pad leading to higher air temperatures and thus to higher viscosities. Therefore, a doubling of the angular velocity results in an increase of the compressibility number by more than the factor of two. Whether the slope of the load capacity function shows an increasing, constant or decreasing behaviour strongly depends on the heat management of the air thrust bearing. But definitely, the slope will be higher than predicted by the isothermal Reynolds equation. This fact is of relevance in load capacity measurements where the minimal film height is constant and the compressibility number is only affected by the dynamic viscosity and the angular velocity.

Differences in heat transfer between oil and air bearings: Figure 4.4 shows some qualitatively similar features for the temperature distribution in the lubricating gap of the adiabatic oil and air thrust pad. A continuous temperature rise is observed from the inlet to the outlet surface. Furthermore, both pads show significantly higher temperatures at the outer radius in comparison to the inner radius due to the radial increase of the circumferential fluid velocity. Nevertheless, there are as well two significant differences between the oil and the air bearing. Firstly, it can be observed that the temperature distribution across the

fluid film height is very homogeneous for the air bearing. By contrast, the oil bearing shows a significant gradient in the $\overline{z}$-direction. This difference indicates that heat conduction across the fluid film height is far more effective for the air bearing than for the oil bearing.

Secondly, a huge discrepancy between the temperature rise in the oil and the air thrust bearing can be stated. The temperature rise in the oil bearing is at most $2°C$ whereas the air is heated up to $T-T_{in} = 223°C$ for the operating condition of $\Omega = 10^3 \frac{rad}{s}$ and $h_2 = 10\mu m$. The discrepancy is even more pronounced by figure 4.5b. It shows the maximal temperature rise in the pad as a function of the angular velocity. Here, the predicted temperatures in the air bearing are above $1000°C$ for $\Omega = 3000 \frac{rad}{s}$ which is still a moderate angular velocity for an air thrust bearing of this size. The unrealistically high temperatures of this example indicate that the heat transfer in oil and air bearings is fundamentally different. Especially, since the load capacities of both bearings and therefore as well the total dissipated heat are of comparable size in the presented comparison.

4.1.4 Magnitude of order analysis of heat fluxes

The identification of the dominant mechanisms of heat transfer in a thrust bearing has several advantages. Firstly, a reasonable reduction of the general energy equation (4.13) can be performed resulting in smaller computational times without significant loss of accuracy. Secondly, once the dominant mechanisms of heat transfer are identified, it is clear which aspects of the heat transfer are to be modeled in depth in order to improve the thermal model. Furthermore, the designer of a thrust bearing gets an idea of the most important parameters that can be optimised for a reduction of bearing temperatures. Because of these reasons and the previously found differences in the temperatures of adiabatic thrust bearings, this section is aimed to perform a magnitude of order analysis of the heat fluxes in an air and an oil thrust bearing.

The mechanisms of heat transfer, that are to be considered, are heat convection due to the fluid's motion and heat conduction (diffusion). Since the characteristic length of the fluid film in the x, y-plane is several orders of magnitude higher than the characteristic length in the z-direction across the fluid film, each of the two mechanisms of heat transfer is further subdivided in a planar and a vertical part, see equation (4.13). Without loss of generality, only the term in x-direction is representatively considered for both, the planar convection as well as the planar diffusion. The choice of a characteristic temperature T_{ref}, characteristic lengths r_{oT} and h_{ref} as well as characteristic velocities $u_{ref} = \frac{1}{2} r_{oT} \Omega$ and w_{ref} leads to the formulae

$$T = T_{ref} \widehat{T}, \qquad x = r_{oT} \widehat{x}, \qquad z = h_{ref} \widehat{z}, \qquad u = \frac{1}{2} r_{oT} \Omega \widehat{u}, \qquad w = w_{ref} \widehat{w}, \tag{4.25}$$

where $\widehat{(\cdot)}$ are dimensionless functions. Using the characteristic values ρ_{ref}, $c_{P,ref}$ and k_{ref} for the fluid

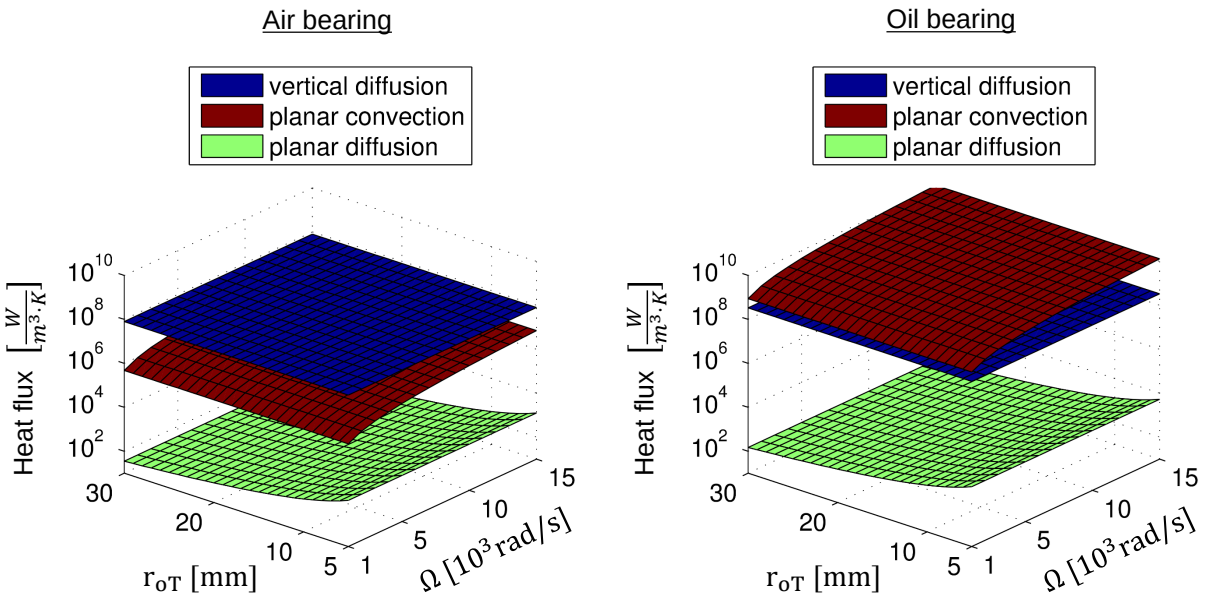

Figure 4.6: Magnitude of order analysis of different specific heat fluxes for the air film (left) and the oil film (right).

properties, the four distinct heat fluxes can be written as

$$\rho c_p u \frac{\partial T}{\partial x} \approx \frac{1}{2}\rho_{ref} c_{P,ref} \Omega T_{ref} \widehat{u} \frac{\partial \widehat{T}}{\partial \widehat{x}}, \quad \text{(planar convection)} \quad (4.26)$$

$$\rho c_p w \frac{\partial T}{\partial z} \approx \rho_{ref} c_{P,ref} \frac{w_{ref}}{h_{ref}} T_{ref} \widehat{w} \frac{\partial \widehat{T}}{\partial \widehat{z}}, \quad \text{(vertical convection)} \quad (4.27)$$

$$\frac{\partial}{\partial x}\left[k \frac{\partial T}{\partial x}\right] \approx \frac{k_{ref}}{r_{oT}^2} T_{ref} \frac{\partial^2 \widehat{T}}{\partial \widehat{x}^2}, \quad \text{(planar diffusion)} \quad (4.28)$$

$$\frac{\partial}{\partial z}\left[k \frac{\partial T}{\partial z}\right] \approx \frac{k_{ref}}{h_{ref}^2} T_{ref} \frac{\partial^2 \widehat{T}}{\partial \widehat{z}^2}. \quad \text{(vertical diffusion)} \quad (4.29)$$

The dimensionless functions $\widehat{(\cdot)}$ are of the order of unity and can be neglected therefore. The reference temperature T_{ref} is a linear factor in all four heat fluxes and does not contribute to differences in the magnitude of order between the heat fluxes. Furthermore, $w_{ref} \approx \frac{1}{2}\Omega h_{ref}$ can be shown to hold from a similar analysis of the continuity equation (1.1). Inserting this expression in equation (4.27) shows that the vertical convection is of the same order as the planar convection. Therefore, only three expressions have to be compared

$$\frac{1}{2}\rho_{ref} c_{P,ref} \Omega, \quad \text{(planar convection)} \quad (4.30)$$

$$\frac{k_{ref}}{r_{oT}^2}, \quad \text{(planar diffusion)} \quad (4.31)$$

$$\frac{k_{ref}}{h_{ref}^2}. \quad \text{(vertical diffusion)} \quad (4.32)$$

Since the fluid properties in these expressions vary at most by the factor of two, compare figure 4.2, they can be considered to be constant in the sense of a magnitude of order analysis. Concretely, the values for a temperature of $T = 100°C$ are used. Figure 4.6 shows a comparison of the expressions (4.30)-(4.32) for

a reference gap height of $h_{ref} = 20\mu m$. Each expression is plotted as a function of the outer radius r_{oT} and the angular velocity Ω. Several conclusions for the thermal behaviour of air and oil thrust bearings can be drawn.

Firstly, it can be clearly seen that planar diffusion is several magnitudes of order smaller than the other two heat fluxes. Consequently, this heat flux has been neglected in the final energy equation (4.14) without loss of accuracy.

Secondly, the ratio between vertical diffusion and planar convection is completely different for oil and air bearings. In case of oil bearings, the planar convection dominates over the vertical diffusion. By contrast, for air bearings the convective heat transport by the motion of the fluid is two to three magnitudes of order smaller than for oil bearings. Note, that this is approximately the ratio that is found in the temperatures of the previous calculations for the adiabatic thrust bearings, compare figure 4.5b. The convective heat transfer in air bearings is so small, due to the very low density of air, that even for high angular velocities the vertical diffusion is one order of magnitude higher. This clearly shows that most of the heat in an air bearing can be efficiently conducted in the direction across the fluid film. In particular, the air bearing is able to conduct a larger amount of heat by vertical diffusion than the oil bearing since the surface area of the air bearing is significantly larger for a comparable load capacity, compare section 4.1.3.

The previous considerations were limited to the heat fluxes within the fluid volume. The amount of heat that is actually conducted out of the fluid into the top foil and the rotor disk strongly depends on the thermal resistances of these components. If the thermal resistances are high or even infinite, as in the adiabatic case of section 4.1.3, the temperature level in the air thrust bearing will be high as well.

This fact clarifies the main difference in the modeling of oil and air bearings:

- For oil bearings, in most cases only the convective heat flux has to be considered in the energy equation. It is only for very slow angular velocities, or extremely small gap heights where vertical diffusion has to be taken into account additionally. Furthermore, a detailed model for the mixing behaviour in the space between two pads is of high significance in order to get correct oil inlet temperatures. Since convection dominates in oil bearings, the inlet temperature massively influences the temperature distribution in the pad.

- For air bearings, a detailed thermal model of the parts surrounding the air film is essential for a correct prediction of bearing temperatures, especially for high load conditions with small gap heights. A precise calculation of the inlet temperature is of subordinate importance since the contribution of the convective heat transfer to an effective removal of the dissipated heat is low.

4.1.5 Reduction of governing equations

The nondimensional generalized Reynolds equation consists of a two-dimensional partial differential equation for the pressure (4.17) and six integral equations (4.18). The latter are rewritten into differential equa-

tions, for example

$$\overline{F}_0(x,y) = \int_{-1}^{1} \frac{1}{\eta(x,y,\overline{z})} d\overline{z}\,, \quad \rightarrow \quad \frac{d\overline{I}_0}{d\overline{z}} = \frac{1}{\eta(x,y,\overline{z})} \quad \text{with} \quad \overline{I}_0(\overline{z}=1) = \overline{F}_0(x,y)\,, \tag{4.33}$$

which are solved analogously to the energy equation on the 3D-nondimensional domain of the lubricating gap, compare figure 4.3. The calculation of the pressure and temperature field in the fluid of a thrust bearing implies therefore the

- discretisation of one 2D pressure equation,
- discretisation of six 3D integral equations,
- discretisation of one 3D energy equation,
- discretisation of one 3D continuity equation for the velocity component w, if the vertical convection is accounted for in the energy equation.

Especially, the six integral equations considerably increase the size of the calculation problem. Because of this reason, various attempts have been made in the literature in order to reduce the calculation time [Elr89, MK07, Mor05, Fen09, MLS16]. The main idea of these approaches is to interpolate the 3D viscosity and density fields in the $\overline{z}$-direction by polynomials. Such an approximation enables the derivation of analytical expressions for the six integral equations (4.18) which can be then inserted in the differential equation for the pressure (4.17). Due to several advantages [MK07], Legendre-polynomials P_i are frequently used in combination with Lobatto-points for the interpolation of the viscosity and density field. For example, Legendre-polynomials are orthogonal

$$\int_{-1}^{1} P_i(\overline{z}) P_j(\overline{z}) d\overline{z} = 0 \quad \text{for} \quad i \neq j\,, \tag{4.34}$$

a property that considerably simplifies the analytical expressions for the integral equations (4.18). Note, that the concrete coordinate transformation (4.15) has been chosen in order to be able to use a reduction approach on the basis of Legendre-polynomials. Detailed studies on the accuracy and computational efficiency of different polynomial reduction approaches have been performed and published in [MLS16]. The results are not repeated in detail, but the main conclusion is given.

For air thrust bearings, it was found that an interpolation of the viscosity and density field by a polynomial of zeroth order already leads to accurate results. In this reduction approach, the viscosity and density are both constant along the $\overline{z}$-direction and are therefore only functions of a two-dimensional temperature field $T_m(x,y)$. Since this field is calculated by

$$T_m(x,y) = \frac{1}{-h(x,y)} \int_{h}^{0} T(x,y,z) dz = \int_{-1}^{1} \frac{1}{2} T(x,y,\overline{z}) d\overline{z}\,, \tag{4.35}$$

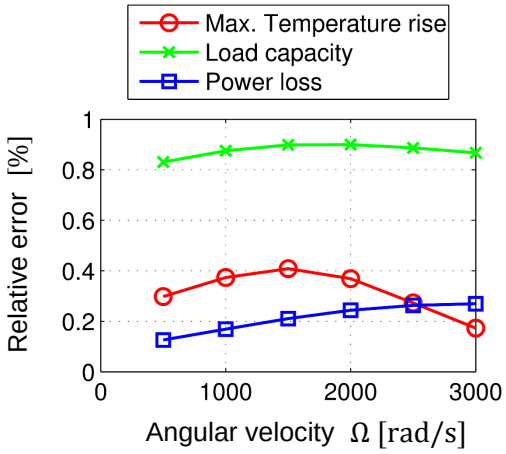

Figure 4.7: Relative error between the predictions of the generalized Reynolds equation and the averaging approach.

the reduction is called *averaging approach*. The two-dimensional viscosity and density fields enable an analytical calculation of the integral equations (4.18) resulting in a considerably simplified Reynolds equation (1.20). Figure 4.7 illustrates the accuracy of the averaging approach for the adiabatic thrust bearing of section 4.1.3. The relative error (for example in the load capacity)

$$\frac{|W_{generalized} - W_{average}|}{W_{generalized}} \tag{4.36}$$

is plotted as a function of the angular velocity. It can be clearly seen that the accuracy is within 1% for the maximal temperature rise, the power loss and the load capacity. The reason for this high accuracy lies in the relatively weak temperature dependence of the dynamic viscosity and density of air, compare figure 4.2. For example, a temperature variation of $20K$ along the $\overline{z}$-direction leads to a variation of only 4% in the air's dynamic viscosity (based on a reference temperature of $T = 100°C$). For oil, the same temperature variation leads to a 50% change in the dynamic viscosity. It is because of this, that the averaging approach can result in relative errors above 10% and is therefore not accurate enough for oil bearings, see [MLS16].

The same line of argumentation can be applied for the neglect of the vertical convection term in the derivation of an appropriate energy equation (4.14) for air bearings. Firstly, it should be noted that in contrast to the other terms in the energy equation, the vertical convection does not contribute to a removal of heat from the lubricating gap since the fluid can not leave the gap in the $\overline{z}$-direction. Therefore, the vertical convection term only influences the temperature distribution in the $\overline{z}$-direction. Several arguments show that the temperature variations across the fluid film induced by the vertical convection have a negligible influence on the pressure distribution of an air thrust bearing. Firstly, the magnitude of order analysis of section 4.1.4 proved that the convection terms are at least one order of magnitude smaller than the vertical diffusion in the air bearing. Thus, the temperature variations resulting from the vertical convection are small anyway. Secondly, as described above, the temperature variations have only a small influence on the dynamic viscosity and density of air due to the relatively weak temperature dependence of these properties.

Again, for oil bearings, both arguments do not hold. On the one hand side, convection has been shown to be the dominant mechanism of heat transfer for oil bearings. On the other hand, the oil's dynamic viscosity shows a strong nonlinear temperature dependence. Therefore, calculations accounting for the vertical convection term in the energy equation show considerable differences for oil bearings but not for air bearings.

Summarising, it could be shown that the averaging approach is an appropriate reduction approach and that the vertical convection term can be neglected for air bearings. Therefore, the simplified approach for the calculation of the pressure and temperature field in the air film of a thrust bearing implies the

- discretisation of one 2D pressure equation,
- discretisation of one 3D energy equation,
- discretisation of one 3D integral equation for the averaged temperature field $T_m(x, y)$.

Compared to the discretisation effort of the unreduced approach (generalized Reynolds equation and full energy equation), it is obvious that the averaging approach in combination with the neglect of the vertical convection term leads to a considerably simplified system of equations without a significant loss of accuracy.

Therefore, for the rest of this work, the simplified Reynolds equation (1.20), the integral equation (4.35) and the energy equation (4.16) are used in combination with the constitutive equations (4.21) and the simplified fluid velocities

$$u(\overline{z}) = -\frac{h^2}{8\eta}\frac{\partial p}{\partial x}[1-\overline{z}^2] + \frac{U}{2}(\overline{z}+1)\,, \tag{4.37}$$

$$v(\overline{z}) = -\frac{h^2}{8\eta}\frac{\partial p}{\partial y}[1-\overline{z}^2] + \frac{V}{2}(\overline{z}+1) \tag{4.38}$$

as a set of equations for the calculation of the pressure and the temperature field in the lubricating gap of an air thrust bearing.

4.2 Thermal modeling of the heat fluxes in an AFTB

The previous section put a focus on the field equations that are necessary in order to calculate the pressure and temperature distribution in the air film of an AFTB. As a side-effect, it was shown that the vertical diffusion (conduction in direction across the fluid film) is the most effective heat transfer mechanism in an air thrust bearing. This result is of extraordinary importance since it stresses the outstanding significance of accurate thermal models for the bearing components. In contrast to oil bearings, an accurate modeling of the pad's inlet temperature is far less important than accurate models for the thermal resistances of the parts that surround the air film.

The main aim of this section is therefore the development of thermal models for the relevant heat fluxes within the AFTB. To come straight to the point, this task can be far more challenging than the thermal

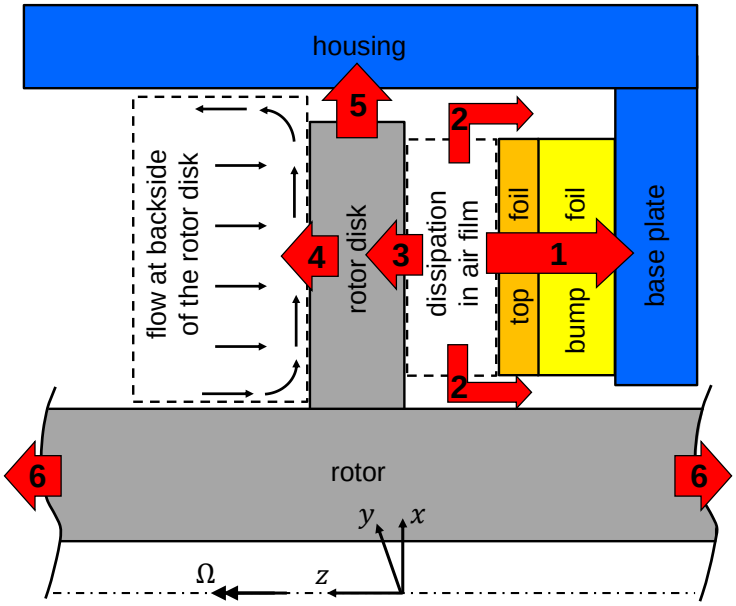

Figure 4.8: Overview of heat fluxes in the passive thermal management of an AFTB.

modeling of the air film in the last section. Particularly, it will be seen that the relative errors, that have been discussed in the context of the averaging approach for the fluid film, are negligible in comparison to the uncertanties of the thermal models for the bearing components.

An overview of the heat fluxes that are discussed in this work is schematically shown in figure 4.8. The pressure generating air film is surrounded by the rotor disk and the top foil. Due to the very small thickness of the film $(2-50\mu m)$ and the high rotational speed of the rotor, substantial viscous dissipation arises in the air film and represents the most significant heat source of the system. The removal of heat from the air film is assumed to proceed along three heat flow paths:

1. Conduction through the foil sandwich: The top foil has a negligible thermal resistance due to its small thickness of $t_T = 100-150\mu m$ and the high thermal conductivity of metals. The main thermal resistance of the foil sandwich is the bump foil. Firstly, the heat flow has to overcome the contact thermal resistance of the contact between top and bump foil as well as between bump foil and base plate. Secondly, the heat has to pass a distance of typically $400-1000\mu m$ (height of the bumps) through the small cross section of the bump foil, compare figure 1.2.

2. Mixing flow between the pads of the thrust bearing: Due to side leakage effects, the (hot air) mass flow that leaves a pad of an AFTB at the trailing edge is considerably smaller than the mass flow that enters the next pad at the leading edge. The difference is balanced by a cool inflowing air stream within the chamber between two pads. Thus, the mixing of cool and hot air in the thrust bearing chamber represents a heat exchange. Note, that the corresponding arrows (number 2) in figure 4.8 illustrate the heat that is removed by the side leakage in the pad.

3. Conduction to the rotor disk: The material of the rotor disk is typically some sort of metal (steel, titanium or even aluminium). The thermal conductivity is therefore very high resulting in a small thermal

resistance of the rotor disk. Nevertheless, due to the relatively high thickness of the rotor disk (order of millimeters) its thermal resistance is high enough to produce temperature differences of the order of some Kelvin along the z-direction. These temperature gradients are sufficient for the appearance of thermally induced deformations of the rotor disk that considerably influence the gap function of the AFTB.

The heat that is conducted from the air film to the rotor disk can leave the latter by different paths.

4. Cooling flow at the backside of the rotor disk: The high rotational speed of the rotor disk induces a cooling flow at the backside of the rotor disk. This is because the boundary layer of the disk is exposed to significant centrifugal forces which push the air outside in radial direction. Due to conservation of mass, cool air is continuously streaming (negative z-direction) into the boundary layer of the disk. For very high rotational speeds, the flow at the backside of the disk becomes turbulent and the heat exchange is even more effective for this case. But, depending on the size and the speed of the disk, the dissipation in the rotating boundary layer can turn out to be a significant heat source as well.

5. Conduction into the housing at the peripherie of the rotor disk: The radial clearance between the rotor disk and the housing is frequently of the order of $100 - 500\mu m$ for turbomachines based on AFBs. During operation, the clearance diminishes due to a centrifugal and thermal growing of the rotor disk. The resulting air gap can be tight enough in order to effectively remove heat by thermal conduction. To the same time, significant viscous dissipation can occur in the gap at the periphery representing a further heat source for the AFTB system.

6. Heat flow into or from other components of the turbomachine: Depending on the position of the thrust bearing in the assembly of the turbomachine and the concrete application, a considerable heat flow can leave the bearing through the rotor. On the other hand, if the thrust bearing is placed for example next to a turbine wheel, the whole bearing can be heated up to a far more degree as would be the case only by the dissipation in the air film of the bearing.

In this section, all of the described heat flows are subsequently modeled and discussed in detail. They represent the main components of a *passive* thermal management. *Active* thermal management by external cooling flows is not part of this work. For this subject, the interested reader is referred to [Ryu11, Ryu12, SSH01, LK11].

4.2.1 Thermal model for the top foil

The thermal model of the foil sandwich consists of two elements, the top foil and the bump foil. Figure 4.9 illustrates the thermal model for the top foil. A part of the heat, that is dissipated in the lubricating gap of the AFTB, is conducted across the air film (z-direction) into the upper surface of the top foil (heat flux $q_{T,in}$). This heat flows within the top foil to the contact lines at the bottom surface, where it leaves the top foil and enters the bump foil (heat flux $q_{T,out}$). In order to get an efficient thermal model for the top foil, several assumptions are applied:

- Analogously to the lubricating gap, the top foil has a high aspect ratio. Since its thickness of $t_T =$

$100 - 150\mu m$ is typically two orders of magnitude smaller than the lateral dimensions, the temperature variations across the top foil thickness are very small and can be neglected. Because of this assumption, a 2D energy equation can be used instead of a 3D formulation.

- The width of the contact surface between the top foil and one bump of the bump foil can be shown to be only of the order of $10\mu m$. As a consequence, the temperature distribution $T_T(x, y)$ of the top foil is not significantly affected if the contact surfaces are approximated by contact lines.
- The top foil is only exposed to a significant incoming heat flux in the region, where it faces the lubricating gap (pad angle φ_{hT}). Therefore, the thermal model of the top foil is restricted to this region. Particularly, the fixing of the top foil on the base plate is not accounted for (frequently, the distance from the leading edge to the fixing is considerably longer than the distance to the next bump foil contact line).

Under these assumptions the energy equation for the top foil is reduced to

$$\frac{\partial}{\partial x}\left[- t_T k_T \frac{\partial T_T}{\partial x}\right] + \frac{\partial}{\partial y}\left[- t_T k_T \frac{\partial T_T}{\partial y}\right] = q_{T,in} + q_{T,out}\,, \tag{4.39}$$

where T_T is the temperature and k_T the thermal conductivity of the top foil. The heat, that is conducted from the air film into the top foil, is modeled as a distributed heat source in the 2D energy equation according to

$$q_{T,in} = -\left(- k \frac{\partial T}{\partial z}\right)\Bigg|_{z=h} \tag{4.40}$$

with T being the temperature and k the thermal conductivity of the air film in the lubricating gap. The outgoing heat flux into the bump foil is given by

$$q_{T,out} = \begin{cases} -\frac{2}{R_{th}}(T_T - T_{base})\,, & \text{at the contact lines}\,, \\ 0\,, & \text{everywhere else}\,, \end{cases} \tag{4.41}$$

which means that the heat can leave the top foil only at the contact lines to the bump foil. Here, R_{th} is the effective thermal resistance per unit length of a half bump arc and can be calculated by equation (4.62). T_{base} is the temperature of the base plate.

Concerning the boundary conditions, the Dirichlet boundary condition $T_T(r) = T(r)|_{z=h}$ is applied to the leading edge of the top foil. This means, that the leading edge of the top foil is assumed to have the same temperature as the air at the inlet surface of the lubricating gap (see figure 4.1). For the remaining boundaries of the top foil, a zero heat flux condition is applied.

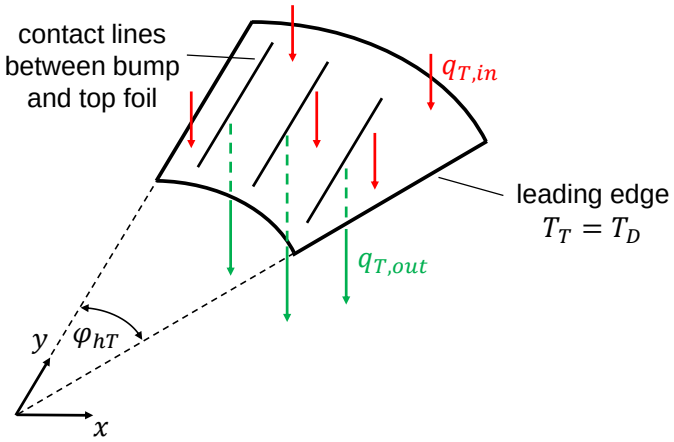

Figure 4.9: Thermal model for the top foil of an AFTB.

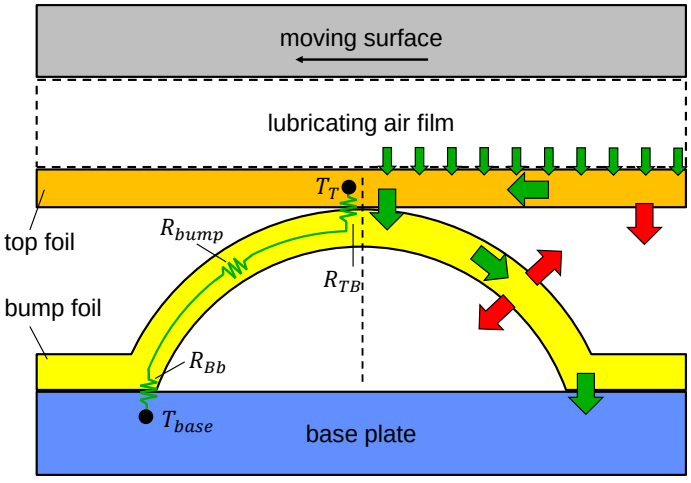

Figure 4.10: Heat flow in the foil sandwich of an AFB.

4.2.2 Thermal model for the bump foil

Figure 4.10 shows the heat transfer in the foil sandwich of an AFB. Possible heat transfer paths are illustrated by arrows in the right part of figure 4.10. The red arrows represent convective heat transfer from the foils to the channels between the foils. Hereby, natural convection can be neglected since in this case the air velocities in the channels are several magnitudes of order smaller than the velocities in the lubricating gap. By contrast, forced convection by an external cooling air flow has been shown to be an effective active thermal management technique in several experimental works [Ryu11, Dyk06]. Models accounting for forced convection in AFBs can be found for example in [SAK10, LK10].

For AFBs with a passive thermal management as considered in this work, the thermal conduction through the foils is the only heat transfer mechanism in the foil sandwich and therefore of outstanding importance. In this case the heat is conducted within the top foil to the contact between top and bump foil. On its way to the base plate, the heat flux has to pass three different thermal resistances which are illustrated in the left part of figure 4.10. The contact resistance R_{TB} between the top and the bump foil, the thermal resistance of the half bump arc R_{bump} and finally the contact resistance between the bump foil and the base plate R_{Bb}. All three can be combined to the effective thermal resistance of the half bump arc

$$R_{eff} = R_{bump} + R_{TB} + R_{Bb}\,, \tag{4.42}$$

which determines the temperature of the top foil T_T at the bump summit with respect to the temperature of the base plate T_{base} close to the contact between bump foil and base plate. It is obvious, that an accurate calculation of the thermal contact resistances is of high importance since they influence R_{eff} and therefore the predicted temperature level in the lubricating air film. In particular, the effective thermal resistance R_{eff} is an unique characteristic of AFBs in comparison to rigid type hydrodynamic fluid film bearings.

Nevertheless, there are only a few works in the literature on AFBs that put emphasis on a detailed modeling of the thermal resistance of the bump foil. Bouchehit et al. [BBSG16] present a comprehensive model for refrigerant-lubricated foil bearings. They formulate the thermal coupling conditions directly between the lubricating gap and the bearing sleeve. Effectively, this approach means a zero effective thermal resistance of the foil sandwich and therefore does not distinguish between foil and rigid type bearings. Peng and Khonsari [PK06] use a 3D energy equation for the air film but do not model the bearing components in detail. Instead, the thermal resistance of the top foil across its thickness and a convective heat transfer coefficient at the top foil's backside are implemented in the boundary condition of the lubricating air film. San Andres and Kim [SAK10] present a very comprehensive thermal model for journal AFBs. They solve only a 2D energy equation (in axial and circumferential direction) and calculate the heat flux from the air film to the rotor and the top foil by the Reynolds-Colburn analogy. The thermal contact resistances are not accounted for at all in their model and the thermal resistance of the bump arc is calculated on the basis of the bump height instead of the real length of the bump arc.

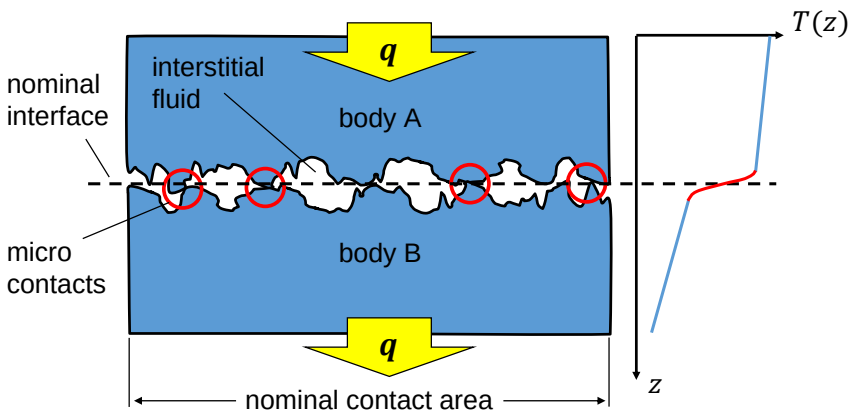

Figure 4.11: Illustration of a general thermal contact and the schematic temperature distribution within two contacting bodies.

To the knowledge of the author, the only theoretical model for the thermal contact resistances in the foil sandwich has been presented by Sim et al. [SK12]. They approximately calculate the contact surface between the bump foil and the top foil and use a formula developed by Yovanovich [Yov81] for the thermal contact resistance of conforming rough surfaces. In particular, their results show a significant dependence of the thermal contact resistances on the pressure within the lubricating air film.

Lee et al. [LK10] use a different approach in their work on the thermo-hydrodynamic analysis of air foil journal bearings. They measure the effective thermal resistance R_{eff} of the bump foil in an experiment and use a curve fit of this data for their full THD model. In a subsequent work on a THD model for AFTBs [LK11] the same authors repeated the measurement for the new bump foil design of the AFTB.

Although the approach by Lee et al. for the determination of the effective thermal resistance of the bump foil is probably the most accurate one, its deficiencies are obvious as well. Firstly, the measurement has to be repeated for every new bump foil geometry. And secondly, information about the thermal behaviour of the foil sandwich is not available in the design process of an AFB until it is actually manufactured.

In order to overcome these shortcomings, an analytical formula for the effective thermal resistance of the half bump arc R_{eff} is derived in this section. For this purpose a detailed analysis of the contact situation between bump and top foil is performed. On the basis of these results a thermal model for the heat conduction through the bump foil is proposed and sharp limits for the effective thermal resistance of half a bump arc are derived. The results are compared to the measurements carried out by Lee et al. [LK10] and the theoretical model by Sim et al. [SK12].

4.2.2.1. Analysis of contact situation

Figure 4.11 illustrates the temperature distribution of two contacting bodies A and B that are exposed to a heat flux $\mathbf{q}$. If the contacting surfaces of the bodies were absolutely smooth, the real contact area at the nominal interface would be equal to the nominal contact area resulting in a constant temperature gradient $\frac{dT}{dz}$ (assuming an identical thermal conductivity for both bodies). For real surfaces, the total contact area is

the sum of all micro-contact areas and therefore is frequently several magnitudes of order smaller than the nominal contact area. As a consequence, the resistance for the heat flux to pass the contact can be as well several magnitudes of order higher than in the case of perfectly smooth surfaces. Because of this, a steep gradient is macroscopically observed in the temperature at the interface between the contacting bodies. If the contact pressure between the two bodies is rised, macroscopic deformations of the contacting surfaces as well as elastic and plastic deformations in the micro-contacts may occur. These deformations result in a larger real contact area which implies a reduced thermal contact resistance. Additionally, the gap between the surfaces becomes closer resulting in an enhanced heat transfer through the interstitial fluid. Due to these mechanisms the thermal contact resistance of two contacting surfaces may vary in the range of several magnitudes of order [MF98, SY94]. Especially, it may be considerably higher than the thermal resistance of each of the two bodies A and B. Since there are two contacts for half a bump arc in the foil sandwich of an AFB, it is obvious that they may significantly influence the thermal behaviour of AFBs and have to be included in a thermal model.

To sum up, the thermal contact resistance is mainly influenced by the factors [YR67]:

- Contact pressure,
- surface roughness and waviness,
- deformation of contacting surfaces,
- and the interstitial fluid,

which are taken into account in the following analysis of the effective thermal resistance for the foil sandwich of an AFB.

The analysis starts with the macroscopic deformation of the contacting surfaces. Figure 4.12 shows a typical loading condition in an AFB. A hydrodynamic pressure p (assumed to be homogenous) acts on a section of the top foil with the width l_T. Due to the load, the original line contact between the top foil and the bump foil becomes a surface contact with a contact width of $2b$.

Since bump and top foil are thin metal sheets with a thickness of the order of $100\mu m$, it is frequently expected that the top foil conforms to the curvature of the bump foil resulting in a large contact width [SK12]. To verify this, a 2D plane strain analysis for the foil sandwich of figure 4.12 has been performed with a very fine finite element mesh in the contact region between bump and top foil. The geometrical parameters for the foils are chosen from reference [LK10] and are given in table 4.2.

Figure 4.13 depicts the half contact width b as a function of the homogenous pressure p. It can be clearly seen that for typical AFB pressures of approximately $1bar$ the contact width between top and bump foil is at most $10\mu m$. In particular, the calculated values are very close to the solution of Hertz for the contact between an elastic cylinder and an elastic plain surface [TG51], namely

$$b = 1.52\sqrt{\frac{p l_T R_B}{E}}\,. \tag{4.43}$$

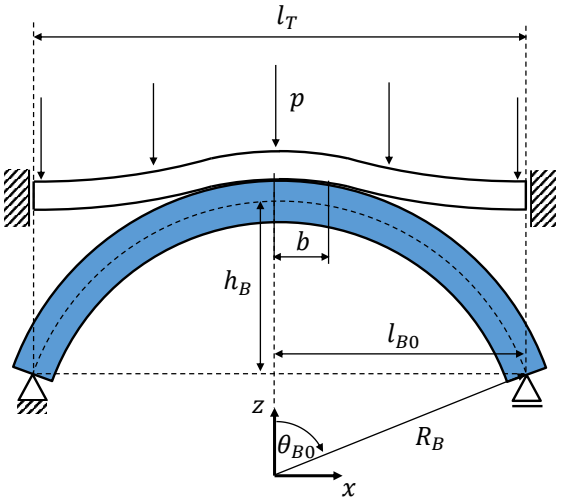

Figure 4.12: Loading condition for the foil sandwich of an AFB.

Young's modulus	E	$210GPa$
Poisson's ratio	ν	0.3
Radius of bump	R_B	$4.105mm$
Nominal bump angle	θ_{B0}	$25.7deg$
Half bump width	l_{B0}	$1.78mm$
Bump height	h_B	$0.406mm$
Bump foil thickness	t_B	$125\mu m$
Top foil thickness	t_T	$125\mu m$
Length of foils	L_B	$38.1mm$
Thermal conductivity of foils	k_B	$15\frac{W}{mK}$

Table 4.2: Geometrical and material parameters of the foils, taken from [LK10].

This indicates, that the contact width is solely determined by local deformations in the contact region and is not influenced by global deformations of the foils for hydrodynamic pressures occuring in AFBs. Furthermore, figure 4.13 shows that the contact width is two magnitudes of order smaller than calculated by Sim et al. in their model for the thermal contact resistances of the foil sandwich, see [SK12] for details.

4.2.2.2. Model for the effective thermal resistance of the bump foil

It has been mentioned previously that the main amount of the dissipated heat in an AFB is conducted across the lubricating air film into the moving surface and the top foil. In spite of the very low thermal conductivity of air, this is possible since the thickness of the air film in the lubricating gap is only of the order of $10\mu m$. The observation, that thin air films can effectively conduct the heat dissipated in AFBs, constitutes the starting point for the derivation of a formula for R_{eff}. The main idea is to not only focus on the actual contact surface and the corresponding heat conduction through the micro-contacts. Instead, the heat flux through the air film within the contact and - much more important - the heat flux through the air film close to the actual contact is taken into account as well. Figure 4.14 illustrates the modeling approach for the effective thermal resistance R_{eff} of half a bump arc. Each of the two contact resistances R_{TB} and R_{Bb} is split into two parts. $R_{(\cdot),micro}$ refers to the heat flux through the micro-contacts and $R_{(\cdot),air}$ refers to the heat flux through the

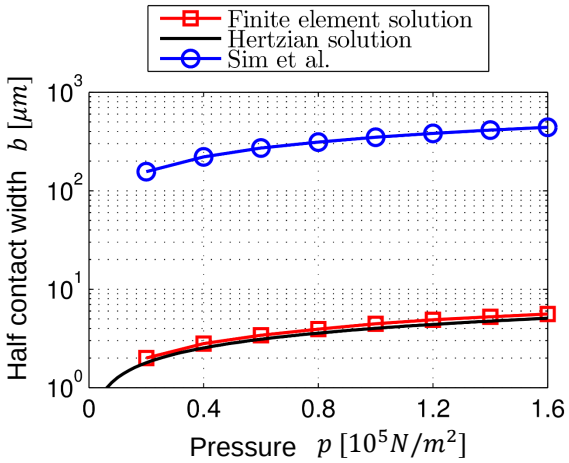

Figure 4.13: Half contact width b between top and bump foil as a function of the pressure p on the top foil.

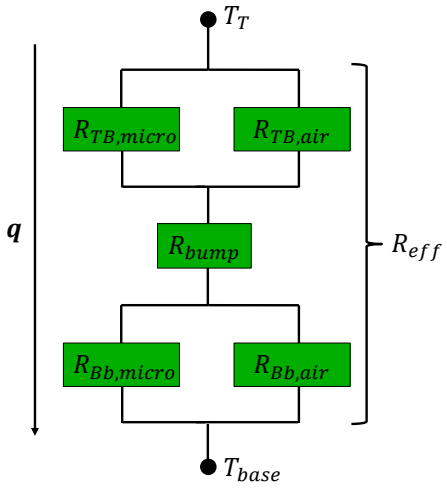

Figure 4.14: Model for the effective thermal resistance of the half bump arc.

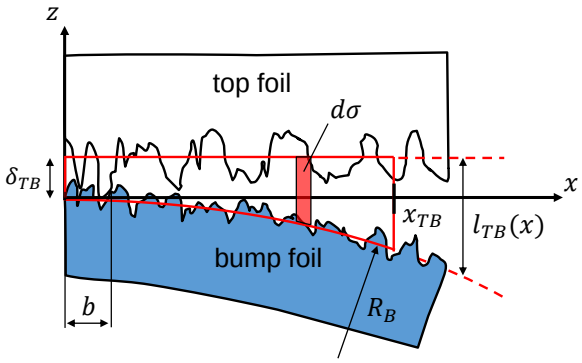

Figure 4.15: Size of the effective air gap $l_{TB}(x)$ in the interface between top and bump foil.

thin air gap in the contact region.

Calculation of $R_{TB,air}$

The interface between top and bump foil for an undeformed configuration ($p = 0$) is illustrated in figure 4.15. The effective gap function $l_{TB}(x)$, that describes the averaged thickness of the air gap in the interface between top and bump foil, can be calculated by

$$l_{TB}(x) = \delta_{TB} + \left(\sqrt{R_B^2 - x^2} - R_B\right) = \delta_{TB} + \frac{1}{2R_B}x^2 + O(x^4)\,. \tag{4.44}$$

Herein,

$$\delta_{TB} = R_{a,top} + R_{a,bump} \tag{4.45}$$

is an average distance between top and bump foil within the contact width $2b$ that is given by the sum of the average deviations $R_{a,top}$ and $R_{a,bump}$. The second term in equation (4.44) accounts for the distance between top and bump foil due to the curvature of the bump arc. In favour of a simpler analytical integration, this term is approximated by a truncated Taylor series. The thermal conductance of an infinitesimal air section is given by

$$d\sigma = \frac{k}{l_{TB}(x)} L_B dx\,, \tag{4.46}$$

where k is the thermal conductivity of air and L_B is the length of the foils in y-direction. The total conductance of the air gap in the interface between top and bump foil can be calculated by

$$\sigma_{TB,air} = \int_0^{x_{TB}} d\sigma = kL_B\sqrt{\frac{2R_B}{\delta_{TB}}} \cdot \operatorname{atan}\left(\frac{x_{TB}}{\sqrt{2\delta_{TB}R_B}}\right) \tag{4.47}$$

and thus the corresponding thermal resistance is given by

$$R_{TB,air} = \frac{1}{\sigma_{TB,air}} = \sqrt{\frac{\delta_{TB}}{2R_B}} \cdot \frac{1}{kL_B \operatorname{atan}\left(\frac{x_{TB}}{\sqrt{2\delta_{TB}R_B}}\right)}\,. \tag{4.48}$$

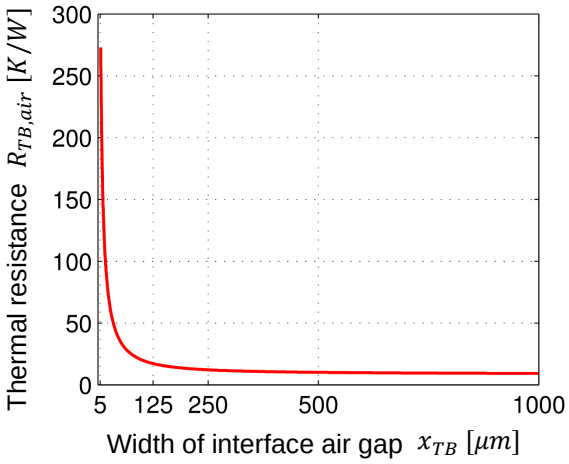

Figure 4.16: Thermal resistance of the air gap in the interface between the top foil and the half bump arc as a function of x_{TB} (half air gap width).

Figure 4.16 depicts the dependency of this thermal resistance on the integration boundary x_{TB} that represents the considered width of the interface air film ($k(75°C) = 0.0298\frac{W}{mK}$ and $R_{a,top} = R_{a,bump} = 1\mu m$). Two important conclusions can be drawn from this figure.

Firstly, it can be seen that the thermal resistance of the air within the contact surface ($x_{TB} = b \approx 5\mu m$) is very high, namely $R_{TB,air}(x_{TB} = 5\mu m) = 270\frac{K}{W}$. This proves that most of the heat, that is conducted through the air gap, does not pass the contact surface but the gap next to the contact surface ($x > b$).

Secondly, since the gap height l_{TB} increases along the x-direction, the thermal resistance $R_{TB,air}$ is found to converge against a limit value for larger values of x_{TB}. In particular, it is evident that most of the heat passes the interface air gap within a width of $x_{TB} = 250\mu m$ which equals two times the bump foil thickness, see table 4.2. Therefore, the choice of

$$x_{TB} = 2t_B \tag{4.49}$$

represents an accurate value (for typical foil sandwich geometries) to be used in equation (4.48) for the calculation of the thermal resistance $R_{TB,air}$. Since this value is still small against the length of the half bump arc

$$2t_B << R_B\theta_{B0}\,, \tag{4.50}$$

the heat flux through the air gap of the interface can be still considered to enter the bump arc very close to its summit. This justifies the serial arrangement of the two thermal resistances $R_{TB,air}$ and R_{bump} in the model of figure 4.14.

In general, the thermal resistance $R_{TB,air}$ is expected to be a function of the pressure on the top foil since the gap size $l_{TB}(x)$ reduces with increasing pressure p. However, the previously performed detailed contact analysis shows the change in the gap size to be negligibly small within the considered interface of $x < 2t_B$. This is because the stiffness of the top foil is typically designed in order to limit the maximal top foil

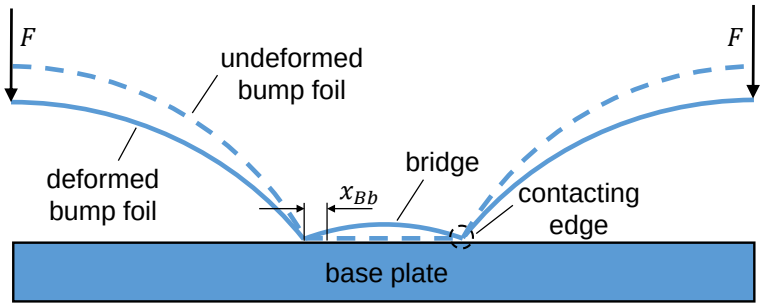

Figure 4.17: Deformation of the bridge between two bump arcs for a loaded bump foil.

sagging (at the end of the top foil at $x = \frac{1}{2}l_T$) to a few microns. A sagging of around $10\mu m$ or more would lead to a very unfavourable lubricating gap function $h(x, y)$ resulting in a low load capacity, see section 3.2. As a consequence, the thermal resistance of the air film in the interface of top and bump foil is almost independent of the load

$$R_{TB,air} \neq R_{TB,air}(p)\,. \tag{4.51}$$

Calculation of R_{bump} and $R_{Bb,air}$

The thermal resistance of the half bump arc is given by

$$R_{bump} = \frac{R_B \theta_{B0}}{L_B t_B k_B}\,, \tag{4.52}$$

where k_B is the thermal conductivity of the bump material and θ_{B0} the nominal bump angle.

Figure 4.17 illustrates the deformation for a loaded bump foil. Due to the induced bending moment by the force F, the bridge between two bump arcs bends (this bending significantly influences the stiffness of the bump foil, see section 3.1.4). The consequence of this is that the contact between the bump foil and the base plate does not take place along the whole width of the bridge. Instead, the contact is limited to the edge of the bump arc resulting in a very small contact width. Furthermore, as it is the case for the top foil, the deformations of the bridge are small in the vicinity of the contact and can be neglected for the calculation of the averaged air gap size between the bump foil and the base plate. Therefore, the air gap size $l_{Bb}(x)$ between the deformed bridge and the base plate can be calculated by

$$l_{Bb}(x) = \delta_{Bb} = R_{a,bump} + R_{a,base}\,, \tag{4.53}$$

that means $l_{Bb}(x)$ is only influenced by the surface roughness. The thermal resistance of the air gap in the interface between bump foil and base plate is then given by

$$R_{Bb,air} = \frac{\delta_{Bb}}{L_B x_{Bb} k} \tag{4.54}$$

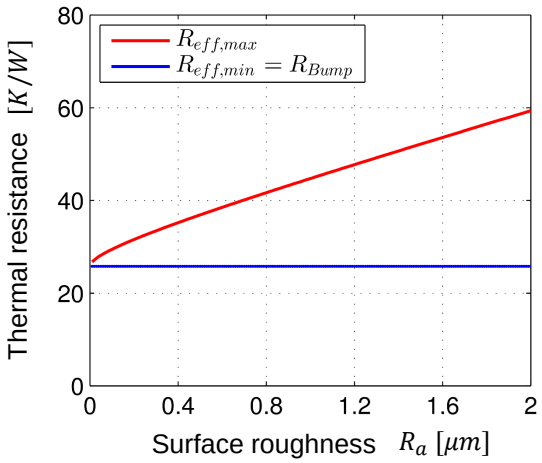

Figure 4.18: Minimal and maximal effective thermal resistance of a half bump arc as a function of the surface roughness of top foil, bump foil and base plate.

with the effective distance of heat transfer being assumed to be limited to two times the bump foil thickness

$$x_{Bb} = 2t_B \,, \tag{4.55}$$

as in case of the interface between bump foil and top foil.

Limits for the effective thermal resistance of a half bump arc

Equations (4.48), (4.52) and (4.54) enable the calculation of three of the five thermal resistances that are used in the model for the effective thermal resistance of a half bump arc, see figure 4.14. On the basis of these equations, it is possible to calculate limit values for the effective thermal resistance R_{eff}:

1. $R_{TB,micro} = R_{Bb,micro} = 0$:

   In this case the complete heat flux is conducted through the micro-contacts resulting in a minimum value for the effective thermal resistance

   $$R_{eff,min} = R_{bump} \,. \tag{4.56}$$

2. $R_{TB,micro} = R_{Bb,micro} = \infty$:

   All of the heat has to pass the thin air gaps in the interfaces. This case represents the maximum value for the effective thermal resistance

   $$R_{eff,max} = R_{bump} + R_{TB,air} + R_{Bb,air} \,. \tag{4.57}$$

Both limit cases are plotted in figure 4.18 as a function of the surface roughness of the foils and the base plate ($R_a = R_{a,top} = R_{a,bump} = R_{a,base}$).

The plot shows a remarkably small difference between the upper and the lower limit for the effective thermal resistance R_{eff} of the half bump arc. Even for a surface roughness of about $2\mu m$ the maximal possible value is only 2.5 times the minimum value. This result is to be stressed since in general the pressure dependence of a thermal contact resistance may already result in a variation of two magnitudes of order for R_{eff} [MF98, SY94]. This proves that the thin air gaps in the interfaces of the foil sandwich are able to effectively conduct most of the heat that enters the top foil from the lubricating gap.

It is obvious from figure 4.18 that the derived limits for R_{eff} are only close to each other for the condition of a small surface roughness. For AFBs this condition is fulfilled because of two reasons. Firstly, a surface roughness for the foils of $1\mu m$ or less is reported in the literature [RD02, Dyk06]. And more importantly, the bump foil of AFBs is known to perform small sliding motions relative to the top foil and the base plate during operation. These motions are the origin of the favourable damping characteristics of AFBs. A consequence of the sliding motions are very smooth surfaces in the vicinity of the contacts which are frequently observed in post-operation investigations.

4.2.2.3. Comparison to results from the literature

The presented model for the effective thermal resistance of the half bump arc is compared to the model by Sim et al. [SK12] and the measurements by Lee et al. [LK10]. Sim et al. use for both contacts - top foil to bump foil and bump foil to base plate - an approach that has been developed by Yovanovich [Yov81] for conforming rough surfaces. The formula used by Sim et al. only accounts for the heat flow through the micro-contacts. The thermal contact resistance of each of the two contacts in the foil sandwich is defined in this case by

$$R_{cont} = R_{(\cdot),micro} = \frac{1}{A_{cont} h_{cont}} \,, \tag{4.58}$$

where A_{cont} is the surface area of the contact and h_{cont} is the thermal contact conductance calculated by

$$h_{cont} = 1.25 k_{eq} \frac{m_{eq}}{\sigma_{eq}} \left(\frac{p_{cont}}{H_{mic}} \right)^{0.95} . \tag{4.59}$$

Herein, k_{eq} is the average conductivity of the two contacting bodies, m_{eq} and σ_{eq} are the equivalent absolute average slope and the standard deviation of the two contacting surfaces. H_{mic} is the micro-hardness and p_{cont} the contact pressure between the surfaces. For detailed definitions of these parameters, see [SK12]. Analogously to the approach in this work, the effective thermal resistance R_{eff} is calculated in the model by Sim et al. as the sum of the two contact resistances and the thermal resistance of the bump arc R_{bump}.

Lee et al. [LK10] do not calculate the effective thermal resistance, but measure it in an experiment. Therefore, the comparison of our model to the two aforementioned approaches is performed for the foil sandwich geometry used by Lee et al., see table 4.2.

Figure 4.19 depicts the results as a function of the homogenous pressure p on the top foil. The most striking point in the measurements by Lee et al. is that the effective thermal resistance shows only a

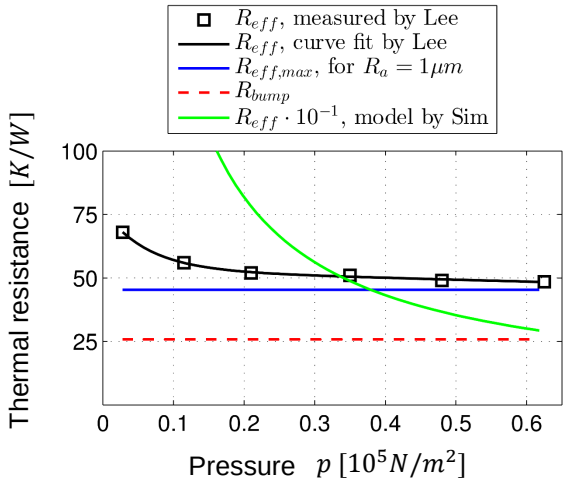

Figure 4.19: Comparison of different models for the effective thermal resistance of a half bump arc to the measurement by Lee et al. [LK10].

very weak dependency on the applied pressure. In the range between $p = 0.2 \cdot 10^5 \frac{N}{m^2}$ and $p = 0.6 \cdot 10^5 \frac{N}{m^2}$, a decrease of less than 10% is observed for R_{eff}. This characteristic behaviour is confirmed by another measurement of Lee et al. [LK11] for the foil sandwich of a thrust bearing, in which the effective thermal resistance is even found to be constant for pressures higher than $p = 0.9 \cdot 10^5 \frac{N}{m^2}$. Note, that the observed pressure dependence for small pressures $p < 0.2 \cdot 10^5 \frac{N}{m^2}$ can not be unambiguously referred to the properties of the thermal contact. This is because it is well known from stiffness measurements for foil sandwiches [Bru04, DBD+08] that the stiffness is considerably smaller for very low loads than for moderate and high loads. Since the foil sandwich is expected to show a linear behaviour for small deformations, the nonlinear stiffness behaviour is frequently referred to the phenomenon that for low pressures only some of the bumps contact the top foil. Therefore, the higher thermal resistance for low pressures observed in the measurements by Lee et al. probably can be partly referred to manufacturing inaccuracies rather than to the properties of the thermal contact.

The predictions of the model used by Sim et al. show mainly two deficiencies in comparison to the measured values by Lee et al.. Firstly, the model overestimates the effective thermal resistance by one magnitude of order (note the factor of 10^{-1} in the legend). Secondly, the model predicts a strong dependency of R_{eff} on the pressure which is not observed in the measurements.

The blue line in figure 4.19 depicts the (maximal) effective thermal resistance predicted by the model of this work. It is evident that for a reasonable surface roughness of approximately $R_a = 1\mu m$ the prediction is close to the measured values. In particular, the model shows no dependency of the (maximal) effective thermal resistance on the applied pressure which is confirmed by Lee et al..

Furthermore, a close examination of the presented results in figure 4.19 enables a further specification for the predicted value of the effective thermal resistance of the half bump arc. It has been seen that the results of the model by Sim et al. are one magnitude of order higher than the measured values (note that Sim et al. assume a very low surface roughness of $R_a = 0.1\mu m$. Higher values would lead to even

higher thermal resistances, compare equation (4.59)). Remembering that the used formulae according to Yovanovich (4.58)-(4.59) describe the thermal resistance of the micro-contacts, it follows directly that for AFBs the thermal resistance of the micro-contacts is a magnitude of order - or even more - higher than the thermal resistance of the thin air films in the interface

$$R_{(\cdot),micro} >> R_{(\cdot),air}\,. \tag{4.60}$$

Thus, case two of section 4.2.2.2 holds and most of the heat passes the thin air gaps in the interfaces because of the very high resistance of the micro-contacts. The value for the effective thermal resistance of a half bump arc is therefore more precisely given by

$$R_{eff} = \frac{1}{\frac{1}{R_{TB,micro}} + \frac{1}{R_{TB,air}}} + R_{bump} + \frac{1}{\frac{1}{R_{Bb,micro}} + \frac{1}{R_{Bb,air}}} \approx R_{TB,air} + R_{bump} + R_{Bb,air} \tag{4.61}$$

with the different terms being defined in equations (4.48), (4.52) and (4.54).

4.2.2.4. Summary and conclusions for the effective thermal resistance of the bump foil

An analytical expression has been derived for the effective thermal resistance of the bump foil in an AFB. The formula accounts for the bump foil geometry and the surface roughness of top and bump foil as well as the base plate. A detailed contact analysis between top and bump foil revealed the nominal contact width to be only around $10\mu m$ for typical loads in AFBs. The thermal resistance of the micro-contacts within the contact area was found to be far too high in order to effectively conduct the heat from the top foil into the bump summit. By contrast, the thin air gap next to the contact was identified to mainly determine the thermal contact resistance between top and bump foil. The air in this gap is thin enough, along a gap width of about two times the bump foil thickness, in order to effectively conduct the heat from the top foil into the bump arc.

The predicted effective thermal resistance by the presented formula was shown to be in good agreement to measurements from the literature. In particular, the weak dependence of the thermal contact resistance on the contact pressure, that was experimentally found for AFBs, is explained by the presented approach. Previously published models in the literature were not able to account for this behaviour but predicted a nearly linear relationship between the thermal contact conductance of the bump foil and the hydrodynamic pressure in an AFB.

The effective thermal resistance per unit length R_{th} of a half bump arc is given by

$$R_{th} = R_{eff} \cdot L_B = \frac{1}{\sigma_{TB,air}} = \sqrt{\frac{R_{a,top} + R_{a,bump}}{2R_B}} \cdot \frac{1}{k \operatorname{atan}\left(\frac{2t_B}{\sqrt{2(R_{a,top}+R_{a,bump})R_B}}\right)} + \frac{R_B \theta_{B0}}{t_B k_B} + \frac{R_{a,bump} + R_{a,base}}{2t_B k} \tag{4.62}$$

and can be used in the thermal model for the top foil in order to calculate the heat flux $q_{T,out}$ that leaves the

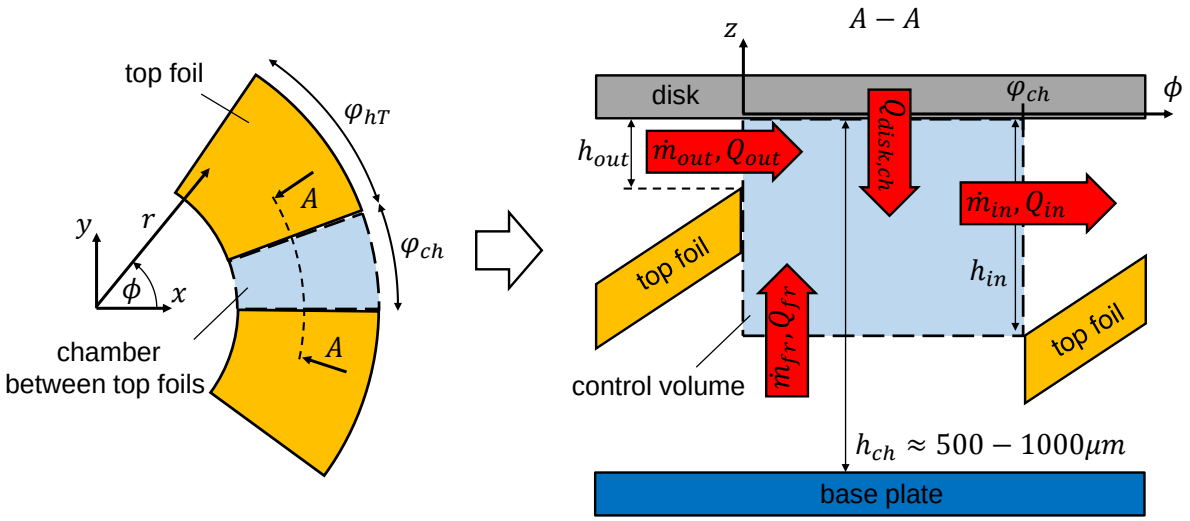

Figure 4.20: Balance of mass flow and heat fluxes in the chamber between two pads.

top foil at the contact lines to the bump foil, see equation (4.41).

4.2.3 Convective heat exchange between pads

Figure 4.20 illustrates the convective heat transfer between two pads of an AFTB. Hot air leaves the preceding lubricating gap at its outlet surface. Due to the converging shape of the lubricating gap, the film height h_{out} at the outlet surface is several times smaller than the film height h_{in} at the inlet surface of the subsequent pad. Furthermore, the existing side leakage within the preceding pad results in the outlet mass flow $\dot{m}_{out}$ being smaller than the inlet mass flow $\dot{m}_{in}$. Because of continuity, a mass flow $\dot{m}_{fr}$ with cold fluid has to enter the control volume. This mass flow is supplied by the fluid reservoir beneath the control volume which is significantly larger than the control volume due to the high height of $h_{ch} \approx 500 - 1000\mu m$ (chamber height between two pads).

For oil bearings, the convective mixing of fluid in this chamber is known to be a very important factor in the thermal management of thrust bearings. Unless detailed fluid flow simulations are performed, a widely used concept for the calculation of the inlet temperature is given by [Pin90]

$$T_{in,mix} = \frac{\dot{m}_{fr} T_{fr} + \lambda_{mix} \dot{m}_{out} T_{out}}{\dot{m}_{in}} , \tag{4.63}$$

where λ_{mix} is the hot oil carry-over factor. A value of $\lambda_{mix} = 1$ represents the case of ideal mixing between the fresh supplied fluid with the temperature T_{fr} and the hot fluid of the preceding pad.

For AFBs, this mixing approach can be found to be frequently adopted in the literature [SAK10, LK10, Fen09]. In this work, a different approach for the inlet temperature T_{in} is chosen which predicts more realistic inlet temperatures for AFTBs. Namely, the inlet temperature $T_{in}(r, z)$ is assumed to be equal to the temperature of the rotor disk

$$T_{in}(r, z) = T_D(r, z = 0) . \tag{4.64}$$

To justify this approach, a transient 1D analysis of the heat exchange between the rotor disk and the air film close to the disk is performed along the height of the control volume (z-direction). Focusing only on the thermal conduction, a transient 1D energy equation is to be solved for the temperature T_{cv} of the moving fluid in the control volume

$$\rho c_p \frac{\partial T_{cv}}{\partial t} = \frac{\partial}{\partial z}\Big[k \frac{\partial T_{cv}}{\partial z}\Big] \tag{4.65}$$

or with the definition of the thermal diffusivity $a_{diff} = \frac{k}{\rho c_p}$,

$$\frac{\partial T_{cv}}{\partial t} = a_{diff} \frac{\partial^2 T_{cv}}{\partial z^2}\,. \tag{4.66}$$

The boundary conditions for the air film within the control volume are chosen to be

$$\begin{aligned} T_{cv}(t, z = 0) &= T_D\,, \\ \frac{\partial T_{cv}}{\partial z}(t, z = -h_{in}) &= 0\,. \end{aligned} \tag{4.67}$$

The initial values are given by

$$T_{cv}(t = 0, z) = \begin{cases} T_D, & z > -h_{out}, \\ T_{fr}, & -h_{in} \leq z \leq -h_{out}. \end{cases} \tag{4.68}$$

Hereby, the initial temperature distribution corresponds to the temperature distribution of the moving fluid at the left interface of the control volume ($\phi = 0$). The heat exchange between the rotor disk and a moving fluid section, along the angular width φ_{ch} of the chamber between pads, is limited to the time period

$$t_{end} = \frac{\varphi_{ch}}{\Omega}\,, \tag{4.69}$$

if the fluid in the control volume is assumed to have nearly the angular velocity Ω of the rotor disk.

The left plot in figure 4.21 illustrates the results of the transient calculation for a typical AFTB ($h_{out} = 10\mu m$, $h_{in} = 40\mu m$, $T_D = 100°C$, $T_{fr} = 20°C$, $\varphi_{ch} = 20°$, $a_{diff}(75°C) = 2.95 \cdot 10^{-5}\frac{m^2}{s}$). It is evident that the time period, which the air film needs to pass the chamber between the pads, is sufficient for the disk to heat up the complete air film section. Even for a very high angular velocity of $\Omega = 10^4 \frac{rad}{s}$, the coldest point at the inlet of the subsequent pad has a temperature of more than $80°C$. This clearly shows that the inlet temperature of a pad in an AFTB is close to the temperature of the rotor disk $T_D(r)$.

Furthermore, it can be seen from figure 4.21 that the higher the bearing temperatures are, the closer is the temperature of the inlet air film to the temperature of the rotor disk. This is because the value of the thermal diffusivity a_{diff} increases resulting in a faster heating of the air film in the chamber between the pads.

Mainly two conclusions can be drawn from these results. Firstly, it is evident that the air temperature at

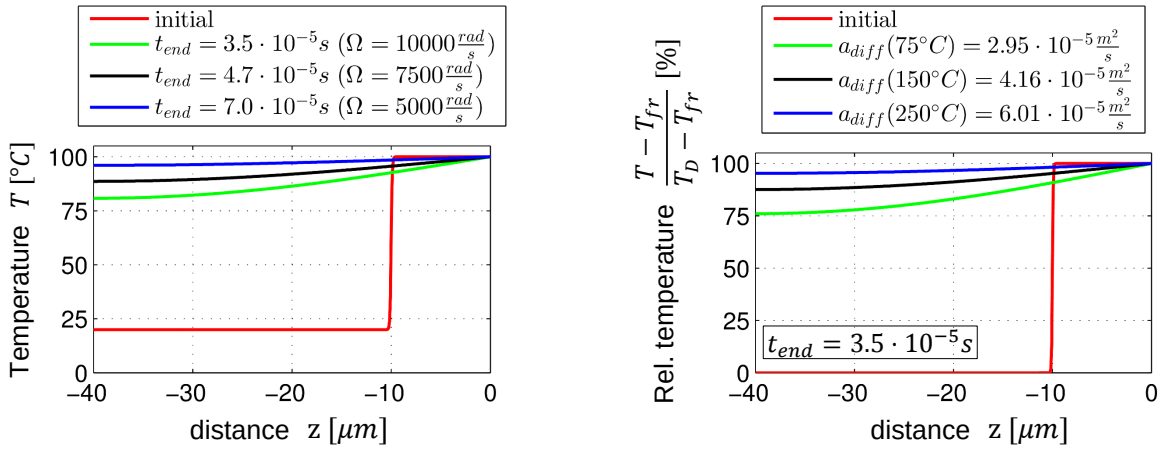

Figure 4.21: Left: Temperature distribution at the inlet of a pad for different rotor speeds Ω. Right: Relative temperature distribution at the inlet of a pad as a function of the thermal diffusivity a_{diff} for a time period of $t_{end} = 3.5 \cdot 10^{-5} s$.

the inlet of a pad can be modeled by equation (4.64). This condition represents a sensible approximation, especially since convective mixing and viscous dissipation in the control volume are additional factors that contribute to a fast heating of the air in the chamber between pads. Secondly, the heat flux $Q_{disk,ch}$ from the rotor disk to the air in the chamber between pads has to be accounted for in a THD model of an AFTB. It can be calculated by

$$Q_{disk,ch} = Q_{in} - Q_{out} - Q_{fr} \,, \tag{4.70}$$

where the heat flux and the mass flow rate for the fresh air are given by

$$\begin{aligned} Q_{fr} &= \dot{m}_{fr} c_{p,fr} T_{fr} \,, \\ \dot{m}_{fr} &= \dot{m}_{in} - \dot{m}_{out} \,. \end{aligned} \tag{4.71}$$

The mass flow rate and heat flux at the inlet surface of the pad can be calculated according to (compare figure 4.1)

$$\begin{aligned} \dot{m}_{in} &= -\iint\limits_{A_{in}} \rho (\mathbf{u} \cdot \mathbf{n}) \, dA_{in} \,, \\ Q_{in} &= -\iint\limits_{A_{in}} \rho c_p T (\mathbf{u} \cdot \mathbf{n}) \, dA_{in} \,, \end{aligned} \tag{4.72}$$

where $\mathbf{n}$ is the normal vector on the inlet surface of the pad.

4.2.4 Thermal and structural model for the rotor disk

The air film in the lubricating gap of an AFTB is confined by the top foil on the one side and the rotor disk on the other side. As has been demonstrated in section 4.1, the main amount of the dissipated heat flows into these neighbouring bearing parts due to the low convective heat transfer of the lubricating air film. Therefore, a thermal model for the rotor disk is presented in this section. Additionally, thermally induced deformations of the rotor disk are accounted for as well by an appropriate structural model.

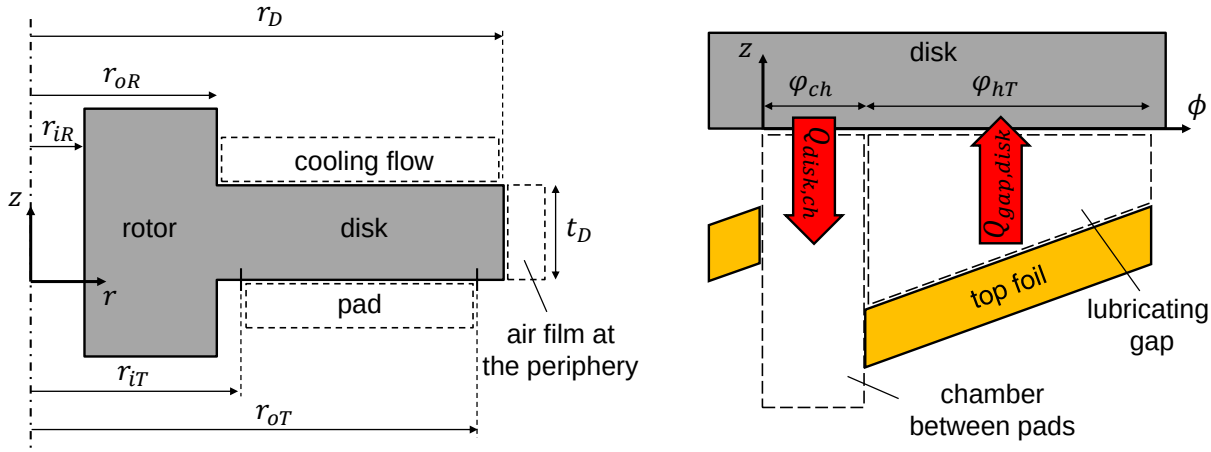

Figure 4.22: Left: Geometry of the rotor disk and the interfaces to the lubricating gap, the cooling flow at the backside of the disk and the air film at the periphery of the disk. Right: Illustration of alternating heat fluxes (circumferential direction) into the disk.

Thermal model

Figure 4.22 (left) illustrates the geometry of the rotor and the disk in the r, z-plane. In the following analysis only a part of the hollow rotor with the inner radius r_{iR} and the outer radius r_{oR} is considered. The disk has a thickness of t_D and the outer radius r_D. Typically, the top foil's radial dimensions (r_{iT} and r_{oT}) are smaller than the radial extension of the disk. Therefore, only a fraction of the disk's bottom surface is exposed to the incoming heat flux from the thrust pad. By contrast, the whole backside surface is in contact to a self-induced cooling flow.

The right part of figure 4.22 shows a cut through the disk in the ϕ, z-plane. As has been seen in the last section 4.2.3, the heat flux into the disk is of alternating character in circumferential direction. Within the lubricating gap of angular extent φ_{hT} heat is conducted from the air film into the disk ($Q_{gap,disk}$). But in the chamber between pads the heat flux $Q_{disk,ch}$ leaves the disk and heats up the inflowing fresh air. In spite of the strong variation of heat fluxes the temperature distribution in the rotor disk can be shown to be nearly constant in the circumferential direction. The reason for that is the high rotational speed of the rotor in typical applications of AFTBs.

The energy equation to be solved for the rotor and the disk yields therefore in axisymmetric coordinates

$$\frac{\partial}{\partial r}\left[k_D r \frac{\partial T_D}{\partial r}\right] + \frac{\partial}{\partial z}\left[k_D r \frac{\partial T_D}{\partial z}\right] = 0\,, \tag{4.73}$$

where k_D and T_D are the thermal conductivity and the temperature of the disk and the rotor. At the interface to the thrust pad, the boundary condition

$$\left[-k_D \frac{\partial T_D}{\partial z}\right]\Bigg|_{z=0} = q_{gap,disk}(r) - q_{disk,ch} \tag{4.74}$$

is applied. Herein,

$$q_{gap,disk}(r) = \frac{1}{r(\varphi_{ch} + \varphi_{hT})} \int\limits_{\varphi_{hT}} \left[-k\frac{\partial T}{\partial z}\right]\Bigg|_{z=0} r d\phi \tag{4.75}$$

is the averaged (along the circumferential direction) heat flux from the lubricating air film to the disk. Analogously,

$$q_{disk,ch} = \frac{E_{pad}}{\pi(r_{oT}^2 - r_{iT}^2)} Q_{disk,ch} \tag{4.76}$$

represents the averaged heat flux from the disk to the chamber between pads. Note that E_{pad} is the number of pads in the AFTB (see table 3.2) and $Q_{disk,ch}$ is calculated by equation (4.70).

The boundary condition on the interface to the cooling flow is given by

$$T_D(r, z = t_D) = T_C(r) \tag{4.77}$$

with T_C being the temperature of the cooling flow, see section 4.2.5. At the periphery of the disk

$$\left[-k_D\frac{\partial T_D}{\partial r}\right]\Bigg|_{r=r_D} = \left[-k_{per}\frac{\partial T_{per}}{\partial r}\right]\Bigg|_{r=r_D} \tag{4.78}$$

holds, where k_{per} and T_{per} are the thermal conductivity and the temperature of the air film at the periphery of the rotor disk.

In figure 4.8, thermal interactions between the rotor and other components of the turbomachine have been indicated by red arrows on the side faces of the rotor. If the heat fluxes across these faces are known, they can be accounted for by appropriate boundary conditions in the presented model. But, in order to study the main heat transfer paths in an AFTB, a vanishing interaction between the rotor and the other components of the turbomachine is assumed in this work. Therefore, the side faces (in axial direction) of the rotor as well as all other faces of the rotor and the disk, that have not been explicitly given a boundary condition in the equations above, are assumed to be thermally insulated.

Structural model

As in case of the thermal model, the deformations of the rotor and the disk are expected to be axisymmetric. The equations of equilibrium are therefore given by

$$\begin{aligned} \frac{\partial \sigma_{rr}}{\partial r} + \frac{\partial \sigma_{rz}}{\partial z} &= -f_r - \frac{\sigma_{rr} - \sigma_{\phi\phi}}{r}\,, \\ \frac{\partial \sigma_{rz}}{\partial r} + \frac{\partial \sigma_{zz}}{\partial z} &= -f_z - \frac{\sigma_{rz}}{r}\,, \end{aligned} \tag{4.79}$$

where σ_{ij} are the stresses in the rotor and the disk. Since gravitational forces can be neglected, centrifugal forces are assumed to be the only external body forces and hence $f_r = \rho_D r\Omega^2$ and $f_z = 0$ holds with ρ_D being the density of the rotor material. The components of strain (assumption of small deformations) and the constitutive equations for a linear elastic, homogeneous, isotropic material are given for example in

[NHT03, Sad05]. Inserting the components of strain in the constitutive equations yields the stresses

$$\begin{aligned}
\sigma_{rr} &= \frac{\nu_D E_D}{(1+\nu_D)(1-2\nu_D)}\left(\frac{\partial v_{rD}}{\partial r}+\frac{v_{rD}}{r}+\frac{\partial v_{zD}}{\partial z}\right)+\frac{E_D}{(1+\nu_D)}\frac{\partial v_{rD}}{\partial r}-\frac{E_D}{(1-2\nu_D)}\alpha_D\Delta T_D\,,\\
\sigma_{\phi\phi} &= \frac{\nu_D E_D}{(1+\nu_D)(1-2\nu_D)}\left(\frac{\partial v_{rD}}{\partial r}+\frac{v_{rD}}{r}+\frac{\partial v_{zD}}{\partial z}\right)+\frac{E_D}{(1+\nu_D)}\frac{v_{rD}}{r}-\frac{E_D}{(1-2\nu_D)}\alpha_D\Delta T_D\,,\\
\sigma_{zz} &= \frac{\nu_D E_D}{(1+\nu_D)(1-2\nu_D)}\left(\frac{\partial v_{rD}}{\partial r}+\frac{v_{rD}}{r}+\frac{\partial v_{zD}}{\partial z}\right)+\frac{E_D}{(1+\nu_D)}\frac{\partial v_{zD}}{\partial z}-\frac{E_D}{(1-2\nu_D)}\alpha_D\Delta T_D\,,\\
\sigma_{rz} &= \frac{E_D}{2(1+\nu_D)}\left(\frac{\partial v_{rD}}{\partial z}+\frac{\partial v_{zD}}{\partial r}\right)
\end{aligned} \tag{4.80}$$

as a function of the radial and axial displacements v_{rD}, v_{zD} and the temperature difference $\Delta T_D = T_D - T_{D,ref}$. Herein, $T_{D,ref}$ is a reference temperature, ν_D Poisson's ratio, E_D Young's modulus and α_D the thermal expansion coefficient of the rotor and the disk. Introducing equations (4.80) into equations (4.79) results in two partial differential equations for the two displacements v_{rD}, v_{zD} of the rotor and the disk. These equations are known as the Navier-Lamé equations in axisymmetric coordinates with an additional account for thermal stresses.

The applied boundary conditions at the inner radius of the rotor are specified by

$$\begin{aligned}
\sigma_{rr}(r = r_{iR}) &= -c_D v_{rD}\,,\\
\sigma_{rz}(r = r_{iR}) &= -c_D v_{zD}\,,
\end{aligned} \tag{4.81}$$

where c_D is an appropriately chosen small stiffness in order to prevent rigid body modes and have a negligible influence on the thermally induced deformations of the rotor and the disk. All other boundaries are assumed to be free of stresses.

The last assumption is not completely correct for the interface between the disk and the pad since the hydrodynamic pressure developing within the AFTB does not only act on the top foil but as well on the rotor disk. If the thickness of the disk is too small, the hydrodynamic pressure may lead to a disk deformation in the range of micrometers with a considerable impact on the real lubricating gap $h(x, y)$. But the calculation of the minimal disk thickness, that is needed in order to keep the pressure induced deformations for example below one micrometer, turns out to be very simple on the basis of the isothermal results of chapter 2. It has been shown there, that the hydrodynamic gauge pressure arising in AFTBs is at most a few times the atmospheric pressure due to compressibility effects. Furthermore, the listed data in the appendix enables the bearing designer to quickly estimate the bearing load which can be used as input for a static, uncoupled analysis of the pressure induced disk deformation. Because of these reasons, the effect of the hydrodynamic pressure on the disk deformation is of subordinate importance in the modeling of AFTBs and is therefore not considered in this work.

By contrast, the modeling of thermally induced disk deformations is of high importance for AFTB [Dyk06] because these deformations can not be significantly reduced by an increase of the disk thickness. Figure 4.23 illustrates principal modes of deformation of the rotor disk that may appear in an AFTB. As the cir-

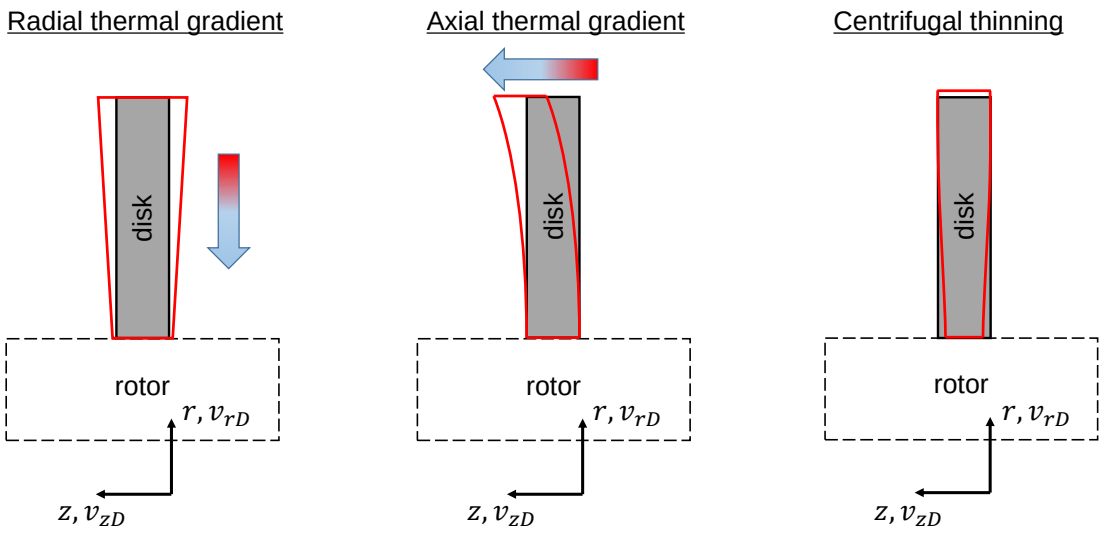

Figure 4.23: Principal modes of deformation of the rotor disk due to a radially increasing temperature (left), an axially increasing temperature (middle), and a centrifugal thinning (right).

cumferential velocity of the lubricating air rises within the pad in direction to higher radii, viscous dissipation increases as well in this direction. As a consequence, a radial thermal gradient is frequently observed in the temperature distribution resulting in an increased, axial thermal expansion of the disk for higher disk radii. A second mode of deformation has its origin in an axial thermal gradient of the disk. This gradient is needed in order to conduct the heat from the pad interface to the cooling flow interface of the disk. As a result, the deformation depicted in the middle of figure 4.23 may occur. Finally, for very high rotational speeds the centrifugal thinning of the disk is to be considered.

All three presented modes of disk deformation are captured by the thermal and structural models presented in this section. Analogously to the top foil deformations discussed for the purely elasto-hydrodynamic case in chapter 3, the disk deformations may be in the range of some micrometers. Since this magnitude is of the order of the height of the lubricating gap, the influence of the disk deformations can not be neglected. The lubricating gap function for the full thermo-elasto-hydrodynamic model (TEHD) yields therefore for an aligned configuration

$$h(x,y) = -(h_{nom} - v_{3T} + v_{zD})\,, \tag{4.82}$$

where h_{nom} is the nominal gap function, v_{3T} the top foil displacement in z-direction and v_{zD} the axial disk displacement. Analogously to equations (3.38) for the purely elasto-hydrodynamic case, the extended definition of the real gap function

$$\begin{aligned} h(x,y) &= -(h_{nom} - v_{3T} + v_{zD}) + h_{shift}\,, \\ h_{shift} &= min(h_{nom} - v_{3T} + v_{zD}) - h_{min} \end{aligned} \tag{4.83}$$

is used for the TEHD model if the minimal gap height h_{min} in the pad is prescribed, compare section 3.2.1.

4.2.5 Cooling flow at the backside of the rotor disk

A part of the heat that flows from the lubricating gap into the rotor disk leaves the latter at its backside surface. At this interface, the rotor disk faces a reservoir of air that is called the *cooling flow region* in this work, compare figure 4.24 (left). An accurate calculation of the heat flux $Q_{disk,cool}$ that flows from the disk to the cooling flow region is important because of two reasons. Firstly, the heat exchange between the rotor disk and the cooling flow region represents the second major heat path in an AFTB with a passive thermal management (in addition to the heat flux through the foil sandwich). Accurate predictions of the air film temperature in the lubricating gap are therefore only possible if this heat path is accounted for. Secondly, it should be noted that the heat flux $Q_{disk,cool}$ has to pass the rotor disk before it enters the cooling flow region. According to Fourier's law of heat conduction the size of this heat flux determines the temperature difference between the front side ($z = 0$) and the backside of the rotor disk for a given disk material. As has been discussed in section 4.2.4, an axially directed thermal gradient results in a bending of the rotor disk that may significantly influence the real lubricating gap function. The prediction of the thermally induced disk bending is therefore highly dependent on the model for the heat exchange at the backside of the rotor disk.

The main difficulty with this model is that the flow in the cooling flow region shows a considerably higher complexity than the flow in the lubricating gap of the AFTB. Since the height of the cooling flow region H_C is an order of magnitude or more higher than the lubricating gap $h(x, y)$, thin film assumptions can not be applied. Furthermore, the geometry of the cooling flow region may be very complex depending on the assembly of the turbomachine. In particular, two cases can be distinguished: Rotordynamic systems with uniformly directed thrust loads are assemblied with only one thrust bearing, see for example figure 4.8. By contrast, systems with alternating thrust loads need a thrust bearing on each side of the disk as it is shown in the configuration of figure 1.1.

For the one-sided case, the flow in the cooling flow region is of boundary layer character since no disturbing parts are apparent. For the two-sided case, the cooling flow region is bounded by the smooth disk surface on the one side and the alternating series of top foils and the chamber between pads on the other side. The result is a rotor stator cavity that can show different types of flow depending on the angular velocity of the disk, the nominal clearance between the disk and the thrust bearings, and the boundary conditions.

In this work, a boundary layer based model is used in order to calculate the heat flux from the disk to the cooling flow region. It is accurate for one-sided thrust bearings and represents a good approximation for two-sided thrust bearing configurations if the nominal clearance between the disk and the AFTBs is sufficiently high.

To understand the basic flow characteristics in the cooling flow region, this section starts with a short investigation of the flow over a single rotating disk. After that, the applied boundary layer type model for the

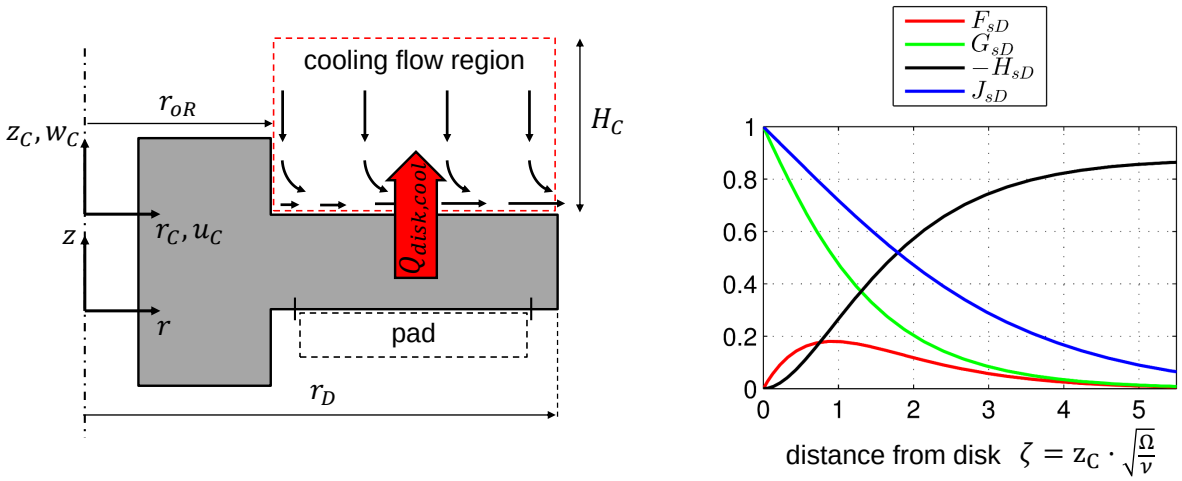

Figure 4.24: Left: Characteristic flow pattern in the cooling flow region. Right: Velocities and temperature in the laminar boundary layer over a single rotating disk.

cooling flow region is presented and fundamental effects are discussed.

Basic flow characteristics in the cooling flow region

For $r_{oR} \to 0$ the flow at the backside of the disk is equal to the flow over a single disk rotating in a quiescent fluid. In the laminar regime the ansatz

$$\begin{aligned} u_C &= r_C \Omega F_{sD}(\zeta)\,, \\ v_C &= r_C \Omega G_{sD}(\zeta)\,, \\ w_C &= \sqrt{\nu_C \Omega} H_{sD}(\zeta)\,, \\ p_C &= p_0 + \rho_C \nu_C \Omega P_{sD}(\zeta) \end{aligned} \tag{4.84}$$

turns out to be a solution to the Navier-Stokes equations without body forces [Kar21, OR89, SG97]. Herein, u_C, v_C and w_C are the radial, azimuthal and axial velocity components, p_C the pressure and ν_C, ρ_C the kinematic viscosity and density of the air in the cooling flow region. In particular, the Navier-Stokes equations are reduced by the ansatz (4.84) to a system of ordinary differential equations in the four variables F_{sD}, G_{sD}, H_{sD} and P_{sD} which are only functions of the dimensionless distance $\zeta = z_C \sqrt{\frac{\Omega}{\nu_C}}$. The boundary conditions can be expressed as

$$\begin{aligned} \zeta = 0: &\qquad F_{sD} = 0,\ G_{sD} = 1,\ H_{sD} = 0,\ P_{sD} = 0\,, \\ \zeta \to \infty: &\qquad F_{sD} = 0,\ G_{sD} = 0\,. \end{aligned} \tag{4.85}$$

Figure 4.24 (right) shows the solution for the velocity components in the laminar flow over the single disk. As to be expected, the maximal value of the azimuthal velocity occurs at the interface to the disk $u_C(\zeta = 0) = r_C \Omega$. With rising distance from the disk, the azimuthal velocity decreases and is only 1% of the disk velocity

at a distance of $z_{C,99} = 5.5\sqrt{\frac{\nu_C}{\Omega}}$ which can be regarded as the thickness of the velocity boundary layer. Since this thickness is considerably higher than the lubricating gap height $h(x, y)$, centrifugal forces are not negligible in comparison to viscous forces as it is the case for the air in the lubricating gap. A consequence of this is that the centrifugal forces induce a radially outward directed mass flow which has a velocity of up to nearly 20% ($\zeta \approx 1$) of the disk velocity. Since the radial velocity component u_C and the perimeter of the disk are directly proportional to the radius r_C, the axial velocity component w_C has to be negative because of continuity. Thus, cool air with the surrounding temperature $T_{C,ref}$ is continuously transported in negative z_C-direction to the hot disk before it leaves the latter in radial direction. This type of flow is illustrated in the left part of figure 4.24 and represents the fundamental mechanism for the convective cooling of the disk at its backside.

For the special case of an isothermal disk temperature T_D, Millsaps and Pohlhausen [MP52] used the ansatz

$$T_C = T_{C,ref} + (T_D - T_{C,ref}) \cdot J_{sD}(\zeta) \tag{4.86}$$

for the temperature distribution T_C of the cooling flow region. By this, the energy equation transforms to an ordinary differential equation in the variable $J_{sD}(\zeta)$ with the known functions F_{sD}, G_{sD} and H_{sD} as coefficients. The solution for the temperature distribution in the cooling flow region over the single disk is shown in figure 4.24 (right) for a Prandtl number of

$$Pr(75°C) = \frac{\eta_C c_{p,C}}{k_C} = 0.703\,, \tag{4.87}$$

where η_C, $c_{p,C}$ and k_C are the dynamic viscosity, the specific heat capacity and the thermal conductivity of the air in the cooling flow region. As for the azimuthal velocity component, the temperature $T_C(z_C)$ has its maximum at the disk surface and decreases with rising distance to the temperature of the surrounding $T_{C,ref}$. Note that the thermal boundary layer is thicker than the velocity boundary layer.

A measure for the cooling of the single disk by the flow over the disk is given by the heat transfer coefficient

$$\alpha_C = \frac{q_{disk,cool}}{T_D - T_{C,ref}} \tag{4.88}$$

with the heat flux from the disk to the cooling flow region being defined as

$$q_{disk,cool} = \left[-k_D \frac{\partial T_D}{\partial z}\right]\Bigg|_{z=t_D}\,. \tag{4.89}$$

A further measure, that is frequently used to characterise the convective heat transfer in rotating disk systems, is the local Nusselt number

$$Nu = \frac{\alpha_C}{k_C} r_C\,. \tag{4.90}$$

For the isothermal single disk without dissipation Millsaps and Pohlhausen [MP52] calculated the local

Nusselt number to be

$$Nu = 0.33\sqrt{Re_\Omega}\,, \tag{4.91}$$

where

$$Re_\Omega = \frac{\Omega}{\nu_C} r_C^2 \tag{4.92}$$

is the rotational Reynolds number. Thus, in the special case of an isothermal disk the heat flux $q_{disk,cool}$ is constant over the whole disk and is proportional to the square root of the angular velocity Ω.

Model for the cooling flow region

The above results for the flow over a single disk contribute to an understanding of the fundamental flow pattern in the cooling flow region of a rotating disk system. Nevertheless, several important aspects have to be accounted for in addition. Firstly, the temperature distribution in the pad of an AFTB is known to be a function of the radius. Thus, the heat flux from the disk to the cooling flow region will not be homogenous. Secondly, significant dissipation can occur at the backside of the disk for high angular velocities that may lead to considerably smaller heat transfer coefficients. And thirdly, it will be seen that for the rotational speeds in typical air foil bearing systems a transition from laminar to turbulent flow conditions may occur in the cooling flow region.

These aspects forbid the use of simple heat transfer correlations as for example given by equation (4.91). Therefore, in this work the boundary layer equations are solved in combination with a turbulence model and the energy equation for the cooling flow region. The model is coupled to the thermal model for the disk by appropriate boundary conditions.

The Reynolds-averaged boundary layer equations for an incompressible, axisymmetric flow (without radial pressure gradients) consist of the continuity equation

$$\frac{1}{r_C}\frac{\partial(r_C u_C)}{\partial r_C} + \frac{\partial w_C}{\partial z_C} = 0\,, \tag{4.93}$$

and the momentum equations in the radial and circumferential direction

$$\begin{aligned} u_C\frac{\partial u_C}{\partial r_C} + w_C\frac{\partial u_C}{\partial z_C} - \frac{v_C^2}{r_C} &= \frac{\partial}{\partial z_C}\left[\nu_C\frac{\partial u_C}{\partial z_C}\right] - \frac{1}{\rho_C}\frac{\partial}{\partial z_C}\left[\rho_C\overline{u_C' w_C'}\right], \\ u_C\frac{\partial v_C}{\partial r_C} + w_C\frac{\partial v_C}{\partial z_C} + \frac{u_C v_C}{r_C} &= \frac{\partial}{\partial z_C}\left[\nu_C\frac{\partial v_C}{\partial z_C}\right] - \frac{1}{\rho_C}\frac{\partial}{\partial z_C}\left[\rho_C\overline{v_C' w_C'}\right]. \end{aligned} \tag{4.94}$$

The last term in each of the momentum equations are the Reynolds shear stresses which are modeled by the eddy viscosity hypothesis

$$\begin{aligned} -\rho_C\overline{u_C' w_C'} &= \rho_C\nu_{CT}\frac{\partial u_C}{\partial z_C}\,, \\ -\rho_C\overline{v_C' w_C'} &= \rho_C\nu_{CT}\frac{\partial v_C}{\partial z_C} \end{aligned} \tag{4.95}$$

resulting in a set of three equations for the calculation of the flow in the cooling flow region

$$\begin{aligned}
\frac{1}{r_C}\frac{\partial(r_C u_C)}{\partial r_C} + \frac{\partial w_C}{\partial z_C} &= 0\,, \\
u_C\frac{\partial u_C}{\partial r_C} + w_C\frac{\partial u_C}{\partial z_C} - \frac{v_C^2}{r_C} &= \frac{\partial}{\partial z_C}\Big[(\nu_C + \nu_{CT})\frac{\partial u_C}{\partial z_C}\Big]\,, \\
u_C\frac{\partial v_C}{\partial r_C} + w_C\frac{\partial v_C}{\partial z_C} + \frac{u_C v_C}{r_C} &= \frac{\partial}{\partial z_C}\Big[(\nu_C + \nu_{CT})\frac{\partial v_C}{\partial z_C}\Big]\,.
\end{aligned} \tag{4.96}$$

These equations are to be solved for the boundary conditions

$$\begin{aligned}
z_C = 0: &\qquad u_C = w_C = 0\,,\; v_C = \Omega r_C\,, \\
z_C = H_C: &\qquad u_C = v_C = 0\,, \\
r_C = r_{oR}: &\qquad u_C = 0\,,\; v_C = \Big(1 - \frac{z_C}{H_C}\Big)\Omega r_C\,.
\end{aligned} \tag{4.97}$$

The turbulent viscosity ν_{CT} in the equations (4.96) is a field function and is modeled for fully developed turbulent flow conditions according to Cebeci and Smith [CS74, CA75, OO91] by

$$\nu_{CT} = \min(\nu_{CTi}, \nu_{CTo})\,. \tag{4.98}$$

Herein, ν_{CTi} is the turbulent viscosity in the inner part of the boundary layer close to the disk and ν_{CTo} is the turbulent viscosity in the outer part of the boundary layer. For the inner part, Prandtl's mixing length hypothesis is used

$$\nu_{CTi} = l_C^2\left[\Big(\frac{\partial u_C}{\partial z_C}\Big)^2 + \Big(\frac{\partial v_C}{\partial z_C}\Big)^2\right]^{0.5} \tag{4.99}$$

with

$$l_C = \kappa_C z_C\left[1 - e^{-\frac{z_C^+}{A^+}}\right], \qquad z_C^+ = \frac{z_C}{\nu_C}\sqrt{\frac{\tau_{Cs}}{\rho_C}}\,, \qquad \kappa_C = 0.4\,, \qquad A^+ = 26 \tag{4.100}$$

and the shear stress on the disk

$$\tau_{Cs} = \rho_C\nu_C\left[\Big(\frac{\partial u_C}{\partial z_C}\Big|_{z_C=0}\Big)^2 + \Big(\frac{\partial v_C}{\partial z_C}\Big|_{z_C=0}\Big)^2\right]^{0.5}. \tag{4.101}$$

The outer turbulent viscosity is modeled by

$$\nu_{CTo} = \beta_C\left|\int_0^{H_C}\Big\{\Omega r_C - \Big[u_C^2 + (\Omega r_C - v_C)^2\Big]^{0.5}\Big\}dz_C\right| \tag{4.102}$$

with

$$\beta_C = 0.0168\Big(\frac{1.55}{1+\chi_C}\Big), \qquad \chi_C = 0.55\Big[1 - e^{-(0.243\cdot O_C^{0.5} + 0.298\cdot O_C)}\Big] \tag{4.103}$$

and

$$O_C = \begin{cases} \frac{R_{C,\delta_C}}{425} - 1, & R_{C,\delta_C} > 425, \\ 0, & R_{C,\delta_C} < 425 \end{cases} \tag{4.104}$$

as well as

$$R_{C,\delta_C} = \delta_C \frac{\Omega r_C}{\nu_C}\,, \qquad \delta_C = \int_0^{H_C} \left| \frac{v_C}{\Omega r_C}\left(1 - \frac{v_C}{\Omega r_C}\right)\right| dz_C\,. \tag{4.105}$$

The definition of the turbulent viscosity, see equations (4.99) and (4.102), is based on empirical correlations for fully developed turbulent flows. In case of the single rotating disk, the laminar regime ends for a rotational Reynolds number of approximately $Re_\Omega = 2.5 \cdot 10^5$, but the flow becomes fully turbulent only for $Re_\Omega = 3.2 \cdot 10^5$. To account for the transition region, Cebeci and Smith propose to use an intermittency factor γ_{tr}. A definition of the turbulent viscosity that accounts for the laminar, transitional and turbulent flow regime is therefore given by

$$\nu_{CT} = \min(\nu_{CTi}, \nu_{CTo}) \cdot \gamma_{tr} \tag{4.106}$$

with the intermittency factor being defined as

$$\gamma_{tr} = 1 - e^{-G_C (r_C - r_{C,tr})^2}\,, \qquad G_C = 8.35 \cdot 10^{-2} \left(\frac{Re_\Omega}{r_C}\right)^2 \left(\frac{\Omega}{\nu_C} r_{C,tr}^2\right)^{-1.34}. \tag{4.107}$$

Note that the rotational Reynolds number Re_Ω is not constant over the disk but rises with the radius r_C. The transition radius $r_{C,tr}$ is defined as the radius at which the laminar region ends and the transitional flow condition begins.

The flow field in the cooling flow region can be calculated by solving the boundary layer equations (4.96) in combination with the Cebeci-Smith model for the turbulent viscosity (4.106) and the boundary conditions (4.97). In order to calculate the heat flux that leaves the disk, the energy equation

$$\frac{\partial}{\partial z_C}\left[k_{C,eff}\frac{\partial T_C}{\partial z_C}\right] = \rho_C c_{p,C}\left[u_C \frac{\partial T_C}{\partial r_C} + w_C \frac{\partial T_C}{\partial z_C}\right] - \rho_C(\nu_C + \nu_{CT})\left[\left(\frac{\partial u_C}{\partial z_C}\right)^2 + \left(\frac{\partial v_C}{\partial z_C}\right)^2\right] \tag{4.108}$$

has to be solved for the cooling flow region. Herein,

$$k_{C,eff} = \rho_C c_{p,C}\left(\frac{\nu_C}{Pr} + \frac{\nu_{CT}}{Pr_T}\right) \tag{4.109}$$

is the effective thermal conductivity and $Pr_T = 0.9$ the turbulent Prandtl number (see, [OO91]). The boundary conditions for the energy equation are

$$\begin{aligned} -k_{C,eff}\left.\frac{\partial T_C}{\partial z_C}\right|_{z_C=0} &= -k_D \left.\frac{\partial T_D}{\partial z_D}\right|_{z=t_D}\,, \\ T_C(z_C = H_C) &= T_{C,ref}\,. \end{aligned} \tag{4.110}$$

Discussion of dissipation and turbulence effects

The boundary layer equations (4.96) combined with the Cebeci-Smith turbulence model and the energy equation (4.108) are used in this work in order to predict the heat transfer at the backside of the rotor disk for an AFTB. Hereby, the model for the cooling flow region is only coupled to the other parts of the presented thermal model by the second of the boundary equations (4.110). In order to validate the implementation and to study the effect of dissipation and turbulence, the heat transfer over a single disk that is exposed to a constant heat flux is calculated and compared to the measurements by Elkins [Elk97]. Some remarks are appropriate before the results of the comparison are presented:

Elkins uses a disk with a radius of $r_D = 0.5m$ and an angular speed of up to $\Omega = 100\frac{rad}{s}$. He measures the temperature along different radii of the disk and calculates the following correlations for the heat transfer from the disk to the air

$$\begin{aligned} Nu_{laminar} &= 0.33 Re_\Omega^{0.5} && Re_\Omega \leq 2.9 \cdot 10^5\,, \\ Nu_{transition} &= 2.65 \cdot 10^{-20} Re_\Omega^{4} && 2.9 \cdot 10^5 < Re_\Omega < 3.6 \cdot 10^5\,, \\ Nu_{turbulent} &= 0.0163 Re_\Omega^{0.8} && Re_\Omega \geq 3.6 \cdot 10^5\,. \end{aligned} \tag{4.111}$$

The disk radius has been explicitly chosen to be very high in order to prevent a self-heating of the disk by dissipation, compare [CAC97]. By contrast, the disk radius in typical AFTB applications is considerably smaller enabling the appearance of significant dissipation that may lower the effective heat transfer. To study this effect, the comparison to Elkins' correlations is drawn for the small disk radius of $r_D = 31mm$ that is used in the reference AFTB of table 3.2. The angular speed is chosen to be $\Omega = 12000\frac{rad}{s}$ resulting in a maximal rotational Reynolds number of $Re_\Omega = 7.5 \cdot 10^5$. The disk is assumed to be heated by a homogenous heat flux of $q_{disk,cool} = 25 \cdot 10^3 \frac{W}{m^2}$.

Another aspect to be discussed is the beginning of the transition region. In this work, the beginning of transition is defined to occur for $Re_\Omega \approx 2.5 \cdot 10^5$. This choice is based on the average value of 25 experimental studies on the heat transfer over a single disk that are listed by Shevchuk [She09]. In Elkins' experiment, transition begins only at $Re_\Omega = 2.9 \cdot 10^5$ which he refers to the small surface roughness of his disk.

Figure 4.25 shows the comparison between the calculations on the basis of the Cebeci-Smith model and the measurements by Elkins. The three lines that are denoted by 'measurement' represent the correlations (4.111) that were obtained by Elkins for the different flow regimes. The blue line depicts the prediction of the CS-model with a deactivated dissipation term in the energy equation (4.108). It can be seen that the prediction shows a good agreement for both, the laminar and the turbulent flow regime. The width of the transition region $\Delta Re_{\Omega,transition} = 0.7 \cdot 10^5$ is as well comparable to the correlation by Elkins. Only the beginning of the transition is (by definition) different to the measurement. The red line shows the prediction if dissipation is accounted for. It can be clearly seen that the difference to the case without dissipation grows

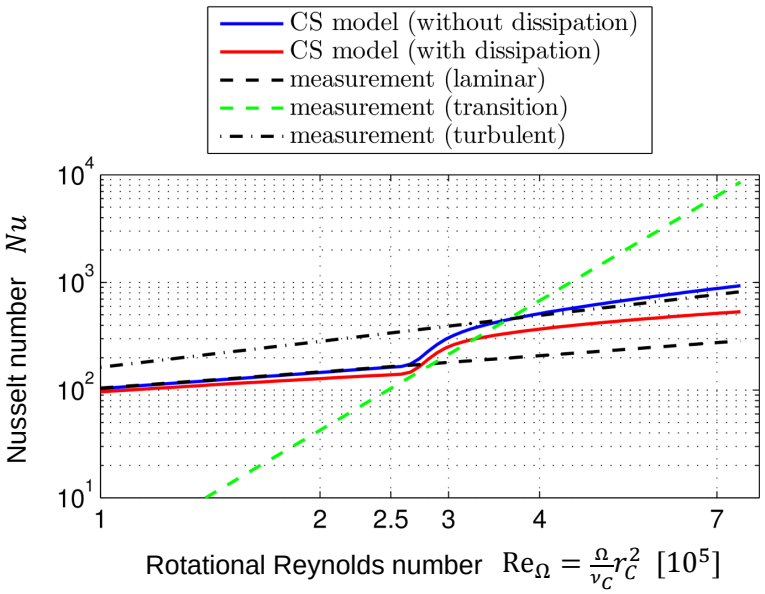

Figure 4.25: Comparison between the predictions of the Cebeci-Smith model and measurements [Elk97] for the heat transfer over a single rotating disk.

continuously with increasing rotational Reynolds number.

Figure 4.26 shows the temperature distribution as a function of the radial coordinate r_C of the disk. For the case without dissipation, a constant temperature can be observed within the laminar region ($r_C < 18mm$). This result is in accordance with the calculation by Millsaps and Pohlhausen, compare equation (4.91). At the radius of $r_C \approx 18mm$ the rotational Reynolds number reaches the critical value for the onset of transition. The heat transfer becomes far more efficient resulting in a steep gradient in the disk temperature. For $r_C > 21mm$ turbulence is fully developed. The temperature still decreases but the slope is smaller than in the transition region.

In practice, dissipation within the cooling flow region can not be neglected. It can be clearly seen that for this case the disk temperature shows a rising behaviour in the laminar region and again considerably decreases with the onset of transition. Within the turbulent region a short interval of constant temperature can be observed before the temperature rises again for higher radii up to a value of $T_D(r_D) = 95K$, which is more than twice as high as for the case without dissipation.

In summary, it can be stated that dissipation as well as turbulence have a significant influence on the heat transfer in the cooling flow region of an AFTB and can not be neglected for accurate predictions.

4.2.6 Conduction into the housing at the periphery of the rotor disk

Figure 4.27 illustrates the thermal situation at the periphery of the disk. If the thickness t_{per} of the air film between the disk and the housing is small enough, the thermal resistance of the air film at the periphery is low and the heat flux $Q_{disk,per}$ may contribute to a cooling of the AFTB. But for a too small air film thickness t_{per}, dissipation effects in the gap between the disk and the housing can occur resulting in a reduced heat

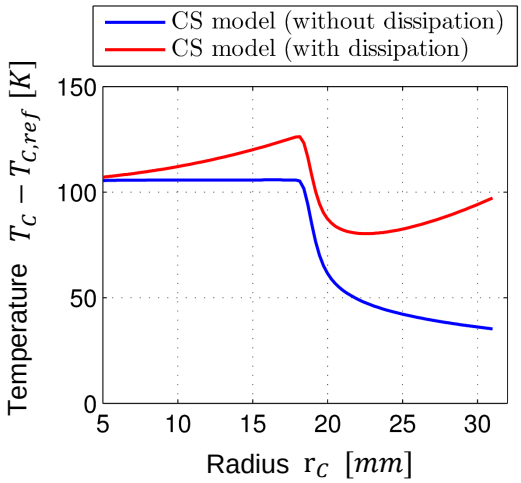

Figure 4.26: Temperature distribution of a single rotating disk that is heated by a constant heat flux of $q_{disk,cool} = 25 \cdot 10^3 \frac{W}{m^2}$ and rotates with an angular velocity of $\Omega = 12000 \frac{rad}{s}$.

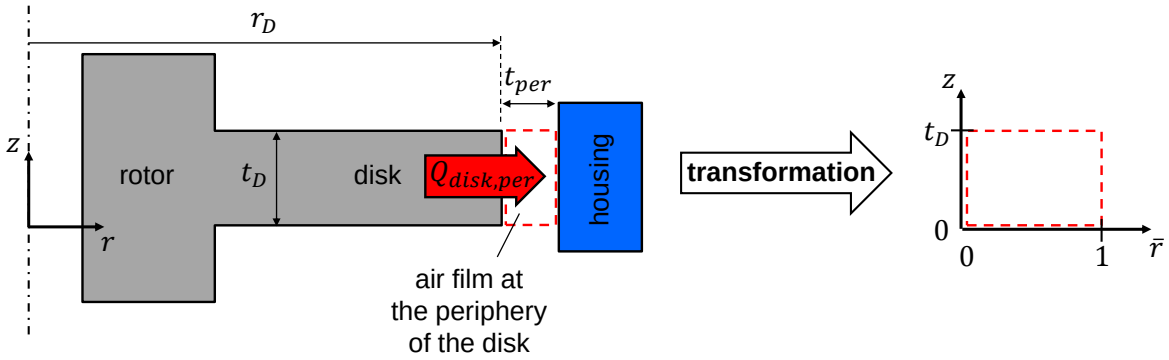

Figure 4.27: Geometry of the air gap at the periphery of the disk.

transfer at the periphery of the disk. In order to capture both effects, the energy equation

$$\frac{\partial}{\partial r}\left[k_{per} r \frac{\partial T_{per}}{\partial r}\right] + \frac{\partial}{\partial z}\left[k_{per} r \frac{\partial T_{per}}{\partial z}\right] = -r\eta_{per}\left[\frac{\Omega r_D}{t_{per}}\right]^2 \tag{4.112}$$

is solved. Herein, T_{per}, $k_{per}(T_{per})$ and $\eta_{per}(T_{per})$ are the temperature, the thermal conductivity and the dynamic viscosity of the air film at the periphery of the disk. The boundary conditions are

$$\begin{aligned} T_{per}(r = r_D) &= T_D \,, \\ T_{per}(r = r_D + t_{per}) &= T_{per,ref} \,, \\ -k_{per}\frac{\partial T_{per}}{\partial z}\bigg|_{z=0} &= -k_{per}\frac{\partial T_{per}}{\partial z}\bigg|_{z=t_D} = 0 \end{aligned} \tag{4.113}$$

with $T_{per,ref}$ being a reference temperature of the housing.

It has to be mentioned that the distance between the disk and the housing is not constant but influenced by the centrifugal and thermal growth of the disk. Both effects are included in the structural model (4.79)-

(4.80) and are captured by the radial displacement coordinate v_{rD} of the disk. Therefore, the air film thickness between the disk and the housing is calculated by

$$t_{per} = t_{per,nom} - v_{rD,ave}\,, \tag{4.114}$$

where $t_{per,nom}$ is the nominal clearance and $v_{rD,ave}$ is the radial disk growth (averaged over the disk thickness). In order to keep the width of the calculation domain constant, the coordinate transformation

$$r = r_D + \overline{r} t_{per} \tag{4.115}$$

is applied to the energy equation (4.112). This results in a dimensionless form of the energy equation

$$\frac{\partial}{\partial \overline{r}}\left[k_{per}\frac{(r_D + \overline{r}t_{per})}{t_{per}^2}\frac{\partial T_{per}}{\partial \overline{r}}\right] + \frac{\partial}{\partial z}\left[k_{per}(r_D + \overline{r}t_{per})\frac{\partial T_{per}}{\partial z}\right] = -(r_D + \overline{r}t_{per})\eta_{per}\left[\frac{\Omega r_D}{t_{per}}\right]^2, \tag{4.116}$$

that is solved on a transformed calculation domain as depicted in figure 4.27.

Air in the lubricating gap	Specific gas constant of air	R_{spec}	$287\frac{J}{kgK}$
	Minimal film height in gap	h_{min}	$5\mu m$
Bump foil	Thermal conductivity	k_B	$12\frac{W}{m\cdot K}$
	Surface roughness average	$R_{a,bump}$	$0.5\mu m$
	Foil thickness	t_B	$100\mu m$
Top foil	Thermal conductivity	k_T	$12\frac{W}{m\cdot K}$
	Surface roughness average	$R_{a,top}$	$0.5\mu m$
	Foil thickness	t_T	$150\mu m$
Base plate	Temperature	T_{base}	$20°C$
	Surface roughness average	$R_{a,base}$	$0.5\mu m$
Heat exchange between pads	Temperature of fresh air	T_{fr}	$20°C$
Cooling flow region	Reference temperature	$T_{C,ref}$	$20°C$
	Height of cooling flow region	H_C	$1mm$
Rotor and rotor disk	Young's modulus	E_D	$210GPa$
	Poisson's ratio	ν_D	0.3
	Outer rotor radius	r_{oR}	$13.5mm$
	Inner rotor radius	r_{iR}	$0.2r_{oR}$
	Disk radius	r_D	$31mm$
	Disk thickness	t_D	$4mm$
	Density	ρ_D	$8200\frac{kg}{m^2}$
	Thermal conductivity	k_D	$12\frac{W}{m\cdot K}$
	Thermal expansion coefficient	α_D	$13\cdot 10^{-6}\frac{1}{K}$
	Reference temperature	$T_{D,ref}$	$20°C$
Air in the periphery of the disk	Nominal gap	$t_{per,nom}$	$200\mu m$
	Reference temperature of housing	$T_{per,ref}$	$20°C$

Table 4.3: Parameters for the structural model of the rotor disk and all thermal models.

4.3 Simulation results for the AFTB including thermal effects

This section is intended to discuss the characteristic thermal properties of AFTBs on the basis of a thermo-elasto-hydrodynamic (TEHD) model. For this purpose, the structural model for the foil sandwich (section 3.1) is coupled to the thermo-hydrodynamic model for the air film (section 4.1) and the thermal submodels for the bearing parts (section 4.2).

Since high load conditions are of particular interest for the analysis of thermal effects, equations (4.83) are used for the real height function with a prescribed small minimal film height of $h_{min} = 5\mu m$ for all presented results. This formulation accounts for the nominal height function h_{nom}, the vertical deformation v_{3T} of the top foil and the axial deformation v_{zD} of the rotor disk.

The geometry of the foils and the nominal height function is mainly given by table 3.2 and is chosen to be nearly identical to the geometry used in the analysis for isothermal elasto-hydrodynamic conditions, see chapter 3. The only exception is made for the thickness of the foils. The thickness of the bump foil is increased from $t_B = 75\mu m$ to $t_B = 100\mu m$ and the thickness of the top foil from $t_T = 100\mu m$ to $t_T = 150\mu m$. This is done in order to reduce elastic effects from the foil sandwich, which have been already discussed in detail in section 3.2, in favour of a clear representation of thermal effects. The parameters connected with the structural model of the rotor disk and all thermal submodels are defined in table 4.3.

Every thermal model for an AFTB depends on the thermal boundary conditions at the interfaces of the thrust bearing to the other parts of the turbomachine. In the present work, these boundary conditions are

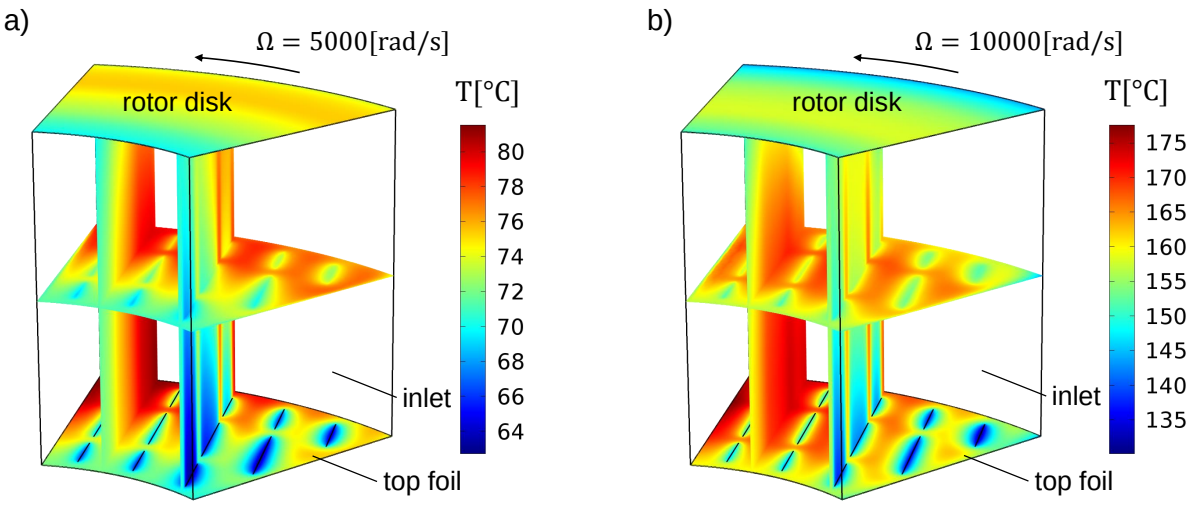

Figure 4.28: Temperature of the air film in the lubricating gap for an angular velocity of a) $\Omega = 5000 \frac{rad}{s}$ and b) $\Omega = 10000 \frac{rad}{s}$.

(compare also figure 4.8): The temperature of the base plate T_{base}, the temperature of the inflowing fresh air in the chamber between pads T_{fr}, the temperature of the cooling flow at the backside of the disk $T_{C,ref}$, as well as the temperature of the housing $T_{per,ref}$. Since it is not possible to determine these boundary conditions without solving for the thermal model of the complete turbomachine, all four temperatures are assumed to stay at the initial temperature level of $20°C$ for all considered operational conditions. The main advantage of this assumption is that the relative magnitude of the different heat fluxes in an AFTB can be clearly studied because all thermal submodels base on the same reference temperature. Experimentally, this condition can be approximately realised if the housing is provided with an efficient water cooling.

4.3.1 Characteristic temperature distribution in the lubricating air film

Figure 4.28 illustrates the 3D temperature distribution of the air film in the lubricating gap for two different angular velocities of the rotor disk. The bottom and the upper horizontal planes correspond to the temperature distribution of the top foil and the rotor disk. The vertical planes show the temperature in the space between the first and the second bumps (left) as well as directly over the third bumps, compare also figure 3.11a.

The most striking feature of figure 4.28 is that the temperature distributions in the air film at the interface to the rotor disk and the interface to the top foil are completely different. Whereas the temperature of the rotor disk is homogenous in circumferential direction, the top foil shows an alternating series of cold and hot sections in circumferential direction. This can be clearly referred to the heat transfer through the contact lines between top and bump foil. Since a forced cooling flow does not exist in the foil sandwich of a passively cooled AFTB, all the heat that enters the top foil has to flow to the lines where the top foil contacts the bump foil. This explains the local thermal gradients within the top foil that are always directed to the contact lines.

Moreover, it can be detected from the two vertical planes that the heat conduction in the vertical direction

is of alternating character within the lubricating gap. Whereas in the left vertical plane the temperature has a maximum value close to the top foil, in the right vertical plane the temperatures next to the top foil are the lowest. This indicates that in the region next to the bump contact lines most of the dissipated heat in the air film is conducted to the top foil. But in the space between two contact lines, the main part of the heat is conducted into the rotor disk.

Another characteristic property of the temperature distribution in an AFTB is the fast heating at the inlet of the lubricating gap. Due to the applied assumption for the temperature distribution at the inlet, compare section 4.2.3, the entering air has a homogenous temperature across the gap height which is identical to the temperature of the rotor disk. But the middle of the horizontal planes clearly shows that already a very small distance downstream the inlet, the temperature of the air in the middle of the lubricating gap is considerably higher than the temperature of the rotor disk. The origin of this behaviour is the very low heat capacity of air. By entering the lubricating gap at the inlet surface, the air is immediately exposed to viscous dissipation resulting in a very fast temperature rise. But the increase in temperature ends if the thermal gradient between the air film and the rotor disk (or the top foil) is high enough in order to conduct the dissipated heat across the air film height in the neighbouring bearing parts.

At the outlet surface, a reversed behaviour can be observed. Although the rotor disk and the top foil show at this surface no significant thermal gradient in circumferential direction, the temperature in the middle horizontal plane shows a sudden decrease close to the trailing edge. Since the pressure in the pad has to reduce to an ambient level in this region due to the boundary condition $p = p_0$ at the trailing edge, the ideal gas law predicts as well a sudden decrease in the density of the air film. The result of this is an expansion induced cooling of the air which is stronger pronounced at high velocities.

Besides the local phenomena at the inlet and the outlet as well as near to the bump contact lines, the temperature distribution of the air film is relatively constant in circumferential direction. This clearly indicates that the vast majority of heat is removed from the air film by conduction into the rotor disk and the top foil and not by convective heat transport.

Finally, a comparison between figure 4.28a and 4.28b reveals a different behaviour with respect to the radial temperature distribution. For the angular velocity of $\Omega = 5000 \frac{rad}{s}$, the air film, the rotor disk and the top foil show the highest temperatures close to the outer radius. This is to be expected since viscous dissipation depends on the air velocity which increases for larger radii. But for $\Omega = 10000 \frac{rad}{s}$, the highest temperatures are only observed for the top foil to be at the outer radius and shift towards smaller radii across the film thickness. Close to the rotor disk, the air film even reveals the lowest temperatures at the outer radius of the pad. This indicates a fundamental change in the thermal management of the AFTB for higher angular velocities which will be studied in section 4.3.3.

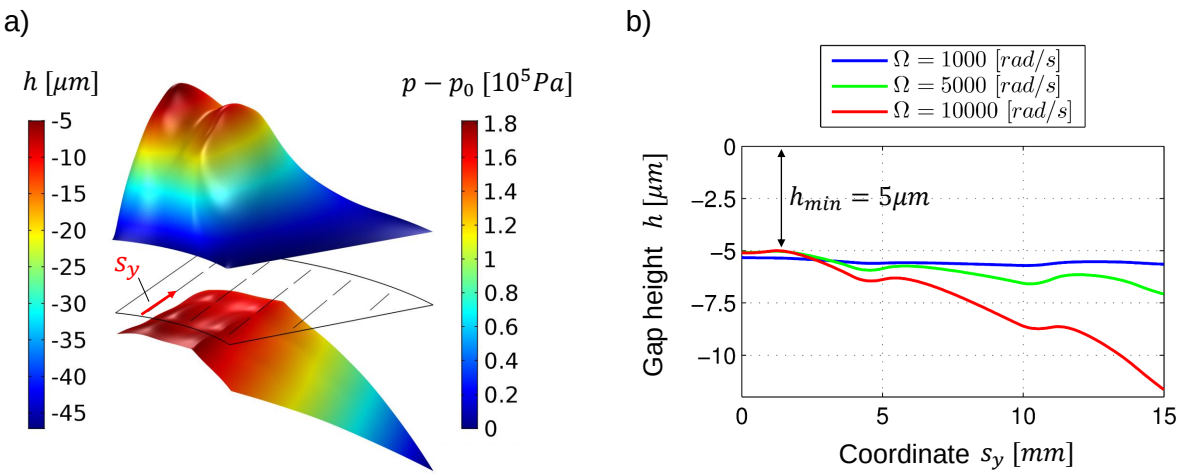

Figure 4.29: a) Pressure distribution (upper part) and height function (lower part) in the lubricating gap for an angular velocity of $\Omega = 10000\frac{rad}{s}$. b) Height function $h(x, y)$ along the direction s_y parallel to the y-axis for different angular velocities Ω, compare also figure 3.11a.

4.3.2 Thermal runaway

Figure 4.29a illustrates the pressure distribution and the height function in the lubricating gap for an angular velocity of $\Omega = 10000\frac{rad}{s}$. Despite the high top foil thickness of $t_T = 150\mu m$, top foil sagging is found to occur in the land region of the pad being the origin of the two pronounced maxima in the pressure distribution.

Another characteristic of the real height function, which can be observed in figure 4.29a, is its diverging behaviour towards the outer radius. To study this point more clearly, the real height function $h(x, y)$ is plotted along the coordinate s_y in figure 4.29b (s_y is zero at the inner top foil radius and increases towards the outer top foil radius). For a small angular velocity of $\Omega = 1000\frac{rad}{s}$ the height function is found to by nearly constant along s_y. But with increasing velocity the gap height at the outer radius becomes significantly larger than the gap height close to the inner radius. In particular, for $\Omega = 10000\frac{rad}{s}$ the distance from the top foil's outer edge to the rotor disk is nearly $12\mu m$ what is more than two times the minimal film thickness of $h_{min} = 5\mu m$ in the pad.

This effect does not originate from top or bump foil deformations and can therefore not be predicted by isothermal elasto-hydrodynamic models for AFTBs. Instead, it can be unambiguously attributed to thermally induced deformations of the rotor disk which as well have an influence on the real height function according to equation (4.83) and are illustrated by figure 4.30a. It shows a deformation plot for the rotor and the rotor disk for an angular velocity of $\Omega = 10000\frac{rad}{s}$. Note that the contour of the plot illustrates both, the axial v_{zD} and the radial displacement component v_{rD}. By contrast, the colors only illustrate the magnitude of the axial displacement component. As to be expected, centrifugal and thermal expansion of the disk material lead to a significant growth in radial direction. But the more interesting point is the observed bending of the disk in positive z-direction. Since the disk is cooled at its backside ($z = t_D$) and heated at the interface to the lubricating gap ($z = 0$), a thermal gradient is always apparent across the disk thickness, compare figure 4.32. As a consequence, the thermal expansion at the disk's front side is higher than at the disk's backside

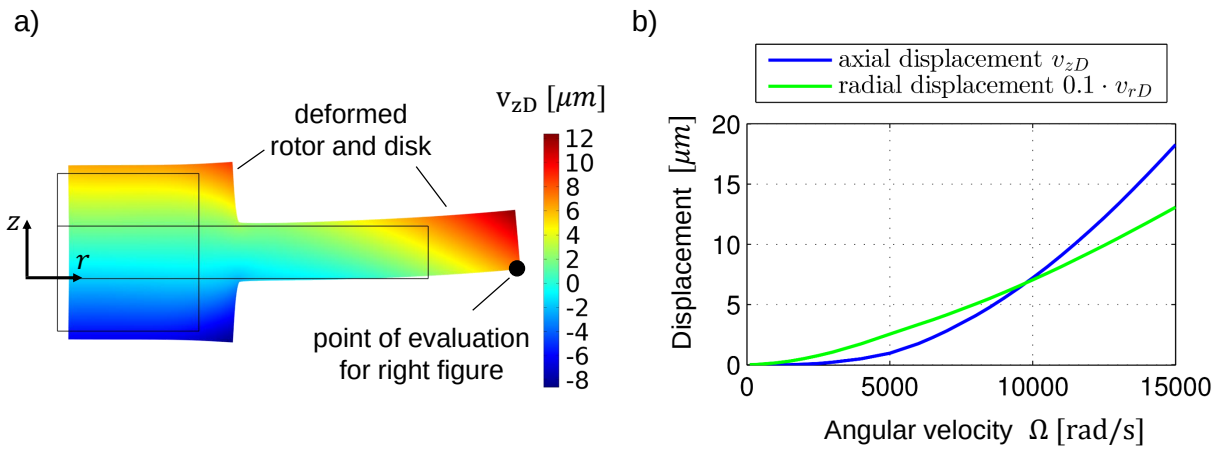

Figure 4.30: a) Deformation of rotor and disk for an angular velocity of $\Omega = 10000\frac{rad}{s}$. The color table shows the axial displacement component v_{zD}, compare figure 4.23. b) Axial and radial displacement of the disk point shown in figure 4.30a (black circle) as a function of the angular velocity Ω.

resulting in the observed bending.

The magnitude of this effect as a function of the angular velocity Ω is illustrated in figure 4.30b. It shows the axial and radial displacement for the outermost point at the front side of the disk (marked by a black circle in figure 4.30a). Although the radial displacement is approximately one magnitude of order higher than the axial displacement, the latter turns out to be the critical one because it directly affects the real gap function. Furthermore, it is found that the axial displacement component shows a highly nonlinear behaviour as a function of the angular velocity. For $\Omega = 4000\frac{rad}{s}$ the axial displacement of the disk is only $v_{zD} = 0.5\mu m$ what is small against the minimal film height $h_{min} = 5\mu m$ and therefore results in a negligible influence on the performance of the AFTB. But already for the case of $\Omega = 8000\frac{rad}{s}$, the axial displacement is found to be $v_{zD} \approx 4\mu m$ and thus in the same magnitude of order as the minimal film height.

The significant influence of the disk deformation on the performance of an AFTB is illustrated the best by figure 4.31a. It shows the predicted load capacity of one pad of the AFTB for the case with and without axial disk deformation. The curves base on identical calculations with the only exception that for the case without disk deformation the axial component v_{zD} of the disk displacement has not been accounted for in equations (4.83) for the real height function. As can be seen, both curves are nearly identical for low angular velocities below $\Omega = 5000\frac{rad}{s}$ which corresponds to the very small axial disk displacement occuring for these small speeds, compare figure 4.30b. But for higher angular velocities, a fundamental difference can be observed between the two models. Whereas the predicted load capacity without disk deformation keeps continuously increasing, a more complex model with an account for disk deformations predicts considerably lower loads which finally culminate at a maximum for $\Omega = 9500\frac{rad}{s}$. Above this critical value load capacity is even found to decrease with angular velocity. This effect is in contradiction to isothermal thin film lubrication theory but has been reported in various experiments on AFTBs [Dyk06, Dic10, Sta12].

Figure 4.31b shows exemplarily the results of Stahl [Sta12] who measured the load capacity as a function of speed for different types of AFTBs (varying in the foil geometry or the conditioning of the AFTB). The

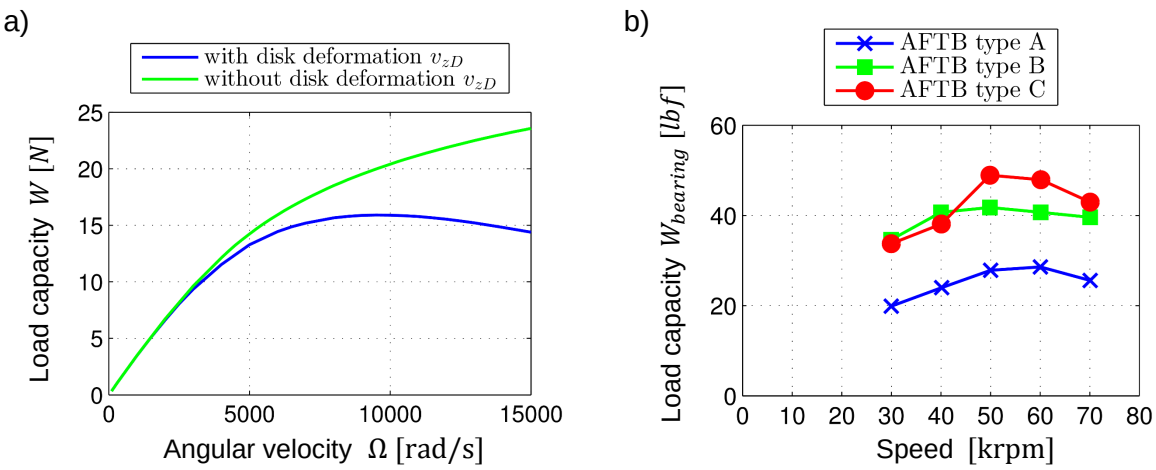

Figure 4.31: a) Comparison of the predicted load capacity (of one pad) by models including or neglecting the disk's axial displacement component v_{zD} in the formulation of the real gap function $h(x, y)$, compare equation (4.83). b) Experimental results for the load capacity $W_{bearing}$ of a whole AFTB illustrating the thermal runaway effect at higher speeds [Sta12].

interesting point of his findings is that the level of load capacity is considerably different between the tested types of AFTBs. But the critical angular speed for which the load capacity starts showing a decreasing behaviour is about $50krpm$ for all three AFTBs (note that Stahl's AFTBs have a diameter of about $100mm$ which is significantly larger than the diameter of the AFTB considered in this work). This indicates that the observed decreasing load capacity for AFTBs has its origin in thermal effects and therefore has been termed as *thermal runaway* [Dyk06, Dic10, Sta12]. Note that the inclusion of the disk deformation in the formulation of the real height function performed in this work is able to reproduce the thermal runaway effect. A discussion of further thermal aspects that have been experimentally shown to influence load capacity is postponed to section 4.3.4 after the fundamental heat fluxes in an AFTB have been presented in the next section.

4.3.3 Self-induced cooling flow and balance of heat fluxes

For a better understanding of the thermal runaway effect, it is necessary to investigate the thermal management of the AFTB in detail. Figure 4.32 starts with an illustration of the temperature distribution in the rotor and the disk for two different angular velocities.

As to be expected, the disk shows significantly higher temperatures for the high speed condition in comparison to the lower disk speed. But the more interesting point are the temperature differences between the front side of the disk that faces the pad and the backside of the disk that is cooled by the self-induced flow in the cooling flow region. With regard to this aspect, a difference of only $3°C$ is found for $\Omega = 5000\frac{rad}{s}$, whereas already up to $15°C$ are observed for $\Omega = 10000\frac{rad}{s}$. Since the temperature difference across the disk thickness determines the magnitude of the disk bending, the presented plot gives an explanation for the highly nonlinear increase of the axial disk displacement v_{zD} with rotor speed that has been found in figure 4.30b.

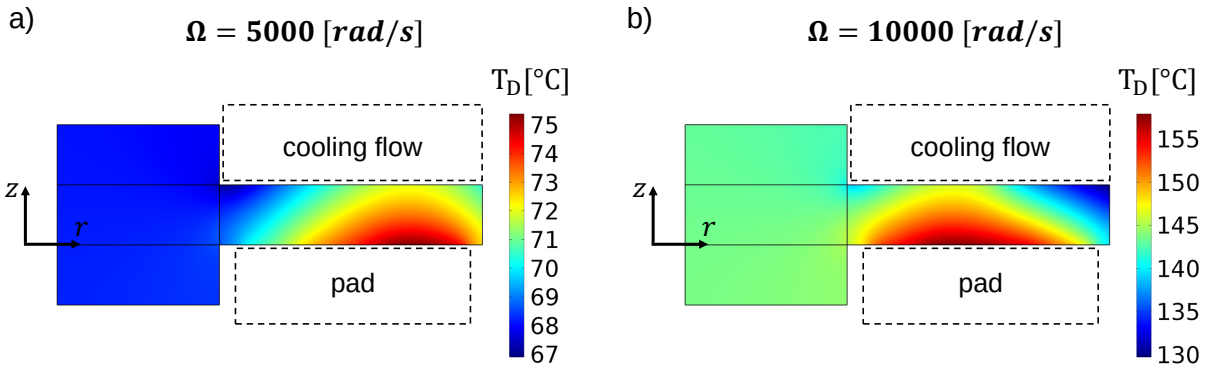

Figure 4.32: Temperature distribution $T_D(r, z)$ in the rotor and the disk for an angular velocity of a) $\Omega = 5000\frac{rad}{s}$, b) $\Omega = 10000\frac{rad}{s}$.

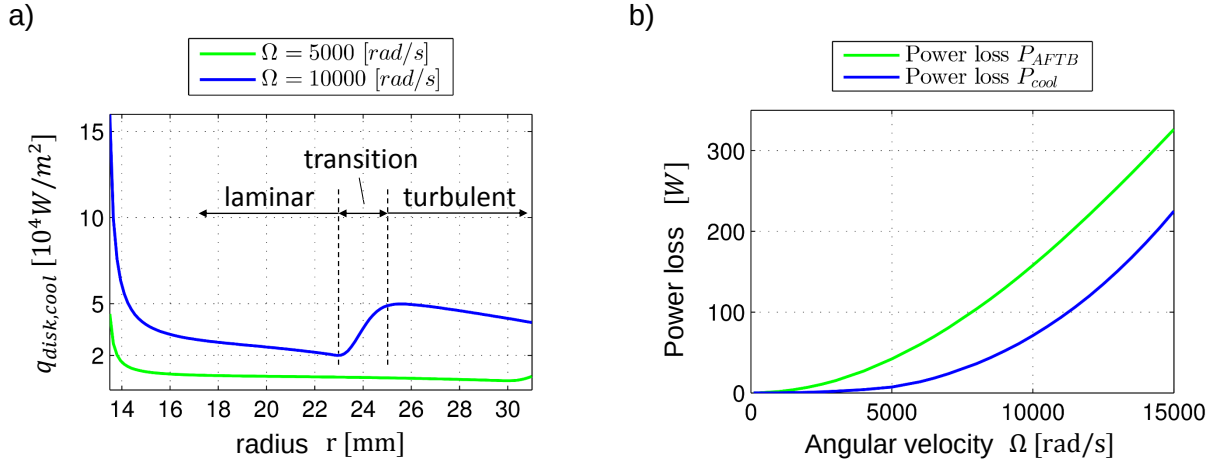

Figure 4.33: a) Heat flux $q_{disk,cool}$ from the disk into the cooling flow region at the backside of the disk. The arrows indicate laminar, transitional and turbulent flow conditions in the cooling flow region for an angular velocity of $\Omega = 10000\frac{rad}{s}$. b) Comparison of the power loss P_{AFTB} in the lubricating gap of all six pads with the power loss P_{cool} at the backside of the rotor disk (cooling flow region).

Another striking aspect revealed by figure 4.32 is the position of the disk's maximum temperature. For the lower speed condition, the maximum temperature is observed near to the outer edge of the pad. This result is reasonable since the dissipation in the pad increases with larger disk radii. Nevertheless, for the angular velocity of $\Omega = 10000\frac{rad}{s}$ the highest temperatures are found to occur close to the middle of the pad. A factor contributing to this result is the increased film thickness at the outer edge of the lubricating gap due to the axial deformation of the disk, see figure 4.29. If reduced dissipation due to thicker air films at the outer pad radius were the only origin of the shifted maximum temperature, the top foil should show the highest temperatures in the middle of the pad as well. Obviously, this is not the case as can be seen from figure 4.28b for the 3D temperature distribution in the lubricating gap.

The main reason for the characteristic shift of the maximal disk temperature at higher angular velocities is illustrated by figure 4.33a. It shows the heat flux $q_{disk,cool}$ from the disk to the cooling flow region as a function of the radial position in the disk, compare also equation (4.89). Besides boundary effects at the inner radius of the disk, the heat flux for the lower angular velocity of $\Omega = 5000\frac{rad}{s}$ is relatively homogenous

along the disk radius. Accordingly, the observed increase of disk temperatures and air film temperatures with the disk radius is reasonable since dissipation in the pad increases with the radius but the cooling of the disk is nearly independent of the disk radius.

The situation is completely different for the higher angular velocity of $\Omega = 10000\frac{rad}{s}$. Here, a sudden increase of the heat flux can be observed at a radius of $r = 23mm$. For this radius, the rotational Reynolds number (4.92) reaches the critical value of $Re_\Omega \approx 2.5 \cdot 10^5$ and the laminar flow region ends. Within the following transitional region the heat transfer improves by a factor of 2.5 until the flow becomes completely turbulent at a radius of $r = 25mm$. It follows from this that for sufficiently high angular velocities of the disk, regions of fundamentally different flow and heat transfer conditions are apparent at the backside of the disk [Elk97, CAC97]. In general, the outer part of the disk is cooled more effectively than the inner part. As a result, the maximum disk temperature shifts towards smaller radii as has been observed in figure 4.32.

It is interesting to note that the change in flow conditions in the self-induced cooling flow at the backside of the disk is difficult to detect by typical experimental set-ups for AFTBs. This is mainly because temperatures are mostly measured by thermocouples placed at the backside of the top foil. But it becomes clear from figure 4.28b that despite the increased heat transfer at the disk's outer radius, the top foil temperatures are still the highest at the outer radius as in the case of low angular velocities.

Figure 4.33b depicts the power loss P_{AFTB} occurring in all six pads of the AFTB in comparison to the power loss P_{cool} due to viscous dissipation in the cooling flow region at the backside of the disk. This comparison is of interest because it stresses the importance of a model for the cooling flow region that accounts for dissipation effects. The ratio between both depicted power losses is 10% for a small angular velocity of $\Omega = 2000\frac{rad}{s}$, increases to 35% for a moderate speed of $\Omega = 8000\frac{rad}{s}$ and is close to 70% for a very high speed of $\Omega = 15000\frac{rad}{s}$. Obviously, the onset of turbulent flow conditions at the backside of the disk improves the heat transfer only for a limited range of speeds. For very high angular velocities the viscous dissipation in the flow of the cooling flow region may diminish the cooling effect at the backside of the disk. An evidence for the reduced heat transfer due to dissipation effects can be already found in figure 4.33a which shows a decreasing heat flux in the turbulent region for radii above $r = 25mm$.

Finally, it is analysed which heat paths contribute the most to the removal of dissipated heat from the lubricating gap. In the presented thermal model for AFTBs four different heat fluxes can be distinguished, which are illustrated in figure 4.34a:

- $Q_{gap,top}$: Heat flux from the lubricating gap into the top foil being further conducted into the bump foil and finally into the base plate.
- $Q_{disk,cool}$: Heat flux that is removed at the backside of the rotor disk by the self-induced cooling flow.
- $Q_{disk,per}$: Heat flux leaving the disk at its outside surface into the housing through the thin air film at the periphery of the disk.

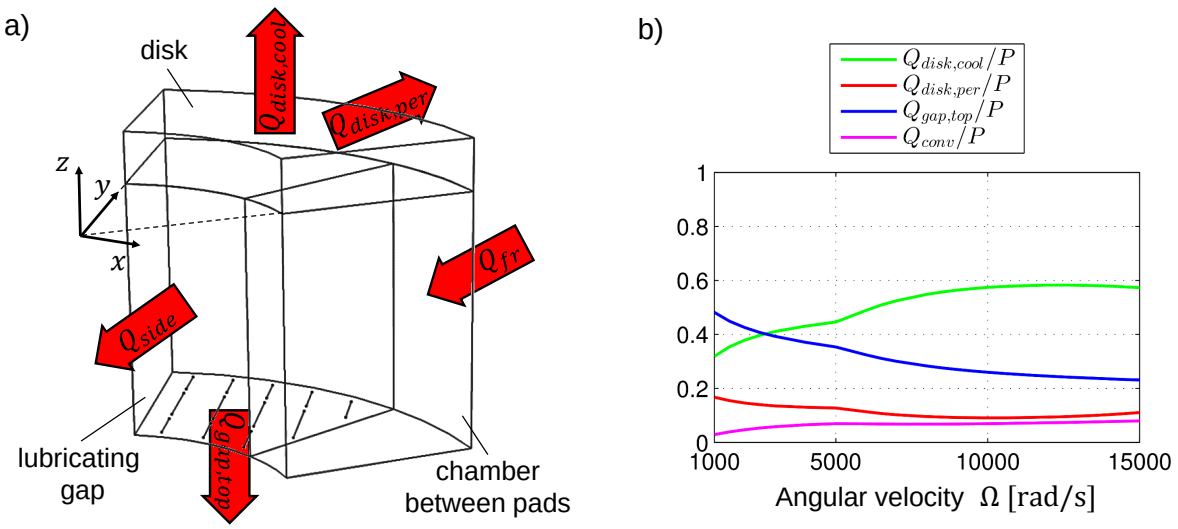

Figure 4.34: a) Illustration of the main heat fluxes that contribute to the cooling of an AFTB. b) Relative magnitude of the four heat fluxes for different speeds of the rotor disk.

- $Q_{conv} = Q_{side} - Q_{fr}$: Net convective heat flux that leaves the pad due to the side leakage (Q_{side}) within the lubricating gap and the inflow of fresh air (Q_{fr}) in the chamber between pads.

Figure 4.34b shows the magnitude of the four heat fluxes scaled by the power loss P for one pad of the AFTB. Obviously, the heat exchange by the self-induced cooling flow at the backside of the disk removes the main part of the dissipated heat for moderate to high velocities. A closer examination of $Q_{disk,cool}/P$ as a function of the angular velocity Ω reveals three different regions. Up to $\Omega = 5000\frac{rad}{s}$, a continuous increase is observed which is reasonable since the flow velocities in the cooling flow region scale directly with the speed of the disk. This rising behaviour is characteristic for heat fluxes based on convection and is therefore as well observed for Q_{conv}/P, but not for $Q_{gap,top}/P$ and $Q_{disk,per}/P$.

At $\Omega = 5000\frac{rad}{s}$, the development of the heat exchange at the backside of the disk shows a discontinuity which can be referred to the onset of turbulence at the outer radius of the disk. With rising speed, the turbulent region covers more and more of the disk surface explaining the increasing behaviour of $Q_{disk,cool}/P$ for angular velocities between $\Omega = 5000 - 10000\frac{rad}{s}$. Finally, for very high speeds dissipation in the cooling flow region becomes dominant which results in a stagnation or even decrease of the cooling effect at the backside of the disk.

The relative magnitudes of the heat fluxes through the foil sandwich $Q_{gap,top}/P$ and at the periphery of the disk $Q_{disk,per}/P$ show mainly a decreasing behaviour with speed which is caused by the rise of $Q_{disk,cool}/P$. The slight increase of the heat flux through the periphery of the disk for $\Omega > 10000\frac{rad}{s}$ can be explained by the smaller gap between the housing and the disk for these high speeds. Thermal and centrifugal growing of the disk diminish the initial gap of $t_{per,nom} = 200\mu m$ to less than $t_{per} = 75\mu m$ for $\Omega = 15000\frac{rad}{s}$, compare figure 4.30b.

The most important characteristic of the thermal management of AFTBs is that the convective heat exchange Q_{conv}/P due to side leakage in the lubricating gap is less than 10% for all speeds and therefore of

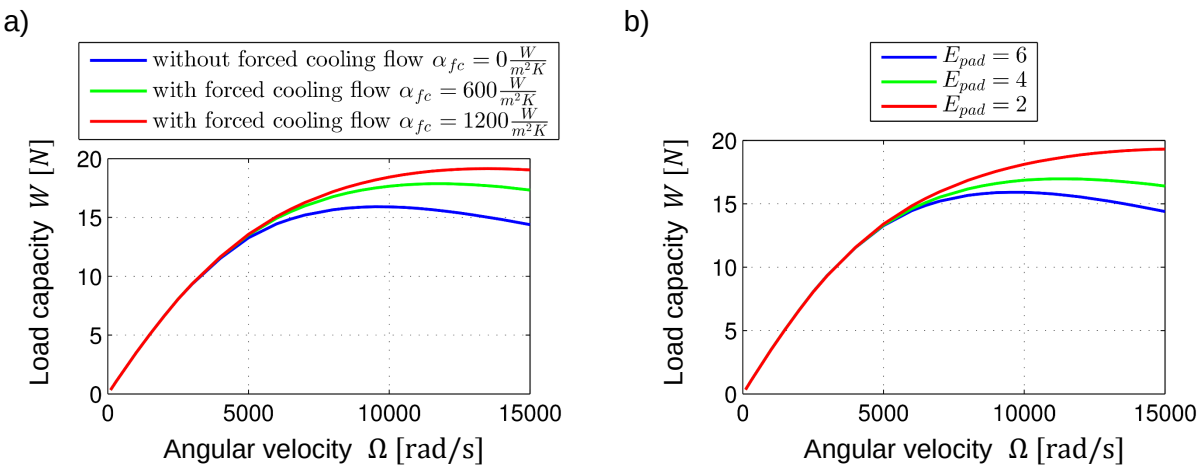

Figure 4.35: Load capacity of one pad in the AFTB for a) different rates of a forced cooling flow (simulated by different heat transfer coefficients α_{fc}) and b) a varying total number of pads in the AFTB.

subordinate importance. This is mainly due to the very low heat capacity of the air film in the lubricating gap. But besides, it should be noted that the ratio between the side leakage mass flow and the inlet mass flow decreases continuously with speed because of compressibility effects that increase with speed.

4.3.4 Effect of forced cooling flow and influence of the number of pads

Although no detailed physical model for a forced cooling flow has been presented in this work, the principal effect of a forced cooling on the load capacity of an AFTB can be studied. For this purpose the energy equation for the top foil (4.39) is replaced by the extended formulation

$$\frac{\partial}{\partial x}\left[- t_T k_T \frac{\partial T_T}{\partial x}\right] + \frac{\partial}{\partial y}\left[- t_T k_T \frac{\partial T_T}{\partial y}\right] = q_{T,in} + q_{T,out} - \alpha_{fc}(T_T - T_{fc})\,, \tag{4.117}$$

where the additional term on the right hand side accounts for a forced cooling flow of the temperature $T_{fc} = 20°C$ that is supplied behind the top foil.

Figure 4.35a shows the load capacity of one pad for different heat transfer coefficients α_{fc}. Note that in case of $\alpha_{fc} = 600 \frac{W}{m^2 K}$, nearly 40% of the dissipated heat is carried away by the forced cooling flow (58% for $\alpha_{fc} = 1200 \frac{W}{m^2 K}$). Obviously, the forced cooling flow has two effects. Firstly, the overall level of the load capacity is increased. And secondly, the critical angular velocity at which the load capacity starts decreasing is shifted towards higher speeds. These trends have been found as well by Dykas [Dyk06], who measured the load capacity for different forced cooling flow rates through the foil sandwich.

Dickman [Dic10] investigated the unit load capacity of identical AFTBs varying only in the number of pads E_{pad}. He found that AFTBs with fewer pads show a higher unit load capacity. The same result is predicted by the model of this work and is depicted in figure 4.35b. It shows the calculated load capacity of one single pad in an AFTB, for which the total number of pads E_{pad} is varied. The origin for the higher unit load capacity of AFTBs with fewer pads can be referred to reduced thermal gradients across the disk thickness.

As the total power loss of the AFTB P_{AFTB} scales nearly linearly with the number of pads, the heat flux entering the front side of the disk is considerably smaller for AFTBs with fewer pads. Thus, the temperature difference between the front side and the back side of the disk is as well smaller for AFTBs with fewer pads resulting in a reduced bending of the disk. As a consequence, the contribution of the disk bending to the real height function in the lubricating gap decreases leading to a more favorable pressure distribution and thus to higher load capacities. The same reasoning explains the improved load capacity for larger forced cooling flow rates that has been observed in figure 4.35a. In this case the heat flux across the disk thickness is reduced since most of the heat is conducted into the foil sandwich were it is effectively removed by the forced cooling flow.

4.3.5 Summary and conclusions

A 3D thermo-elasto-hydrodynamic model for an one-sided air foil thrust bearing with a passive thermal management has been presented. Next to a shell model for the top and bump foil, particular emphasis was put on thermal submodels for the different parts of the bearing which are accounted for by:

- A cross-film averaged Reynolds equation for the pressure and a 3D energy equation for the temperature in the lubricating air film.
- A 2D energy equation for the top foil in combination with a developed analytical formula for the effective thermal resistance of the bump foil that accounts for the geometry of the bumps as well as the surface roughness of the foils and the base plate.
- Coupled axisymmetric energy and structural equations for the rotor and the rotor disk that are able to model a thermally induced bending of the disk.
- Axisymmetric boundary layer equations with an eddy viscosity turbulence model for the self-induced cooling flow at the backside of the rotor disk.
- A 2D energy equation for the heat transfer through the thin air film at the periphery of the disk.

The real height function in the lubricating gap has been modeled taking into account the nominal height function, the deformation of the top foil and the deformation of the rotor disk. The influence of the latter was found to be the origin of thermal runaway for high load and high speed conditions. It could be clearly shown that the load capacity of AFTBs increases with speed only up to a certain critical speed. Above this, load capacity was found to decrease with speed, an effect that has been documented in several experimental works [Dyk06, Dic10, Sta12] but could not be explained so far by isothermal models for AFTBs. The source of this phenomenon was demonstrated to be a thermally induced bending of the disk that leads to an unfavourable gap function resulting in a poor pressure distribution.

An analysis of the main heat fluxes in a passively cooled AFTB revealed that the convective heat exchange due to side leakage removes less than 10% of the dissipated heat. This is fundamentally different

to hydrodynamic oil bearings where most of the heat is carried away by the exchange of fluid. Fortunately, the thermal conductivity of air is high enough - in combination with the small gap sizes typical for AFTBs - in order to efficiently conduct nearly all of the dissipated heat into the rotor disk and the top foil. But once the heat reaches these bearing parts the main problem in the thermal management of AFTBs becomes apparent.

Due to Fourier's law of heat conduction both, the top foil and the rotor disk, need to establish a thermal gradient across their thickness in order to conduct the dissipated heat out of the lubricating air film. Unfortunately, this thermal gradient induces structural deformations that result in an unfavourable lubricating gap function. Thus, the higher the heat flux that is removed across the thickness of the top foil and the rotor disk, the higher are the structural deformations in these bearing parts.

At least for the top foil, the thermally induced structural deformations are probably of subordinate importance. This can be concluded from experimental results [Dyk06] that showed the load capacity to increase if a forced cooling flow was supplied at the backside of the top foil. Since the latter enhances the heat flux that passes the top foil, the thermal gradient across the thickness of the top foil has to rise as well. Henceforth, the thermally induced deformations of the top foil should be more and not less pronounced (resulting in smaller load capacities) if a forced cooling flow is supplied.

The experimentally observed higher load capacities for increased rates of forced cooling flow are therefore not to be traced back to reduced top foil deformations. Instead, it could be shown in this work that they have their origin in reduced deformations of the rotor disk. This is because a forced cooling flow removes a significant part of the dissipated heat and therefore indirectly diminishes the heat flux that flows into the rotor disk. As a consequence, thermal gradients across the disk thickness are smaller, resulting in smaller disk deformations and thus in the measured and calculated higher load capacities.

5 Comparison to measurements

After basic thermal characteristics of AFTBs have been studied in the last section, it is the aim of this section to compare the predictions of the presented model to measurements. For this purpose, the AFTB shown in figure 5.1 is analysed. It consists of five pads each composing of a top foil and a supporting bump foil. The hydrodynamically active region of the top foil is defined by the circular edges at the foil's inner and outer radius as well as by a spiral shaped leading edge and a parabolic trailing edge. The latter is approximated in the model by a straight edge, see figure 5.3b. The fixing of the top foil on the base plate is far away from the top foil's leading edge resulting in a large chamber between pads. The convergent nominal gap function between the rotor disk and the top foil is created by bumps of different height. Details about the geometry and thickness of the foils can not be given due to proprietary rights.

Typically, temperatures in AFBs are measured by thermocouples which are placed directly behind the bump foil at a point where the bump foil contacts the top foil [Dyk06]. Since this method requires to drill a hole in the base plate for each thermocouple, it is obvious that temperatures can only be evaluated at few points within the pad area [SSH01, Dyk06]. An alternative for a more complete evaluation of bearing temperatures are optical temperature measurements.

Figure 5.2 schematically illustrates the test rig which has been designed in order to apply an infrared (IR) radiation technique. Two disks are mounted on an electromagnetically driven rotor. The right disk is exposed to an externally supplied hydrostatic pressure by which a well defined thrust load is established. The AFTB to be tested is placed at the left end of the rotor near to the second rotor disk. If the base plate of the bearing is made of a material with a high transmission for infrared radiation (e.g. Zinc Sulphide), it is not only a support for the foils but serves as well as an IR window. Thus, foil temperatures can be measured by an IR camera.

Figure 5.3 shows a comparison between measured (left) and calculated (right) top foil temperatures for a rotor speed of $65000rpm$ and a thrust load of $80N$. Note the different orientation of the pad for the measured and the calculated case (leading edge is marked). Since for the analysed design the top foil extends the bump foil at all four edges (compare also position of contact lines in figure 5.3b), the top foil temperature can be clearly studied at the leading edge as well as close to the inner and the outer radius. The comparison between measurement and calculation for three different points in these regions shows a good agreement.

In particular, it is noteworthy that the measured temperature at the leading edge is $T_T = 123°C$ and thus close to the maximal top foil temperature of $T_T = 125°C$ which occurs close to the outer radius. This finding indicates that the air does not enter the pad with a mixed temperature as calculated by equation (4.63). If this where the case, the top foil should show significantly lower temperatures at the leading edge. Instead, the high temperatures measured at the leading edge justify the applied assumption (in the calculation model) that the temperature of the inlet air is close to the temperature of the rotor disk, compare also section 4.2.3.

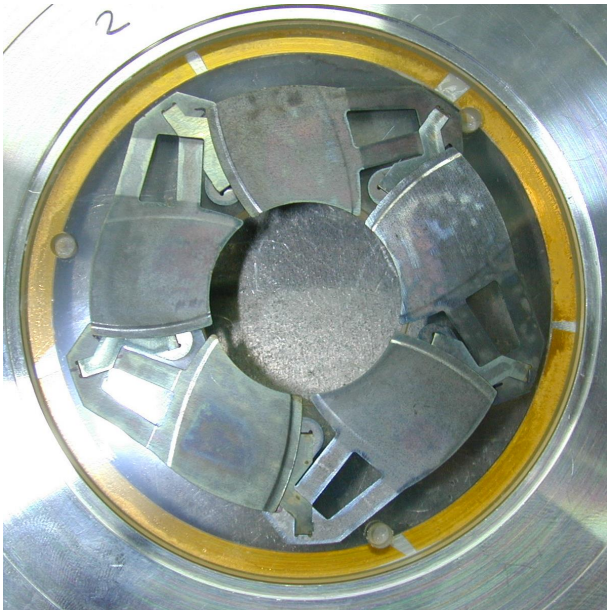

Figure 5.1: Tested AFTB.

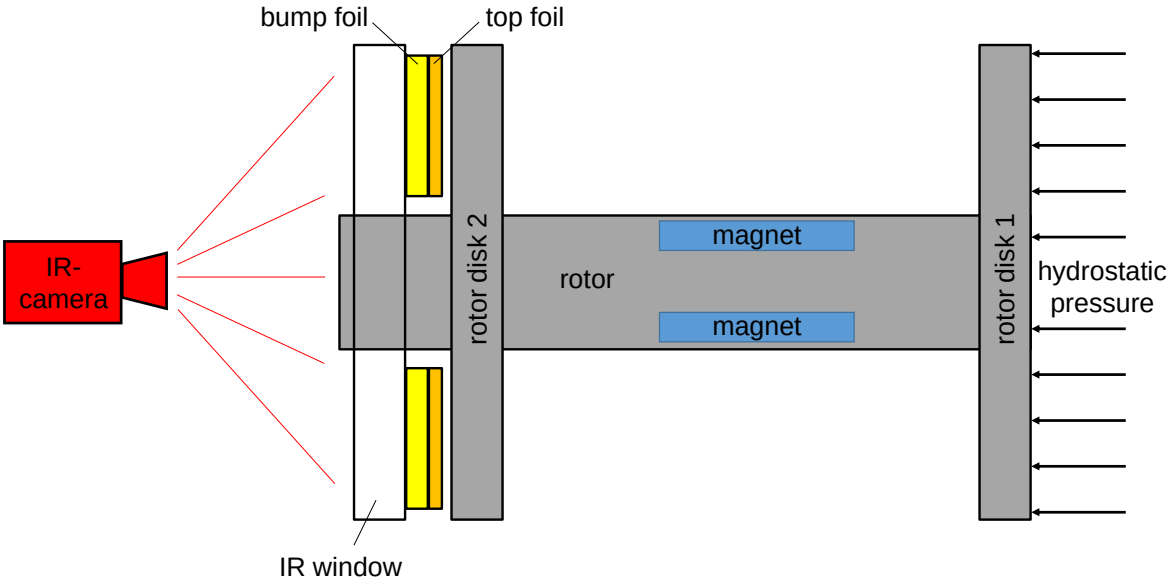

Figure 5.2: Schematic illustration of the test rig used for the measurement of temperatures in an AFTBs.

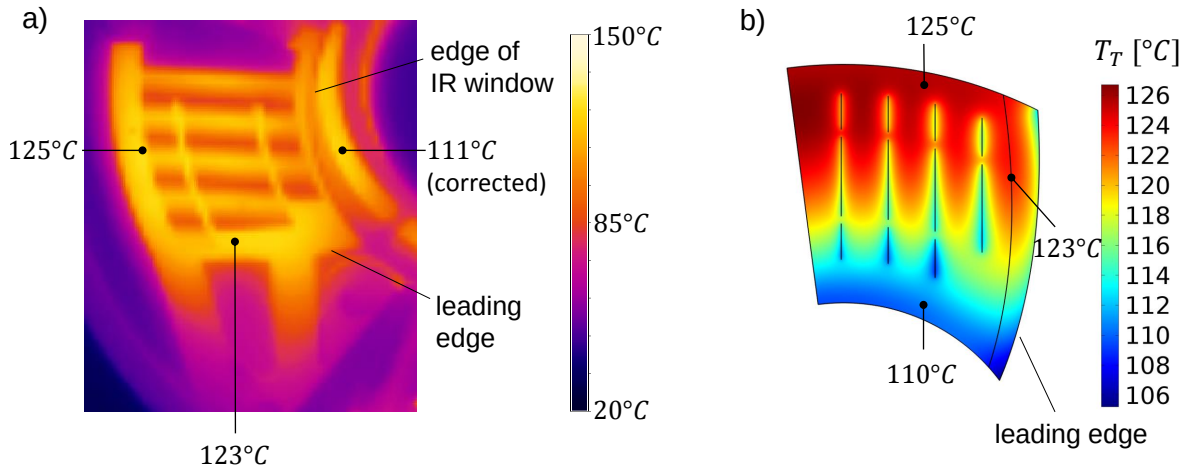

Figure 5.3: Comparison of measurement and calculation for a rotor speed of $65000rpm$ and a bearing load of $80N$. a) Infrared temperature measurement for one pad of an AFTB. b) Calculated temperatures for the hydrodynamically active region of the top foil.

Rotor speed [rpm]	Thrust load [N]	$T_{T,max}$ (measured)	$T_{T,max}$ (calculated)
65000	45	102	100
65000	60	113	111
65000	80	125	126
85000	5	83	84

Table 5.1: Comparison of calculated and measured maximal top toil temperatures $T_{T,max}$ for different loads and speeds.

Another aspect to be stressed is the relatively small temperature difference of approximately $15°C$ between the inner and the outer radius. Here, it is important to mention that the region close to the inner radius of the top foil is not covered by the IR window. As a consequence, temperatures in this region are depicted approximately $10°C$ higher as they are in reality (note the discontinuity in the color field close to the inner bump strip). This is because the material of the IR window absorbs a part of the infrared radiation which has been already accounted for in the calibration of the IR camera.

Table 5.1 shows the maximal top foil temperature $T_{T,max}$ for different bearing loads and rotor speeds. The good agreement between the predictions and the measurement indicates that the presented model accounts for the most relevant mechanisms of heat transfer in a passively cooled AFTB. In particular, the effect of both - variations in load and speed - is accurately predicted by the model.

Finally, an issue is addressed that can not be covered by the model presented in this work, but reveals a further advantage of the infrared radiation technique for the measurement of bearing temperatures: The failure of an AFTB. The theoretical analysis of AFTBs presented in this work is only valid for full hydrodynamic flow conditions. It should be stressed that currently no model exists in the literature that can predict the load capacity limit for a given AFTB. This is because nobody knows the exact value for the critical minimal film height h_{min} at which mixed lubrication occurs between the rotor disk and the top foil resulting in a bearing failure. Mostly, monitoring of the bearing's power loss is used to determine the point of time when a bearing failed, and post-operational investigation of wear scars may allow for conclusions about the contacting area

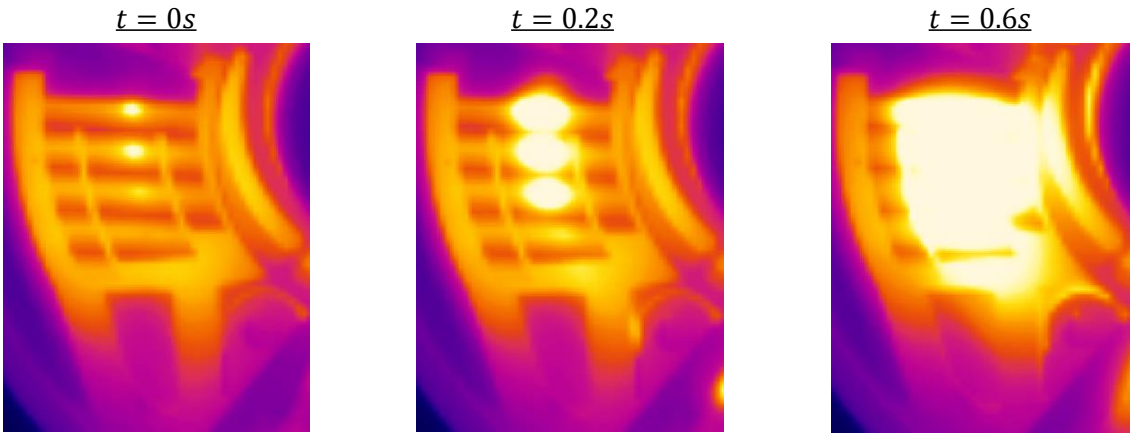

Figure 5.4: Measured temperature distributions in the foil pad for three different times during the process of bearing failure.

during mixed lubrication.

Figure 5.4 demonstrates that the infrared radiation technique can additionally provide information about the origin of the bearing failure. All three plots show the temperature distribution in one pad of an overloaded AFTB for a rotor speed of $65000rpm$. The color table for the temperatures is the same as in figure 5.3. It can be clearly seen in the left plot that two points close to the first and second line of bump contacts in the middle of the pad show significantly higher temperatures ($> 150°C$) than the rest of the foil pad. Since increased friction occuring in a mixed lubrication contact results in a sudden local heating of the foils, the bright spots in the left plot can be regarded as the exact position at which the bearing failure started.

Only 0.2 seconds later (middle plot), the area of the bright spots is found to be significantly larger and 0.6 seconds after the first mixed lubrication contact already half of the pad is exposed to a mixed lubrication condition. Note that the first bumps of all three bump strips are of identical height. Therefore it is astonishing that the first detected mixed lubrication contact is in the middle of the pad and not at the outer radius. For a perfectly smooth rotor disk, the first contact should be expected to occur at the outer edge since misalignment can not be completely avoided in a real AFTB application. The fact that the bearing failure originates from the middle of the pad allows for the conclusion that either the bump foil deforms the most near to the outer edge or the rotor disk is thermally distorted. Or - more simply - a manufacturing inaccuracy is responsible for the concrete position where the bearing failure started.

It becomes clear that even with the use of an infrared radiation technique the origin of a bearing failure for a concrete foil design is still not unambiguous. But at least, the starting point of mixed lubrication can be determined to a far better degree than by post-operational investigations. Furthermore, differences between pads, for example because of misalignment, can be revealed and local hot spots due to severe manufacturing inaccuracies are rapidly found.

6 Summary

A thermo-elasto-hydrodynamic calculation model for bump type air foil thrust bearings has been developed. A 2D Reynolds equation - based on cross-film averaged fluid properties - and a 3D energy equation are solved in order to obtain the pressure and temperature distribution in the lubricating air film. Elastic deformations of top and bump foil are calculated by a Reissner-Mindlin type shell theory. The deformation of the rotor disk, due to thermal gradients, is accounted for by axisymmetric Navier-Lamé equations. Both, foil and disk deformations, are used in order to calculate the real gap function of the lubricating air film, which is the most important factor in hydrodynamic lubrication.

Apart from the real gap function, the properties of the lubricating air are the second factor that determines the performance of air foil thrust bearings. Because of this, different thermal submodels for the bearing parts are solved in addition to the 3D energy equation for the air film: Heat conduction in the rotor disk and the rotor is modeled by axisymmetric equations. For the small air gap between the rotor disk and the housing at the periphery of the disk, a 2D energy equation is solved, that accounts for dissipation effects and thermal and centrifugal growth of the disk. The thermal model for the foil sandwich consists of a 2D heat conduction equation for the top foil and a carefully calculated effective thermal resistance for the bump foil. The self-induced cooling flow at the backside of the disk is modeled by appropriate boundary layer equations including an eddy viscosity turbulence model. All presented equations for the different submodels are fully coupled and discretized by a finite element method.

Besides the development of a comprehensive calculation model for air foil thrust bearings, an analysis of the principal hydrodynamic, elastic and thermal effects has been carried out. The main motivation for this part of the work was the simple question of how to design a well performing air foil thrust bearing.

Reducing the full model to the rigid isotherm case, the influence of the gap function has been studied with respect to a maximum load capacity and a minimum friction coefficient. Basic gap geometries (e.g. taper, step, taper land, pocket), that are defined by only a few parameters have been optimised and compared to more complex gap functions. It was found that the pocket type gap geometry significantly outperforms the other basic gap functions for small to medium compressibility numbers. For high compressibility numbers, the taper land geometry can achieve higher load capacities than the pocket geometry depending on the aspect ratio of the pad. Taper and stepped gap functions should be avoided in all cases. The analysis of more complex gap functions for cylindrically shaped pads revealed that pocket type gap functions operate close to the optimum load capacity for the whole range of analysed compressibility numbers. Therefore, if a significant improvement of the load capacity is needed, it makes no sense to refine a pocket type gap function. Instead, at least for medium to high compressibility numbers, a replacement of sector-shaped pad topologies by grooved geometries as for example the spiral groove bearing should be considered. For the taper land and the pocket type gap function, optimal geometrical parameters are delivered for different compressibility numbers and aspect ratios in the appendix. Given a defined thrust load, the tabulated data

enables the designer to quickly estimate the minimal needed thrust bearing size.

In a next step, the influence of the foils has been studied. The main result is that predictions based on elastic foundation type foil models can be very inaccurate. It could be shown that different mechanisms as cumulated friction forces, interacting bending moments, two-dimensional curvature effects and two-dimensional friction forces determine the deformation of the bump foil. It is therefore nearly impossible to estimate an appropriate stiffness for a simple elastic foundation type model. The main advantage of the shell model used in this work lies in the fact that the bump foil geometry is exactly modeled. Furthermore, the chosen formulation can be adopted to the various bump foil designs presented in the literature.

The impact of the foils on the performance of the air foil thrust bearing has been studied in detail. The main finding was that for perfectly aligned conditions of the rotor disk and the bearing surface, air foil thrust bearings show a lower load capacity than rigid thrust bearings. The origin of that was revealed to stem from top foil sagging effects and uneven bump foil deformations that lead to unfavorable gap functions. Furthermore, a single foil pad was demonstrated to be unable to effectively compensate for runner distortions and misaligned conditions. The main advantage of foil bearings was found to originate from the global compliance of the pads. This leads to a more homogenous loading condition between the foil pads in comparison to the pads of a rigid thrust bearing. Therefore, foil bearings can outperform rigid bearings for misaligned conditions or in case of manufacturing inaccuracies. Both are always apparent to some degree and can not be completely avoided.

Finally, thermal aspects of air foil bearings have been studied. The properties of air are found to be the origin of several distinguishing characteristics of air foil bearings in comparison to classical hydrodynamic oil bearings. Firstly, the dynamic viscosity of air increases with rising temperature. Because of this, air foil bearings show an improved load capacity in a high temperature environment. Secondly, the properties of air are less sensitive to temperature variations in comparison to for example the dynamic viscosity of oil. This fact was explored in order to replace the generalized Reynolds equation by a cross-film averaged Reynolds equation resulting in a significantly lower computational effort. The relative error of this reduction was found to be below one percent with respect to the maximal temperature rise, the load capacity and the power loss.

The most important characteristic property of air foil bearings can be referred to the very small heat capacity of air. It could be shown that less than 10% of the dissipated heat in an air foil thrust bearing is removed by convective heat transport within the lubricating film. As a result, nearly all of the heat flows in cross-film direction into the rotor disk and the foil sandwich. This heat flow turns out to be problematic since it establishes a thermal gradient in the rotor disk that distorts the disk and results in an unfavorable gap function. As a consequence, it could be demonstrated that the load capacity of air foil bearings increases only up to a critical rotational speed. Above this, the load capacity was found to slightly decrease with increasing rotational speed. Therefore, it can be stated that the load capacity of air foil bearings is not only limited by compressibility effects, but as well by the amount of dissipated energy within the bearing.

7 Appendix

φ_{hT}/λ_r	Λ	LPGF	$\overline{W}$	f	λ_h	λ_φ	$\lambda_{\Delta r}$
30°/0.3	1	taper land	5.37e-03	1.35e+01	2.37e+00	2.36e-01	
		pocket	6.40e-03	1.17e+01	2.04e+00	2.66e-01	9.23e-02
	100	taper land	4.63e-01	1.59e+01	3.29e+00	4.54e-01	
		pocket	4.84e-01	1.55e+01	2.60e+00	4.40e-01	7.57e-02
	500	taper land	1.35e+00	2.61e+01	5.52e+00	5.48e-01	
		pocket	1.29e+00	2.76e+01	3.90e+00	5.37e-01	5.56e-02
30°/0.5	1	taper land	5.38e-03	1.53e+01	2.44e+00	2.56e-01	
		pocket	6.90e-03	1.23e+01	2.15e+00	2.45e-01	9.70e-02
	100	taper land	4.84e-01	1.75e+01	3.40e+00	4.81e-01	
		pocket	5.26e-01	1.62e+01	2.72e+00	4.16e-01	7.84e-02
	500	taper land	1.44e+00	2.83e+01	5.70e+00	5.69e-01	
		pocket	1.42e+00	2.85e+01	4.06e+00	5.17e-01	5.65e-02
30°/0.7	1	taper land	3.83e-03	2.45e+01	2.74e+00	2.96e-01	
		pocket	6.30e-03	1.55e+01	2.52e+00	1.95e-01	9.04e-02
	100	taper land	4.17e-01	2.45e+01	3.59e+00	5.47e-01	
		pocket	5.18e-01	1.93e+01	3.01e+00	3.69e-01	8.04e-02
	500	taper land	1.38e+00	3.61e+01	5.87e+00	6.25e-01	
		pocket	1.50e+00	3.19e+01	4.38e+00	4.84e-01	6.08e-02
40°/0.3	1	taper land	6.12e-03	1.17e+01	2.42e+00	2.48e-01	
		pocket	7.60e-03	9.80e+00	2.10e+00	2.57e-01	1.14e-01
	100	taper land	5.25e-01	1.40e+01	3.51e+00	4.86e-01	
		pocket	5.55e-01	1.34e+01	2.74e+00	4.53e-01	8.99e-02
	500	taper land	1.52e+00	2.32e+01	6.00e+00	5.74e-01	
		pocket	1.46e+00	2.46e+01	4.15e+00	5.57e-01	6.36e-02
40°/0.5	1	taper land	5.72e-03	1.41e+01	2.54e+00	2.76e-01	
		pocket	8.04e-03	1.04e+01	2.27e+00	2.25e-01	1.18e-01
	100	taper land	5.32e-01	1.59e+01	3.65e+00	5.21e-01	
		pocket	5.99e-01	1.41e+01	2.92e+00	4.14e-01	9.41e-02
	500	taper land	1.60e+00	2.57e+01	6.20e+00	6.00e-01	
		pocket	1.60e+00	2.52e+01	4.38e+00	5.24e-01	6.59e-02
40°/0.7	1	taper land	3.50e-03	2.59e+01	2.98e+00	3.03e-01	
		pocket	6.83e-03	1.38e+01	2.80e+00	1.70e-01	1.00e-01
	100	taper land	4.22e-01	2.44e+01	3.86e+00	5.93e-01	
		pocket	5.66e-01	1.73e+01	3.30e+00	3.54e-01	9.23e-02
	500	taper land	1.46e+00	3.46e+01	6.33e+00	6.65e-01	
		pocket	1.66e+00	2.86e+01	4.77e+00	4.84e-01	7.04e-02

Table 7.1: Dimensionless load capacity $\overline{W}$, friction coefficient f and gap parameters λ_h, λ_φ, $\lambda_{\Delta r}$ for optimized (maximal load capacity), cylindrically sector-shaped pads as function of the topological parameters φ_{hT}, λ_r and the compressibility number Λ. See section 2.1.1 for the definition of all parameters and variables.

φ_{hT}/λ_r	Λ	LPGF	$\overline{W}$	f	λ_h	λ_φ	$\lambda_{\Delta r}$
60°/0.3	1	taper land	6.82e-03	1.02e+01	2.53e+00	2.71e-01	
		pocket	9.36e-03	7.83e+00	2.24e+00	2.34e-01	1.50e-01
	100	taper land	6.05e-01	1.21e+01	3.85e+00	5.35e-01	
		pocket	6.59e-01	1.12e+01	2.98e+00	4.57e-01	1.16e-01
	500	taper land	1.76e+00	2.02e+01	6.72e+00	6.12e-01	
		pocket	1.70e+00	2.11e+01	4.54e+00	5.79e-01	7.77e-02
60°/0.5	1	taper land	5.56e-03	1.40e+01	2.79e+00	3.01e-01	
		pocket	9.46e-03	8.65e+00	2.55e+00	1.92e-01	1.45e-01
	100	taper land	5.78e-01	1.48e+01	4.03e+00	5.82e-01	
		pocket	7.00e-01	1.18e+01	3.27e+00	4.01e-01	1.20e-01
	500	taper land	1.79e+00	2.32e+01	6.94e+00	6.48e-01	
		pocket	1.88e+00	2.12e+01	4.92e+00	5.22e-01	8.32e-02
60°/0.7	1	taper land	2.78e-03	3.02e+01	3.42e+00	2.89e-01	
		pocket	7.24e-03	1.23e+01	3.37e+00	1.35e-01	1.11e-01
	100	taper land	3.97e-01	2.62e+01	4.29e+00	6.53e-01	
		pocket	6.17e-01	1.54e+01	3.84e+00	3.23e-01	1.08e-01
	500	taper land	1.52e+00	3.42e+01	7.00e+00	7.21e-01	
		pocket	1.88e+00	2.50e+01	5.43e+00	4.73e-01	8.61e-02

Table 7.2: Continuation of table 7.1.

References

[Agr97] G. L. Agrawal. Foil air/gas bearing technology - an overview. *ASME International Gas Turbine and Aeroengine Congress and Exhibition*, pages 1–11 (Publication 97–GT–347), 1997.

[ALA87] L. A. Abdel-Latif and A.-M. A. Amman. Inertia effects on thrust bearings with michell pads running under thermohydrodynamic conditions. *Forschung im Ingenieurwesen*, 53:189–195, 1987.

[BBA96] T. S. Brockett, L. E. Barrett, and P. E. Allaire. Thermoelastohydrodynamic analysis of fixed geometry thrust bearings including runner deformation. *Tribology transactions*, 39(3):555–562, 1996.

[BBSG16] B. Bouchehit, B. Bou-Said, and M. Garcia. Static and dynamic performances of refrigerant-lubricated bearings. *Tribology International*, 96:326–348, 2016.

[BK85] Y. Basar and W. Kraetzig. *Mechanik der Flaechentragwerke*. Vieweg, 1985.

[BK00] Y. Basar and W. Kraetzig. *Theory of shell structures*. VDI Verlag GmbH, 2000.

[Bru04] R. Bruckner. *Simulation and modeling of the hydrodynamic, thermal, and structural behavior of foil thrust bearings*. Phd, Case Western Reserve University, 2004.

[Bru12] R. Bruckner. Performance of simple gas foil thrust bearings in air. Report TM-2012-217262, NASA, 2012.

[Bru13] R. Bruckner. The chevron foil thrust bearing: Improved performance through passive thermal management and effective lubricant mixing. *Conference paper on World Tribology Congress 2013 Torino*, pages 1–4, 2013.

[BS13] H. D. Baehr and K. Stephan. *Waerme-und Stoffuebertragung*. Springer Vieweg, Berlin Heidelberg, 2013.

[Buc87] R. H. Buckholz. The effect of lubricant inertia near the leading edge of a plane slider bearing. *Journal of tribology*, 109(1):60–64, 1987.

[CA75] T. Cebeci and D. E. Abbott. Boundary layers on a rotating disk. *AIAA Journal*, 13(6):829–832, 1975.

[CAC97] G. Cardone, T. Astarita, and G. M. Carlomagno. Heat transfer measurements on a rotating disk. *International Journal of Rotating Machinery*, 3(1):1–9, 1997.

[CMP94] M. Carpino, L. A. Medvetz, and J.-P. Peng. Effects of membrane stresses in the prediction of foil bearing performance. *Tribology transactions*, 37(1):43–50, 1994.

[Con64] V. N. Constantinescu. On gas lubrication in turbulent regime. *Journal of Basic Engineering*, 86(3):475–482, 1964.

[CS74] T. Cebeci and A. Smith. *Analysis of turbulent boundary layers*. Academic Press, New York, 1974.

[Day76] D. R. Dayton. Gas lubricated foil bearing development for advanced turbomachines. Report AFAPL-TR-76-II4, Garett, 1976.

[DBD+08] B. Dykas, R. Bruckner, C. DellaCorte, B. Edmonds, and J. Prahl. Design, fabrication, and performance of foil gas thrust bearings for microturbomachinery applications. Report TM - 2008-215062, NASA, 2008.

[Dic10] J. R. Dickman. *An investigation of gas foil thrust bearing performance and its influencing factors*. Master thesis, Case Western Reserve University, 2010.

[DLV+00] C. DellaCorte, V. Lukaszewicz, Mark J. Valco, K.C. Radil, and H. Heshmat. Performance and durability of high temperature foil air bearings for oil-free turbomachinery. Report TM - 2000-209187/REV1, NASA, 2000.

[Dow62] D. Dowson. A generalized reynolds equation for fluid-film lubrication. *International Journal of Mechanical Sciences*, 4(2):159–170, 1962.

[DRBH08] C. DellaCorte, K. C. Radil, R. Bruckner, and S. A. Howard. Design, fabrication, and performance of open source generation i and ii compliant hydrodynamic gas foil bearings. *Tribology Transactions*, 51(3):254–264, 2008.

[Dyk06] B. D. Dykas. *Factors influencing the performance of foil gas thrust bearings for oil-free turbomachinery applications*. Phd, Case Western Reserve University, 2006.

[DZR04] C. DellaCorte, A. R. Zaldana, and K. C. Radil. A systems approach to the solid lubrication of foil air bearings for oil-free turbomachinery. *Journal of Tribology*, 126(1):200–207, 2004.

[EB86] H. G. Elrod and D. E. Brewe. Thermohydrodynamic analysis for laminar lubricating films. Report 86-C-33, NASA, 1986.

[EC65] C. Ettles and A. Cameron. The action of the parallel surface thrust bearing. *Proc. Fourth Lubric. Wear Conv., Instn mech. Engrs*, 180:61–65, 1965.

[Elk97] C. J. Elkins. *Heat transfer in the rotating disk boundary layer*. Phd, Harvard University, 1997.

[Elr89] H. G. Elrod. Efficient numerical method for computation of thermohydrodynamics of laminar lubricating films. Report 89-C-015, NASA, 1989.

[ER73] H. A. Ezzat and S. M. Rohde. A study of the thermohydrodynamic performance of finite slider bearings. *Journal of Lubrication Technology*, 95(3):298–307, 1973.

[ES93] H. Eschenauer and W. Schnell. *Elastizitaetstheorie*. BI-Wiss.-Verlag, 1993.

[Fen09] K. Feng. *Prediction of Static and Dynamic Performance and Thermohydrodynamic Analysis of Gas Foil Bearings*. Phd, University of Tokyo, 2009.

[GS13] B. S. Grigor'ev and D. B. Smirnov. Calculation of static characteristics of spiral-grooved thrust bearings over a wide compressibility range. *Journal of Machinery Manufacture and Reliability*, 42(3):236–239, 2013.

[HE88] D. D. Heckelman and C. M. Ettles. Viscous and inertial pressure effects at the inlet to a bearing film. *Tribology Transactions*, 31(1):1–5, 1988.

[Hes05] H. Heshmat. Major breakthrough in load capacity, speed and operating temperature of foil thrust bearings. *ASME Proceedings of WTC2005*, pages 111–112, 2005.

[Hor06] Y. Hori. *Hydrodynamic lubrication*. Springer-Science & Business Media, Tokyo, 2006.

[HSJ04] B. J. Hamrock, S. R. Schmid, and B. O. Jacobson. *Fundamentals of fluid film lubrication*. Dekker, New York City, 2004.

[Hue74] K. H. Huebner. A three-dimensional thermohydrodynamic analysis of sector thrust bearings. *ASLE TRANSACTIONS*, 17(1):62–73, 1974.

[HWP83a] H. Heshmat, J. A. Walowit, and O. Pinkus. Analysis of gas lubricated compliant thrust bearings. *Journal of lubrication technology*, 105(4):638–646, 1983.

[HWP83b] H. Heshmat, J. A. Walowit, and O. Pinkus. Analysis of gas-lubricated foil journal bearings. *Journal of Lubrication Technology*, 105(4):647–655, 1983.

[HWT05] H. Heshmat, J. F. Walton, and M. J. Tomaszewski. Demonstration of a turbojet engine using an air foil bearing. *Proceedings of 2005 ASME Turbo Expo (Reno, Nevada): Power for Land, Sea and Air*, pages 919–926, 2005.

[IBSMB08] I. Iordanoff, B. Bou Said, A. Mezianne, and Y. Berthier. Effect of internal friction in the dynamic behavior of aerodynamic foil bearings. *Tribology International*, 41(5):387–395, 2008.

[Ior99] I. Iordanoff. Analysis of an aerodynamic compliant foil thrust bearing: method for a rapid design. *Journal of tribology*, 121(4):816–822, 1999.

[JBI04] M. Jai, G. Buscaglia, and I. Iordanoff. Multi-constrained optimization of running characteristics of mechanisms lubricated with compressible fluid. *Journal of tribology*, 126(1):132–136, 2004.

[Kar21] T.v. Karman. Ueber laminare und turbulente reibung. *ZAMM Journal of Applied Mathematics and Mechanics*, 1(4):233–252, 1921.

[KH92] C.-P. R. Ku and H. Heshmat. Compliant foil bearing structural stiffness analysis: part i-theoretical model including strip and variable bump foil geometry. *Journal of Tribology*, 114(2):394–400, 1992.

[KH94] C.-P. R. Ku and H. Heshmat. Structural stiffness and coulomb damping in compliant foil journal bearings: parametric studies. *Tribology transactions*, 37(3):455–462, 1994.

[Kho87] M. M. Khonsari. A review of thermal effects in hydrodynamic bearings part i: slider and thrust bearings. *ASLE transactions*, 30(1):19–25, 1987.

[Kim07] D. Kim. Parametric studies on static and dynamic performance of air foil bearings with different top foil geometries and bump stiffness distributions. *Journal of tribology*, 129(2):354–364, 2007.

[KL10] D. Kim and D. Lee. Design of three-pad hybrid air foil bearing and experimental investigation on static performance at zero running speed. *Journal of Engineering for Gas Turbines and Power*, 132(12):122504, 2010.

[KLC14] D. Kim, A. S. Lee, and B. S. Choi. Evaluation of foil bearing performance and nonlinear rotor-dynamics of 120kw oil-free gas turbine generator. *Journal of Engineering for Gas Turbines and Power*, 136(3):032504, 2014.

[KZ12] D. Kim and G. Zimbru. Start-stop characteristics and thermal behavior of a large hybrid airfoil bearing for aero-propulsion applications. *Journal of Engineering for Gas Turbines and Power*, 134(3):032502, 2012.

[LK10] D. Lee and D. Kim. Thermohydrodynamic analyses of bump air foil bearings with detailed thermal model of foil structures and rotor. *Journal of Tribology*, 132(2):021704–1–12, 2010.

[LK11] D. Lee and D. Kim. Three-dimensional thermohydrodynamic analyses of rayleigh step air foil thrust bearing with radially arranged bump foils. *Tribology Transactions*, 54(3):432–448, 2011.

[LKA+05] Y. B. Lee, C. H. Kim, S. Y. Ahn, Y. M. Choi, B. K. Ahn, and J. Oh. Turbo blower for 80 kw proton exchange membrane fuel cell vehicle. *5th WSEAS Int. Conf. on Power Systems and Electromagnetic Compatibility*, pages 182–187, 2005.

[LKCS11] Y.-B. Lee, Y.-S. Kwak, J. T. Chung, and K. Sim. Microturbocharger with air foil bearings for a 100-w class micro power system and improvement of rotordynamic performance. *Tribology Transactions*, 54(6):939–948, 2011.

[LKK08] D.-H. Lee, Y.-C. Kim, and K.-W. Kim. The static performance analysis of foil journal bearings considering three-dimensional shape of the foil structure. *Journal of Tribology*, 130(3):031102–1–10, 2008.

[LKKK11] Y.-B. Lee, T. Y. Kim, C. H. Kim, and T. H. Kim. Thrust bump air foil bearings with variable axial load: theoretical predictions and experiments. *Tribology Transactions*, 54(6):902–910, 2011.

[LKKK12] Y.-B. Lee, C. H. Kim, T. H. Kim, and T. Y. Kim. Effects of mesh density on static load performance of metal mesh gas foil bearings. *Journal of Engineering for Gas Turbines and Power*, 134(1):012502, 2012.

[LKKS13] Y.-B. Lee, S. B. Kwon, T. H. Kim, and K. Sim. Feasibility study of an oil-free turbocharger supported on gas foil bearings via on-road tests of a two-liter class diesel vehicle. *Journal of Engineering for Gas Turbines and Power*, 135(5):052701, 2013.

[LLAF07a] S. Le Lez, M. Arghir, and J. Frene. A new bump-type foil bearing structure analytical model. *Journal of Engineering for Gas Turbines and Power*, 129:1047–1057, 2007.

[LLAF07b] S. Le Lez, M. Arghir, and J. Frene. Static and dynamic characterization of a bump-type foil bearing structure. *Journal of tribology*, 129(1):75–83, 2007.

[LS15] A. Lehn and B. Schweizer. Generalized reynolds equation for fluid film problems with arbitrary boundary conditions: application to double-sided spiral groove thrust bearings. *Archive of Applied Mechanics*, 86(4):743–760, 2015.

[MF98] E. E. Marotta and L. S. Fletcher. Thermal contact conductance for aluminum and stainless-steel contacts. *Journal of thermophysics and heat transfer*, 12(3):374–381, 1998.

[MK07] L. Moraru and T. G. Keith. Lobatto point quadrature for thermal lubrication problems involving compressible lubricants. ehl applications. *Journal of Tribology*, 129(1):194–198, 2007.

[MLS16] M. Mahner, A. Lehn, and B. Schweizer. Thermogas- and thermohydrodynamic simulation of thrust and slider bearings: Convergence and efficiency of different reduction approaches. *Tribology International*, 93:539–554, 2016.

[Mor05] L. Moraru. *Numerical predictions and measurements in the lubrication of aeronautical engine and transmission components*. Phd, University of Toledo, 2005.

[MP52] K. Millsaps and K. Pohlhausen. Heat transfer by laminar flow from a rotating plate. *Journal of the Aeronautical Sciences*, 19(2):120–126, 1952.

[MP65] S. B. Malanoski and C. H. T. Pan. The static and dynamic characteristics of the spiral-grooved thrust bearing. *Journal of Basic Engineering*, 87(3):547–555, 1965.

[MTM85] A. Mori, K. Tanaka, and H. Mori. Effects of fluid inertia forces on the performance of a plane inclined sector pad for an annular thrust bearing under laminar condition. *Journal of tribology*, 107(1):46–52, 1985.

[Mui64] E. A. Muijderman. *Spiral groove bearings*. Phd, University of Delft, 1964.

[NHT03] N. Noda, R. B. Hetnarski, and Y. Tanigawa. *Thermal Stresses*. Taylor & Francis, 2003.

[OO91] C. L. Ong and J. M. Owen. Computation of the flow and heat transfer due to a rotating disc. *International Journal of Heat and Fluid Flow*, 12(2):106–115, 1991.

[OR89] J. M. Owen and R. H. Rogers. *Flow and heat transfer in rotating disc systems, Vol. 1: Rotor-Stator systems*. Wiley & Sons, New York, 1989.

[Pin90] O. Pinkus. *Thermal aspects of fluid film tribology*. American Society of Mechanical Engineers, 1990.

[PK04] Z.-C. Peng and M. M. Khonsari. On the limiting load-carrying capacity of foil bearings. *Journal of tribology*, 126(4):817–818, 2004.

[PK06] Z. C. Peng and M. M. Khonsari. A thermohydrodynamic analysis of foil journal bearings. *Journal of tribology*, 128(3):534–541, 2006.

[PKJL08] D.-J. Park, C.-H. Kim, G.-H. Jang, and Y.-B. Lee. Theoretical considerations of static and dynamic characteristics of air foil thrust bearing with tilt and slip flow. *Tribology International*, 41(4):282–295, 2008.

[PS65] C. H. T. Pan and B. Sternlicht. Distortion of gas thrust bearing due to viscous shear. Report MTI-65TR49, DTIC Document, 1965.

[PS67] C. H. T. Pan and B. Sternlicht. Thermal distortion of spiral-grooved gas-lubricated thrust bearing due to self-heating. *Journal of Lubrication Technology*, 89(2):197–202, 1967.

[RC75] C. L. Robinson and A. Cameron. Studies in hydrodynamic thrust bearings. i. theory considering thermal and elastic distortions. *Philosophical Transactions of the Royal Society of London A: Mathematical, Physical and Engineering Sciences*, 278(1283):351–366, 1975.

[RD02] K. C. Radil and C. DellaCorte. The effect of journal roughness and foil coatings on the performance of heavily loaded foil air bearings. *Tribology transactions*, 45(2):199–204, 2002.

[RM76] S. M. Rohde and G. T. McAllister. On the optimization of fluid film bearings. *Proceedings of the Royal Society of London A: Mathematical, Physical and Engineering Sciences*, 351(1667):481–497, 1976.

[Ryu11] K. Ryu. *Effect of cooling flow on the operation of a hot rotor-gas foil bearing system*. Phd, Texas A&M University, 2011.

[Ryu12] K. Ryu. Prediction of axial and circumferential flow conditions in a high temperature foil bearing with axial cooling flow. *Journal of Engineering for Gas Turbines and Power*, 134(9):094503–1–6, 2012.

[Sad05] M. H. Sadd. *Elasticity: Theory, Applications and Numerics*. Elsevier Butterworth-Heinemann, 2005.

[SAK10] L. San Andres and T. H. Kim. Thermohydrodynamic analysis of bump type gas foil bearings: A model anchored to test data. *Journal of Engineering for Gas Turbines and Power*, 132(4):042504–1–10, 2010.

[SG97] H. Schlichting and K. Gersten. Grenzschicht-theorie, 1997.

[She09] I. V. Shevchuk. *Convective heat and mass transfer in rotating disk systems*. Springer Science & Business Media, 2009.

[SHW03] M. Salehi, H. Heshmat, and J. F. Walton. On the frictional damping characterization of compliant bump foils. *Journal of tribology*, 125(4):804–813, 2003.

[SK07] J.-h. Song and D. Kim. Foil gas bearing with compression springs: Analyses and experiments. *Journal of Tribology*, 129(3):628, 2007.

[SK12] K. Sim and T. H. Kim. Thermohydrodynamic analysis of bump-type gas foil bearings using bump thermal contact and inlet flow mixing models. *Tribology International*, 48:137–148, 2012.

[SKK13] S. K. Shrestha, D. Kim, and Y. C. Kim. Experimental feasibility study of radial injection cooling of three-pad air foil bearings. *Journal of Tribology*, 135(4):041703, 2013.

[SLK14] K. Sim, Y.-B. Lee, and T. H. Kim. Rotordynamic analysis of an oil-free turbocharger supported on lobed gas foil bearings - predictions versus test data. *Tribology Transactions*, 57(6):1086–1095, 2014.

[SLKL12] K. Sim, Y. B. Lee, T. H. Kim, and Y. Lee. Rotordynamic performance of shimmed gas foil bearings for oil-free turbochargers. *Journal of Tribology*, 134(3):031102, 2012.

[Sny63] W. T. Snyder. The nonlinear hydrodynamic slider bearing. *Journal of Basic Engineering*, 85(3):429–433, 1963.

[Sny65] W. T. Snyder. Temperature variations across the lubricant film in hydrodynamic lubrication. *Applied Scientific Research*, 14(1):1–12, 1965.

[SSH01] M. Salehi, E. Swanson, and H. Heshmat. Thermal features of compliant foil bearings - theory and experiments. *Journal of Tribology*, 123(3):566–571, 2001.

[Sta12] B. J. Stahl. *Thermal Stability and Performance of Foil Thrust Bearings*. Master thesis, Case Western Reserve University, 2012.

[SY94] M. R. Sridhar and M. Yovanovich. Review of elastic and plastic contact conductance models - comparison with experiment. *Journal of Thermophysics and Heat Transfer*, 8(4):633–640, 1994.

[TG51] S. Timoshenko and J. Goodier. *Theory of elasticity*. McGRAW-HILL BOOK COMPANY, New York, 1951.

[VWP+06] P. Vleugels, T. Waumans, J. Peirs, F. Al-Bender, and D. Reynaerts. High-speed bearings for micro gas turbines: stability analysis of foil bearings. *Journal of Micromechanics and Microengineering*, 16(9):S282–S289, 2006.

[WA75] J. Walowit and J. Anno. *Modern developments in lubrication mechanics*. Applied Science Publishers Ltd, 1975.

[Wri06] P. Wriggers. *Computational contact mechanics*. Springer, 2006.

[XWH+97] L.-Y. Xiong, G. Wu, Y. Hou, L.-Q. Liu, M.-F. Ling, and C.-Z. Chen. Development of aerodynamic foil journal bearings for a high speed cryogenic turboexpander. *Cryogenics*, 37(4):221–230, 1997.

[Yov81] M. Yovanovich. New contact and gap conductance correlations for conforming rough surfaces. *AIAA-81-1164*, 1981.

[YR67] M. Yovanovich and W. Rohsenow. Influence of surface roughness and waviness upon thermal contact resistance. Report 76361-48, Massachusetts Institute of Technology, 1967.

[Zie57] O. C. Zienkiewicz. Temperature distribution within lubricating films between parallel bearing surfaces and its effect on the pressures developed. *Proceedings of Conference on Lubrication and Wear*, 1957.

List of abbreviations

AFB	air foil bearing
AFJB	air foil journal bearing
AFTB	air foil thrust bearing
FE	finite element
HPGF	gap function based on a high number of parameters
IR	infrared
LPGF	gap function based on a low number of parameters
SGB	spiral groove bearing

Nomenclature

$a_{\alpha\beta}$	covariant metric tensor
$a^{\alpha\beta}$	contravariant metric tensor
a_{diff}	thermal diffusivity
$\mathbf{a}_i$	local covariant base vectors
$\mathbf{a}^i$	local contravariant base vectors
A_{pad}	surface of one pad
b	half width of the mechanical contact between top foil and bump foil
$b_{\alpha\beta}$	covariant curvature tensor
b^{α}_{β}	mixed curvature tensor
B	bending stiffness
c_P	isobaric specific heat capacity
c_V	isochoric specific heat capacity
div	divergence operator
D	stretching stiffness
E	elastic modulus
E_{pad}	number of pads in the AFTB

f	friction coefficient defined in equation (2.15)
$f_\square$	body force in $\square$-direction
F	shell middle surface
F_N	normal contact force
F_T	friction force
F_i	abbreviation for integral expressions defined in equations (1.12)
G_i	abbreviation for integral expressions defined in equations (1.12)
Gt	shear stiffness
h	real gap function
h_1	gap height at the leading edge
h_2	gap height at the trailing edge
h_{ref}	reference gap height
h_{min}	minimal gap height
h_{nom}	nominal gap function
h_{shift}	axial rigid body displacement of the rotor disk
h_{dist}	part of the gap function that is induced by a distortion of the rotor disk
h_{mis}	part of the gap function that is induced by misalignment
$H_\square$	distance of surface $\square$ from the reference plane
$H^{\alpha\beta\lambda\mu}$	elasticity tensor
$\mathbf{i}_i$	base vectors of global coordinate system
k	thermal conductivity
k_S	shear correction factor
L_b	length of the bridge
L_{b0}	nominal length of the bridge
m	slope of taper in the cartesian taper land gap function
$\dot{m}$	mass flow
$m^{\alpha\beta}$	moment tensor
$\mathbf{m}^\alpha$	internal force variable defined in equation (3.8)
M	torque
$n^{\alpha\beta}$	stress resultant tensor
$\mathbf{n}^\alpha$	internal force variable defined in equation (3.8)
Nu	Nusselt number defined in equation (4.90)
p	pressure
p_0	reference pressure
p^i	components of the vector of external forces
$\mathbf{p}$	vector of external forces

P	power loss
P	point of shell middle surface
P^*	point of shell continuum
P_i	Legendre polynomials
Pr	Prandtl number
q^α	transverse shear stress vector
$q_{T,in}$	heat flux from the lubricating air film into the top foil
$q_{T,out}$	heat flux from the top foil into the bump foil
$\mathbf{q}$	heat flux
Q	objective function in the optimization
$Q_{disk,ch}$	heat flux from the rotor disk to the fluid in the chamber between pads
$Q_{gap,disk}$	heat flux from the lubricating gap into the rotor disk
$Q_{disk,cool}$	heat flux from the rotor disk to the cooling flow region
$Q_{disk,per}$	heat flux from the rotor disk to the air gap at the periphery of the disk
$Q_{gap,top}$	heat flux from the lubricating gap into the top foil
r	radial coordinate direction
r_{iT}	inner top foil radius
r_{oT}	outer top foil radius
r_{iB}	inner radius of bump strip
r_{oB}	outer radius of bump strip
r_{iR}	inner radius of the rotor
r_{oR}	outer radius of the rotor
r_D	radius of the rotor disk
rpm	revolutions per minute
$\mathbf{r}$	position vector
R	curvature of the representative shell middle surface
R_{spec}	specific gas constant of air
Re^*	modified Reynolds number defined in equation (1.24)
Re_Ω	rotational Reynolds number defined in equation (4.92)
R_B	radius of bump
R_r	radius of rounding
R_{th}	effective thermal resistance per unit length
R_{eff}	effective thermal resistance
R_{TB}	thermal contact resistance between the top and the bump foil
R_{Bb}	thermal contact resistance between the bump foil and the base plate
R_{bump}	thermal resistance of the half bump arc

$R_{a,top}$	average deviation for the top foil (surface roughness)
$R_{a,bump}$	average deviation for the bump foil (surface roughness)
$R_{a,base}$	average deviation for the base plate (surface roughness)
$\mathbf{S}$	Cauchy stress tensor
t	time
t	shell thickness
t_T	top foil thickness
t_B	bump foil thickness
t_D	rotor disk thickness
T	temperature
T_m	cross-film averaged temperature
T_{in}	inlet temperature at the leading edge of the pad
$\mathbf{T}$	viscous stress tensor
u	fluid velocity in x-direction
$\mathbf{u}$	vector of fluid velocity
U	velocity of the disk in x-direction
$U_\square$	surface velocity in x-direction
v	fluid velocity in y-direction
v_i	displacement variables for the shell middle surface
v_{rD}	radial displacement of the disk
v_{zD}	axial displacement of the disk
v_{3T}	axial displacement of the top foil
$\mathbf{v}$	displacement vector for the shell middle surface
V	velocity of the disk in y-direction
$V_\square$	surface velocity in y-direction
w	fluid velocity in z-direction
w_α	components of difference vector $\mathbf{w}$ accounting for rotations and shear deformations of cross sections of the shell
$\mathbf{w}$	difference vector accounting for rotations and shear deformations of cross sections of the shell
W	load capacity of one pad
$W_{bearing}$	load capacity of the whole bearing
$W_\square$	surface velocity in z-direction
$\overline{W}$	nondimensional load capacity defined in equation (2.14)
$\overline{W}_{tl,\Lambda=1}$	nondimensional load capacity of the taper land LPGF for a compressibility number of $\Lambda = 1$

$\overline{W}_{HPGF,\Lambda=\square}$	nondimensional load capacity of the HPGF for a compressibility number of $\Lambda = \square$
$W_{generalized}$	load capacity calculated by the generalized Reynolds equation
$W_{average}$	load capacity calculated by the cross-film averaged Reynolds equation
x_{land}	x-coordinate at which the land region ends and the taper starts
x^i	coordinate directions
α_x	misalignment angle about the x-axis
α_y	misalignment angle about the y-axis
δ_α^β	Kronecker symbol
ϵ	internal energy
η	dynamic viscosity
γ_α	strain variable defined in equations (3.6)
$\kappa_{\alpha\beta}$	strain variable defined in equations (3.6)
$\lambda_\square$	nondimensional parameters for the pad geometry defined in equations (2.8)
Λ	compressibility number
μ_o	friction coefficient between the top foil and the bump foil
μ_u	friction coefficient between the base plate and the bump foil
ν	kinematic viscosity
ν	Poisson's ratio
ν_{CT}	turbulent viscosity
Ω	angular velocity of the disk
ϕ	circumferential coordinate direction
φ	circumferential coordinate direction
φ_1	angular extent of land region in the pad
φ_2	tapered or stepped region in the pad
φ_{hT}	hydrodynamically active region of the top foil
φ_{Top}	total circumferential extent of the top foil
$\varphi_{\alpha\beta}$	strain variable defined in equations (3.6)
φ_{ch}	angular extent of the chamber between pads
Φ	dissipation function
ρ	density
ρ_0	reference density
θ_B	bump angle
θ_{B0}	nominal bump angle
Θ^α	convective coordinates

$\square_{,\alpha}$	derivative with respect to the convective coordinate Θ^{α}
$\square_{\|\alpha}$	covariant differentiation
$\square_{b}$	variables associated with the bridges of the bump foil
$\square_{base}$	variables associated with the base plate of the AFTB
$\square_{B}$	variables associated with the bumps of the bump foil
$\square_{cyl}$	variables associated with a cylindrically sector-shaped pad and a circumferential taper land gap function that is optimized with respect to a maximal load capacity
$\square_{C}$	variables associated with the cooling flow region at the backside of the rotor disk
$\square_{D}$	variables associated with the rotor disk
$\square_{fr}$	variables associated with the inflowing fresh air in the chamber between pads
$\square_{in}$	variables associated with the inlet surface of the pad (leading edge)
$\square_{nC}$	variables associated with the new design of a topologically optimized pad with a deep chamber
$\square_{out}$	variables associated with the outlet surface of the pad (trailing edge)
$\square_{per}$	variables associated with the gap at the periphery of the rotor disk
$\square_{r}$	variables associated with the roundings of the bump foil
$\square_{ref}$	variables representing the characteristic size of a particular variable
$\square_{Sp}$	variables associated with the spiral groove bearing
$\square_{T}$	variables associated with the top foil
$\overline{\square}$	nondimensional variables defined in equations (2.10)
$\overline{\square}$	variables associated with a deformed shell